CRYOGENIC CURRENT COMPARATORS

WITH OPTIMUM SQUID READOUT

FOR CURRENT AND RESISTANCE QUANTUM METROLOGY

Cover: Schematics of a Cryogenic Current Comparator with direct coupling to a dc SQUID readout sensor.

The work described in this thesis has been financially supported by the "Stichting voor Technische Wetenschappen" (STW) and the National Metrology Institute (Delft). It has been performed in the Low Temperature Division of the Dept. of Applied Physics at the University of Twente, 7500 AE Enschede, The Netherlands, in co-direction with the Dept. of Condensed Matter at the University of Zaragoza, 50009 Zaragoza, Spain.

E. Bartolomé,
"Cryogenic Current Comparators with optimum SQUID readout for current and resistance quantum metrology",
Proefschrift Universiteit Twente, Enschede.

ISBN 90-365-1701X
Druk: Ipskamp Print Partners, Enschede.

© E. Bartolomé, 2002.

CRYOGENIC CURRENT COMPARATORS

WITH OPTIMUM SQUID READOUT

FOR CURRENT AND RESISTANCE QUANTUM METROLOGY

PROEFSCHRIFT

ter verkrijging van
de graad van doctor aan de Universiteit Twente,
op gezag van de rector magnificus,
prof. dr. F.A. van Vught,
volgens besluit van het College voor Promoties
in het openbaar te verdedigen
op vrijdag 1 maart 2002 te 15:00 uur.

door

María Elena Bartolomé Porcar
geboren op 21 augustus 1974
te Zaragoza (Spanje)

Dit proefschrift is goedgekeurd door:

Prof. dr. H. Rogalla (promotor)
Dr. ir. J. Flokstra (assistent-promotor)
op de Universiteit Twente.

The direction at the University of Zaragoza has been performed by:
Dr. Conrado Rillo.

Contents

Introduction 9

Part I: The CCC with SQUID readout: Theory 13

1 CCC-SQUID systems 15

1.1 Superconductivity 15
1.2 The Cryogenic Current Comparator 16
1.2.1 Principle of operation of the CCC 16
1.2.2 The ratio error 18
1.3 dc SQUIDs 20
1.3.1 Josephson junctions 20
1.3.2 The dc SQUID 23
1.3.3 Noise in dc SQUIDs 24
1.3.4 The washer type dc SQUID with tightly coupled input coil 26
1.3.4.1 Resonances 28
1.3.5 dc SQUID readout 30
1.3.5.1 Flux modulation scheme with resonant transformer 31
1.3.5.2 Two-Stage system 32
1.4 The CCC with SQUID readout 35
1.4.1 CCC with superconducting flux transformer 35
1.4.2 CCC ideally coupled to the SQUID 39
1.4.3 Influence of external and trapped flux noise 40
1.5 CCC-SQUID bridges 41
References 42

PART II: RESISTANCE BRIDGES BASED ON THE CCC-SQUID 45

2 User-friendly resistor bridges based on the CCC-SQUID 49

2.1 CCC-SQUID resistance bridge in a transportable dewar 49
2.1.1 Description of the bridge 50
2.1.1.1 The cryogenic system 50
2.1.1.2 The CCC-SQUID 52
2.1.1.3 The *R*-bridge electronics 55
2.1.2 Bridge balancing: the “difference compensator” method 56
2.1.3 Test of the new *R*-bridge 58
2.2 Outlook of a planar HTS CCC-SQUID 60
2.2.1 HTS massive CCC’s and planar LTS CCC’s 60
2.2.2 A planar YBCO CCC-SQUID: feasibility and expectations 62
References 62

PART III: ULTRA SENSITIVE CCC-SQUID CURRENT AMPLIFIER 63

3 Low (white) noise, well coupled SQUIDs 65

3.1 Fabrication and test of Nb/Al based SQUIDs 66
3.1.1 Nb/Al SQUID fabrication process 66
3.1.2 SQUID characterization set-up 69
3.2 Matched SQUIDs for CCC 70
3.2.1 Design 70
3.2.2 Fabrication and characterization 71
3.3 80$\hbar$, direct coupled SQUIDs 72
3.3.1 Design 73
3.3.2 Specific capacitance determination 75
3.3.3 PdAu characterization 75
3.3.4 Fabrication and characterization 76
3.3.5 Large β_c SQUIDs 77
3.3.6 Resonances 78
3.4 Double-barrier junction based dc SQUIDs 80
3.4.1 Design and fabrication 80
3.4.2 Characterization at 4.2 K 81
3.4.3 Temperature dependence 82
3.5 Noise measurements 85
3.6 Conclusions 89
References 90

4 SQUID readout 93

4.1 SQUID and electronics contribution to the noise 93
4.2 Readout with flux-modulation electronics 95
4.2.1 "Oxford Instruments" electronics 95
4.2.2 "19 Channel" home-made electronics 100
4.2.3 "Conductus" electronics 100
4.3 Two-Stage: SQUID for CCC + reference junction DROS 101
4.4 Comparison of the electronics 104
4.5 Conclusions 108
References 109

5 Low frequency noise reduction 111

5.1 Sources of 1/*f* noise and corresponding reduction techniques 111
5.2 LTS slotted SQUIDs 115
5.2.1 Slotted SQUIDs theory 115
5.2.2 Washer-structured SQUID design 118

5.2.3 Measurements 121
5.2.3.1 Fabrication and Characterization; coupling 121
5.2.3.2 Noise measurements 122
5.3 1/*f* noise reduction by modulation at flux transformer 123
5.3.1 Modulation at the flux transformer technique 124
5.3.2 CCC-SQUID with modulation at the flux transformer 125
5.3.3 Experimental verification of the signal-modulation technique 129
5.3.3.1 Experimental set-up 129
5.3.3.2 Measurements 130
5.4 Conclusions 133
References 133

6 CCC-SQUID system integration 135
6.1 Test 1:1, large CCC 135
6.1.1 Description of the system 136
6.1.2 Superconducting bonding 137
6.1.3 Experiments 139
6.2 1:30 000 CCC 143
6.2.1 Description of the system 143
6.2.2 Experiments 147
6.2.3 Current uncertainty; frequency considerations 152
6.3 Conclusions 153
References 154

7 An outlook of the Quantum Metrological Triangle of electrical units 155
7.1 The QMT experiment and implications 155
7.2 Elements in the QMT realization 158
7.3 Equivalent noise circuit of the QMT 161
7.4 QMT uncertainty expectations 162
References 163

Appendix A: Simplified calculus for the design of a CCC 165
Appendix B: Comments on forward estimate of the sensitivity of a CCC 169
Appendix C: Integrated Two-Stage for CCC-SQUID readout 175
Summary 181
Samenvatting (Summary in Dutch) 185
Resumen (Summary in Spanish) 189
Acknowledgements 193
Curriculum Vitae 195

Introduction

Today's scientific and technological developments as well as worldwide trade relations rely on the international acceptance of a set of measurement *units*. The International System of Units[1] (SI), adopted throughout the world since 1960, consists of seven basic units, from which all the others can be derived according to physical or chemical equations. The National Metrology Institutes (NMI's), in cooperation with the BIPM (Bureau International des Poids et Measures), are in charge of the realization of the units according to their SI definition, the storage of the results as representations (standards) of the units and the dissemination to all users. The *direct realization* of the unit involves complex, laboratory dependent experiments. Alternatively, *quantum standards*, based on quantum physical effects provide very reproducible, environmental independent, non time-drifting references linked to natural fundamental constants. Quantum standards have been adopted in the last decade as primary standards because the reproducibility of the quantum effects (10^{-9}) is much better than the uncertainty attained from the direct realization of the units (10^{-7}). One should bare in mind though that these quantum references are very precise *reproductions* but not realizations of the units.

Concerning electrical units, the discovery of the Quantum Hall Effect[2] (QHE) and the ac Josephson effect[3] made the establishment of the quantum standards for resistance and voltage respectively possible. The quantum current standard, at present under development, could be based on the Single Electron Tunneling (SET) effect[4]. The availability of the three quantum standards would allow closing the metrological triangle of electrical units[5]. This experiment, which would consist in realizing Ohm's law ($V=IR$) using the voltage, resistance and current quantum standards, would allow the verification of the coherence of the fundamental constants involved with a high level of accuracy.

Primary quantum standards are used to calibrate secondary (classical) standards, which on their turn serve to calibrate other standards and instruments. Therefore, the existence of extremely accurate calibration methods is very important, to avoid the progressive lost of information in the chain of measurements. At present, the most accurate resistance and current comparison bridges are both based on the Cryogenic Current Comparator (CCC) with a Superconducting Quantum Interference Device (SQUID) readout.

The CCC works basically as a dc-dc current transformer. The so-called type I CCC[6] consists in essence of a superconducting tube containing two sets of windings N_1 and N_2, carrying the two currents I_1 and I_2 to be compared. As a result of the Meissner effect, a screening current equal to the difference in magnetomotive forces (I_2N_2-I_1N_1) will circulate in the tube. The flux associated to this unbalance current, is then coupled to a dc SQUID, at present the most sensitive flux sensor existing. The superconducting tube, usually made of lead, is overlapped "like a snake swallowing its own tail" to shield the windings from the sensing circuit. Using this system, current ratios $I_2/I_1=N_1/N_2$ with a relative accuracy better than 10^{-10} can be achieved.

The SQUID is basically a superconducting ring interrupted by one (rf SQUID) or two (dc SQUID[7]) weak links, called Josephson junctions. The device works basically as a flux-to-voltage converter. In practice it can be used to sense any kind of signal that can be converted into flux. Thanks to this versatility, SQUIDs have a wide field of application in areas such as biomagnetism, particle and gravitational wave detection[8], non-destructive evaluation, susceptometry and magnetic microscopy. In metrology, SQUIDs are used not only in the readout of CCC's, but also as nano/pico-voltmeters, or voltage-to-frequency converters (R-SQUID) and preamplifiers in low temperature thermometry. Today's most sensitive SQUIDs are based on the washer type dc SQUID, fabricated in Nb/Al low T_c (critical temperature) superconducting thin film technology.

The CCC-SQUID has been mainly used in resistance ratio bridges[9]. The uncertainty reached ($<10^{-8}$) in the calibration of standard resistors to the QHE and the comparison of secondary resistor is at least one order of magnitude better than that attained by room temperature bridges. The need for helium recycling facilities to operate the CCC-SQUID bridge has limited its use to a few specialized laboratories, mostly NMI's. This fact triggered our interest to develop a user-friendly CCC-SQUID system, mainly intended for routine calibration of secondary resistors, that could be easily cooled down in a commercial transportable Dewar (periodically refilled outside the user's institute or industry). The system developed in this thesis could reach e.g. an uncertainty of 7.10^{-9} in the comparison of two 100:100 Ω resistors.

The CCC-SQUID is also a key element in the future establishment of a quantum current standard[10]. Today's best SET devices can deliver quantized currents $I=ef$ (e the electron charge) with quantum precision, only for clock frequencies $f<10$ MHz. Hence the yielded current is very small (1-10 pA), and still not useful for practical calibrations. A large-ratio CCC-SQUID is necessary to amplify the pA current to the μA level without losing the relative accuracy. In this thesis we aimed to develop a complete large ratio (1:30000) CCC-SQUID system for accurate SET current amplification. The final current resolution of a CCC-SQUID system will be determined by the sensitivity of the SQUID, and the efficiency of the coupling between the CCC and the SQUID. Conventional systems can be limited by the use of a commercial SQUID, non-optimally coupled to the CCC. We aimed to improve the current resolution by using a home-made low-noise SQUID, directly coupled to the CCC, in a configuration in which optimal coupling is obtained per definition. An integrated set-up has been successfully completed, reaching an experimental current noise level ~3.0

fA/Hz$^{1/2}$ (down to 0.1 Hz), which implies that a SET current of 10 pA could be measured with an uncertainty ~10^{-6} in a 2 h measurement.

The University of Twente, the NMi van Swinden laboratory (The Netherlands) and the University of Zaragoza (Spain) work together since 1997 in the optimization of CCC-SQUID systems for resistance and current standard bridges. The present work has been performed in the frame of this collaboration. The thesis is divided in three different parts.

In the *first*, *theoretical part*, after a brief review of some superconductivity concepts, the basic principles of the CCC, Josephson junctions and the dc SQUID will be presented. The design guidelines to obtain optimal current resolution in a complete CCC-SQUID system will be discussed.

The *second part* treats the application of the *CCC-SQUID to resistance bridges*. The quantum standard of resistance and the different calibration methods allowing the traceability of resistances to the QHE will be introduced. The need to develop accurate, user-friendly resistor bridges for the calibration of secondary resistors will become apparent. Chapter 2 describes the development of a user-friendly CCC-SQUID, and outlooks the possibility of a CCC-SQUID fabricated completely in planar HTS technology.

The *third part*, containing several chapters, deals with the development of a *CCC-SQUID system for SET current amplification*, towards the establishment of the quantum current standard and, eventually, the closure of the metrological triangle. The development of different sorts of low-noise dc SQUIDs, able to couple optimally to the CCC will be presented in Chapter 3. The electronic readout of these SQUIDs will be the subject of Chapter 4. In Chapter 5 the reduction of flicker noise affecting the SQUID at the very low operation frequency of the system (10^{-3}-1 Hz) will be treated. The integration of a complete large ratio CCC with optimal coupling to the readout SQUID is described in Chapter 6. An outlook of the metrological triangle experiment and the levels of uncertainty expected will be presented in Chapter 7. Finally, a summary of the main results and conclusions closes this thesis.

References

[1] SI brochure, Bureau International des Poids et Mesures, www.bipm.fr, 7th edition (1997).
[2] K. Klitzing *et al*., *Phys. Rev. Lett*. **45**(6), 494 (1980).
[3] B.D. Josephson, *Phys. Rev. Lett*. **1**, 251 (1962).
[4] L.J. Geerlings *et al*., *Phys. Rev. Lett*. **64**, 22, 2691 (1990).
[5] F. Piquemal and G. Geneves, *Metrologia*. **37**(2), 207 (2000).
[6] I.K. Harvey, *Rev. Sci .Instrum*. **43**, 1626 (1972).
[7] R.C. Jaklevic *et al*., *Phys. Rev. Lett*. **12**, 159 (1964).
[8] Ed. D.G. Blair, *The detection of gravitational waves*, Cambridge University Press, Cambridge (1993).
[9] F. Delahaye, *IEEE Trans. Instrum. Meas*. **27**, 426, (1978).
[10] Y. de Wilde *et al*., *IEEE Trans. Instrum. Meas*. **50**, 231, (2001).

Part I

THE CRYOGENIC CURRENT COMPARATOR WITH SQUID READOUT: THEORY

Chapter 1

CCC-SQUID SYSTEMS

The Cryogenic Current Comparator (CCC) with Superconducting Quantum Interference Device (SQUID) readout is the most accurate system to compare two currents. Both the CCC and the SQUID are based on superconducting effects. The basics of superconductivity are summarized in section 1.1. The principle of operation and concepts of the CCC are presented in section 1.2. The current unbalance in the CCC, converted to a flux signal, is read out by a dc SQUID. Section 1.3 revisits the fundamentals of the dc SQUID theory. Finally, section 1.4 describes the operation of a complete CCC-SQUID system, and its application to resistance and current bridges (section 1.5).

1.1. Superconductivity

Superconductors are a group of materials showing particular physical properties[1]; we sketch here only the superconducting effects necessary to understand the operation of the CCC-SQUID.

The electrical resistance of these materials drops abruptly to zero at a critical temperature T_c. Two kinds of superconductors can be distinguished: type I and type II. Below T_c, a type I superconductor shows perfect diamagnetism. The flux density $\boldsymbol{B}$ inside the bulk is 0, phenomenon known as the *Meissner effect*. $\boldsymbol{B}$ decreases within a distance λ_L (London penetration depth) from the surface of the material. The expulsion of magnetic field is caused by screening supercurrents flowing in this external layer. Type II superconductors only show perfect diamagnetism below a certain field H_{c1}, above which some vortices can penetrate the material. For fields larger than a field H_{c2} the material is completely filled with vortices and passes to the normal state. In both sorts of superconductors, and below T_c, the strong electron-phonon interaction makes it energetically more favorable for the electrons to condensate in Cooper pairs that can travel through the crystal lattice without collisions. Cooper pairs behave like bosons, and can be described by the macroscopic wave function: $\Psi = |\Psi| \cdot e^{i\delta}$ (δ is the phase of the wave

function). At T=0 K, all Cooper pairs occupy the Fermi level E_F, located in the center of an energy gap ΔE, which is the energy necessary to break the superconducting state. These concepts will be relevant for the understanding of the Josephson junction, on which SQUIDs are based. Another important effect for the operation of the SQUID is the *flux quantization*, which states that the total magnetic flux enclosed by a superconductor ring is quantized in units of $\Phi=n\Phi_0$, where $\Phi_0=h/2e=2.07.10^{-15}$ Wb is the *flux quantum*.

Superconductors are generally divided in two families. Low T_c metallic superconductors (LTS), e.g. Pb, Nb or NbN, are operated at 4.2 K in liquid helium. The SQUIDs described in this thesis are made of niobium ($T_{c,Nb}$=9.2 K), and aluminium ($T_{c,Al}$=1.1 K). The complex 3D geometry of the CCC and its shields are made of soft, moldable lead ($T_{c,Pb}$=7.2 K). Much higher critical temperatures are observed in some ceramic materials, such as $YBa_2Cu_3O_{7-\delta}$ ($T_{c,YBCO}$~92 K), and since recently[2] in metallic MgB_2 ($T_{c,MgB2}$~39 K). The fabrication of complex SQUID-based chips or CCC's with these HTS materials is still intricate.

1.2. The Cryogenic Current Comparator

The Cryogenic Current Comparator (CCC), introduced for the first time by Harvey[3] in 1972, is basically a current transformer, thanks to which the ratio I_1/I_2 between two currents can be determined with an error better than 10^{-10}. By profiting from the properties of superconductors and operation at cryogenic temperatures, the CCC can attain current resolution levels 4 orders of magnitude better than conventional Current Comparators (CC) working at room temperature, used e.g. in resistance bridges (see Part II). The main concepts about the CCC transformer are discussed in this section.

1.2.1. Principle of operation of the CCC

The principle of operation of a CCC is illustrated in Figure 1.1. Imagine that N_1 wires, carrying a current I_1, and N_2 wires carrying an opposite current I_2, are placed inside a superconducting hollow cylinder. Ampere's law states that the integral of the magnetic field along a contour C is equal to μ_0 (the vacuum permeability) times the integral of the current density $\boldsymbol{J}$ through the surface S enclosed by this path[4]. For a cylindrical geometry, the magnetic field enclosed by the path C is proportional to the sum of all currents and independent of the position of the current leads, thus Ampere's law reduces to:

$$\oint_C \boldsymbol{B}\cdot d\boldsymbol{l} = \mu_0 \int_S \boldsymbol{J}\cdot \boldsymbol{n} d\boldsymbol{a} = \mu_0 \sum I. \tag{1.1}$$

If the integration contour C is chosen inside the superconductor, the integral of the current density will be zero, since $\boldsymbol{B}$=0. In consequence, a Meissner current $-I_i$ appears in the interior of the tube to compensate the unbalance between the two applied currents. For continuity, this current returns through the external surface as I_e:

$$I_e = -I_i = (N_1 I_1 - N_2 I_2). \tag{1.2}$$

Therefore, it is possible to compare two currents I_1, I_2 with a well-defined ratio N_1/N_2, if we are able to exclude other field sources and detect accurately I_e. In practice, this is done by

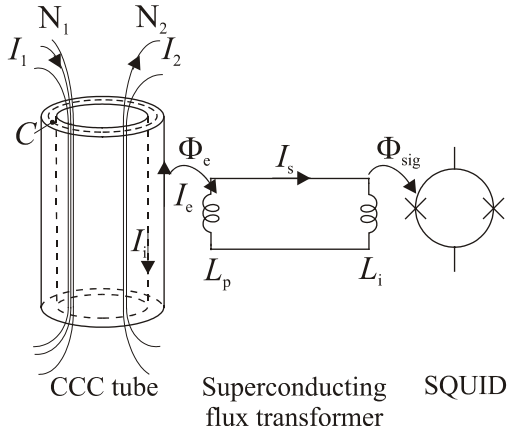

Figure 1.1- *Principle of operation of a CCC with SQUID readout.*

measuring the flux Φ_e created by the current I_e with a SQUID, at present the most sensitive flux detector. Φ_e is usually sensed by a pick-up coil connected to the input coil of the SQUID, forming a superconducting flux transformer.

The flux measured by the SQUID should be uniquely the one caused by I_e, and not by the currents I_1, I_2.. Hence, the wires N_1, N_2 have to be shielded from the flux sensor. Two different configurations have been proposed for this purpose. In the type I CCC geometry[5], the superconducting tube is overlapped over itself like a snake swallowing its own tail, and contains the primary windings (Figure 1.2a). Only a very small flux can leak via the small gap left at the point where the tube overlaps. In a type II CCC[6], the primary turns are placed outside the overlapped tube, whereas the sensing coil is inside the tube (Figure 1.2b). The type I CCC is preferable when large current ratios are required, given its simplicity of construction, small ratio error and better sensitivity than a type II CCC with similar dimensions. In the following we will always refer to type I CCCs.

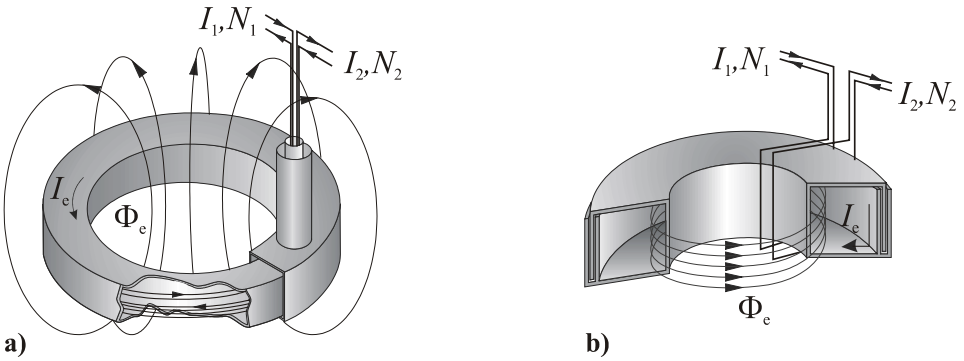

Figure 1.2- *a) Type I CCC; b) type II CCC.*

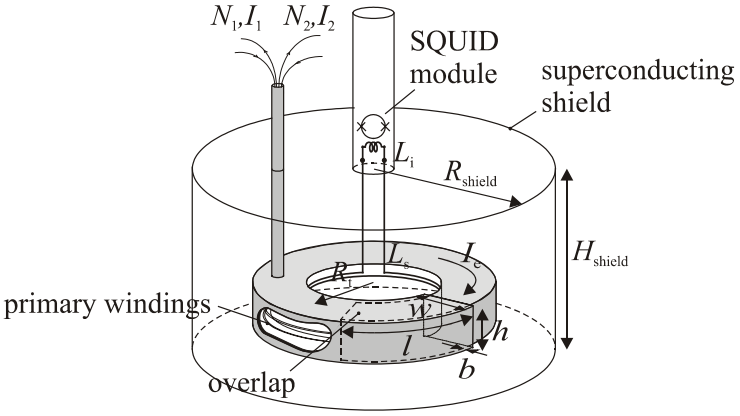

Figure 1.3- *Typical general aspect of a type I CCC connected to the SQUID, inside the superconducting shield. The inductance of the torus is reduced by the image effect of the shield. The relevant dimensions for the estimate of the ratio error in a CCC are given.*

The self-inductance of the CCC toroid, L_{CCC}, will play an important role in the optimization of the system current resolution, as will be seen in section 1.4.1. The CCC-SQUID will be surrounded by a closed superconducting shield (Figure 1.3) to avoid the influence of external magnetic noise (section 1.4.3). As a consequence of the "image effect", the nominal L_{CCC} inductance is reduced to an effective value, $L_{CCC,eff}$, which depends on the distance from the overlapped tube to the walls, top and bottom of the shield. $L_{CCC,eff}$ can be calculated with the "method of the strips"[7], or with the help of finite element programs[8], like e.g. Maxwell or Quickfield[9]. A simplified calculus for the optimization of the CCC and its surrounding shield is given in Appendix A.

1.2.2. The ratio error

Due to the open structure of the CCC, magnetic flux leakage cannot be completely eliminated. There is always a small gap through which field from the primary windings can leak and couple into the SQUID, causing a *ratio error*. The ratio error is defined as the deviation of the currents ratio from the ratio winding, when the magnetic flux detector indicates zero. Experimentally, the ratio error is determined as the ratio between the SQUID signal detected when a current I is passed through the series-opposition connection of two windings with equal number of turns, divided by the SQUID signal when the same current is applied to only one of the windings. In short:

$$F = \frac{V(\Phi)_{\infty\infty}}{V(\Phi)_{\infty}} \tag{1.3}$$

An estimate of the dc ratio error of a square-section CCC, described by Seppä *et al.*[10], can be calculated with:

$$F_{e,squared} = \frac{be^{-l\pi/h}}{\pi R_t \ln(\pi R_t / h)}, \tag{1.4}$$

where l is the overlap length, R_t is the mean radius of the CCC torus, h is the height and width of the cross section and b is the gap width of the overlap (Figure 1.3). The expression holds if $b<<h$, $h<<R_t$, $l>>h$, which is in fact a very realistic situation. Figure 1.4 gives an idea of the orders of magnitude of $F_{e,squared}$ as function of the overlap length. One can see that in theory, a very small ratio error could be achieved with only 1 turn overlap. In practice, however, incompletely soldered seam, small holes in the CCC tube or bad shielding of the current leads can cause the ratio error to be larger than expected. According to Eq. 1.4, the ratio error can be improved by having a small cross section h, narrow gap b, maximum radius R_t and long overlap length l. However, the cross section size is determined by the space required to fit the primary turns. The minimum gap size is given by the thickness of the insulation between overlapping layers. The toroid radius is limited by the cryostat dimensions. Thus, in most practical situations the ratio error can only be improved by making a sufficiently long overlap.

Resistive current leakage between the windings can also produce a ratio error. Assume that N primary turns are made of wire of radius r_c and resistivity ρ_c, surrounded by an insulated layer of thickness t_i and resistivity ρ_i. The contribution to the ratio error, calculated with a simple model[11], can be approximated by:

$$F_{I,R-leak} \approx 34 \frac{R_t}{t_i r_c} \frac{\rho_c}{\rho_i} \text{N}. \tag{1.5}$$

Therefore, ρ_c/ρ_i should be as small as possible to minimize $F_{I,R\text{-}leak}$. The windings can be made of superconducting wire ($\rho_c=0$) to make the $F_{I,R\text{-}leak}$ ratio error exactly zero.

Finally, if the frequency of the current circulating through the windings is high, a current leakage through the parasitic capacitance between the windings will also produce a

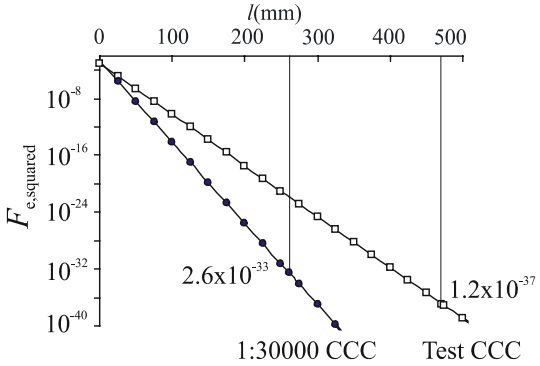

Figure 1.4- *Estimate of the ratio error $F_{e,squared}$ as a function of the overlap length for two real cases (Chapter 6): Test 1:1 CCC (R_t=75 mm, h=19 mm) and 1:30000 CCC (R_t=41.5 mm, h=12 mm). In both cases b=0.5 mm. The $F_{e,squared}$ for a 1-turn overlap is given.*

ratio error, $F_{I,C\text{-leak}}$. This sets the maximum operation frequency of the CCC. Ac CCC bridges reach always worse ratio errors than dc ones, and their operation frequency is limited to a few Hz.[12] The ratio error due to all different sources of a dc CCC is typically better than 10^{-10}.

1.3. dc SQUIDs

1.3.1. Josephson junctions

The basic element of a SQUID is the *Josephson junction* (jj). The most commonly used type of junction in LTS consists of two superconducting electrodes separated by a thin non-superconducting barrier of thickness d (Figure 1.5a). The wave function of each superconductor $\Psi_{A,B}$ decays exponentially in the barrier within a characteristic *coherence length*, $\xi_{A,B}$. If $d<<\xi_{A,B}$, the two wave functions have an overlap (*weak link*), and Cooper pairs can tunnel through the barrier while the dc voltage across it is zero. This supercurrent I_{CP} depends on the phase difference between the superconducting electrodes, $\delta = \delta_A - \delta_B$ according to the *dc Josephson equation*:

$$I_{CP} = I_0 \sin\delta. \tag{1.6}$$

The maximum supercurrent, I_0, is called the critical current. If a current larger than I_0 is applied to the junction, a voltage V arises, and the phase difference δ becomes time dependent, as given by the *ac Josephson equation*[13]:

$$\frac{\partial\delta}{\partial t} = \frac{2e}{\hbar}V, \tag{1.7}$$

where $\hbar$=1.05x10^{-34} Js is the Dirac constant and e=1.60x10^{-19} C is the electron charge. In consequence, the supercurrent will oscillate sinusoidally, with a *Josephson frequency* $f_J=(2e/2\pi\hbar).\langle V\rangle=(483.59767\ \text{MHz}/\mu\text{V}).\langle V\rangle$.

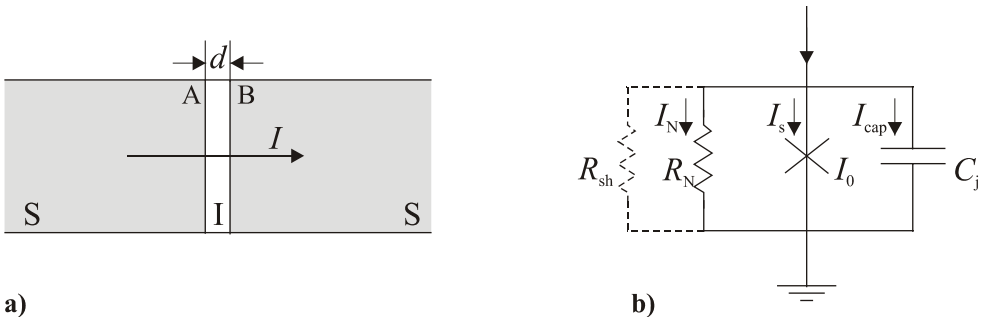

a) **b)**

Figure 1.5- *a) Superconducting Josephson tunnel junction; b) the RCSJ-model for a jj (the optional shunt resistor is depicted in dashed lines).*

In the presence of a potential $V\neq0$, a quasiparticle current will appear. If V is smaller than the gap voltage V_g (2.8 mV for Nb based junctions), only a small amount of thermally excited quasiparticles will be able to tunnel across the junction, thus this current will be very small and temperature dependent. At $V=V_g$, the quasiparticle current will increase abruptly. In terms of the band theory, this happens because quasiparticles from the completely full band (below the Fermi energy E_F) of electrode A can directly tunnel to the almost empty energy band (above E_F) on electrode B. If $V>>V_g$, the quasiparticle current simply follows an ohmic law: $I_N=V/R_N$, where R_N is the intrinsic junction resistance. Also, the two electrodes see the junction barrier as a planar capacitor C_j. Summarizing, the junction can be described by the sum of three contributions[14]: a Cooper pair, quasiparticle and capacitive interaction (Figure 1.5b):

$$I = I_0 \sin\delta + \frac{V}{R_N} + C_j \frac{\partial V}{\partial t} = I_0 \sin\delta + \frac{1}{R_N}\frac{\hbar}{2e}\frac{\partial\delta}{\partial t} + C_j \frac{\hbar}{2e}\frac{\partial^2\delta}{\partial t^2}. \tag{1.8}$$

The current-voltage characteristic (IVC) of the junction will be respectively hysteretic (non-hysteretic) if the so-called Steward McCumber parameter:

$$\beta_c = \frac{2\pi I_0 R_N^2 C_j}{\Phi_0}, \tag{1.9}$$

is larger (smaller) than 1. LTS single-barrier SIS non-shunted junctions are usually hysteretic (Figure 1.6a). The hysteresis can be removed by shunting the junction with an external resistor R_{sh}, such that $\beta_c<1$ (R_N in Eq. 1.9 is then replaced by the parallel resistance $R=R_N//R_{sh}$, in most cases approximately equal to R_{sh}, since $R_N>>R_{sh}$), Figure 1.6b.

Eq. 1.8 can be renormalized by a factor of $\hbar$/2e, to obtain the following energy equation:

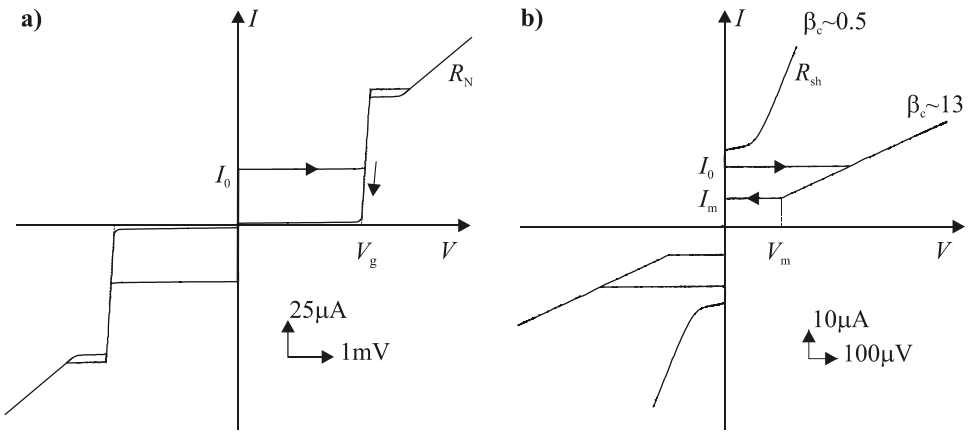

Figure 1.6- *I-V characteristics of LTS (SIS) a) Non-shunted, hysteretic junction; b) Shunted junctions: hysteretic jj (β_c~13) and non hysteretic jj (β_c~0.5).*

$$\left(\frac{\hbar}{2e}\right)^2\left(\frac{1}{R}\frac{\partial\delta}{\partial t}+C_j\frac{\partial^2\delta}{\partial t^2}\right)=-\frac{\partial E}{\partial\delta}\ ,E=-\frac{\hbar I_0}{2e}\left(\frac{I}{I_0}\delta+\cos\delta\right). \tag{1.10}$$

Although Eq. 1.10 cannot be solved analytically due to the cosine term, it can be interpreted with a mechanical analogue[1] that helps understanding qualitatively the IVC of the junction. In this model, E represents a tilted *washboard*-like potential (Figure 1.7a) in which a ball with "mass" C_j is confined. δ represents the "position of the ball", and therefore V is proportional to the "velocity" $\partial\delta/\partial t$ of the particle. The $1/R$ term gives the viscous damping of the motion, and the ratio I/I_0 indicates the relative tilt of the washboard. The height of a potential well at zero current, $\hbar I_0/2e$, is the *Josephson coupling energy*. If $\boldsymbol{I<I_0}$, the ball is trapped in one of the wells, oscillating periodically with a plasma frequency f_p. Then, on the average, the velocity of the ball is zero, and thus the voltage in the superconductor state is $V=0$. If we increase the tilt of the washboard so that $I>I_0$, there will not be local minima anymore and the ball will roll down acquiring a certain "speed", i.e., the voltage in the normal state is $V\neq0$. If $\boldsymbol{I>>I_0}$, the velocity of the ball is determined by the damping $1/R$, hence the system enters the Ohmic regime. When I is decreased (equivalent to recovering the initial tilt of the washboard) the ball will tend to be trapped again. If the movement is only weakly damped (small $1/R$), the inertia of the ball makes it continue rolling even at a slope smaller than the one at which the ball started rolling. In other words, a voltage V will persist until a certain *return minimal current* I_m, smaller than I_0, is reached. A hysteretic IVC will result. However, if the damping is sufficiently large, the ball will be re-trapped at the same tilt at which it started rolling, and no hysteresis will appear.

The most successful kind of jj in LTS thin film technology consists of a "sandwich", formed by a niobium base electrode, a layer of aluminium oxidized to form an insulating Al_2O_3 barrier (~1 nm), an anti-oxidizing top Al layer and a top niobium electrode. These are the highest quality junctions at present. They show small leakage current in the subgap voltage region, a sharply defined gap voltage, and excellent stability both against long term storage and thermal cycles.

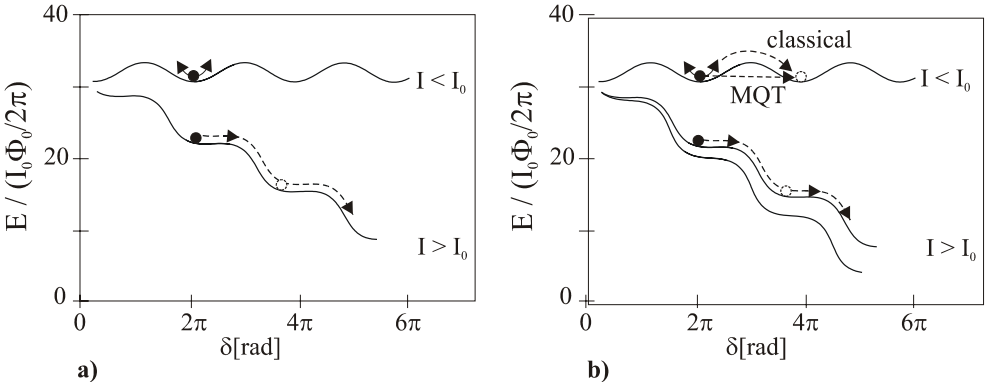

Figure 1.7- *a) Washboard model for the Josephson junction; b) Mechanisms producing white noise.*

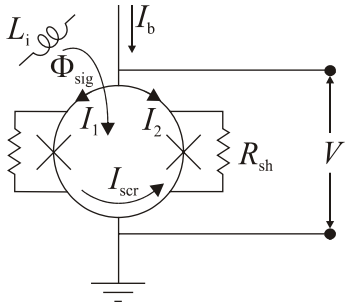

Figure 1.8- *Schematics of a dc SQUID.*

1.3.2. The dc SQUID

Roughly speaking, there are two types of SQUIDs: the *rf SQUID*, based on a superconducting ring interrupted by a single junction, and the *dc SQUID*, including two identical junctions. Most of the devices described in this thesis are dc SQUIDs, since they are more sensitive than rf SQUIDs. A schematic of a dc SQUID is shown in Figure 1.8. It consists of a superconducting ring with inductance L_{sq}, interrupted by two junctions, usually shunted to remove the hysteresis. The dc SQUID is biased with a current I_b. A signal flux Φ_{sig} can be applied via an input coil, with inductance L_i. The principle of operation of the dc SQUID is based on the combination of the flux quantization and the Josephson effect. The flux quantization condition, adapted to take into account the phase differences across the junctions, δ_1 and δ_2, is written as:

$$(\delta_1 - \delta_2) - \frac{2\pi\Phi_{sig}}{\Phi_0} + \frac{2\pi(I_1 - I_2)L_{sq}}{\Phi_0} = 2\pi n \tag{1.11}$$

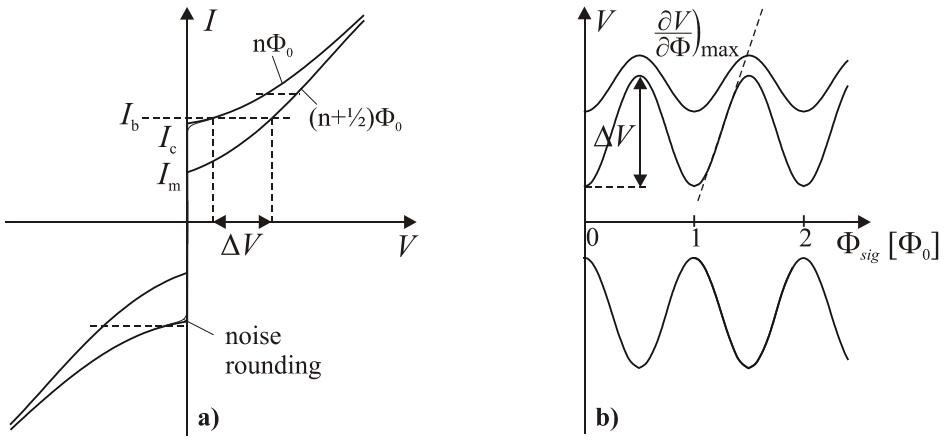

Figure 1.9- *a) I-V characteristic and b) V-Φ curves at several bias points of a non-hysteretic dc SQUID.*

The second and third terms are the phase contribution due to the signal flux Φ_{sig} and the screening current $I_{scr}=(I_1-I_2)/2$. If the signal flux is $\Phi_{sig}=n\Phi_0$, with n an integer, no screening current runs in the SQUID loop, and the bias current distributes symmetrically over the two junctions: $I_1=I_2=I_b/2$ (assuming the two jj's are identical). In this case, the IVC is simply that of two parallel junctions. The SQUID critical current is the maximum, $I_c=2I_0$, and the total resistance is the parallel of the two junction resistances: $R=(R_N//R_{sh})/2\sim R_{sh}/2$.
For non-integer values of Φ_{sig}/Φ_0 a screening current appears as a result of the non-symmetrical distribution of current through the junctions. In consequence, one of the two junctions reaches the critical current before the other does, and the total SQUID critical current is smaller than $2I_0$. For $\Phi_{sig}=(n+1/2)\,\Phi_0$ the uneven distribution of currents through the junctions is the largest, and therefore the critical current reaches a minimum value I_m (Figure 1.9a). The modulation depth of the critical current ΔI_c is given by:

$$\Delta I_c = 2I_0 - I_m \approx \frac{1}{1+\beta}\cdot 2I_0, \tag{1.12}$$

where β is the screening parameter:

$$\beta = \frac{2I_0 L_{sq}}{\Phi_0}. \tag{1.13}$$

In an optimized SQUID, β should be ~1.[15] If the SQUID is biased with a constant bias current $I_b>I_c$, the voltage across the SQUID varies periodically (with period Φ_0) between a maximum and a minimum voltages as a function of the applied flux (Figure 1.9b). Therefore, the SQUID works basically as a flux-to-voltage converter. The transfer function is maximum for values of $\Phi_{sig}=(n+1/4)\,\Phi_0$, and can be approximated to be[16]:

$$\frac{\partial V}{\partial \Phi_{sig}} \approx \frac{2\beta}{1+\beta}\cdot\frac{R}{L_{sq}}. \tag{1.14}$$

For a conventional SQUID, the flux-to-voltage transfer typically amounts ~100 $\mu V/\Phi_0$.

1.3.3. Noise in dc SQUIDs

The minimum flux that can be detected by a SQUID is limited by the flux noise, $S_\Phi^{1/2}(f)$. The typical flux noise spectrum of a dc SQUID presents two regions: below the corner frequency f_c, the noise behaves as $1/f$, whereas above f_c the noise is f independent (*white*). The $1/f$ noise comes from at least two known sources: fluctuations in the critical current of the junctions, due to the random trapping and de-trapping of electrons in the junction barrier, and thermally activated hopping of trapped flux lines in the SQUID washer. Chapter 5 treats more extensively the $1/f$ noise and its reduction techniques.

In order to understand the origin and effects of the white noise, it is useful to consider again the washboard model (Figure 1.7b). Consider first that the bias current is smaller than the noise-free critical current, $\boldsymbol{I_b<I_0}$. The ball, trapped in one of the potential wells, is subject to thermal energy fluctuations. Thanks to this Brownian motion, the ball has a certain probability of escaping from the well and move into the next one(s). If the

junction is **hysteretic**, the ball will roll down the board with little damping. The result will be a change from the superconducting to the voltage state at a current smaller than I_0. In **non-hysteretic** junctions, the ball can only sporadically jump from one well to the next one, since due to the high damping the ball is immediately re-trapped. Thus, voltage pulses are produced across the junction, and this results into a noise rounding[17] of the IVC at a bias current near ~I_0 (Figure 1.7b). Thermal noise becomes important if the thermal energy, $k_B T$ (k_B is Boltzmann's constant, 1.38×10^{-23} J/K), is comparable to the Josephson coupling energy (height of the well) $I_0\Phi_0/2\pi$. For a proper operation of the junction, the noise parameter Γ, defined as the ratio:

$$\Gamma = \frac{2\pi k_B T}{I_0 \Phi}, \tag{1.15}$$

should be smaller than 0.1

Consider now a **(shunted) junction** biased at $\boldsymbol{I_b > I_0}$. Thermal (Nyquist) noise in the shunt resistors will produce a current power noise:

$$S_I = \frac{4k_B T}{R_{sh}} \tag{1.16}$$

In the washboard model, this thermally induced current noise would be seen as random fluctuations in the angle of the tilt, which lead to changes in the velocity of the rolling ball (voltage noise). In a dc SQUID, the noise generated in the two shunt resistors gives an in-phase component and an out-of-phase component, but usually only the first one is significant, and hereon we will always refer to the in-phase noise contribution. The power voltage noise across the SQUID has been numerically calculated to be[16]:

$$S_V = \gamma \cdot 2 S_I \cdot R_{dyn}^2 \approx \gamma \cdot 2 k_B T R, \tag{1.17}$$

where the dynamical resistance of the SQUID, $R_{dyn}=\partial V/\partial I_b$, was approximated by $R/2$, for the common case that $I_b \sim I_0$. The factor γ, somewhat model dependent[16,18], can take $\gamma \sim 8, 9$. This voltage power noise translates into a SQUID power flux noise, via the transfer function of the SQUID:

$$S_\Phi = \frac{S_V}{(\partial V / \partial \Phi)^2} \approx \gamma \cdot \frac{2 k_B T L_{sq}^2}{R}. \tag{1.18}$$

It is normal to describe the sensitivity of the SQUID by the energy resolution:

$$\varepsilon = \frac{S_\Phi}{2L_{sq}} = \frac{\gamma \cdot k_B T L_{sq}}{R}, \tag{1.19}$$

, which is commonly expressed in units of $\hbar$. This equation suggests that decreasing the temperature, one could reduce the sensitivity indefinitely. However, eventually quantum mechanic effects impose a lower limit to ε. In fact, the noise theory developed above is just the classical approximation of a more general theory, which includes the quantum

mechanical effects appearing at very low temperatures or high frequencies compared with the Josephson frequency.

Now in the washboard model, the ball must be treated as a quantum-mechanical wave packet that has a certain probability of penetrating the well barrier by macroscopic quantum tunneling (MQT)[19]. For a bias current $\boldsymbol{I_b<I_0}$, noise rounding is present (even at T=0), due to the possibility for the "ball" to tunnel to consecutive wells. If $\boldsymbol{I_b>I_0}$, a voltage noise appears given by:

$$S_V(0) = \frac{4k_BT}{R} R_{dyn}^2 + \frac{2eV}{R} R_{dyn}^2 \left(\frac{I_0}{I}\right)^2 \cdot \coth\left(\frac{eV}{k_BT}\right). \tag{1.20}$$

The first term stems for noise generated at the measurement frequency, while the second term is noise generated near the Josephson frequency that is mixed down to the measurement frequency by the inherent non-linearity of the junction.
Eq. 1.20 reduces to the Johnson voltage noise given by Eq. 1.17 in the classical limit $eV \ll k_BT$. If $eV \geq k_BT$, the mixed-down term becomes comparable to the first term, and quantum corrections become important. In the extreme *quantum limit*, $eV \gg k_BT$, Eq. 1.20 reduces to:

$$S_V(0) = R_{dyn}^2 \frac{2eV}{R} \left(\frac{I_0}{I}\right)^2, \tag{1.21}$$

and the observed noise is generated solely by *zero point fluctuations* in the shunt resistors. The resistor can be modeled as a large collection of harmonic oscillators, so at T=0, although there are no thermal fluctuations, the zero-point energy still produces fluctuations in the tilt of the washboard generating a randomness in the voltage.

Owing to these quantum effects, the energy resolution of the dc SQUID deviates from the linear classical behavior as temperature decreases. Numerical simulations[20] predict that the energy resolution will tend to $\varepsilon \sim \hbar$. Due to the *hot electron effect*[21] the effective temperature in the shunt resistors can be larger than in the bath, and the energy resolution saturates before the predicted quantum limit is reached.

1.3.4. The washer type dc SQUID with tightly coupled input coil

A very successful SQUID configuration is *the washer type dc SQUID with tightly coupled input coil* fabricated in thin film technology, introduced by Jaycox and Ketchen[22]. The SQUID loop is formed by a square washer with a hole of size D in the center. The washer thickness t must be larger than 2λ to ensure a complete Meissner effect. The signal flux is introduced via an integrated, n-turns input coil placed on top of the washer (an insulating layer is deposited in between to avoid electrical contact). The input coil is wound around the washer hole, and returns through a strip line that separates the washer slit into two slots (Figure 1.10). The total SQUID inductance is the sum of three contributions: $L_{sq}=L_h+L_{slit}+L_p$. The hole inductance can be approximated as:

$$L_h \approx 1.25 \cdot \mu_0 \cdot D, \tag{1.22}$$

if the outer size of the washer is much larger than the hole size (at least >3D). L_p is a (usually) negligible parasitic inductance, due to the area enclosed in the junction region.

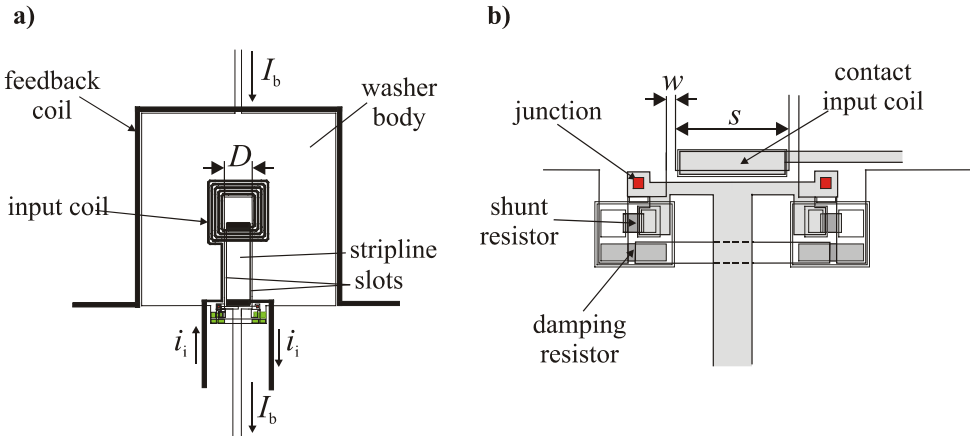

Figure 1.10- *a) Washer type dc SQUID; b) Detail of the junction area (the damping resistors shown are placed to avoid LC washer resonances, see section 1.3.4.1)*

When the hole inductance is small, the slit will contribute significantly to the total SQUID inductance. The *slit inductance* can be estimated as[23]:

$$L_{slit} = l_{slit} \cdot 3600\pi\varepsilon_0 \ln\left(2\frac{1+\sqrt{k}}{1-\sqrt{k}}\right), \quad k = \sqrt{1-\left(\frac{s}{s+2w}\right)^2}, \tag{1.23}$$

where s is the strip line width, w the slot width, l_{slit} the slit length and ε_0 is the dielectric constant in vacuum (=8.85x10^{-12} C^2/N.m^2). The specific slit inductance L_{slit}/l_{slit} is typically 0.3..0.4 pH/μm. The inductance of the input coil is approximately given by:

$$L_i \approx n^2 L_{sq} \tag{1.24}$$

The mutual inductance between the input coil and the SQUID inductance is given in general by:

$$M_i = k_{sq}\sqrt{L_i L_{sq}}\,. \tag{1.25}$$

The coupling factor k_{sq} represents the coupling efficiency, and amounts 0.8..0.9.

The experiments described in section 3.2.2 will show that, because the input coil only covers part of the slit, Equations. 1.24 and 1.25 overestimate the values of L_i and M_i. The formula have to be modified to take into account that only a fraction of the slit will contribute to the coupling between the washer and the input coil, and become:

$$L_i \approx n^2\left(L_h + \frac{1}{3}\frac{n}{n_{\max}}L_{slit}\right) + L_{strip}, \tag{1.26}$$

$$M_i \approx n\left(L_h + \frac{1}{2}\frac{n}{n_{\max}}L_{slit}\right), \tag{1.27}$$

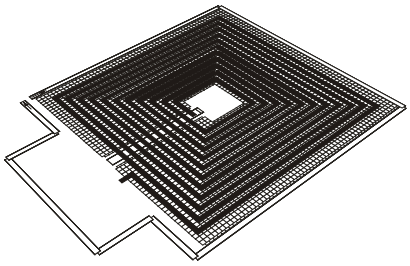

a)

SQUID		Measured	Analytical	Corrected analytical	Fast Henry
"250 pH /9 turns"	L_{sq}(pH)	250	250	250	251
	L_i (nH)	–	20	13.4	13.6
	M_i(nH)	1.25	2.25	1.45	1.29
"200 pH /20 turns"	L_{sq}(pH)	–	200	200	194
	L_i (nH)	–	80	57.9	54
	M_i(nH)	2.68	4.00	2.97	2.60

b)

Figure 1.11- *a) Fast Henry definition of the SQUID. The washer is defined as a ground plane, discretised in a large number of squared segments connected to each other, into which the central hole and slit are defined as holes. In this modelization the current flows around the central hole. The input coil is defined as several linear segments connected at the corners, grouped together to form a single conducting element; b) Comparison between the measured L_{sq}, L_i, M_i and the calculated values using the analytical Eq. 1.23-1.25, the corrected expressions Eq. 1.26-1.28 and Fast Henry (for two SQUIDs described in section 3.2.2).*

where n_{max} is the number of turns that would cover completely the slit. L_{strip} is the strip inductance of the input coil with respect to the SQUID washer:

$$L_{strip} = \mu_0 l\left(\frac{t_i + 2\lambda}{a}\right), \tag{1.28}$$

where t_i is the thickness of the insulator layer between the washer and the input coil and a is the width of the input coil stripline. For a given SQUID with inductance L_{sq}, the maximum signal-to-noise ratio will be obtained when the washer is completely filled with input coil turns, in which case n/n_{max}=1.

Alternatively, L_{sq}, L_i and M_i can be determined using finite element based numerical programs adapted for superconductors (see Ref. 24 for a survey). The self and mutual inductance of some SQUIDs described in this thesis where calculated using the finite element program Fast Henry[25]. The values found agreed with the experimental values within 3% (Figure 1.11). Though Fast Henry yields the most accurate prediction for the inductances, the calculation is very time-consuming. For most design purposes the analytical expressions provide sufficiently good approximations.

1.3.4.1. Resonances

The *I-V* and *V*-Φ curves of a multi-turn washer SQUID can present undesired structures, resulting from resonance phenomena excited by the ac Josephson effect. The performance of the SQUID at those points is degraded, since sometimes the *V*-Φ curves turn so irregular that typical flux locked loop operation becomes difficult. Besides, the complex dynamics

related to resonances usually result in an increase of the flux noise. Therefore, resonances should be properly damped.

Even in the absence of an input coil, *LC* washer resonances[26] occur in the circuit formed by the SQUID inductance L_{sq} in parallel with the junction capacitances C_j. If the substrate on top of which the SQUID is deposited has a small dielectric constant (e.g. SiO_2, ε_r~4), the washer inductance can be treated as a lumped element, and the impedance seen by the junctions will be simply $z_{AB}=j2\pi f L_{sq}$. Washer resonances will appear if the characteristic frequency of the *LC* circuit:

$$f_r = \frac{1}{2\pi\sqrt{L_{sq}C_j/2}}, \tag{1.29}$$

coincides with the Josephson frequency $f_J=2eV/2\pi\hbar$. As a result, the $n\Phi_0$ and $(n+1/2)\,\Phi_0$ IVC branches can cross each other.

Washer resonances are somewhat damped by the shunt resistors, and can be further damped with a resistive/capacitive shunting of the washer across the slot. The addition of a damping resistor R_d across the washer improves the SQUID performance, but it also causes extra Johnson noise. The design of R_d should be a trade-off between damping the *LC* resonances while minimizing the additional noise. To ensure effective overdamping in the equivalent *RLC* tank circuit, the damping parameter $\beta_{damp}=(1/R_d).(L_{sq}/2C_j)^{1/2}$ should be larger than 1. Therefore, the upper limit for the damping resistance is:

$$R_{d,T} < \sqrt{\frac{L_{sq}}{2C_j}}, \tag{1.30}$$

with $R_{d,T}=2R_{sh}//R_d$. On the other hand, the flux noise $L_{sq}^2 S_I$ caused by the current noise of the damping resistor $S_I=4k_BT/R_d$ should be smaller than the noise of the SQUID $S_\Phi=16k_BTL_{sq}^2/R_{sh}$. This condition leads to the lower limit for the damping resistor:

$$R_d > \frac{R_{sh}}{4}. \tag{1.31}$$

In practice, due to mixing-down effects, the effect of the S_I caused by the damping resistor may be larger, so for security the value of R_d is taken around 2 to 3 times larger than R_{sh}.[27] Other methods have been proposed to reduce the influence of washer resonance, like using a double transformer circuit[28], or adding an extra slit in the washer; however the mutual inductance between the input coil and the washer degrades in the later case[29].

When an input coil is present, the *LC* washer resonances occur at much higher frequencies than in the bold SQUID, because the effective washer inductance seen by the junctions $L_{sq,eff}$ is smaller[30]. In addition, lower frequency resonances appear due to standing waves occurring in the input coil transmission line, with length l_i. Those resonances appear at frequencies:

$$f_n = \frac{c}{2l_i}\frac{1}{\sqrt{\varepsilon_r}}n\left(\frac{\lambda}{2}\text{ resonances}\right), \qquad f_n = \frac{c}{4l_i}\frac{1}{\sqrt{\varepsilon_r}}n\left(\frac{\lambda}{4}\text{ resonances}\right), \tag{1.32}$$

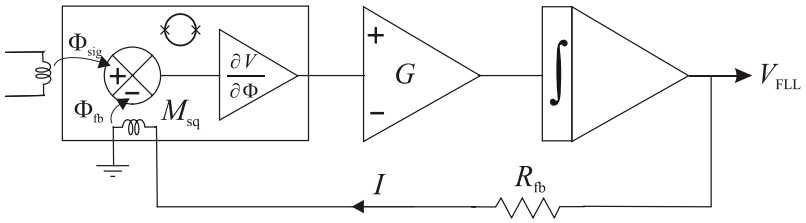

Figure 1.12- *SQUID in flux locked loop scheme.*

respectively if the input coil is opened at both ends (λ/2 resonances) or the input coil is shorted to the washer (λ /4 resonances). Different techniques have been proposed to reduce input coil resonances, e.g.: adding an *RC* filter across the input coil leads, connecting the washer and input coil through an *R* or *R-C* damping[31], introducing shunt resistors across the input coil turns ("intra-coil damping")[32], or placing distributed eddy current damping filters on top of the input coil[33]. None of the methods is able to eliminate completely the effect of input coil resonances, and in general, they add some extra noise.

1.3.5. dc SQUID readout

In order to linearise the periodic SQUID response and obtain a larger dynamic range, the SQUID is usually operated as a *null detector* in a *flux locked loop configuration* (FLL), like in Figure 1.12. The SQUID block consists of an adding point for the signal and feedback flux, and a flux-to-voltage amplifier of gain $\partial V/\partial\Phi$. The forward line contains also a room temperature amplifier of gain G, and an integrator that controls the stability of the loop. The feedback line consists of a resistance R_{fb} that converts the output voltage V_{FLL} into a current, and a feedback coil (with mutual inductance with the SQUID, M_{fb}) that couples the feedback flux into the SQUID. If the SQUID detects a flux change $\delta\Phi_{sig}$, a feedback flux $\delta\Phi_{fb} = M_{fb}.(V_{FLL}/R_{fb}) = -\delta\Phi_{sig}$ is fed back into the SQUID so as to compensate exactly $\delta\Phi_{sig}$.

Since the transfer function of the dc SQUID $\partial V/\partial\Phi$ is usually quite small, the noise in the simplistic FLL configuration described above would be dominated by the room

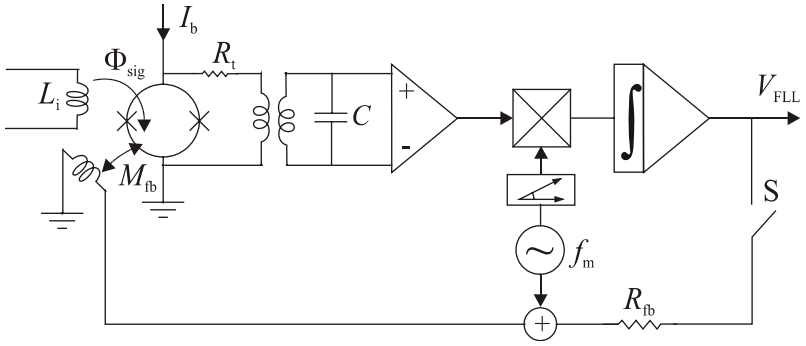

Figure 1.13- *SQUID readout with flux modulation and resonant transformer.*

temperature amplifier. Two different approaches can be followed to avoid this situation: to read out the (standard) dc SQUID with a flux modulation scheme with a resonant transformer, or to use a SQUID based sensor with a much higher flux-to-voltage transfer. The two possibilities are described next.

1.3.5.1. Flux modulation scheme with resonant transformer

A schematic of a typical flux modulation SQUID readout system[34] is shown in Figure 1.13. The SQUID V-Φ curve is flux modulated by a (sinusoidal or block-shaped) signal of peak-to-peak amplitude $\Phi_0/2$ and frequency f_m~100..500 kHz, usually applied via the same line used for the feedback. The signal is modulated at such high frequency to have a large bandwidth of the system. The modulated signal $V_{sq}(t)$ obtained depends on the operation point, as explained in Figure 1.14a1 and a2.

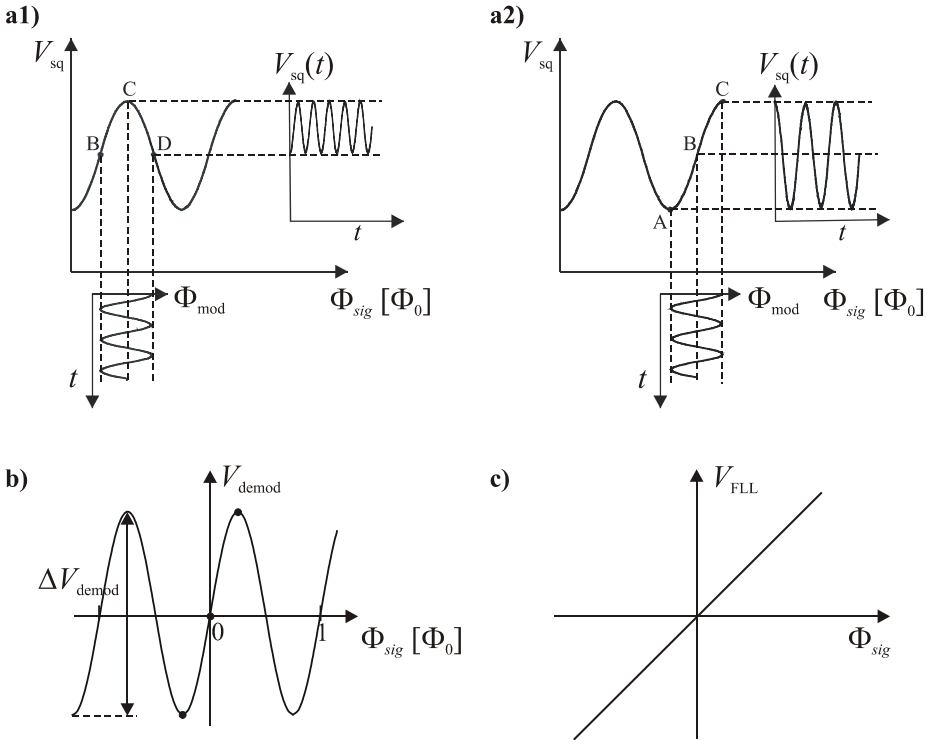

Figure 1.14- *a) Flux modulation at different operation points: a1) $\Phi=n\Phi_0$ point: the $V_{sq}(t)$ will be a rectified version of the input signal, with frequency $2f_m$; a2) $\Phi=(n+1/4)\Phi_0$ point: $V_{sq}(t)$ will be a signal of frequency f_m, in phase (0°) with the input signal; (if $\Phi=(n+3/4)\Phi_0$, $V_{sq}(t)$ would be out-of-phase (180°) with respect to the input signal); b) Demodulated signal V_{demod} as function of the applied flux Φ_{sig} in open loop; c) Closed locked loop V_{FLL} (Φ_{sig}) linear signal.*

In order to have a good noise performance, the output impedance of the SQUID and the preamplifier input impedance have to be matched with an intermediate matching circuit, tuned at the modulation frequency. The matching circuit can consist e.g. of a transformer, an *LC* resonant circuit or a combined, resonant transformer. The latter is the most versatile solution, because of its large transfer factor, and large available bandwidth achieved through a large scaling factor m, and moderate quality factor Q.

After amplification, the modulated signal $V_{sq}(t)$ is lock-in detected, using f_m as reference frequency. The phase between the oscillator and modulated signals are adjusted in order to obtain the maximum output at the lock-in detector. Usually modulation takes place between the points B and D around C. If the switch is S open and a flux $n\Phi_0$ or $(n+1/2)\Phi_0$ enters the SQUID, the demodulated signal V_{demod} will be zero, since $V_{sq}(t)$ is contained only the frequency $2f_m$. V_{demod} will be maximum/minimum respectively if a flux $(n\pm1/4)\,\Phi_0$ is applied. The demodulated curve $V_{demod}(\Phi_{sig})$ will be an amplified, less noisy version of the applied flux signal (Figure 1.14b). In FLL operation the $V_{demod}(\Phi_{sig})$ response is linearized (Figure 1.14c). In other modulation schemes, the bias current is also reversed at a frequency $f_a << f_m$, to get rid of the SQUID $1/f$ noise due to critical current variations (Chapters 5).

1.3.5.2. Two-Stage system

The use of a matching circuit in the flux modulation scheme is an important drawback in applications where a large bandwidth and slew rate are required (e.g. in the readout of X-ray detectors) or where the readout should be as simple as possible (e.g. in multi-channel systems used in biomagnetism). Alternative "second generation SQUIDs", with a larger flux-to-voltage transfer function, have been developed, that allow direct readout without need of transformers or resonant circuits.

An example of this is the Additional Positive Feedback (APF) scheme[35], consisting of a non-hysteretic SQUID shunted by a resistance R_{APF} and an inductance L_{APF} . The latter couples an extra flux that adds to the signal flux, such that the V-Φ curve becomes

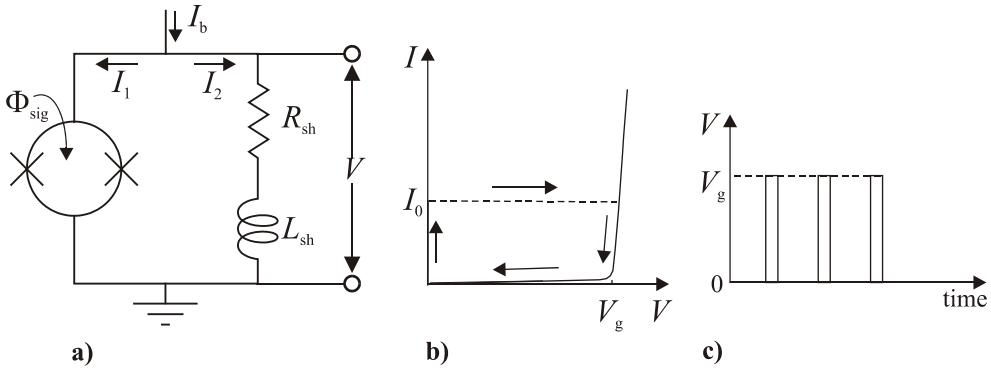

Figure 1.15- *a) Schematic of a ROS; b) Oscillation relaxations in the IVC and c) Voltage pulses produced, according to a simplified ROS model. In practice, the ROS will relax to the V=0 state much before reaching V_g.*

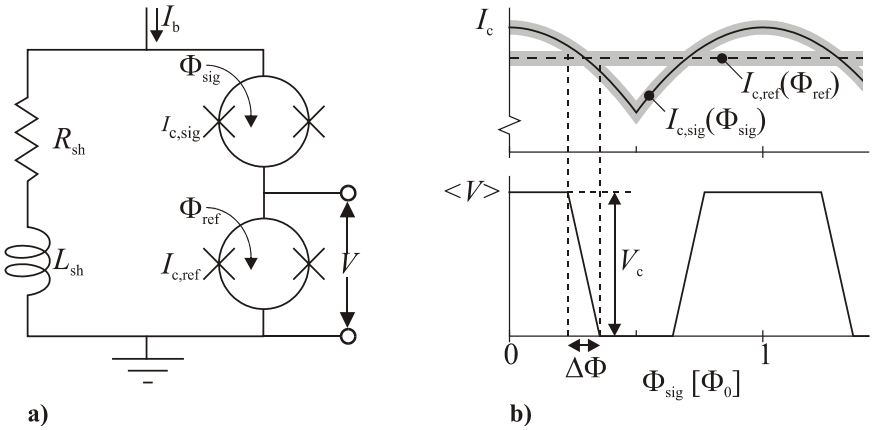

Figure 1.16- *a) Schematic of a DROS; b, above) critical currents of the signal and reference SQUIDs vs. the applied flux; b, below) DROS voltage vs. applied flux curve.*

asymmetrical. A disadvantage of this scheme is the non-trivial tuning of R_{APF} and L_{APF}, such that a large enough gain is reached, without entering the hysteretic regime.

Another group of alternative SQUIDs are based on the relaxation oscillations that arise when a hysteretic Josephson element is shunted by an *L*-*R* circuit. The Relaxation Oscillation SQUID (ROS) consists of a hysteretic SQUID in parallel with an L_{sh}-R_{sh} circuit (Figure 1.15a)[36]. If the current biasing the tank circuit I_b is larger than the critical current of the SQUID and I_bR_{sh} is smaller than the gap voltage V_g of the SQUID, relaxation oscillations will occur (Figure 1.15b). As a consequence, voltage pulses will appear across the SQUID (Figure 1.15c), with a frequency f_{RO} typically ~1 GHz. Thus, the ROS is basically a flux-to-frequency converter. (It can be also used as a flux-to-voltage converter, but the transfer is not much larger than that of a standard dc SQUID).

Based on the ROS, the Double Relaxation Oscillation SQUID (DROS) has been developed[37,38]. The DROS consists of two hysteretic SQUIDs: a signal SQUID and a reference SQUID (Figure 1.16a). The signal flux, applied to the signal SQUID, modulates its critical current $I_{c,sig}(\Phi_{sig})$. A constant reference flux Φ_{ref} is applied to the reference SQUID, and used to tune its critical current $I_{c,ref}$ in the middle of the modulation range of the signal SQUID. In every relaxation oscillation cycle, the two currents $I_{c,sig}$ and $I_{c,ref}$ are compared. The SQUID with the smallest I_c will participate in the oscillations while the other will remain in the superconducting V=0 state. If the output is readout across the reference SQUID, the time-averaged dc component of the pulses $<V>$ as a function of the applied flux is a V-Φ curve with a sharp transfer function ~1 mV/Φ_0 (Figure 1.16b).

A conventional SQUID can be optimized to reach a very low flux noise; however the voltage-to-flux transfer is limited to ~100 μV/Φ_0. On the other hand, second generation SQUIDs, like the DROS or the APF SQUID can be designed to have very large transfers, and moderate flux noise levels. The best properties of the two kinds of SQUIDs can be naturally combined in a *Two-Stage*[39] system (Figure 1.17a). In a Two-Stage system, the output of the first, sensor stage is preamplified by a large-transfer second stage.

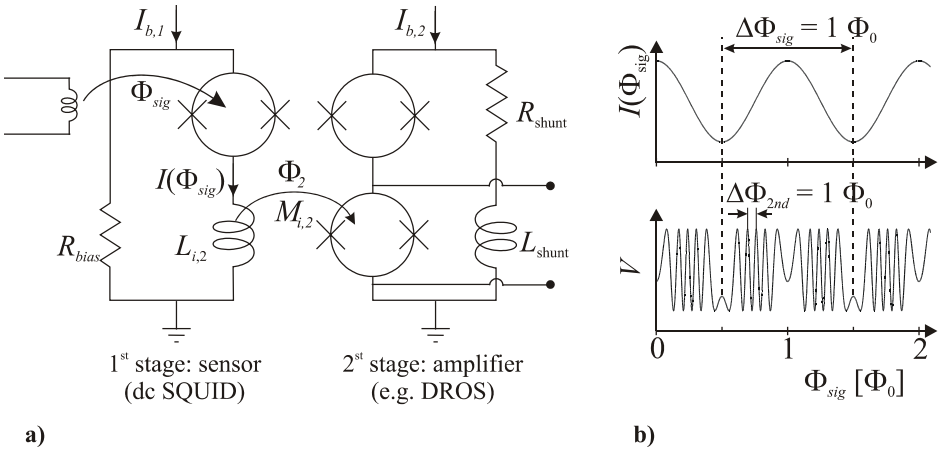

Figure 1.17- *a) Schematic of a Two-stage system using e.g. a DROS as second stage; b) modulation of the current through the sensor SQUID and Two-stage V-Φ curve.*

By putting a bias resistor R_{bias}, the current through the sensor SQUID is modulated by the applied flux Φ_{sig}. The sensor SQUID is connected in series with the input coil $L_{i,2}$ of the second stage SQUID, so the current I through the first SQUID couples a flux $\Phi_2=M_{i,2}I$ into the second one. This flux is finally converted into a voltage at the second stage SQUID, subsequently read out by the room temperature readout electronics. The total Two-Stage flux-to voltage transfer is thus:

$$\left.\frac{\partial V}{\partial \Phi_{sig}}\right|_{TS} = \frac{\partial I}{\partial \Phi_{sig}} \cdot M_{i,2} \cdot \frac{\partial V}{\partial \Phi_2} = G_\Phi \cdot \frac{\partial V}{\partial \Phi_2}. \tag{1.33}$$

The voltage V across the second stage as a function of the applied flux Φ_{sig} presents "wiggles", because for each 1 Φ_0 coupled into the first stage, several flux quanta are induced into the second stage (Figure 1.17b). In other words, the Two-Stage flux gain $G_\Phi=\partial\Phi_2/\partial\Phi_{sig}$ is larger than 1, as should be expected. Note that several multiple FLL operation points at the V-Φ_{sig} curve are possible, but only the point around (n/2+1/4) Φ_0 has the largest $(\partial V/\partial\Phi_{sig})_{TS}$ transfer. The maximum flux gain available at this point is given by:

$$G_\Phi = \frac{\partial \Phi_2}{\partial \Phi_{sig}} = M_{i,2} \cdot \frac{\partial I}{\partial I_c} \cdot \frac{\partial I_c}{\partial I_{sig}}, \tag{1.34}$$

,where $\partial I/\partial I_c$ and $\partial I_c/\partial I_{sig}$ can be respectively approximated by[40]:

$$\frac{\partial I}{\partial I_c} = \frac{R_{dyn}}{R_{dyn} + R_{bias}} \approx \frac{R_{sh}/\sqrt{2}}{(R_{sh}/\sqrt{2}) + R_{bias}}, \tag{1.35}$$

$$\frac{\partial I_c}{\partial \Phi_{sig}} \approx \frac{4.4}{1+\beta_L} \cdot \frac{I_0}{\Phi_0}. \tag{1.36}$$

From Eq. 1.36 is clear that G_Φ can be made larger by increasing the current modulation at the first stage, and/or the mutual inductance $M_{i,2}$ between the input coil $L_{i,2}$ and the second stage SQUID. The Two-Stage transfer is typically as large as ~2-4 mV/Φ_0.

A particular Two-Stage including a DROS as second stage was used in this work, and will be further described in Chapter 4.

1.4. The CCC with SQUID readout

This section treats the combination of the CCC with its SQUID readout. The sensitivity and current resolution of the system are calculated in terms of an equivalent electrical circuit. The different strategies to achieve optimal coupling between the CCC and the SQUID are discussed.

1.4.1. CCC with superconducting flux transformer

The schematic circuital representation of a type I CCC coupled to the readout SQUID via a superconducting flux transformer is shown in Figure 1.18. Optionally, a ferromagnetic core can be used to increase the coupling between the CCC tube and the sensing coil[41]. Assume that one of the primary windings with N_P turns is fed with a current I_P. All the noise sources in the system can be translated back to an equivalent input noise current $\langle I_P^2 \rangle$ in the winding N_P. The current resolution per single turn ($\langle i_P^2 \rangle = \langle I_P^2 \rangle . N_P^2$) can be expressed as:

$$\left\langle i_P^2 \right\rangle = \frac{S_{\Phi,T}}{M_{OV,sq}^2} + \frac{S_{\Phi,ext}}{\left(L_{CCC,eff} + L_i\right)^2}. \tag{1.37}$$

The first term stems for the flux noise power $S_{\Phi,T}$ (coming from the SQUID $S_{\Phi,sq}$ and, if present, from the ferromagnetic core, $S_{\Phi,c}$) that couples back to the CCC via the flux transformer. $M_{OV,sq}$ represents the mutual inductance between the SQUID and the CCC. The second term accounts for the current noise due to parasitic external magnetic flux $S_{\Phi,ext}$

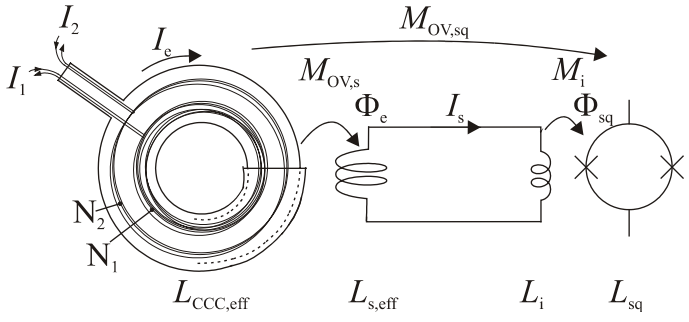

Figure 1.18- *CCC coupled to a SQUID through a superconducting flux transformer.*

coupled into the CCC loop, with effective inductance $L_{CCC,eff}$ (see section 1.4.3). *If* this contribution is negligible compared to the SQUID noise, Eq. 1.39 reduces to:

$$\left\langle i_P^2 \right\rangle \approx \frac{S_{\Phi,T}}{M_{OV,sq}^2} \tag{1.38}$$

In order to have the best current resolution possible, the noise $S_{\Phi,T}$ should be minimum and the coupling CCC-SQUID $M_{OV,sq}^2$ maximum.

Let us study the coupling between the CCC and the SQUID more carefully. The magnetic flux Φ_e due to the unbalance current I_e in the CCC is picked-up by a secondary, sensing coil with N_s turns. The sensing coil needs to be wound as close as possible to either the inner or the outer side of the toroid. The effective self-inductance of the sensing coil $L_{s,eff.}$ in the presence of the overlapped tube can be approximated by[8]:

$$L_{s,eff} \approx L_s(1-k') + kN_s^2 L_{CCC,eff} \tag{1.39}$$

The first term represents the reduction of the sensing coil nominal self-inductance L_s due to the coupling (with a factor k') between the real sensing coil and its image with respect to the wall of the superconducting tube. The second term accounts for the fact that the overlapped tube is not closed and the current of the sensing coil image returns via $L_{CCC,eff}$. The factor k can be approximated by: $k \approx 1-d/R$, where R is the radius of the sensing-coil and d is its distance to the wall of the overlapped tube. If the pick-up coil is wound very close to the surface of the toroid ($d/R \ll 1$), then $k \approx 1$. Under this condition, the mutual inductance $M_{OV,s}$ between the CCC and the sensing coil reduces to: $M_{OV,s} \approx N_s L_{CCC,eff}$. The wires connecting the sensing coil to the SQUID input coil introduce a small inductance L_w. The mutual inductance between the input coil inductance L_i and the SQUID self-inductance L_{sq} is given by: $M_i = k_{sq}(L_i L_{sq})^{1/2}$.

When the unbalance flux $\Phi_e = M_{OV,s} I_e$ is detected by the sensing coil, a screening current I_s is induced in the superconducting flux transformer, so that the total flux in it remains constant. The screening current, $I_s = \Phi_e/(L_{s,eff} + L_w + L_i)$, runs through the input coil, producing a flux $\Phi_{SQ} = I_s M_i$ that is finally detected by the SQUID. Resuming, the flux transfer equation in the system can be written as:

$$\Phi_e = I_e M_{OV,s} = I_S (L_{s,eff} + L_i + L_w); \quad I_S M_i = \Phi_{sq}. \tag{1.40}$$

From this equation, the current transfer of the system can be derived:

$$\frac{I_s}{I_e} = \frac{M_{OV,s}}{L_{s,eff} + L_i + L_w}. \tag{1.41}$$

The CCC to SQUID mutual inductance is simply $M_{OV,sq} = (I_s/I_e).M_i$. Under the conditions of $k \approx 1$ and ideal coupling ($k' \approx 1$), $M_{OV,sq}$ can be approximated by:

$$M_{OV,sq} = M_i \frac{N_s L_{CCC,eff}}{N_s^2 L_{CCC,eff} + L_i + L_w} \tag{1.42}$$

When the inductance of the wires L_w is very small compared to $L_{CCC,eff}+L_i$, Eq. 1.42 can be written as universal function of the "match factor" $x \equiv N_s (L_{CCC,eff}/L_i)^{1/2}$, to obtain a form with an easier physical interpretation[42]:

$$S_{CCC} = \frac{N_s \sqrt{L_{CCC,eff} / L_i}}{\left(N_s \sqrt{L_{CCC,eff} / L_i}\right)^2 + 1} \equiv \frac{x}{x^2 + 1}. \tag{1.43}$$

S_{CCC} is the *dimensionless sensitivity of a CCC*, defined as the squared ratio of the energy stored at the input coil divided by the energy available at the overlapped tube:

$$S_{CCC} = \frac{\sqrt{\frac{1}{2} L_i I_s^2}}{\sqrt{\frac{1}{2} L_{CCC,eff} I_e^2}} = \frac{I_s}{I_e} \sqrt{\frac{L_i}{L_{CCC,eff}}} \approx \frac{x}{x^2 + 1}. \tag{1.44}$$

Thus the "match factor" gives an idea of the repartition of the energy between the CCC and the SQUID. A plot of the function S_{CCC} can be seen in Figure 1.19. The maximum value for the dimensionless sensitivity, $S_{CCC,OPT}=1/2$ occurs when $N_s (L_{CCC,eff}/L_i)^{1/2}=1$. At that point the inductances at both sides of the flux transformer coincide: $L_{s,eff}=N_s^2 L_{CCC,eff}=L_i$, and the maximum energy is transferred from the CCC to the SQUID input coil. This result is equivalent to the better-known theory of maximum power transfer in electronics: For a voltage source V_{so} with impedance R_{so}, the maximum power that can be supplied to a load resistor R_{load} occurs when $R_{so}=R_{load}$, and this power is ¼ of the maximum available for the source, V_{so}^2/R_{so}.

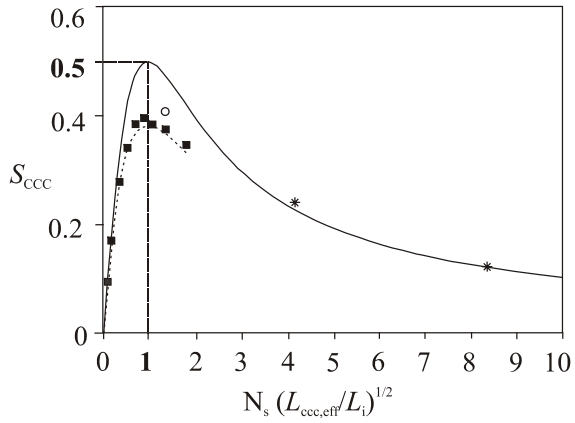

Figure 1.19- *Dimensionless sensitivity of a CCC. Solid line: optimal sensitivity curve for ideal coupling (k'=1). Experimental points: (■): CCC (L_{CCC}=10 nH) coupled to an rf SQUID using a wire sensing coil; (○): same CCC connected through a lead-foil sensing coil; (*) CCC with a ferromagnetic core (A_c=56 μH, with N_s=1 and ½) coupled to a uhf SQUID (from Ref. 45)*

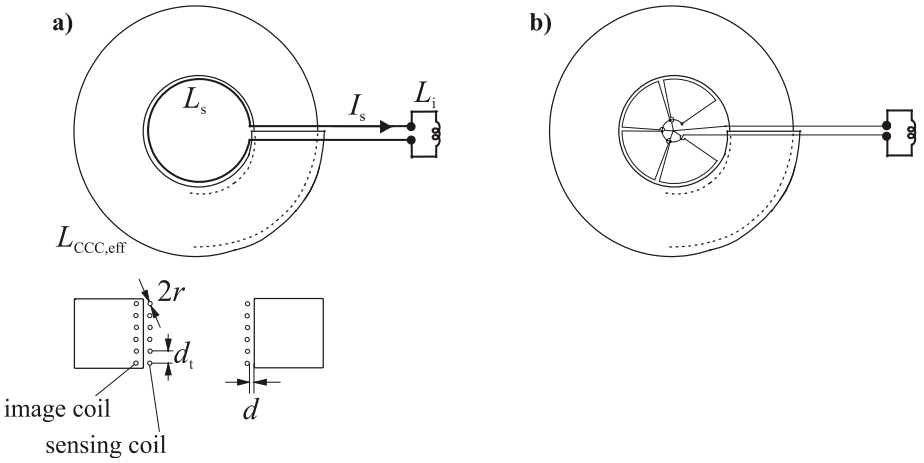

Figure 1.20- *Use of a pick-up coil to sense the unbalance flux Φ_e in the CCC; a) CCC with an internally wire-wound sensing coil, with an integer number of turns N_s (top view and cross section shown); b) sensing coil with a "fractional" number of turns.*

When a certain SQUID is coupled to a CCC, two situations can be encountered, depending on the relative magnitudes of $L_{CCC,eff}$ *and* L_i:

If $\boldsymbol{L_{CCC,eff}<L_i}$, a sensing coil with a number of turns N_s the integer number closer to $(L_i/L_{CCC,eff})^{1/2}$ will be needed (Figure 1.20a). For instance, a sensing coil of 4 turns would be necessary to couple a commercial SQUID with a typical value of L_i=1 μH, to a $L_{CCC,eff}$=80 nH CCC. Experimentally, the measured sensitivity values are lower than ideally expected, due to the non-ideal coupling (k'<1) between the overlapped tube and the pick-up coil. The reduction of sensitivity depends on the number of turns necessary to reach the maximum. E.g., a reduction of 20% was measured when the number of turns necessary was N_s=10 (Figure 1.19). A larger decrease in the sensitivity is expected when only a few turns are necessary to reach the maximum, a situation that will be encountered for high values of $L_{CCC,eff}$. When a sensing coil with a number N_s>1 of turns is used, the coupling factor k'<1 due to the coupling between each turn of the real coil with all the (rest of) real and image coils. In that case the sensitivity does not take the universal form of Eq. 1.46. This case is more extensively treated in Appendix B. The sensitivity can be slightly improved if the sensing coil is made of lead foil wounded around the CCC, instead of a wire coil.

If $\boldsymbol{L_i<L_{CCC,eff}}$, a sensing coil with a "fractional number of turns" would be required. This can be implemented with a lead-foil sensing coil folded in the "chariot-wheel" configuration[43] schematically shown in Figure 1.20b. Due to the practical complexity of fabrication, this geometry is only used to reach reasonable fractions (N_s=1/2-1/6). It would be impossible to couple, e.g. an $L_i=L_{isq}$ ≈10 pH (quantum limited) SQUID to a $L_{CCC,eff}$=80 nH CCC, because an N_s~1/100 fractional coil would be necessary.

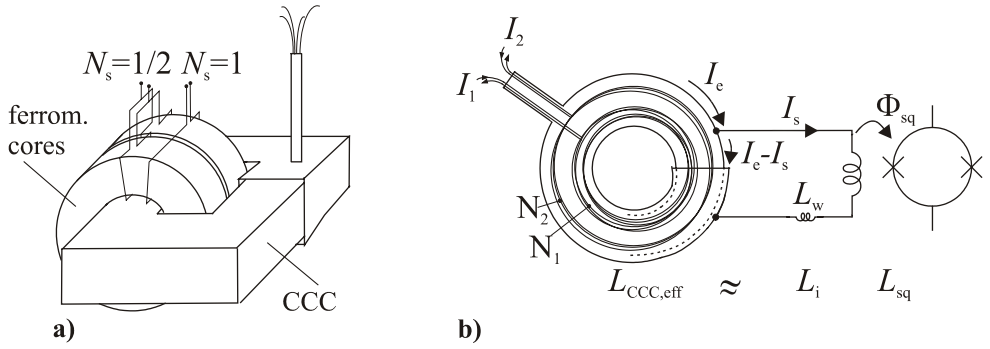

Figure 1.21- *Two manners of reaching ideal coupling; a) Using a set of n ferromagnetic cores placed inside a square-shape overlapped tube. By connecting the single-turn pick up coil of each core either in series or in parallel, a sensing coil with an integer (N_s=n) or fractional (N_s=1/n) number of turns can be achieved; b) CCC overlapped tube directly coupled to the SQUID.*

1.4.2. CCC ideally coupled to the SQUID

There are in principle two ways of circumventing the above undesirable situations and reach an ideal coupling (*k'*=1) between the CCC and the SQUID.

One possibility is to wound the sensing coil on a ferromagnetic core, with high permeability; in that case $L_{CCC,eff}$ equals the magnetic conductance A_c. Depending on the relative magnitudes of $L_{CCC,eff}$ and L_i, an integer or fractional sensing coil might be needed, which could be implemented as explained in Figure 1.21a. It has been shown however that in practice this is not a good alternative because of the large 1/*f* magnetic noise $S_{\Phi,c}$ added by the ferromagnetic cores[44], which dominates over SQUID noise $S_{\Phi,sq}$.

An alternative, straightforward way of reaching ideal coupling is to use the overlapped tube itself as a single-turn (N_s=1) pick-up coil, directly attached to the input coil of the SQUID by means of a galvanic connection (Figure 1.21b). In this configuration, suggested by Sesé *et al.*[45,46], ideal coupling (*k'*=1) is obtained per definition. Besides, problems arising from relative mechanical vibrations of the sensing coil with respect to the tube are eliminated. A requirement for this simple configuration is that the inductances of the overlapped tube and the SQUID input coil have to match:

$$L_{CCC,eff} = L_i . \tag{1.45}$$

In this (from now-on called) "direct-coupling" configuration, and if the inductance of the wires is negligible small ($L_w << L_{CCC,eff}, L_i$), the current noise reduces to:

$$\left\langle I_P^2 \right\rangle \approx \frac{1}{N_P^2} \frac{4S_{\Phi,sq}}{k_{sq}^2 L_i L_{sq} L_{CCC,eff}} = \frac{1}{N_P^2} \frac{8\varepsilon}{k_{sq}^2 L_{CCC,eff}} . \tag{1.46}$$

In conclusion, to obtain the optimal current noise of a CCC with SQUID readout, i) the CCC should have the largest $L_{CCC,eff}$ and N_P possible, and ii) the SQUID energy resolution ε

should be as small as possible, and at the same time the matching condition $L_{CCC,eff}=L_i$ should be fulfilled. The development of such specific low-noise, directly coupled SQUIDs will be treated in Chapter 3.

1.4.3. Influence of external and trapped flux noise

In order to eliminate completely the environmental noise contribution $S_{\Phi,ext}$ to the system current resolution (Eq. 1.37), the CCC-SQUID must be surrounded by an extremely efficient magnetic shield. The influence of external time varying fields can be almost completely eliminated by using several concentric superconducting shields (made of Pb or Nb). Due to the Meissner effect, magnetic fields within the superconductor bulk will be rejected. However, the Meissner effect is never perfect; a small part of the field can be trapped e.g. at defects or grain boundaries in the material. To hinder this possibility, a combination of high permeability ferromagnetic shields (e.g. μ–metal at room *T,* or cryoperm at 4.2 K) are used to reduce the ambient magnetic field before the interior shields become superconducting.

Let us consider the influence of trapped flux within the shielding. Consider that the CCC-SQUID is cooled down in a remaining background field B_b. The trapped flux within the circuit will be approximately given by $B_b A_{CCC}$, where A_{CCC} is the area enclosed by the CCC tube. The result of a current unbalance in the CCC will produce a screening current $\Delta I_{scr}=B_b A_{CCC}/(L_{CCC,eff}+L_w+L_i)$ in the flux transformer. If the background field varies ΔB_b, or if the CCC area ΔA_{CCC} or inductance $\Delta L_{CCC,eff}$ change due to mechanical vibrations and/or thermal expansion (Figure 1.22), additional screening currents will appear, that will be indistinguishable from the unbalance current signal:

$$\Delta I_{scr} = \frac{M_{ov,s} I_e}{L_{CCC,eff} + L_i} + \\ + \frac{B_b}{L_{CCC,eff} + L_i} \Delta A_{CCC} + \frac{A_{CCC}}{L_{CCC,eff} + L_i} \Delta B_b + \frac{I_s}{L_{CCC,eff} + L_i} \Delta L_{CCC,eff} \cdot \tag{1.47}$$

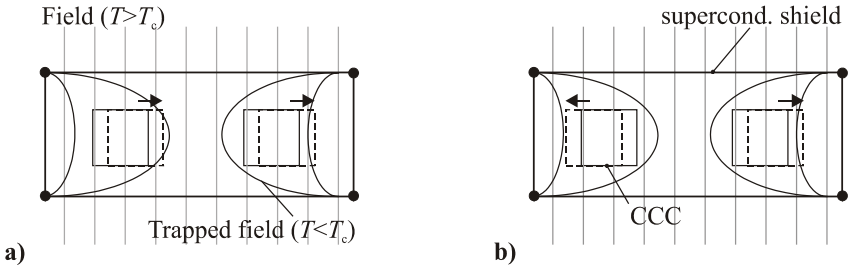

Figure 1.22- *Effect of a trapped field within the superconducting shield. a) Mechanical vibrations produce a relative displacement of the CCC with respect to the walls of the shield, thus varying $L_{CCC,eff}$; b) Thermal variations produce variations of the CCC enclosed area, and thus also of $L_{CCC,eff}$.*

Therefore, the CCC shielding should be designed to reduce as much as possible the influence of background field variations, and the CCC itself should be properly fixed to avoid mechanical displacements. The importance of these problems will become apparent in the integrated CCC-SQUID system described in Chapter 6.

1.5. CCC-SQUID bridges

The most natural application of a CCC-SQUID system is as a very accurate amplifier of an extremely small current. The realization of a practical current quantum standard depends on the ability to amplify (with parts in 10^8) the tiny (1-10 pA) quantized current delivered by a Single Electron Tunneling (SET) device[47], to the order of μA. A schematic of the CCC-SQUID based *I*-bridge that would be necessary for the comparison of currents is shown in Figure 1.23a. The SET current feeds a many-turns winding $N_1 \equiv N_{CCC}$, while a secondary current source S_2 feeds a single-turn winding $N_2 \equiv 1$. The unbalance flux is detected by the SQUID, transformed into a voltage output, and fed back as a current, either into the secondary source (external loop) or into the SQUID (internal loop). Thus, I_2 is automatically adjusted by the feedback electronics so as to keep the error current $I_e=0$, and therefore the ratio between the primary (SET) and the secondary current standard equals N_2/N_1. To avoid drift errors, the SET current must be periodically reversed. Part III of this thesis deals with this kind of bridge.

The CCC-SQUID has been mainly used in *R*-bridges[48] to calibrate accurately ($<10^{-8}$-10^{-9}) a primary resistor with respect to the quantum Hall standard resistance $R_1 \equiv R_H$, or secondary resistors between them (Figure 1.23b). The feedback of the CCC bridge guarantees that $N_1 I_1 = N_2 I_2$. A nano-voltmeter is used to measure the difference in voltage

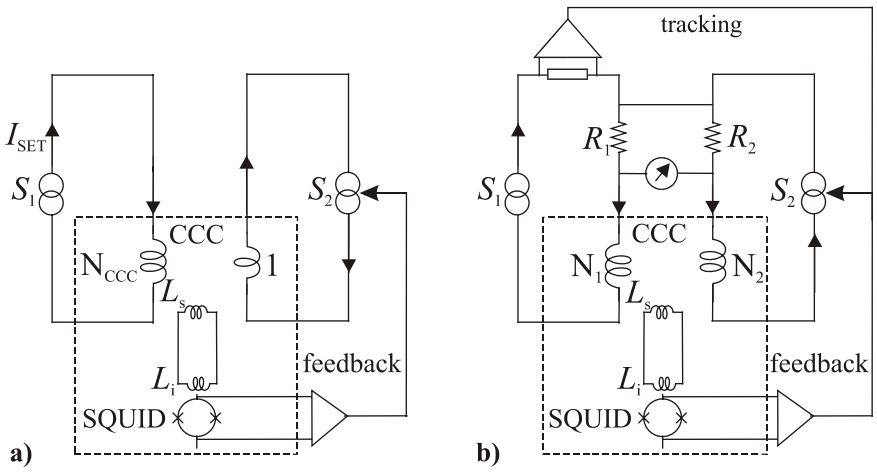

Figure 1.23- *a) I-bridge based on the CCC-SQUID for SET current amplification; b) R-bridge based on the CCC-SQUID for resistor calibration.*

drop across the resistors, ΔV. When the two resistances are exactly in the same ratio as the two windings: $R_2=(N_2/N_1)R_1$, then $\Delta V=0$. A deviation ΔR_2 of the secondary resistance from its nominal value, will produce a proportional voltage signal ΔV, thus: $\Delta R_2=\Delta V/I_2$. The polarity of S_1 is also periodically reversed with a very low frequency to avoid null errors of the nano-voltmeter. The large swings produced when the current is reversed can easily unlock the SQUID. For that reason, a tracking system usually takes care that S_2 follows the reversals of S_1, so that the SQUID loop has to cope only with the small unbalance. Part II of this thesis describes a bridge form this sort.

The frequency bandwidth limitations of the above CCC-SQUID systems are given by the following. The current applied to the CCC should be of very low frequency, otherwise parasitic capacitive effects between the primary turns would give an error due to current leakage. Seppä[49] and Delahaye[50] showed that for a ~2000 turns CCC, the frequency was limited to a few Hz to keep the error below 10^{-9}. For a CCC with a larger number of turns capacitive effects will be even more important. The very low frequency of operation of the CCC represents a main problem for the SQUID, which has a large 1/*f* noise at those frequencies. Possible solutions will be discussed in Chapter 5. The upper BW limit will be determined by the rest of the components of the bridge.

References

[1] M. Tinkham, *Introduction to superconductivity*, Eds. McGraw-Hill International, New York, 2nd edition (1996).
[2] J. Nagamatsu *et al*., *Nature*. **410**, 63 (2001).
[3] I.K. Harvey, *Rev. Sci. Instrum*. **43**, 1626 (1972).
[4] J.R Reitz *et al*., *Foundations of Electromagnetic Theory*, Addison-Wesley Publishing Company, 204, (1993).
[5] D.B. Sullivan and R.F. Dziuba, *Rev. Sci. Instrum*. **45**, 517 (1974).
[6] K. Grohman *et al*., *IEEE Trans. Instrum. Meas*. IM-**23**(4), 261 (1974).
[7] E. Frantsuz, *Metrologia*. **35**, 847 (1998).
[8] J. Sesé *et al*., *IEEE Trans. Appl. Supercond.* **9**, 58 (1999).
[9] Quickfield 4.0 for Windows 95/NT 93-97, student edition, http:/www.tera-analysis.com
[10] J. Seppä, *IEEE Trans. Instrum. Meas.* **39**, 689, (1990).
[11] M. Hiddink, MSc Report, University of Twente (1999).
[12] D. Delahaye, *IEEE Trans. Instrum. Meas*. **40**(6), 883 (1991).
[13] B.D. Josephson, *Phys. Lett*. **1**, 251 (1962).
[14] W.C. Steward, *Appl. Phys. Lett*. **12**, 277 (1968).
[15] R.L. Peterson and C.A. Hamilton, *J. Appl. Phys*. **50**, 8135 (1979).
[16] C.D. Tesche and J. Clarke, *J. Low Temp. Phys.* **29**, 301 (1997).
[17] J.D. Feder *et al*., *IEEE Trans. Appl. Supercond*. **3**, 2760 (1993).
[18] J. Clarke, *Physica*. **126B**, 441 (1984).
[19] R.H. Koch *et al*., *Phys. Rev. B*.**26**,74 (1982).
[20] R.H. Koch *et al*., *Appl. Phys. Lett.* **35**(5), 380 (1981).
[21] F.C. Wellstood *et al*., *IEEE Trans. Magn.* **25**, 1001 (1989).

[22] J.M. Jaycox and M.B. Ketchen, *IEEE Trans. Magn.* **17**, 400 (1981).
[23] K.C. Gupta *et al*., *Microstrip lines and slot line*s, Artech house, Ind., Dedham, Massachussetts, USA (1979).
[24] J. Mieog, MSc report, University of Twente (2000).
[25] http://henry.ee.rochester.edu:8080/users/sde/cad/IND.html
[26] S.M. Faris *et al*., *J.Appl. Phys*. **52**(2), 915 (1980).
[27] K. Empuku *et al*., *J.Appl. Phys*. **58**, 1916 (1985).
[28] J. Knuutila *et al*., *J.Low Temp. Phys.* **71**, 369 (1988).
[29] K. Empuku *et al*., *J.Appl. Phys*. **3**(1), 1858 (1993).
[30] K. Empuku *et al.*, *J.Appl. Phys.* **72**(3), 1000 (1992).
[31] K. Empuku *et al.*, *J.Appl. Phys.* **71**(3), 2338 (1992).
[32] R.H. Ono *et al.*, *IEEE Trans. Appl. Supercond.* **7**(2), 2538 (1997).
[33] I. Jin *et al.*, *Appl. Phys. Lett.* **70**(16), 2186 (1997).
[34] *SQUID sensors: Fundamentals, Fabrication and Applications*, Ed. H. Weinstock, NATO ASI Series 329, Kluwer Academic Publishers, Dordrecht/ Boston/ London (1996).
[35] D. Drung and H. Koch, *Supercond. Sci. Technol.* **7**, 242 (1993).
[36] M.J. van Duuren *et al*., *J. Appl. Phys.* **80**, 4164 (1996).
[37] D.J. Adelerhof *et al*., *J. Appl. Phys.* **76**, 3875 (1994).
[38] M.J. van Duuren *et al*., *J. Appl. Phys.* **82**, 3598 (1997).
[39] M. Podt *et al*., *Appl. Phys.Lett.* **75**, 2316 (1999).
[40] D.J. Adelerhof, PhD Thesis, University of Twente, (1993).
[41] k. Grohmann and D. Hechtfischer, PTB Mitteilungen. **92**, 328, (1982).
[42] J. Sesé *et al*., *IEEE Trans. Appl. Supercond*. **9**(2), 3487 (1999).
[43] H. Seppä, *private communication*.
[44] O.V. Snigirev *et al*., *J. Appl. Phys*. **79**, 960 (1996).
[45] J. Sesé *et al*., *IEEE Trans. Instrum. Meas.* **48**(6), 1306 (1999).
[46] G. Rietveld *et al*., *IEEE Trans. Instrum. Meas*. **161** Dig. CPEM98, (1998).
[47] L.J. Geerlings *et al*., *Phys. Rev. Lett*. **17**(3), 249 (1992).
[48] B. Jeckelmann and B. Jeanneret, *submitted to Rep. Prog. Phys.*
[49] H. Seppä *et al*., *IEEE trans. Instrum. Meas*. **44**(2), 276 (1995)
[50] F. Delahaye, *IEEE Trans. Instrum. Meas*. **40**(6), 883 (1991).

Part II

RESISTANCE BRIDGES BASED ON THE CCC-SQUID

One of the responsibilities of the NMI's is the legal calibration of standard resistors with respect to the representation of the resistance unit. In the SI, the Ohm is a derived unit, defined as: 1 Ω=1V/A=1 $kgm^2s^{-3}A^{-2}$. Up to 1980, the direct realization of the Ohm (based on a Thomson-Lampard calculable capacitor[1,2]) could only be realized with an uncertainty of 10^{-7}. This quite complicated realization was done only by a few institutes, while most of them used a selected group of resistors as their main standard. The mean value of these resistors represented the unit of resistance for calibrations in the country: "Ω_{LAND}". Because the value of this resistors drifted somewhat in time, Ω_{LAND} was also time dependent. A lot of different time-dependent representations: $\Omega_{LAND,1}(t)$, $\Omega_{LAND,2}(t)$…existed through the various NMI's, with values that could differ form each other as much as μΩ's.

The discovery in 1980 of the Quantum Hall Effect (QHE) by von Klitzing[3] changed radically this scenario, since it allowed the reproduction of certain resistances, independent of space and time. The QHE results from the macroscopic quantum properties of a bidimensional electron gas, appearing in semiconductors devices with high mobility such as MOSFET or heterostructures of GaAs/GaAlAs, at low temperatures (T~1 K) and high magnetic fields (B~10 T). Assume that a current I traverses the Hall sample, and a variable, perpendicular magnetic field $\boldsymbol{B}$ is applied. The transversal resistance $R_{xy}=V_{xy}/I$ presents "plateaus" at quantized values :

$$R_{xy} = R_H(i) = \frac{R_K}{i}, \quad i = 1,2,3... \tag{II.1}$$

i being an integer and R_K the Von Klitzing constant, which is related by theory to fundamental constants: $R_K=h/e^2$. The longitudinal resistance $R_{xx}=V_{xx}/I$ becomes zero at the values of $\boldsymbol{B}$ such that R_{xy} is in a plateau (Figure II.1a). For good quality Hall samples, the "flatness" of the plateau is better than $\Delta R_{xy}/R_{xy}<10^{-9}$. The width of the plateau depends on

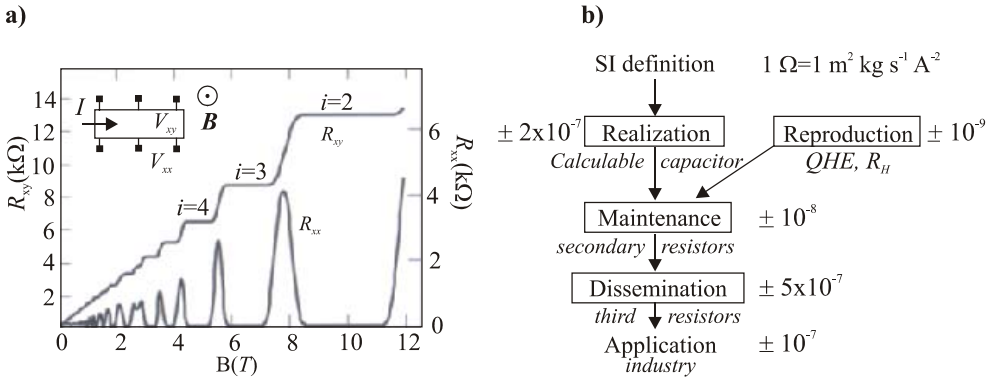

FigureII.1- *a) Typical QHE measurement in a GaAs/AlGaAs heterostructure (at 0.3 K): transversal R_{xy} and longitudinal R_{xx} resistance as function of the applied magnetic induction B; b) Chain of comparisons for the ohm and traceability to the QHE (adapted from Ref. 4*

the current through the sample. Typical values ~50 μA are used. Above a certain current *I*, characteristic of each sample, no plateau occurs. It has been shown[5] that the value of R_{xy} in the plateaus is independent of parameters like the sort and geometry of sample, impurity contents, temperature and plateau number, within $3x10^{-10}$.

At the view of the extremely good reproducibility of the effect, the "Comité International des Poids et Mesures" (CIPM) recommend in 1988 to base the as-maintained unit of resistance, used for the dissemination, on the QHE. To guarantee international uniformity, the value for the von Klitzing constant was recommended to be: R_{K-90}=25812.807 Ω. This value was found as the average of different values for the R_k constant known from various direct methods and indirect methods[2]. All values of the R_k coincide within a standard deviation $\sigma=2.10^{-7}$ with the R_{K-90} value.

Usually, the QH resistances $R_H(2)$=12906.4035 Ω or $R_H(4)$=6453.20175 Ω corresponding to the 2nd and 4th plateaus are adopted as primary standards, to which other secondary standard resistors R_s have to be calibrated. These secondary standards are in practice wire wound resistors made of special alloys (e.g. "Manganin" or "Evanohm"[6]), generally taking the values 1 Ω, 100 Ω or 10 kΩ (known *a priori* with parts in 10^6). Stored in a temperature controlled oil bath, these resistors are very stable over long periods of time. They can serve also as traveling resistors, and can be owed by other institutes or industry different than the NMI's. Periodical inter-comparisons are needed to trace the value of these resistors to the QHE. Other resistors are then calibrated to the secondary resistors. The chain of inter-comparisons is summarized in Figure II.1b.

To compare standard resistors, the following methods can be used:

- The Hamon set up: it consists of N (nominally) equal resistors placed first in series and then in parallel. Commercially available 100 Ω/1 Ω and 10 kΩ/100 Ω set-ups with an accuracy of 1 part in 10^8 are available. They are commonly used for scaling 1 Ω to 10 kΩ resistance standards[6]. The disadvantage of this method is that only ratios equal to N^2 can be obtained.

- **The Warshawsky bridge:** is a bridge of the Wheatstone type that can accommodate 4 four-terminal resistance standards, with nominal ratios $R_1/R_2=R_3/R_4$. This kind of bridge[6] is attractive for comparisons of 10 kΩ resistance standards with uncertainty ~10^{-8}.

- The potentiometric method: A current I_x is passed through the series connection of the QH resistance R_H and the secondary resistance R_s, and the voltages V_H and V_s across them are measured (Figure II.2a). R_s is then $R_s=V_sR_H(i)/V_H$ (i=2 or 4). The insulation of the circuit must be high (>10^{12} Ω) to guarantee that the same current I_x flows through R_s and R_H. The polarity of the source is reversed to avoid the influence of additional e.m.f's. The two voltages are compared to the Josephson voltage standard. Ideally the two voltages should be measured simultaneously. In practice, the same instrument is used to measure the two voltage drops, and there is a time difference between the two measurements. Thus: $R_s=V_s(t_0)R_H/V_H(t_0+\Delta t)$. Therefore, the current must be stable at least over a period Δt between the two measurements. Zener diodes are used as very stable sources. Since the value of the standard resistors depends on the temperature, pressure, dissipated power and time, the appropriate coefficients of correction must be known. This method is used for calibrating resistors with values R_s of the order of R_H with an uncertainty of 10^{-8}. For comparisons of large value resistors, this method is as good as the CCC but much simpler to operate[7].

- Ratio-bridge based on a Current Comparator (CC): the schematics of this bridge, the room temperature approach of the CCC, is shown in Figure II.2b. Two currents I_1 and I_2 feed, respectively, the resistors R_1 and R_2, and the windings N_1 and N_2, wound on a high-

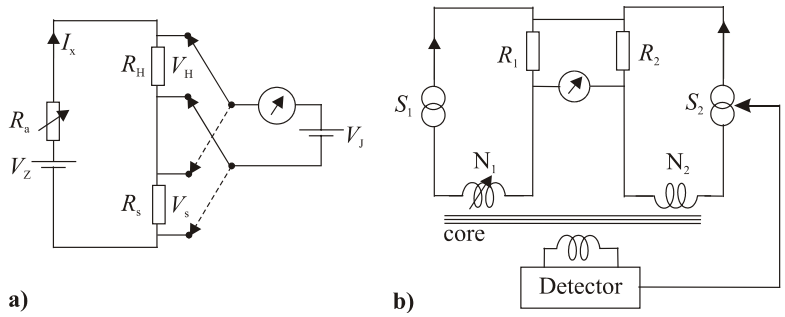

Figure II.2- *Principle of a) the potentiometric method; b) the resistance-ratio bridge based on the current comparator (CC), at room temperature.*

permeability toroidal core. A flux detecting system senses the difference between N_1I_1 and N_2I_2. The output is fed back to the I_2 current source. The bridge is balanced by adjusting the number of turns N_1. In the balanced situation, the voltage drop across the two resistors is zero, and $R_2=R_1.(I_1/I_2)$. Commercially available CC bridges are particularly used for calibration of 1 Ω resistors, with an uncertainty of 10^{-7}. However CC's cannot reach high resolutions with the low currents needed for calibrating resistors R_2>100 Ω. Therefore they cannot be used to calibrate secondary resistors to the QH resistor. The ratio error is limited to 10^{-7} due to non-perfect screening of the high-permeability materials used in the construction.

- Ratio-bridge based on the Cryogenic Current Comparator: this bridge, whose principle of work was already explained in Chapter 1, is at present the most accurate method to compare two resistors, reaching uncertainty levels better than 10^{-9}. In principle, any two resistors in a ratio N_1/N_2 (with N_1, N_2 integer numbers) can be compared. Mostly, the CCC is used for the calibration of resistors in relation 1:1, 1:10, 1:100, or for the traceability of 100 Ω resistors to the R_H (i=2 or 4).

Today CCC *R*-bridges are not commercially available. Some commercial tentatives were initiated in the past (by "Oxford Instruments" and "Cryogenics"). However, the production stopped after 1998, due to the difficulty of making the CCC bridges work on-place. Indeed, these systems are very sensitive to particular environmental noise, vibration and grounding conditions. Most NMI's have developed their own systems, e.g., at the LCIE in France[8], NPL in England[9], VTT in Finland[10], EL in Japan[11] etc… A CCC *R*-bridge prototype for the Spanish TPYCEA calibration institute was made at the University of Zaragoza[12,13]. The fabrication and test of a new more user-friendly, optimized system is the main subject of Chapter 2.

References

[1] A.M. Thompson and D.G. Lampard, *Nature (London)*. **177**, 888 (1956).
[2] E. Braun, *Metrology at the frontiers of Physics and Technology, Proc. of the International school of physics "Enrico Fermi"*, Ed. Crovini and T.J. Quinn (North Holland) (1989).
[3] K.v. Klitzing, G. Dorda and M. Pepper, *Phys. Rev. Lett*. **45**(6), 494 (1980).
[4] D. Kind and T. Quinn, *IEEE Trans. Instrum. Meas*. **44**(2) 85 (1995)
[5] A. Hartland, J.M. Williams, *Phys. Rev. Lett*. **66**, 969 (1991).
[6] F. Delahaye, *Metrologia.* **29**, 81 (1992).
[7] R. Behr *et al*., *IEEE Trans. Instrum. Instrum*. **50**(2), 185 (2001).
[8] F. Delahaye, *IEEE Trans. Instr. and Meas*. **40**(6), 883 (1991).
[9] J.M. Williams and P. Kleinscmidt, *IEEE Trans. Instr. Meas*. **48**(2), 375 (1999).
[10] H. Seppä and A. Satrapinski, *IEEE Trans. Instr. Meas*. **46**(2), 463 (1997).
[11] M. Nakanishi *et al*., *Jpn. J. Appl. Phys.* **34**(1, 6A), 3284 (1995).
[12] A. Camón, PhD Thesis, University of Zaragoza (1996).
[13] J. Sesé, PhD Thesis, University of Zaragoza (1999).

Chapter 2

USER-FRIENDLY RESISTANCE BRIDGES BASED ON THE CCC-SQUID

The legal calibration of primary resistors to the QHR has necessarily to take place at the NMI's. However, for a number of non-official institutes and industry, the existence of a user-friendly CCC-SQUID bridge for the routine calibration of secondary resistors, and eventually the independent calibration of resistors to the QHE, would be very desirable. The characteristics of the system will be conditioned to the fact that it should work outside the community of specialists, at places where usually cryogenic facilities are not available. To justify the expense and inconvenience of using cryogenic fluids, the accuracy of the CCC bridge should be at least one order of magnitude better than that of room temperature CC's ($<10^{-7}$). Once the cryogenic liquid (bought outside) is at place, the system should be easy to cool-down and stay operable for weeks. Therefore, a low-evaporation rate cryostat should be chosen, and the different resistance ratio comparisons should be available with no need to warm up the system. The bridge electronics should be reliable, well protected against environmental noise and able to work on batteries for a long time. Section 2.1 describes the development and test of such a CCC bridge, whose cryogenic part can simply work in a transportable helium Dewar. In section 2.2 we briefly outlook the possibility of fabricating a CCC-SQUID in planar HTS technology. This would open the door for using liquid nitrogen, much cheaper than liquid helium.

2.1. CCC-SQUID resistance bridge in a transportable Dewar

The aim of this work was to develop a relatively economic bridge, that could be directly cooled down in a transportable, long holding He Dewar, periodically refilled outside the measuring institute. Inconvenient frequent He transfers would be thus avoided. The requirement of fitting the CCC in a commercial Dewar limits the CCC diameter and thus its inductance $L_{CCC,eff}$, which is directly related to the current resolution of the system (Eq.

Figure 2.1- *Overview of the CCC based resistance bridge. a) Bridge electronics (from top to bottom): integrator, SQUID readout, "difference compensator", current sources, two test 100 Ω resistors (inside an Al box) and nano-voltmeter; b) transportable Dewar with telescopic insert.*

1.46). Yet an accuracy in the comparisons better than 10^{-8} should be reached, to make the system competitive with respect to room temperature CC's. A compromising design was implemented[1].

2.1.1. Description of the system

The new CCC based resistance bridge (Figure 2.1) consists of several parts: the two resistors to be compared; the CCC-SQUID cryogenic part, fixed at the end of an insert immersed in a transportable helium Dewar; the SQUID electronic readout and the bridge control electronics.

2.1.1.1. The cryogenic system

The Dewar was chosen to be the one with the largest diameter neck among the commercially available low-evaporation rate, medium-capacity He transportable vessels. The CH-120 (120 liters) Dewar, from "Wessington cryogenics", is provided with a standard NW50KF (50 mm) top opening and has a small evaporation rate of 1.2 % per day[2]. Normally, the vessel neck contains a long fiber-glass cylinder, at the top of which the Dewar standard closing is fixed. This piece can be removed, leaving a 70 mm diameter

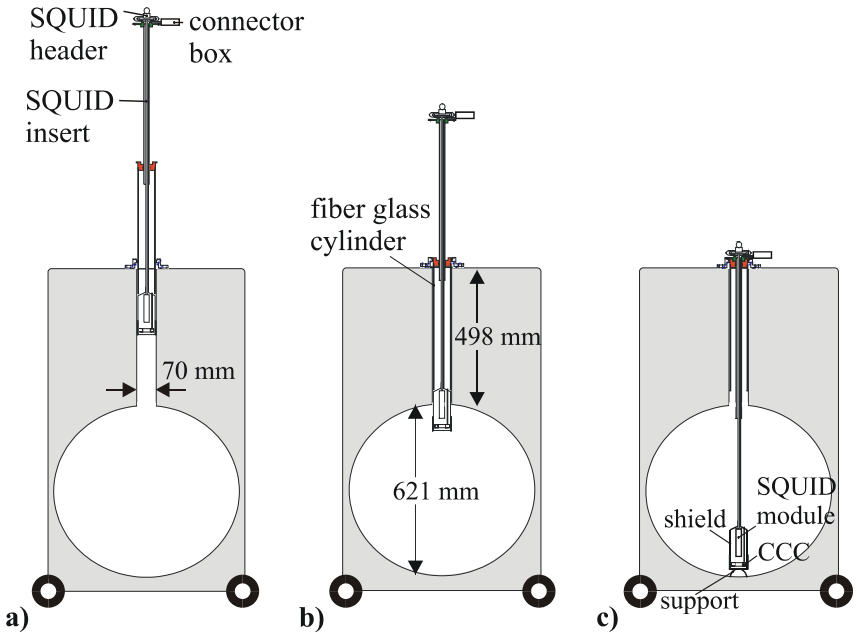

Figure 2.2- *Cooling down of the CCC-SQUID with a telescopic insert, adapted to fit in the neck of a commercial transportable Dewar.*

available neck, in which the complete CCC-insert should be fitted. A telescopic probe (Figure 2.2) allowing the slow cooling-down and long-storage time of the system was fabricated. The innermost, support tube of the probe was the rigid insert of a commercially available SQUID. The CCC and a superconducting magnetic field around it were tightly fixed at the cold-end of this tube.

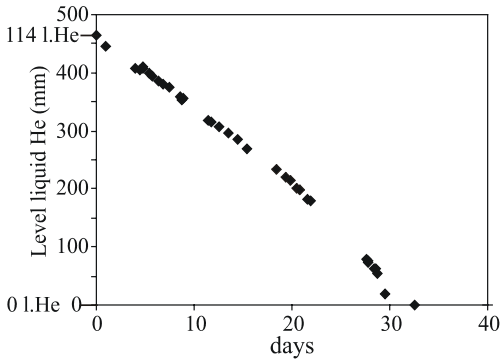

Figure 2.3- *Helium consumption of the CCC bridge in the transportable dewar. The helium lasted for ~1 month (the CCC was warmed up 6 times).*

The CCC winding wirings were brought to a connection box at the warm-side of the tube, to allow easily switching between the different possible N_1/N_2 ratios. This central tube slides into a concentric fiber-glass cylinder, that fits closely into the vessel neck. With this construction, the evaporated He gas is obliged to circulate along and refrigerate the walls of the vessel neck, thus slowing the loss of He through thermal conduction. The bottom of the insert could be rested at the bottom of the Dewar, to avoid noise arising from pendule oscillations. The telescopic mechanism allowed cooling down the CCC-SQUID in about 30', with an evaporation of only ~0.5 liters of liquid He. A month of continuous operation is possible (Figure 2.3).

2.1.1.2. The CCC-SQUID

The core of the bridge is a (type I) CCC with rf SQUID readout. To allow the comparison of resistances with the ratios 1:1, 1:10, 1:100, R_H(i=2):100 Ω and R_H(i=4):100 Ω the CCC contained windings with the following number of turns: 1, 1, 2, 4, 16, 16, 32, 64, 128, 465, 800 and 800 turns. The binary progression of turns allows a self-check of the CCC ratio error. The windings were made of superconducting (70-μm monofilament NbTi with copper matrix) wire, so as to eliminate completely the possible ratio error due to capacitive current leakage between the turns.

In order to enhance the CCC current resolution, $\langle I_p^2\rangle^{1/2}/N_{CCC}$, the CCC overlapped tube inductance L_{CCC} should be as large as possible. The nominal L_{CCC} increases approximately linearly with the diameter of the CCC toroid, but is reduced to an effective

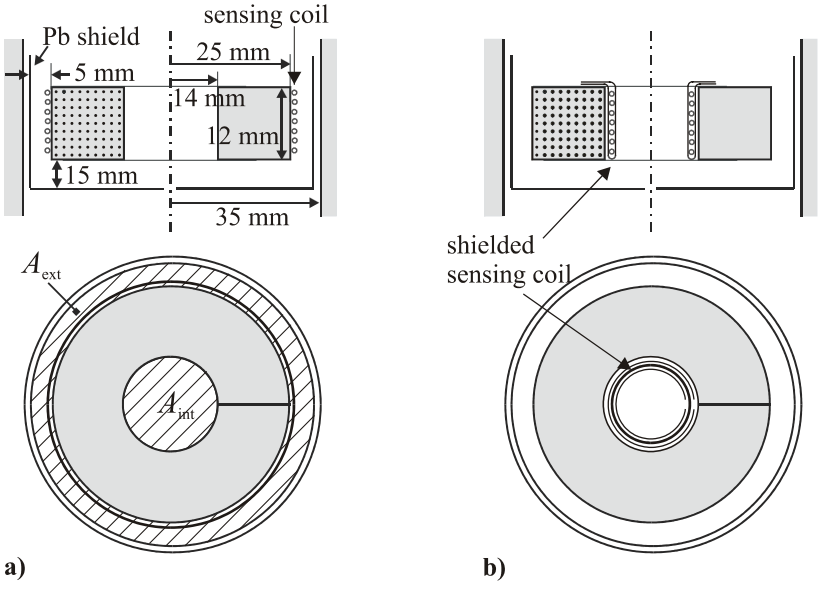

Figure 2.4- *CCC cross section and bottom view; a) in the original design the sensing coil was wound around the CCC external wall; b) modified design, in which the sensing coil was shielded by a lead foil, and placed at the inner side of the torus.*

value $L_{CCC,eff}$ when the distance between the CCC external wall approaches the superconducting magnetic shield, due to the image effect[3]. Given the size of the Dewar's neck and the lateral space needed for mounting the shield, the external radius of the CCC overlapped tube was limited to D_{ext}~50 mm. In order to have the maximal $L_{CCC,\,eff}$, the area enclosed by the CCC and the area comprised between the CCC external wall and shield should be equal: $A_{int}=A_{ext}$ (Figure 2.4a). The numerical demonstration of this statement can be found in Apendix B. Intuitively, one can imagine that because the density of flux lines is the same in the two area, the supercurrent induced in the walls of the superconducting shield, which causes the reduction of L_{CCC} , will be the minimum. With this condition, the CCC internal diameter was set d_i~28 mm. The CCC height was h~12 mm to accommodate all the windings. The lateral and bottom distances between the CCC and the shield were 5 mm and 15 mm, respectively. The upper shield cover was sufficiently far from the CCC, so that its shielding effect could be neglected. The effective CCC inductance simulated with the "Quickfield" finite element program as described in Ref. 4, was $L_{CCC,\,eff}\approx$17 nH. The CCC tube was made in 0.125 mm-thick, high purity (99.95%) lead to avoid the presence of magnetic impurities. The toroid was overlapped 3.5 times. The ratio error for this CCC, calculated according to Eq. 1.4 should be $F_{e,squared}\sim 2.7.10^{-18}$. The isolator used between the different overlapping turns was kapton. The fabrication process of the CCC is resumed in Figure 2.5.

The readout SQUID used was a commercial "Oxford Instruments" rf SQUID ("model Φ_0") [*], with an input coil inductance of L_i=1.3 μH, mutual inductance of M_{sq}=15 nH, intrinsic energy resolution of $\varepsilon=9x10^{-29}$ J/Hz$^{1/2}$ (in the white region) and a corner frequency < 0.1 Hz. Due to the mismatch between L_i and $L_{CCC,eff}$, a N_s=8 turn sensing coil was required to couple the maximum flux of the CCC into the SQUID. The sensing coil was (initially) tightly wound around the CCC. In this way the coil can be much closer to the CCC walls than if the coil is placed inside the torus, so the coupling CCC-sensing coil and thus the sensitivity should be better[3]. Measurements showed however that this configuration presented other disadvantages (2.1.3).

If the coupling between the CCC and SQUID was ideal (k'=1), the best current resolution that might be expected from this system would be (Eq. 1.48): $<i_P^2>^{1/2}\sim$200 pA.turn/Hz$^{1/2}$. Because of the reduction of sensitivity following from the use of a sensing coil, this value could be degraded by ~20%.

The SQUID module was surrounded by a Nb shield. The CCC was mounted on a celotex support that provided mechanical rigidity, and fixed at the end of the SQUID module. The whole CCC-SQUID system was surrounded by a superconducting shield (initially made of Pb, and later replaced by a Nb shield). A cryoperm shield was not included, given the restricted space inside the Dewar's neck, and the will of keeping the budget low. Other reported CCC R-systems[5] showed to perform sufficiently well without the need of this ferromagnetic shielding.

---

[*] The reason to use this particular rf SQUID system was mainly the fact that it had a rigid insert, which allowed mounting the telescopic probe on it. A dc SQUID (specially a home-made dedicated one) would be certainly more sensitive, but as will be shown, for the relatively modest current resolution exigencies of this bridge (compared to the CCC-SQUID amplifier of Part III) this commercial rf SQUID was sensitive enough.

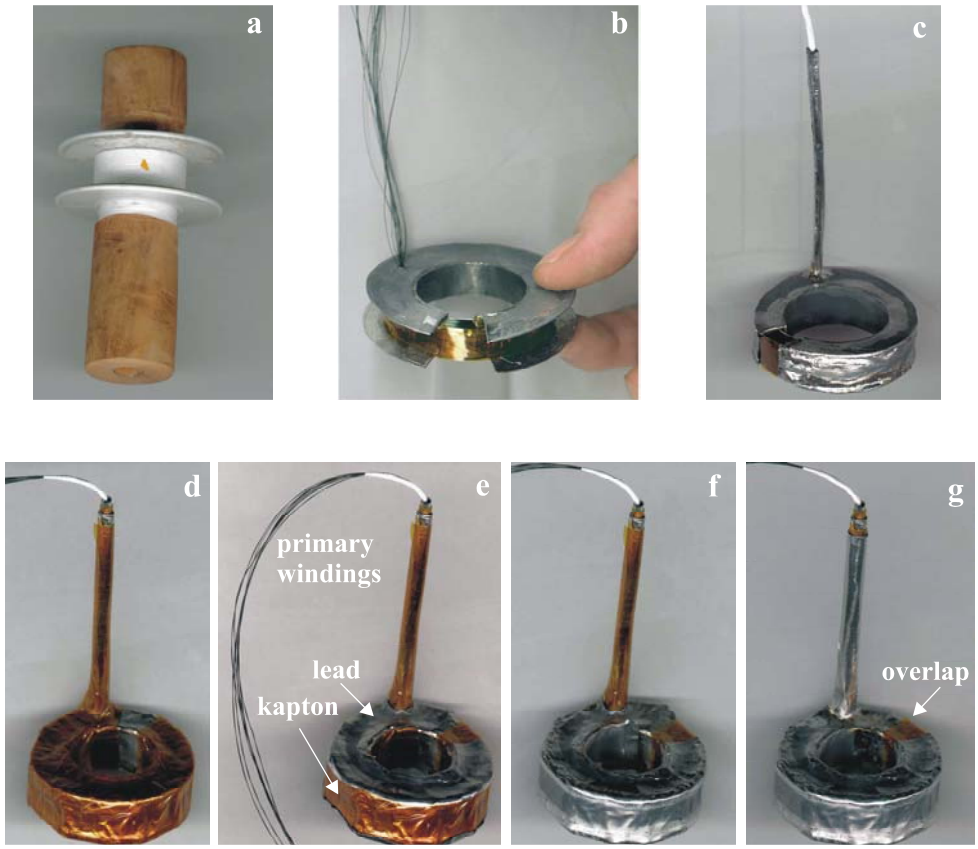

Figure 2.5- *Fabrication of the CCC for the R-bridge: a) Dismountable plastic holder mounted on a wooden axis, used for spooling the primary windings; b) Aspect of the CCC after winding. Kapton is used to protect the windings while soldering the different lead layers and provide the necessary isolation between successive layers. The ends of the windings are taken out through a small hole at the top of the CCC, protected with Teflon tape and the different windings identified; c) The first layer has been finished. A small gap in the torus is left open, since the CCC must be an open structure. The next (2^{nd}) layer will be soldered to this point; (d to g) As an example, fabrication of the 4^{th} layer: d) kapton foil is deposited all over the previous (3^{rd}) lead layer for insulation, e) the top of the 4^{th} layer is deposited; f) the interior and external walls are soldered. Before soldering any layer to the previous one, the proper insulation between the two layers is checked; g) the 4^{th} layer is soldered to the 3^{rd} and the lead tube covering the primary windings is completed. The total overlapping length of this CCC tube is ~3.5 turns.*

2.1.1.3. The R-bridge electronics

The resistance bridge (Figure 2.6) was based upon the design described in Ref. 6. A primary current I_p created by the primary current source S_p feeds the reference resistance R_p and the CCC winding N_p. A secondary current I_s, generated by a secondary current source S_s (slave of S_p), feeds the resistance to be compared R_s, and the CCC winding N_s. A voltage ramp generator feeds the two voltage-controlled current sources, so that the polarity and magnitude of the two currents can be inverted simultaneously. The two currents traverse *RC* filters, to reduce the noise coupling to the SQUID. The values of *R* an *C* can be adjusted to maintain the filter frequency constant when a different resistance R_s is placed. A first, coarse adjustment (parts in 10^5) of the bridge is realized by a manual tracking system, leaving the fine adjustment (parts in 10^{10}) to the SQUID feedback loop. In this way the SQUID does not have to cope with large signal variations, and remains locked. The isolation stage provides an isolation better than 10^{13} Ω between the two branches of the bridge. A model N11 nano-voltmeter from EM measures the difference in the voltage across the two resistors. It can be connected to an $8^{1/2}$ digits multimeter (HP3458A) and be readout as a function of time with a computer. The unbalance flux Φ_e is detected by the "Oxford" rf SQUID, and the output feeds-back the secondary source via a fiber optic stage, which isolates perfectly the current-control and SQUID electronics. When a coaxial cable was used instead, SQUID operation in FLL was impossible, probably because of the coupling between the groundings of the two electronics. An integrating stage in the feedback loop was designed to compensate for the filter pole and fix the system cut-off

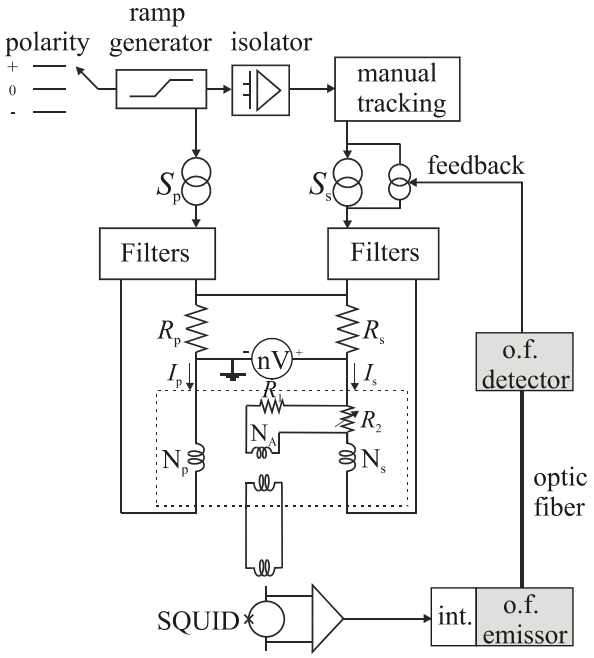

Figure 2.6- *Schematics of the CCC resistance bridge.*

frequency at ~110 Hz, while keeping a high gain (>10^5). With these precautions, the feedback loop will be stable independently of the ratio of windings chosen, facilitating the use of the bridge. The whole system is fed by (long time working) NiCd batteries to avoid interferences from the power grid. Each part of the system is closed in separately guarded boxes to minimize electronic cross-talk. The V^- input of the nano-voltmeter is used to ground the whole bridge. The nano-voltmeter has to be connected in such a way that the windings are close to the ground, as shown in Figure 2.6. It has been observed that if the nano-voltmeter is placed before the resistors, continuous SQUID jumps occur. We believe that in the later case the windings find themselves at a higher potential, and sudden capacitive currents can develop between the turns and the CCC ground, unlocking the SQUID.

2.1.2. Bridge balancing: the "difference compensator" method

The feedback of the CCC bridge guarantees that $N_pI_p=N_sI_s$. The nano-voltmeter measures the difference in voltage drop across the resistors, ΔV. When the two resistances are exactly in the same ratio as the two windings: $R_s=(N_s/N_p)R_p$, then $\Delta V=0$. A deviation ΔR_s of the secondary resistance from its nominal value, will produce a proportional voltage signal ΔV, thus: $\Delta R_s=\Delta V/I_s$. Since the secondary current I_s is not known with high accuracy, a calibration method is needed. An earlier version of the bridge[6] used a calibration pulse method to obtain the value of ΔR_s. A resistor, R_{cp} shunts R_s for a short time, so a known resistance variation of e.g. 1 ppm is introduced. A voltage pulse V_{cp} is produced, which can be used to scale the value of ΔV and obtain ΔR_s. This calibration method presents several problems. First, in order to scale the ΔV with V_{cp}, both voltages must be read in the same scale, and since V_{cp} can be very different from ΔV, ΔV is obtained with poor resolution and errors due to the non-linearity of the nanovolt-meter have to be taken into account. Besides, the sudden variation in the bridge introduced by the pulse easily unlocks the SQUID.

An alternative, "difference compensator" method[7,8] has been implemented to solve these problems. It consists in deviating a well known part of the secondary current I_s through an auxiliary CCC winding N_A, owing to a current divisor composed of R_1 and R_2 (Figure 2.6), such that: $I_A=R_2I_s/(R_1+R_2)$. R_1 and/or R_2 can be varied so as to balance the bridge. The secondary resistor will be:

$$R_s = R_p \frac{N_s}{N_p}(1+\varepsilon_R), \qquad \text{where } \varepsilon_R = \frac{N_A}{N_s}\cdot\frac{R_2}{R_1+R_2}. \tag{2.1}$$

If the two resistors compared have deviations from their nominal values: $R_s=R_{s,nom}\,(1+\varepsilon_s)$ and $R_p=R_{p,nom}(1+\varepsilon_p)$, (impossible to measure in absolute values), then $\varepsilon_R=\varepsilon_s-\varepsilon_p$ is a (relative) measure of the deviation from the ratio. Since the nano-voltmeter works as null detector, no error due to the non-linearity of the instrument is introduced. In addition, no sudden change is introduced in the bridge, so the SQUID does not unlock. The accuracy with which the resistors R_1 and R_2 must be known depends on the value of ε_R. For instance, if ε_R=1 ppm, in order the error committed by the difference compensator to be less than 1 part in 10^8, we should know R_1 and R_2 with 1% accuracy. It is not necessary to achieve a perfect zero in the nano-voltmeter to deduce the exact value of R_1 and R_2 that balance the bridge. It is enough

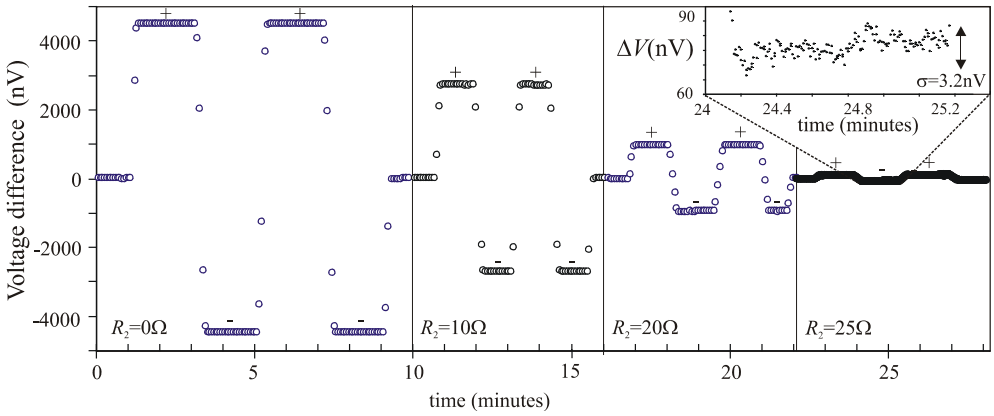

Figure 2.7- *Voltage ΔV in the nano-voltmeter as a function of time for three different values of the adjustable resistor R_2. The polarity change in I_p (0, +, -, +, 0) is indicated. The inset shows the stability within a plateau.*

to take some points as close as possible to zero and calculate the exact value of $R_2/(R_1+R_2)$ to balance the bridge by interpolation. As a consequence, it is not necessary to control ε_R with accuracy 10^{-8}.

The new transportable CCC bridge includes a difference compensator method, that we have tested first on the existing bridge. We compared two resistors with nominal value 100 Ω, using two $N_s=N_p=32$-turn windings, and an auxiliary $N_A=64$ turn-winding. R_1 was a precision resistor with fixed value $R_1=4.9999026$ MΩ, and R_2 could be varied with parts in 10^4. We made four automated measurements, with the following values of R_2: 0, 10, 20 and 25 Ω. In each ~6 minutes run, the primary current I_p is switched from 0 to alternatively +, -, +, - 4.18 mA. Results are shown in Figure 2.7. The voltage standard deviation, obtained from the voltage statistic spread within a typical plateau was $1\sigma_V=3.2$ nV. The value of R_2 compensating exactly the bridge, obtained by interpolation (Figure 2.8), was $R_2=25.44\pm0.03\Omega$. Therefore, the two resistors are in relation $R_s/R_p=1+\varepsilon_R$, with: $\varepsilon_R=10.2$ ppm.

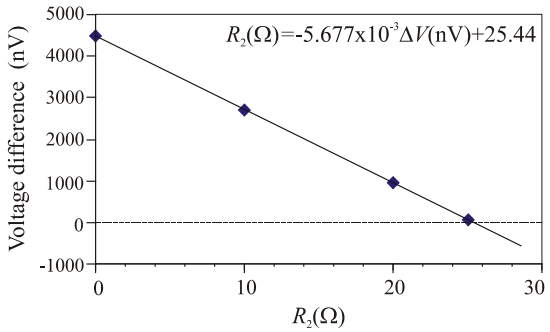

Figure 2.8- *Interpolation to obtain the exact value of R_2 balancing the bridge.*

The type A (statistical) uncertainty of the measurement was $\sigma_V/(2I_pR_p)=4x10^{-9}=4$ ppb, better than the best uncertainty that could be reached with a room temperature CC (10^{-7}) or with the potentiometric method (10^{-8}).

2.1.3. Test of the new *R*-bridge

The main characteristics of the new CCC-SQUID system were measured. The CCC ratio error *F* was determined dividing the SQUID signal measured when a 4 mA current was applied to the series-opposition of two 800-turn windings, by the signal detected when the same current was simply applied to only one of the windings (Eq. 1.3). The SQUID output when passing the current through the series-opposition of turns was indistinguishable from the SQUID noise, thus the ratio error could only be estimated to be $<10^{-9}$. In fact, following from the theoretical calculation (Eq. 1.4), the real error was probably much smaller ($2.7.10^{-18}$). The CCC-SQUID sensitivity, e.g. the current necessary to be applied to 1 CCC turn to detect $1\Phi_0$ at the SQUID, was S=4 μA.turn/Φ_0.

The zero stability of the CCC-SQUID was measured recording the SQUID output in FLL as function of time, without applying any current to the windings. Initially, a quite poor current resolution of $1\sigma_I$~13 nA.turn for a 5' measurement was obtained (a). In addition, the system was be very sensitive to accidental or deliberately produced (e.g. by opening and closing the He recycling valve) pressure variations in the cryostat. We found that flux could be easily trapped during cool-down at the type II superconductor Pb-Sn tin used for soldering together the different parts of the CCC. Changes in the cryostat pressure produce the random movement of the trapped vortices with respect to the sensing coil, tightly wound around the external wall of the CCC. To solve the problem, the sensing coil was shielded by a lead foil construction, and placed at the inner side of the toroid (Figure 2.4b). With this configuration, the measured resolution was much better ($1\sigma_I$ ~1.2 nA.turn) (a) and the system was insensitive to pressure variations. The sensitivity was the same as when having the sensing coil at the external side of the CCC.

In order to test the current control bridge electronics, the nano-voltmeter output was

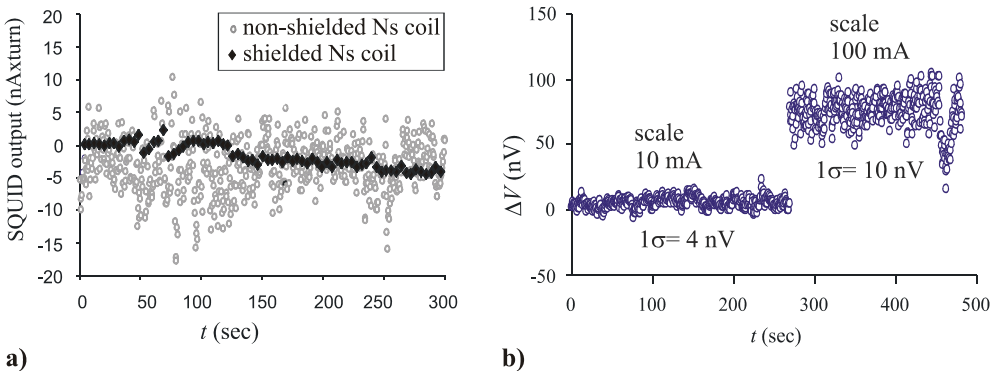

Figure 2.9- *a) SQUID output in FLL as function of the time, before and after shielding the pick-up coil (see text); b) nano-voltmeter output for two of the primary current ranges.*

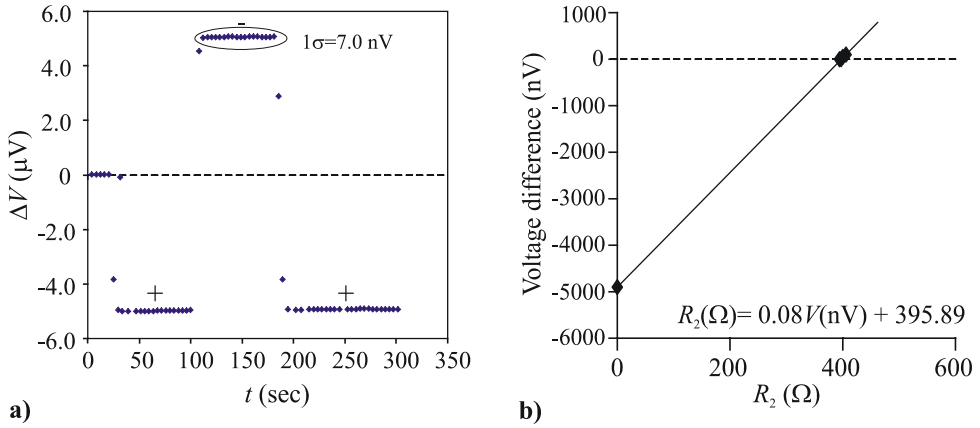

Figure 2.10- *a) Nano-voltmeter output as a function of time for R_2=0; b) Interpolation to obtain the value of R_2 balancing the bridge.*

recorded for the four primary source S_1 current ranges available. If the gain of the feedback loop was sufficiently large, the noise should not scale with the current range. We checked that, indeed, for the ranges 0.1 mA, 1 mA and 10 mA the noise was the same (1σ~4 nV), whereas for the 100 mA range, the noise was larger (1σ~10 nV) (Figure 2.9b).

We compared two 100 Ω resistors, using the "difference compensator method" explained in section 2.1.2, implemented in the new bridge. The winding ratio was N_s:N_p=16:16 , while the auxiliary winding had N_A=2 turns. The nano-voltmeter output was recorded for the values of R_2: 0, 395, 396, 400 and 405 Ω (see e.g. Figure 2.10a). In each run, the primary current I_p was switched from 0 to +, -, + 5 mA. The typical voltage standard deviation was $1\sigma_V$=7 nV. Since the value of R_2 compensating bridge was found to be R_2=395.89±0.01Ω (Figure 2.10 b), the result of the comparison was ε_R=9.90 ppm, with an uncertainty of 7 ppb.

Finally, we performed the calibration of a 100 Ω resistor with respect to a 12.9 kΩ resistor (simulating the QHE resistance), to test the performance of the bridge for a larger number of turns ratio (N_s:N_p=2065:16 turns). The bridge turned to be inoperable due to constant jumps of the SQUID. We believe that the environmental and trapped flux noise, amplified by the large CCC ratio, prevents the SQUID FLL operation. Therefore, for resistance calibrations to the QHE, the use of an additional cryoperm shielding would be indispensable.

In conclusion, an optimized resistance bridge based on the CCC-SQUID, with a user-friendly, transportable cryogenic system has been developed and tested. The relative simplicity, low cost and better uncertainty level makes the instrument competitive respect to today's more extended room temperature current comparators. Using the difference compensator method, type A uncertainty levels of 7 ppb have been achieved. The present system will be transferred to the TPYCEA[9] Spanish secondary metrology institute.

2.2. Outlook of a planar HTS CCC-SQUID

The fabrication of a completely integrated thin film CCC-SQUID in HTS technology would represent a great step forward towards the development of a user-friendly, yet accurate system for the routine 1:1, 1:10 calibration of resistors. The CCC-SQUID chip could be ideally cooled down in a small nitrogen Dewar at 77 K. Besides, problems arising from mechanical vibrations in massive CCC's could be avoided. In this section we study the feasibility and expected performance of a planar CCC-SQUID fabricated with present HTS technology.

2.2.1. HTS massive CCC's and planar LTS CCC's

HTS CCC's have been fabricated, though only in the massive version. The construction of accurate HTS CCC's runs into the difficulty of making the conventional overlapped three-dimensional geometry in HTS bulk ceramics, which are mechanically difficult to handle. Alternative shielding solutions have been proposed. Elmquist[10] made a HTS CCC with a ratio error limited to 10^{-6} using two parallel BSCCO tubes and a YBCO RF-SQUID placed in between. Arri[11] considered a design where the windings were located near the bottom of an open toroidal gutter. Further, Early[12] proposed a toroidal shape where the windings were enclosed by a series of split shells, oriented in an alternative fashion. An LTS prototype showed that a ratio error of $\sim 10^{-8}$ could be achievable with this geometry.

On the other hand, a sort of integrated thin-film CCC (intended for ac metrology) has been fabricated, though only in LTS technology[13]. This planar LTS CCC did not exactly reproduce the overlapping geometry. It rather consisted of a washer, on top of which two separate windings of 13 turns layed, interlaced for symmetry. A low-noise LTS SQUID was assembled in the center of the CCC by flip-chip bonding. The dc ratio error of a CCC with this geometry was large (at best, 450×10^{-6}) since the windings were not shielded, and was temperature dependent, via the London penetration depth $\lambda_L(T)$.

2.2.2. A planar YBCO CCC-SQUID: feasibility and expectations

In this paragraph we discuss the possible fabrication of a simple planar CCC-SQUID with today's state-of-the-art HTS technology and approximate performance.

HTS thin film devices are mainly made of $YBa_2Cu_3O_{7-x}$ (YBCO), a ceramic superconductor with a typical critical temperature T_c between 88-91 K, depending on the quality of the film[14]. As a result of the anisotropy of the YBCO's unit cell, the electrical properties in the *ab*-plane are different than in the *c*-direction. In particular the critical current in the c-direction $I_{c,\,c}$ is very small, around 10 times smaller than in the a-b plane. Therefore, the implementation in HTS of structures including multilayer contacts and crossovers (like e.g. coils) is technologically quite complicated.

The most simple HTS planar CCC-SQUID we might think of could be based on the "direct-coupled magnetometer" geometry, shown in Figure 2.11. The pick-up loop would serve as base layer for the CCC loop. A set of primary windings (e.g. 1, 1, 10 wirings) should be sandwiched between two isolator layers, placed on top of the base CCC loop, and

covered by a top CCC layer in the shape of a "U" (with the gap opposite to the SQUID side, to reduce the ratio error).

A commercial $SrTiO_3$ (STO) bicrystal could be used as substrate for the epitaxial growth of YBCO. The STO substrate has to be annealed to reinstall the crystal structure of the as-received amorphous surface. The YBCO CCC base (and top) layer should shield the primary windings from the SQUID. This means that the thickness of these layers should be larger than YBCO London penetration depth in the c-direction, temperature dependent as: $\lambda_{L,c}(T)=\lambda_c(0)/\sqrt{1-(T/T_c)^{\alpha}}$, where $\lambda_c(0)\approx 700$ nm and $\alpha=2$.[15] Since typical, good quality YBCO layers deposited by Pulsed Laser Deposition are only ~100 nm thick, a rather large ratio error due to the insufficient shielding would arise. Thicker YBCO layers of up to 2 μm can be reached by spray, but then the epitaxial growth of the successive thin/thick layers would be problematic.

Structures in the YBCO layer can be formed by Ar^+ ion beam etching (IBE) the YBCO layer (covered by a patterned photoresist layer mask) under an angle. The SQUID junctions consist of bridges of ~2-4 μm width patterned across the ~20-30° bicrystal grain boundary. To have a good superconducting contact between the bottom and the top CCC layers, the bottom CCC layer should have beveled edges. Due to the high dielectric constant of the substrate STO, a parasitic capacitance shunting the inductive structures on top is present, and *LC* resonances are likely to appear at high frequencies. This would not disturb the operation of the CCC, which works at very low frequencies, but would induce resonances in the SQUID. Next, an STO layer, thick enough to guarantee a good isolation between the CCC base layer and the windings, should be deposited. The primary windings should be then made in YBCO. Since the minimum winding width and winding separation is ~2 μm, the width of the base CCC layer should be larger than w_d~48 mm to allocate all the primary windings. The top STO isolation layer and YBCO layer should be then deposited. The top CCC layer must be as thick as the bottom one, to reach a good shielding. Finally, gold contact paths for the SQUID and CCC windings should be made with rf sputtering.

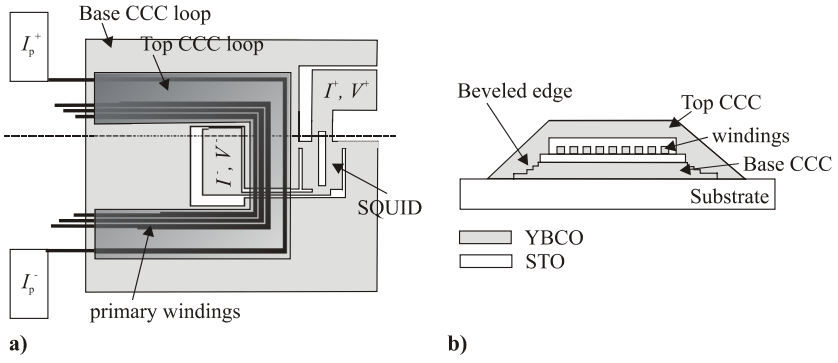

Figure 2.11- *Schematic of a simple CCC-SQUID made in HTS planar technology (not in scale). The dotted line represents the grain boundary. a) Top view of the CCC-SQUID; b) Cross section of the CCC "tube".*

Let us consider the current resolution that might be expected from this planar CCC. The chip should be extremely well shielded by ferromagnetic shields, to avoid the increase of low-frequency noise, due to the hopping of flux lines in the YBCO CCC walls. In first approach, consider that the noise was only determined by the SQUID. Since the CCC loop coincides practically with the pick-up coil of the SQUID, an almost perfect coupling could be achieved. For a typical gradiometric HTS SQUID[14], the SQUID inductance is L_{sq}~100 pH, the pick-up inductance $L_p \sim L_{CCC}$=5 nH, and the flux noise is ~100 $\mu\Phi_0/Hz^{1/2}$ at 1 Hz. Therefore, the current resolution would be $\langle i_p^2 \rangle^{1/2}$=630 pA.turn/$Hz^{1/2}$.

In principle this level is better than the current resolution of room temperature CC's, typically ~100 nA.turn/$Hz^{1/2}$. The limitation of the planar CCC might come form a too large ratio error, owing to the non-overlapped geometry of the CCC "tube" and the imperfect shielding of the YBCO CCC walls. To compete with room temperature CC's, a ratio error better than 10^{-7} should be achieved. Future investigation of new HTS materials and development of the fabrication techniques, specially in the integration of structures in the c-direction, might open new perspectives.

References

[1] E. Bartolomé *et al*., *IEEE Trans. Appl. Supercond*. **11**(1) 867 (2001).
[2] http://www.wessingtoncryogenics.co.uk/ch_series.htm
[3] J. Sesé *et al*., *IEEE Trans. Instrum. Meas*. **48**(6), 1306, (1999).
[4] J. Sesé *et al.,IEEE Trans. Appl. Supercond*. **9**(1), *58, (1999).*
[5] F. Delahaye and D. Bournaud, *IEEE Trans. Instrum. Meas*. **40**(2), 237, (1991).
[6] A. Camón, PhD Thesis, University of Zaragoza, (1996).
[7] F. Delahaye and D. Reymann, *IEEE Trans. Instrum. Meas.* **34**(2), 316, (1985).
[8] J. Sesé, PhD Thesis, University of Zaragoza (1999).
[9] TPYCEA stands for "Taller de Precisión y Centro Electrotécnico de Artillería", see for instance http://www.enac.es/anx/lc/TPYCEA_LC089_REV3.pdf
[10] R. E. Elmquist and R.F. Dziuba, *IEEE Trans. Instrum. Meas.* **44**(2), 262, (1995).
[11] E. Arri *et al., Conf. on Precision Electromagnetic Measurements Digest*, 221, (1998).
[12] M.D. Early *et al*., *Proc. of the European Conference on Applied Superconductivity, Sitges*, Spain, (1999).
[13] H. Seppä, *IEEE Trans. Instrum. Meas.* **39**(5), 689, (1990).
[14] A. Jansman, PhD Thesis, University of Twente, The Netherlands.
[15] J.Y. Lee and T.R. Lemberger, *Appl. Phys. Lett*. **62**, 2419 (1993).

Part III

ULTRA-SENSITIVE CCC-SQUID CURRENT AMPLIFIERS

The very accurate measurement of extremely small currents is a very important issue e.g. in the semiconductor industry, where the continuous miniaturization of chips requires the control of everyday smaller currents. The ability to perform these highly accurate measurements relies on the existence of a very precise current standard and calibration techniques. In the SI, the unit of current, the Ampere (A), is defined as "that constant current which, if maintained in two straight parallel conductors of negligible cross section and placed one meter apart in a vacuum, would produce between these conductors a force equal to $2x10^{-7}$ Newton per meter of length". The definition of the Ampere can be realized in a Watt balance, that compares the mechanical and electrical Watt. However, the uncertainty in the realization is very large (10^{-7}) and therefore, in practice, it is not used as the current representation. Instead, the (classical) current standard is derived via Ohm's law ($V=IR$) from the voltage and resistance standards, which are much easier to maintain.

There is nowadays much interest in developing a quantum current standard. This would allow the maintenance of a very precise, independent current primary standard to which other currents could be calibrated. On the other hand, it would make it possible to close the quantum metrological triangle of electrical (see Chapter 7).

The realization of a current quantum standard is based on some special devices which can deliver quantized currents: $I=nef$, where n is an integer, and f is the driving frequency, that can be adjusted very precisely (parts in 10^{10}). Two different sorts of devices can provide a quantized current (an extended review will be presented in Chapter 7). Single Electron Tunneling (SET) devices can give only very small currents of 1-10 pA, with an uncertainty of 10^{-8}-10^{-6}. Devices based on Surface Acoustic Waves (SAW) can yield larger currents ~1 nA, but the uncertainty attained is insufficient (10^{-3}). In order to fabricate a standard interesting from the metrological point of view, the tiny, quantized currents should be amplified to the order of μA, while maintaining the uncertainty as low as possible.

The dc SQUID based CCC is the most sensitive system for the accurate (with parts in 10^8) scaling of very small dc currents. To enhance the current noise of the system, $\langle I_P^2\rangle^{1/2}=\langle i_P^2\rangle^{1/2}/N_{CCC}$, the number of primary windings N_{CCC} should be as large as possible, whereas the current resolution per unit turn $\langle i_P^2\rangle^{1/2}$ should be minimized. As we saw in section 1.4, the last requires ideal magnetic flux coupling between the CCC and the SQUID and the use of extremely sensitive SQUIDs.

At the moment of start of this thesis, there had been two different trials to build up a CCC-SQUID SET current amplifier. At the NPL, Hartland[1] had made a large (16 cm diameter), large ratio 1:109999 CCC, which was coupled through a 3-turn sensing coil to a Quantum Design dc SQUID, with an input coil inductance of L_i=2.2 μA and flux noise ~3.2 $\mu\Phi_0/Hz^{1/2}$. The current resolution was expected to be 8.4 pA.turn/$Hz^{1/2}$. In practice, the system was inoperable due to multiple problems, believed to arise from the non-ideal coupling between the CCC and the SQUID, the huge number of turns, thermal instabilities drifts, vibrations etc. At the LCIE[2], a medium size (4.5 cm diameter), moderate ratio (1:10000) CCC was built up. The readout was done with a commercial Quantum Design dc SQUID, with a relatively high flux noise ~10 $\mu\Phi_0/Hz^{1/2}$. The large input coil inductance obliged to use a 11-turn sensing coil, with the subsequent reduction of sensitivity. A quite high current resolution of ~50 pA.turn/$Hz^{1/2}$ was reported.

We undertook then the development of a new, optimized CCC-SQUID current amplifier for the realization of a SET based quantum current standard and, eventually, the closure of the metrological triangle. In order to optimize $\langle I_P^2\rangle^{1/2}$, it was chosen to build a relative large size (10 cm), large ratio (1:30000) CCC, directly coupled to a home-made, low noise (~1 $\mu\Phi_0/Hz^{1/2}$) dc SQUID. When all external noise sources are excluded and the system noise is limited by the SQUID sensitivity, this design would allow to reach a current resolution of 1 pA.turn/$Hz^{1/2}$. Chapter 3 treats the development of devoted low-noise dc SQUIDs that can be directly coupled to the CCC. The readout of the SQUID should be such that the noise is limited by the SQUID and not by the electronics. Different readout systems have been studied and are described in Chapter 4. The frequency of the current circulating in the primary windings has to be very low (10^{-3}-1Hz) to avoid a large ratio error coming from capacitive leakage current. Chapter 5 deals with different techniques that can be applied to reduce the excess noise affecting the SQUID at those low frequencies. The integration of the CCC with direct connection to the SQUID is the subject of Chapter 6. Finally, in Chapter 7 an outlook on the possible realization of the metrological triangle will be given.

References

[1] A. Hartland, *Proc. of the International Conference on Electromagnetic Measurements*, **18**, 1 (1993).
[2] F. Piquemal, SETamp project, SMT-CT96-2049 3156 proposal, progress report (1998).

Chapter 3

LOW (WHITE) NOISE, WELL-COUPLED SQUIDS

As was shown in Chapter 1, the ideal current resolution of a CCC-SQUID system can be achieved in the direct-coupling configuration. If the inductances of the two sides of the transformer match, $L_{CCC,eff}=L_i$, the current resolution (per turn CCC) is given by: $\langle i_P^2\rangle^{1/2}=(8\varepsilon/k_{sq}^2 L_{CCC,eff})^{1/2}$. In practice, the value of $L_{CCC,eff}$ is upper limited by the size of the cryostat neck; for a quite large diameter neck ~160 mm, $L_{CCC,eff}$ will be of the order of 100 nH. In order to obtain the best $\langle i_P^2\rangle^{1/2}$, the SQUID intrinsic energy resolution ε should be small and at the same time the matching condition should be fulfilled.

Using a commercial dc SQUID, with typically $\varepsilon \sim 10^4\hbar$, one could (ideally) reach an $\langle i_P^2\rangle^{1/2}$ of only ~10 pA.turn/Hz$^{1/2}$. In practice, this value is further degraded due to the necessity of using a sensing coil to match the SQUID high input coil inductance (in the order of μH) to the low CCC inductance. On the other hand, using one of the very low inductance (L_{sq}~1-2 pH) quantum limited SQUIDs described in literature[1,2], which can reach a sensitivity ε of a few $\hbar$, an $\langle i_P^2\rangle^{1/2}$~0.1 pA.turn/Hz$^{1/2}$ could be in principle attained. However, in these SQUIDs the flux is simply coupled via a current line passing nearby the SQUID loop, or by a few-turns input coil. Thus, L_i is just ~1 pH to 2 nH maximum, and a direct connection between the SQUID and the CCC is impossible. In order to couple the SQUID to the CCC, a 1/300 "fractional-turn" sensing coil (Figure 1.20b) would be necessary, which is in practice impossible to realize.

In this chapter, we describe the development of different kinds of SQUIDs, designed to reach low ε values and be able to couple directly to the CCC. The fabrication process of the SQUIDs in the Nb/Al technology available and the characterization set-up are described in section 3.1. Section 3.2 describes SQUIDs designed specifically to match the CCC inductance. Section 3.3 treats the optimization of the washer-type dc SQUID with respect to the noise and direct coupling in a more general way. An approach to reduce the white noise produced by the shunt resistors was the development of intrinsically shunted, double-barrier SQUIDs (section 3.4). The noise levels measured with a Two-Stage readout system on the three kinds of SQUIDs are presented and compared in section 3.5.

3.1. Fabrication and test of Nb/Al based SQUIDs

3.1.1. Nb/Al SQUID fabrication process

The SQUIDs of this thesis were made in LTS Nb/Al (AlO_x) thin-film technology. The fabrication process incorporated some modifications and improvements with respect to the junction process reported by Adelerhof *et al*.[3], and will be here described.

The chip layout was designed with the help of the program Clewin[4] and the patterns replicated in chromium lithography masks. The minimum feature size was 1 μm. A 2" diameter, thermally oxidized silicon wafer (SiO_2: 600 nm) was used as substrate. The photolithographic steps for the deposition of a typical layer are detailed in Figure 3.2. The fabrication process usually starts with the deposition of the ***shunt and damping resistors*** (Figure 3.1a), with the help of a positive mask. (Alternatively, the resistors can be deposited after the trilayer, but the risk of adhesion failure increases). Resistors are made by rf sputtering of Pd in a Nordiko[5] system. A thin (2 nm) Al layer is previously deposited to increase the adhesion of resistors to the SiO_2 wafer. The sheet resistance of Pd is ~1 Ωm/m. When high resistance values are needed, resistors are made of PdAu (on top of a thin, adhesive Cr layer), a material with a larger sheet resistance (section 3.3.3), deposited by rf sputtering in a Perkin Elmer[6] system.

With the help of a 2nd positive mask, the ***Nb/Al/AlO$_x$/Al/Nb/Al trilayer*** is formed (Figure 3.1b). All Nb/Al layers are deposited by dc-magnetron sputtering in the Nordiko system. The background pressure is typically less than 10^{-7} mbar, and during the Ar induced sputtering the total gas pressure is 7.3×10^{-3} mbar. The 150 nm Nb bottom electrode is covered by a 5 nm Al layer, that forms by *wetting effect* a very planar surface on top of the columnar Nb. This Al layer is exposed to an oxygen atmosphere at a pressure pO_2, at room temperature during 1 h in the load-lock chamber of the Nordiko, to form the AlO_x junction barrier. The critical current density of the junction J_0 depends directly on the thickness of the barrier, which can be tuned varying the oxidation pressure. The critical current density J_0 dependence on the pressure pO_2 in our set-up is shown in Figure 3.3. Typically, a pressure of 100 mbar is chosen to obtain a J_0~40 A/cm^2. Unfortunately, the reproducibility of the oxidation process is affected by the level of humidity in the chamber. Usually the load-lock is heated for several hours, to evaporate remains of water vapor.

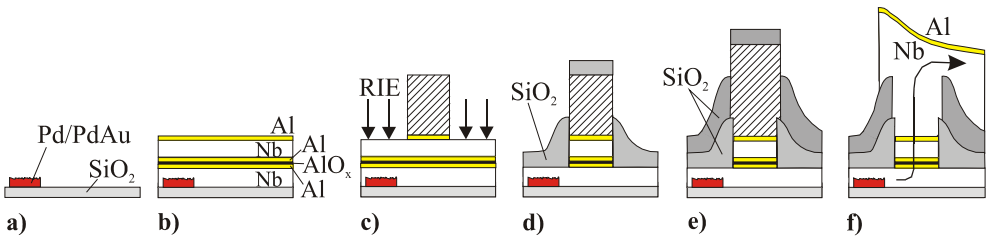

Figure 3.1- *Schematics of the fabrication of Nb/Al(AlO_x) devices.*

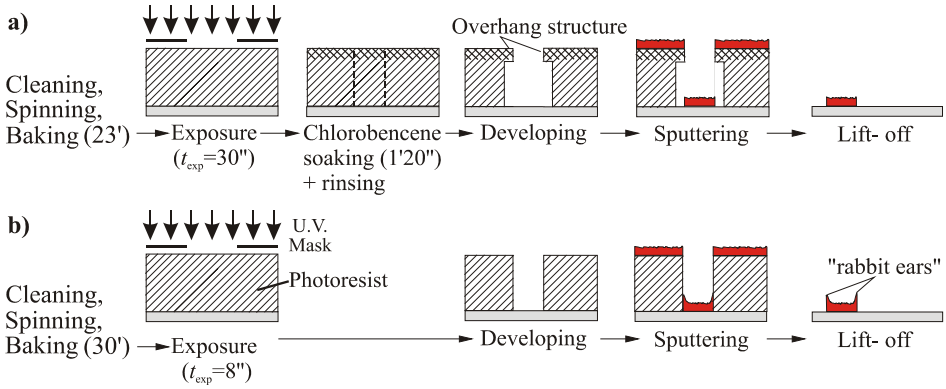

Figure 3.2- *b) A **typical photolithographic step starts cleaning** the substrate in an acetone ultrasonic (US) bath, rinsing it in an ethanol US bath and drying it thoroughly with nitrogen-gas. The wafer can be further dried for about 2' in the oven (90°) to evaporate possibly remaining water that would prevent the adhesion of photoresist (PhR) to the substrate. Optionally, a couple of droplets of HMDS can be deposited previous spinning, to improve the adhesion of PhR. By dropping 25 droplets of photoresist (Shipley 1813) in the center of the wafer and **spinning** it at high speed (4000 rpm) during 43'', a uniform 1.3 μm thick layer is formed. The wafer must be **baked** in the oven (90°) during 30' to harden the PhR. After cooling, the photolithographic mask is **aligned** with respect to previously patterned structures (this step is not needed for the first mask), and the PhR is **exposed** with ultraviolet light (wavelength=365 nm, intensity 10 W/cm^2) during t_{exp}=8''. The exposed areas of PhR are removed by **developing** the wafer in a 1:5 (Microposit 351:water) solution during a time t_{dev}. The wafer is then rinsed in water and dried with nitrogen-gas. After sputtering (respectively etching), the PhR pattern is **lifted-off** by solving it in an acetone US bath. Lift-off can be helped by scrubbing gently the surface with a lens-paper torch, while constantly wetting the wafer with acetone to avoid scratches. The growth of material along the walls of the PhR can make the lift-off difficult. At the edges of the sputtered material the so-called **"rabbit ears"** will appear, which increase the risk of shorts with the next deposited layer. To avoid this problem, a PhR pattern with an **"overhang"** structure can be made (a). In this case, the PhR is baked during 20-25' at 90°, and the exposure time is prolonged to t_{exp}=30''; the wafer is **soaked in chlorobencene** (C_6H_5Cl) during ~1'20'' and thoroughly **rinsed** in water (during >2'; no "gasoline" droplets should be seen). Because the soaked portion of PhR is more difficult to solve than the non-soaked portion, an undercutting is achieved. The overhang thickness and length depends on the PhR baking time, exposure time, chlorobencene soaking-rinsing, and developing time. A too short time or low baking temperature increases the overhang thickness, but decreases the adhesion of PhR to the substrate. Usually a quite long, high T baking is chosen at the expense of the thickness. Too long chlorobencene soaking or incomplete rinse results in partial polymerization of the PhR and inhibits partially the development of the PhR pattern. Overhang structures are used for the lift-off after deposition of quite thick layers (e.g. the trilayer and second SiO_2 layer).*

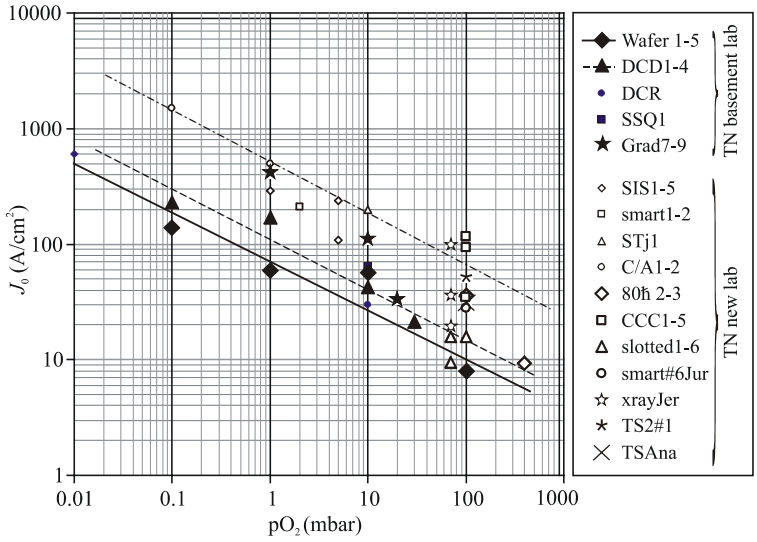

Figure 3.3- *Critical current density as function of the barrier oxidation pressure. Jumps in the $J_0(pO_2)$ dependence occasionally occur, probably as result of different levels of humidity in the load-lock oxidation chamber (e.g. different trends were observed when the sputtering system was moved from location).*

Nevertheless, occasional uncontrolled jumps in the $J_0(pO_2)$ curve with time have been observed. The AlO_x barrier is covered by a 5 nm-Al anti-oxidation layer, on top of which the 150/5 nm Nb/Al top electrode electrode is deposited.

A 3rd, negative mask is used to define the ***junctions*** and via contacts. The developing process is critical to obtain non-rounded, well-defined junctions. We perform it in two steps: first the wafer is bathed very shortly (7-8'') in a 1:5 concentrated solution, to structure the junctions, and immediately after bathed for a longer time (~20'') in a more diluted solution (1:25), to remove the top Al-layer from the unprotected areas of trilayer. A too long developing time causes the rounding of the PhR junction area, making the lift-off after deposition of next SiO_2 layer difficult, and reducing the value of the aimed critical current value. If the developing time is too short, the Al layer might not be completely removed, and the etching of the top Nb layer would turn impossible.

The top Nb electrode is removed from the PhR unprotected areas by Reactive Ion Etching (RIE[7]) of SF_6 plasma (Figure 3.1c), in a system built up in Twente[3]. The careful cleaning of the chamber and sample holder before the actual etching is essential to guarantee the reproducibility of results. The cleaning consists of i) an SF_6/O_2 plasma to remove NbF_x etch products, ii) an O_2 plasma to remove sulfur and iii) an Ar plasma for physical etching. The etching is performed with the following parameters: a SF_6 pressure 1.5 Pa (flow rate 5 ml/min), power density of 0.13 W/cm^2 and dc self-bias voltage -100 V. Under these conditions, the etch rate of Nb is ~60 nm/min, while the Al is not etched; hence the Al layer can be used as a stopping layer[3]. The fluorine radical emission line at λ=703.7

nm, recorded with the help of a XINIX spectrometer, can be used to monitor the etch process. Typically a total etch time of 9 min is needed to remove completely the top 150 nm Nb layer. If the etching is too long the junction PhR would be also etched, making the lift-off after the next SiO_2 layer extremely difficult. If the etch time is too short, shorts between junctions and contacts will appear through the incompletely removed Nb layer.

The remaining $Al/AlO_x/Al$ layer is chemically etched away in a solution of developer:water solution (1:25 during ~40''). The Nb is not etched by the developer. Next, a self-aligned 100 nm ***first SiO_2 insulator layer*** is deposited by rf sputtering in the Perkin Elmir system (Figure 3.1d). An O_2/Ar gas mixture (in ratio 1:10) is introduced, to ensure that isolating SiO_2 and not SiO is formed. The sample should be glued with sufficient vacuum grease to the target, and the deposition should be carried out on in several steps separated by cooling intervals to avoid the burning of PhR at high temperatures, which would turn the lift-off impossible.

Using a 4th negative mask, a ***second***, thicker (200 nm) ***SiO_2 layer*** is deposited (Figure 3.1e), to ensure a good insulation between the SQUID washer and the input coil on top. The lift-off of PhR after the two SiO_2 depositions should be done if possible without scrubbing the wafer, to avoid damaging the junctions.

Finally, with a 5th positive mask, ***wiring, feedback and input coils*** are patterned in 350/5 nm thick Nb/Al (Figure 3.1f).

3.1.2. SQUID characterization set-up

The electrical characterization of the SQUIDs is done in a home-made set-up developed at the Low Temperature Division. The SQUID chips are glued on an epoxy printed circuit board (PCB) with room for 6 chips. The electric contacts between the chips and the copper transmission lines on the PCB are made by means of ultrasonic wedge bonding with 25 μm diameter Al wires. The PCB is mounted at the cold side of the insert and shielded from external fields with a Nb can. The probe is cooled down in a stainless steel liquid helium cryostat (T=4.2 K). By pumping the He gas down, a temperature of 1.4 K can be attained. A carbon-glass resistance thermometer[8] is available in one of the PCB's. The entire cryostat is surrounded by a cylindrical μ-metal shield. The connections from the cold end to the control box (at the warm end of the insert), are made with twisted pairs of wires, shielded by a grounded stainless steel tube. A switch in the control box allows selecting the device to be measured. The bias current is supplied by a home-built current source, battery powered for ground isolation. The I_b is converted to a V signal through a 1 kΩ resistance, and amplified by x10. The voltage across the SQUID is separately amplified by a factor x10^3 with a second low noise differential amplifier. The flux is applied to the SQUID via a current (produced by a voltage source through a 1 kΩ resistor) passing through either the feedback or the input coil. Low pass filters are implemented in the insert wiring to reduce the influence of rf interferences. The I_b line is filtered with a cutoff frequency of 25 kHz, whereas the voltage, feedback and input coil lines have a cutoff frequency of 1 MHz, to enable modulation. The I-V and V-Φ curves can be visualized on an oscilloscope, and printed on paper with the help of a graphic recorder.

3.2. Matched SQUIDs for CCC

3.2.1. Design

A series of SQUIDs with different input coil inductances L_i around the value of the CCC overlapped tube inductance were designed by Vargas[9]. The design followed the next reasoning. To avoid a too large noise rounding, the parameter Γ should be <0.05. At 4.2 K this implies that I_0 should be larger than 3.5 μA. Since I_0 can be affected by the barrier oxidation process, to be safe, a value of I_0=8 μA was chosen. The screening parameter β relates I_0 and L_{sq}. For the optimal case, β=1, an inductance L_{sq}~130 pH is obtained. It was decided to make devices with L_{sq}~100..250 pH. In order to have non-hysteretic devices, the McCumber parameter should be β_c<1. This condition can be rewritten as:

$$R_{sh}C_j^{1/2} < \sqrt{\frac{\Phi_0}{2\pi I_0}}. \tag{3.1}$$

According to Eq. 1.19, R_{sh} should be large to achieve a low ε. Therefore the junction capacitance C_j should be as small as possible. Junctions with a reasonable area were chosen (4x4 μm^2). Using a value for the specific capacitance of $C'=C_j/A$~0.04 pF/μm^2, a junction capacitance of 0.64 pF is calculated. Then Eq. 3.1 limits R_{sh} to <8 Ω. To guarantee the non-hysteretical behavior, a very safe value of 2 Ω was chosen, giving a β_c=0.02. The predicted values for β, $\partial V/\partial\Phi$, M_i, $S_\Phi^{1/2}$ and ε for the different SQUIDs designed are given in Table 3.1. The SQUIDs have different number of input coil turns, to obtain a range of input coil inductances L_i between 20 to 160 nH. Thus, there is a reasonable chance that one of the SQUIDs will have an L_i close to the $L_{CCC,eff}$ of the CCC. The SQUID inductance was calculated taking into account the hole and slit inductance (Eq. 1.22-1.23). As the number of input coil turns increases, the washer outside size W becomes larger and the slit inductance contribution increases. The outer dimension W of all washers was the same, and

L_{sq} (pH)	β	$dV/d\Phi$ ($\mu V/\Phi_0$)	$S_\Phi^{1/2}$ ($\mu\Phi_0/Hz^{1/2}$)	ε ($\hbar$)	L_i=20nH	L_i=40nH	L_i=80nH	L_i=160nH
100	0.8	36.0	1.2	297.2	n=14 M_i=1.4nH	n=20 M_i=2.0nH	____	____
150	1.2	29.6	1.6	324.4	n=11 M_i=1.7nH	n=16 M_i=2.4nH	n=23 M_i=3.5nH	n=32 M_i=4.8nH
200	1.6	25.2	2.0	398.4	n=10 M_i=2.0nH	n=14 M_i=2.8nH	n=20 M_i=4.0nH	n=28 M_i=5.6nH
250	1.9	21.8	2.4	458.7	n=9 M_i=2.3nH	n=13 M_i=3.3nH	n=18 M_i=4.5nH	n=25 M_i=6.3nH

Table 3.1 - *Main design parameters for the "CCC matched SQUIDs".*

equal to the necessary dimension needed to allocate the turns of the SQUID with the maximum L_i considered (160 nH). However, for a washer with an L_{sq}=100 pH, only a maximum of ~20 turns (L_i=40 nH) could be placed, or the slit contribution would be too large. A damping resistor R_d=7 Ω was placed across each washer to damp washer resonances.

3.2.2. Fabrication and characterization

A series of "CCC matched SQUIDs" was fabricated (following the process explained in section 3.1.1) on chips containing 7 SQUIDs on a row. The main results of the characterization[10] are here resumed. The measured critical current was larger (30..35 μA) than designed; as a consequence, β was about a factor of 2 larger than expected. The noise parameter Γ was always smaller than 0.05. The value of the shunt resistors R_{sh} was in agreement with the design values, ~2 Ω. The modulation depth ΔV was about 25 μV, for a bias current close to $2I_0$. The IVC's were smooth and did not cross, indicating that resonances were effectively damped.

The SQUID inductance L_{sq} can be only roughly determined from the value of I_0 measured on the IVC and Eq. 1.12-1.13 To determine L_{sq} more accurately, some SQUIDs were made hysteretic by interrupting the shunt resistors on the chip. From the measurement of the hysteretic SQUID critical current dependence on the applied flux (I_c-Φ *threshold* curve), the value of I_c, and thus also of L_{sq} could be obtained. The measured values of L_{sq} were in good agreement with the calculated ones using Eq. 1.22-1.23 and simulated with the finite element program Fast Henry[11].

The experimental values of the mutual inductance M_i (measured from the V-Φ curve when the flux is applied via the input coil inductance) were about a 40% lower than the designed value, calculated as $M_i \approx n.L_{sq}$. Using the modified expression Eq. 1.27 that takes into account that only the part of the slit covered by turns contributes to the mutual inductance, the recalculated values agreed within 10% with the experimental values[10].

The input coil inductances, calculated as $L_i=n^2L_{sq}$ were also larger than measured. E.g., the L_i of one of the SQUIDs (with 200 pH and 20 turns) was measured at 4.2 K with the help of an impedance/gain phase analyzer[10]. In order to subtract the inductance contribution of the connecting wires, L_i was calculated as the difference in inductance when a short was made at the cold side of the connecting wires, or when the input coil was connected. A known capacitance was placed in series with the circuit, so as to form a resonant circuit, from which the inductance could be more easily determined. To have a more precise measurement, 9 input coils were connected in series. We obtained an $L_i \approx 55.7$ nH, smaller than the calculated value (80 nH). Considering the expression (Eq.26) that takes into account that only the covered part of the slit contributes to the input coil inductance, the recalculated L_i=57.9 nH was very close to the measured value. The L_i and M_i were also calculated with Fast Henry; results agreed with the experimental values within 3% (see section 1.3.4).

Three SQUID designs (A, B and C) from the above series were chosen, to make new 3x3 mm^2 chips, containing a single SQUID each, that could be conveniently placed and bonded in modules of an "Oxford Instruments" commercial readout electronics (Chapter 4).

SQ	L_{sq} (pH)	n (turns)	I_c (μA)	β	R_{sh} (Ω)	dV/dΦ (μV/Φ_0)	L_i (nH)	$L_{i,rec}$ (nH)	$L_{i,exp}$ (nH)	M_i (nH)	$M_{i,rec}$ (nH)	$M_{i,exp}$ (nH)
(A)	200	14	12.8	1.2	2.0	22.9	40	27.5	—	2.8	1.96	1.72
#16			9.6	1.1	2.3	29.9						
(B)	200	20	12.8	1.2	2.0	22.9	80	57.9	55.7	4.0	2.97	2.65
#1			12.3	1.4	1.9	29.2						
#5			12.9	1.6	2.1	32.4						
#6			11.8	2.2	1.9	34.6						
#13			7.1	0.9	2.0	22.0						
(C)	150	23	12.8	0.9	2.0	26.6	80	45.0	—	3.5	2.11	1.92
#7			11.8	1.0	2.2	31.0						
#10			16.6	1.6	2.1	45.0						
#11			10.4	0.9	2.5	34.5						
#12			12.0	1.0	2.6	30.5						

Table 3.2- *Type A, B and C "CCC matched SQUIDs", designed to fit in "Oxford" modules. Left: expected (in gray) and experimental main parameters; Right: theoretical, recalculated and measured values for L_i and M_i.*

The wiring layout was optimized to avoid crosstalk. The L_i of these SQUIDs were around the estimated $L_{CCC,eff}$ (~40 nH-80 nH) of the designed CCC current amplifier (Chapter 6). The input coil paths were made especially large, to facilitate the superconducting bonding necessary to connect the SQUID to the CCC. A run of these SQUIDs was fabricated and characterized. The measured values for I_c, β, R_{sh} and $\partial V/\partial\Phi$ were in very good agreement with the expected values, as can be seen in Table 3.2. Note that the results concerning the L_{sq}, L_i and M_i of these SQUIDs can be extrapolated from the measurements on the previous series, since the SQUIDs have identical geometry.

3.3. 80ħ, direct coupled SQUIDs

The design of the "CCC matched SQUIDs" focused on obtaining devices with L_i values close to the $L_{CCC,eff}$, while the rest of the SQUID parameters were chosen within very "safe" working limits. As consequence of the low value chosen for β_c (~0.02), the designed energy resolution was still rather high (200..400 ħ), and the transfer function quite small (~25 μV/Φ_0), making more difficult the readout of the SQUID with conventional electronics (Chapter 4). In this section, the optimization of the washer type dc SQUID with Nb/Al/AlO_x/Al/Nb jj with respect to the energy resolution and coupling[12] is treated in a formally more general manner. In fact, the previous series of SQUIDs could be considered a particular case. This approach allows studying also "extremer" SQUID designs that enhance ε while facilitate the coupling to the CCC, and increase the transfer function of the SQUID.

3.3.1. Design

In order to study the practical optimization of the washer type SQUID, the energy resolution $\varepsilon=f(L_{sq}, T, R)$ given by Eq.1.19 should be written as a function of the fabrication parameters of the SQUID and the temperature of work. The SQUID inductance was for simplicity approximated by $L_{sq}\approx L_h$. The resistance R at the optimum bias point $I_b\sim 2\ I_0$ is the parallel of the shunt R_{sh} and intrinsic subgap resistance. The last one is difficult to estimate, but will be for sure large compared with R_{sh}; in first approach we considered that it could be approximated by the also very large normal resistance (above the gap-voltage), given by[13,14]:

$$R_N \approx \frac{2\pi}{I_0}\frac{\Delta(0)}{k_B T}, \tag{3.2}$$

the gap voltage being $\Delta(0)/e\approx 2.8$ mV, if $T<T_c/2$.
L_{sq}, T and R are linked to each other by the SQUID operating conditions, as shown in Figure 3.4. The following requirements were applied to the design: i) the screening parameter should be $\beta=1$; ii) the McCumber parameter $\beta_c\leq 1$ and iii) the noise parameter $\Gamma<0.1$. The capacitance per unit area was taken as $C/A\approx 0.03$ pF/μm^2, a value confirmed by the measurements described in section 3.3.2. A typical value for the critical current density (J_0=40 A/cm^2) was assumed. These conditions allow expressing the energy resolution in the white noise region in terms of the washer hole size D and the junction size d; the temperature of work T, and the parameter β_c:

$$\varepsilon(\hbar) = 0.453 \cdot T[\mathrm{K}]d[\mu\mathrm{m}]D[\mu\mathrm{m}]^{1/2}\,\beta_c^{-1/2}, \tag{3.3}$$

T and D fulfilling the operational condition:

$$\Gamma = 0.625x10^{-4} \cdot T[\mathrm{K}]D[\mu\mathrm{m}] < 0.1. \tag{3.4}$$

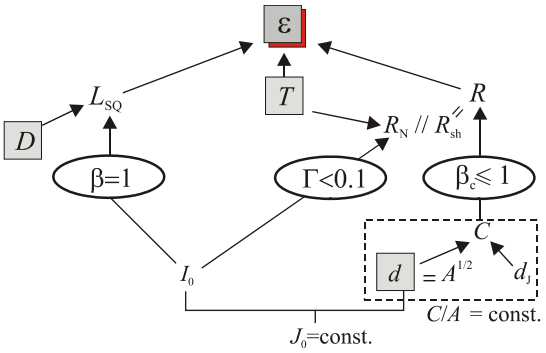

Figure 3.4- *Relations between the different parameters affecting the energy resolution of the SQUID. The imposed requirements are inside the ovals. Inside the squares, the dimensions that can be varied in the SQUID design (the junction and washer-hole size) and the temperature of work.*

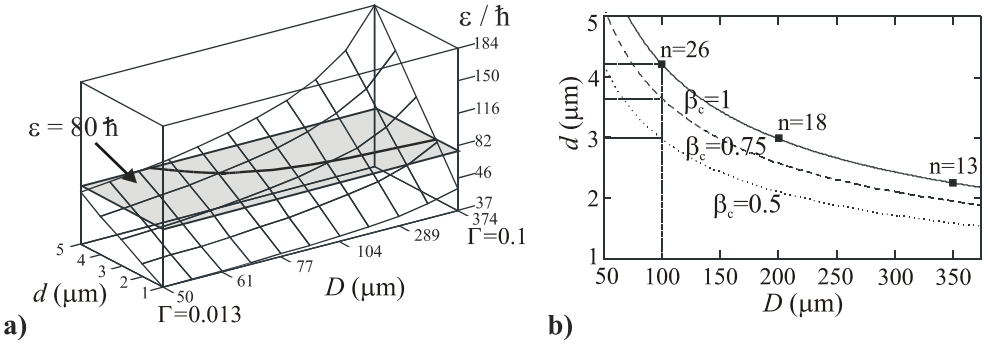

Figure 3.5- *a) Theoretical energy resolution of a washer-type dc SQUID as a function of the junction size d and the washer hole D for J_0=40 A/cm^2, β_c=1, at T=4.2 K; b) Plane of constant sensitivity ε=80ħ (at 4.2 K). SQUID design lines for 3 different values of β_c.*

In Figure 3.5a, the sensitivity $\varepsilon(\hbar)=f(d,D)$ at T=4.2 K for the limit case β_c=1 is shown. At this temperature, the maximum washer hole, given by Eq. 3.4 is D=374 μm. Assume we aim to design SQUIDs with an energy resolution ε~80 ħ, that would give for a $L_{CCC,eff}$=100 nH CCC, a current resolution of 1 pA.turn/Hz$^{1/2}$. The intersection of the 80 ħ constant plane with the sensitivity surface defines a line on which a series of SQUIDs, described by (d, D) can be chosen. Note that according to the linear dependence of ε with T, these SQUIDs would reach an energy resolution ε~2ħ, near the quantum limit, at 0.1 K. Figure 3.5b shows the relation between the fabrication parameters of the 80 ħ SQUIDs and the number of turns necessary to couple them to a 100 nH CCC. The larger the washer hole size D, the easier (with less number of input coil turns) the SQUID can be coupled. In exchange the junction size required is smaller, thus less reproducible to fabricate. On the opposite, more reliable, larger junctions would imply the need of a smaller washer hole, and a large number of turns to couple the SQUID, which can cause non-desirable resonances in the SQUID.

From Eq. 3.3 it is clear that the sensitivity can be improved by increasing the McCumber parameter up to unity. Besides, Figure 3.5b shows that for a given ε, the conditions on the fabrication become less exigent when $\beta_c \to 1$. However, the hysteretic regime should not be entered, or the SQUID would become inoperable. Hence, it is crucial to know accurately each one of the parameters affecting β_c. The capacitance per unit area of the Nb/Al/AlO$_x$/Al/Nb tunnel junctions was known from literature[15,16,17] to be 0.03-0.06 pF/μm^2. The experiment described in section 3.3.2 was realized to determine the specific capacitance $C'=C/A$ of our junctions with better precision. The practical realization of $\beta_c \approx 1$ SQUIDs implies the use of large value shunt resistors, ranging from 6 to 20 Ω. These resistors would occupy a large space when made in standard Pd technology. Section 3.3.3 treats the characterization of resistors made in PdAu, a material with a larger sheet resistance.

3.3.2. Specific capacitance determination

In order to determine accurately *C/A*, we fabricated 6 series of junctions with areas ranging from 2x4 to 10x10 μm^2, and shunt resistors R_{sh} varying such that the Mc Cumber parameter passed from the hysteretic to the non-hysteretic regime. β_c was deduced from Zappe's expression[18]:

$$\beta_c = \frac{2-(\pi-2)(I_m / I_0)}{(I_m / I_0)^2}, \tag{3.5}$$

where the return minimum current I_m and the critical current I_0 were measured from the hysteretic jj IVC's (Figure 3.6a). The capacitance was then calculated for each series. The linear fit of *C* as a function of the effective area A_{eff} (corrected from rounding) gives a specific capacitance of 0.03±0.01 pF/μm^2 at 4.2 K and 0.034±0.001 pF/μm^2 at 1.6 K (Figure 3.7). Accuracy was gained at lower temperature thanks to thermal noise reduction.

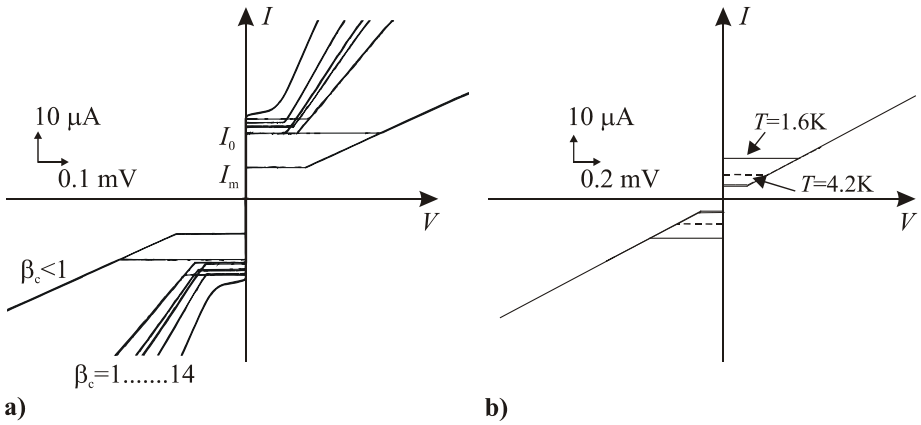

Figure 3.6- *a) Experimental determination of β_c from the series of junctions with A=5x5 μm^2 (4.2 K); b) Effect of temperature on the β_c determination.*

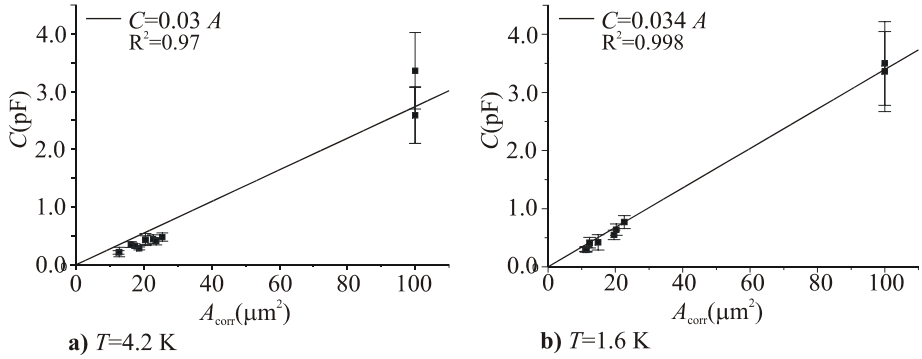

Figure 3.7- *Capacitance per unit area determination. a) at 4.2 K; b) at 1.6 K.*

3.3.3. PdAu characterization

The fabrication of the large value shunt and damping resistors in Pd, a material with a small sheet resistance R_{sheet} of 1 Ωm/m, would present two problems: the large space occupied, and the associated inductance, which could cause a relaxation oscillation effect in the SQUID. Therefore we decided to fabricate the resistors with PdAu, a material known to have a larger sheet resistance than Pd. Because the PdAu sheet resistance very much depends on the deposition conditions, the sheet resistance under our particular sputtering set-up had to be determined. Several series of stripe resistors with varying width w and length l were fabricated, so as to determine the sheet resistance: $R=R_{sheet}\, l/w$.

From the scaling of the resistance with the length and width, a sheet resistance of 8±2 Ωm/m for a layer thickness of 66 nm was obtained. Some resistors were fabricated in the shape of loops and meanders. These configurations are sometimes adopted to spare space on the chip. A reduction in the resistance value of about 20% for the meander shape, and 3% for the loop shape with respect to the resistance value in the stripe configuration was measured. This effect is due to the rounding in the interior side of the loops, resulting in an effective wider resistor area.

3.3.4. Fabrication and characterization

Two series of "80$\hbar$" SQUIDs[19] were fabricated using our standard Nb/Al technology. The first included SQUIDs with β_c tending to one (0.5, 0.75 and 1), junction areas 5x5, 4x4, 2x4 μm^2 and a single input turn on top. The second series comprised SQUIDs with β_c=0.5, 5x5 μm^2 junctions and increasing number of turns n, in order to study the coupling. We avoided the use of known techniques generally applied to prevent resonances, e.g. intra-coil

SQUID	*dxd* (μm^2)	*D* (μm)	*n* turns	*C* (pF)	L_{SQ}+L_{slit} (pH)	I_0 (μA)		R_{sh} (Ω)		β_c	
#1	5x5	66	0	0.75	104+47	20	*18.8*	5	*3.9*	0.5	*0.3*
#2	5x5	66	1	0.75	104+47	20	*18.4*	5	*4.4*	0.5	*0.4*
#5	5x5	66	10	0.75	104+47	20	*18.5*	5	*8.9*	0.5	*1.7*
#6	5x5	66	20	0.75	104+47	20	*17.5*	5	*2.9*	0.5	*0.2*
#7	5x5	66	50	0.75	104+97	20	*17.9*	5	*4.1*	0.5	*0.3*
#8*	5x5	66	20	0.75	104+47	20	*17.8*	5	*5.7*	0.5	*0.7*
#10	5x5	66	1	0.75	104+47	20	*18.5*	6	*7.6*	0.75	*1.2*
#11	2x4	206	1	0.24	320+115	6.4	*6.4*	18	*10.8*	0.75	*0.2*
#12	5x5	66	1	0.75	104+47	20	*17.3*	7	*11.4*	1	*2.6*
#13	2x4	206	1	0.24	320+115	6.4	*3.4*	21	*31.0*	1	*1.2*
#15	4x4	103	1	0.48	160+66	12.8	*11.4*	9	*16.2*	0.75	*2.2*
#16	4x4	103	1	0.48	160+66	12.8	*10.9*	11	*19.3*	1	*2.9*

Table 3.3- *Main parameters of SQUIDs with junction area 5x5 μm^2. Regular: designed values; italic: experimental values. *SQUID #8 was made on purpose without a damping resistor.*

damping, because they introduce extra noise[20]. Only a damping resistor R_d was placed shunting the washer. Table 3.3 shows the results of the characterization measurements on SQUIDs with junction area 5x5 μm^2. The critical current values were as expected for the SQUIDs with large area junctions. In some cases (e.g. SQ#5, 12), only one of the shunt resistors made contact, resulting in a measured R_{sh} around twice the expected value. A large spread in the R_{sh} values was measured. The SQUIDs with the smallest junction sizes were poorly reproducible.

3.3.4.1. Large β_c SQUIDs

The SQUIDs with small β_c values showed quite regular characteristics (Figure 3.9a). In contrast, $\beta_c \approx 1$ SQUIDs presented peculiar *I-V* and *V*-Φ curves. These anomalous characteristics could be also calculated back with the help of the Josephson element simulation program JSIM[21] (Figure 3.8). We recorded very large values for the transfer function $\partial V/\partial\Phi$. Refs. 22, 23 reported also very large values of $\partial V/\partial\Phi$, up to ~3 mV/Φ_0, for SQUIDs approaching the hysteretic regime. The usual expression for the SQUID transfer function $\partial V/\partial\Phi$, is linearly dependent on $\beta_c^{1/2}$:

$$\frac{\partial V}{\partial \Phi} = \frac{R_{sh}}{L_{sq}}\left(\frac{2\beta}{1+\beta}\right) = \frac{1}{\beta}\left(\frac{2I_0}{\pi C_j \Phi_0}\right)^{1/2}\left(\frac{2\beta}{1+\beta}\right)\beta_c^{1/2}. \tag{3.6}$$

This holds only for $\beta_c << 1$. When β_c increases, the measured values are much larger than the ones predicted by this formula and follow an exponential dependence (Figure 3.9b). The JSIM simulations suggest an even stronger exponential behavior. The large transfer of these SQUIDs facilitates the readout with conventional electronics, as will be seen in Chapter 4.

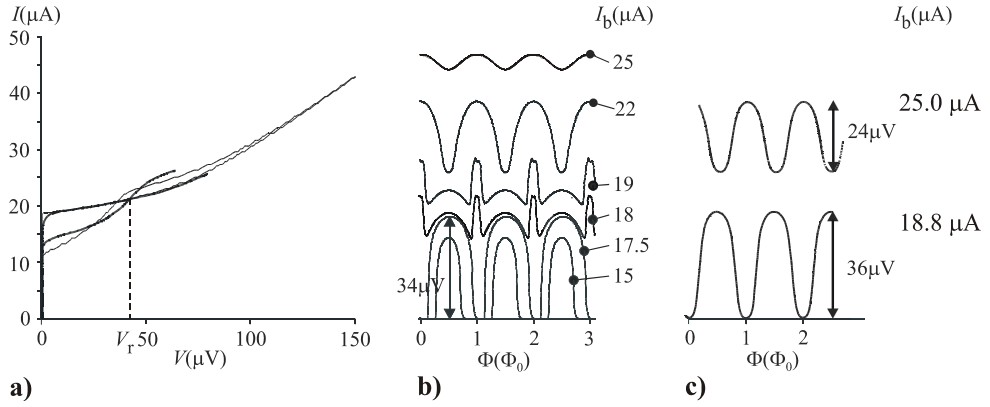

Figure 3.8- *a) Measured (thick line) and JSIM simulated (thin line) IVC's of SQ#10 with β_c~1.2; b) Simulated V-Φ curves at different bias points; c) Measured V-Φ curves at $I_b=2I_0=18.8$ μA, and at the resonance bump (I_b~25μA). The characteristic shapes of the curves at I_b~18 μA and 19 μA were also observed.*

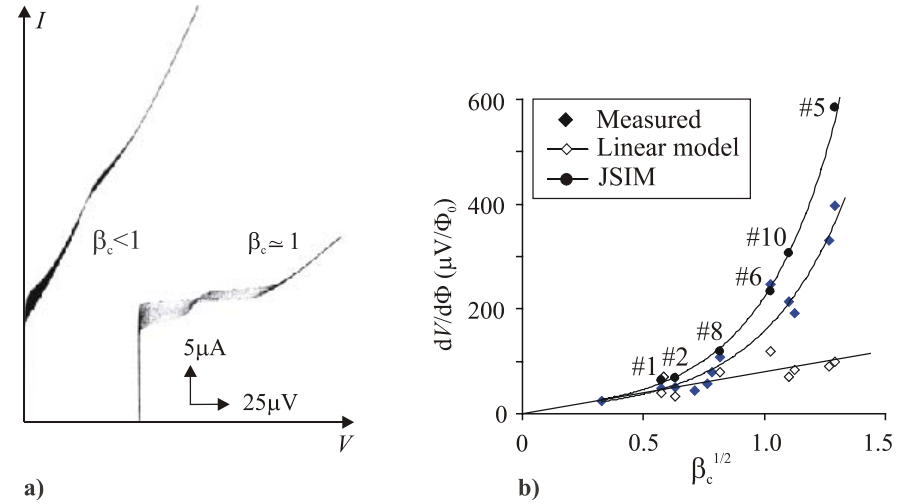

Figure 3.9- *a) I-V curves of a small β_c~0.3 SQUID (#1) and β_c≈1 SQUID (#12) (origin shifted in the x-axis for clarity); b) Transfer function $\partial V/\partial \Phi$ dependence on $\beta_c^{1/2}$.*

3.3.4.2. Resonances

The 0 and $\Phi_0/2$ flux IVC branches of all the SQUIDs crossed at around ~47 μV. Since this intersection was observed even for the SQ#1 without an input coil, it must result from a washer resonance. The voltage at which the two branches cross coincides with the expected

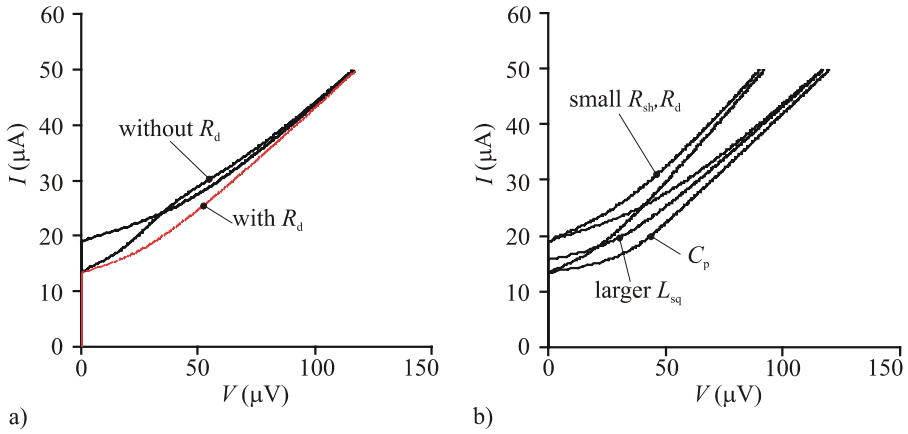

Figure 3.10- *a) Simulated IVC's of SQ#1 (n=0), with and without a damping resistor R_d; b) JSIM damped IVC's: A possible spread in the R_d (values from ~3 to 10 Ω were simulated) cannot explain the damping failure; a parasitic capacitance (1..10 pF) only flattens the $\Phi_0/2$ flux IVC, but does not make the IVC cross; a different value of L_{sq} shifts the $\Phi_0/2$ branch, but cannot explain the crossing either.*

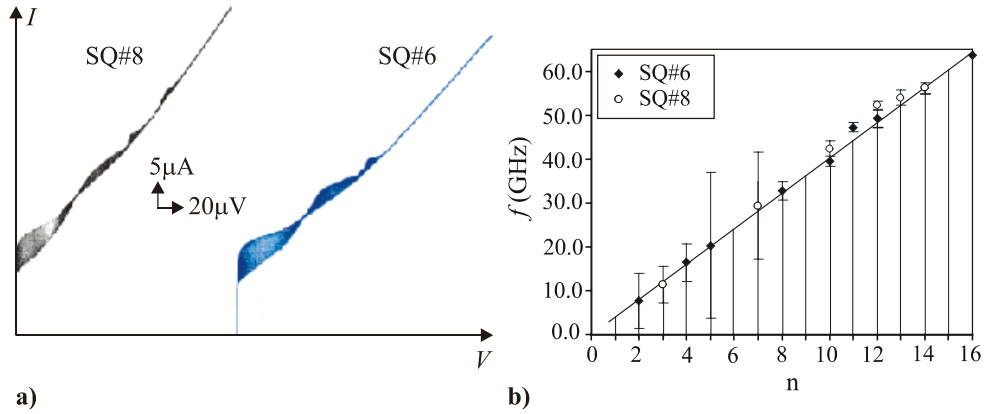

Figure 3.11- *a) IVC's of SQ#6 (with an R_d) an SQ#8 (without R_d; b) input coil resonances.*

value $V_r=\Phi_0/2\pi(L_{sq}C_j/2)^{1/2}$, when the slit inductance is taken into account in L_{SQ} and a ~10% junction area reduction due to rounding is assumed. Apparently, the damping resistor R_d did not suppress efficiently the washer resonance, although according to JSIM simulations, R_d should have damped sufficiently the SQUID. The measured IVC's resembled rather the non-damped JSIM curves (Figure 3.10a). We simulated different situations that could have explained the inefficiency of the damping (Figure 3.10b). However, non of them could stem for the damping failure. The particular geometry of the SQUID, not taken into account in the model, might play a role in the excitement of washer resonances.

A single turn input coil on top of the washer does not affect appreciably the SQUID characteristics. As n becomes larger, additional resonance deeps and bumps appear in the IVC's, due to EM λ/2 input coil resonances (Figure 3.11a).

The frequency of the m^{th} resonance is given by (Eq. 1.32): $f_m=m(c/2l_i)(1/\varepsilon_r)^{1/2}$. For instance, for SQ#6 with a 20-turn input coil measuring l_i=18.6mm, and an insulator dielectric constant $\varepsilon_r(SiO_2)$~4, resonances would be expected at: f_m=m.4 GHz. Indeed, resonances in the IVC can be found at some (m=2, 4, 5, 8, 10, 11, 12, 16) multiples (Figure 3.11b). An *RC* filter shunting the input coil was only able to damp the m=2, 4 resonances. For comparison, Figure 3.11a shows the IVC of an identical SQUID to #6, but without a damping resistor R_d (SQ#8). In the later case, only the resonances at multiples m=3, 7, 12, 13, 14 can be observed. The excitement of certain multiples and not others depends much on the parasitic elements around the junctions and on the non-linear dynamics of the SQUID.

3.4. Double-barrier junction based dc SQUIDs

Double-barrier SIS'IS (I is a tunnel barrier, S the superconducting electrodes and S' a thin film with a critical temperature lower than that of the electrodes, $T_{cS'}<T_{cS}$) Josephson junctions (jj) are currently being intensively investigated. From the theoretical point of view, these structures allow to study the change in the transport behavior due to the second barrier[24]. From the application point of view, SIS'IS jj are potential candidates to replace SIS jj in large-scale integrated technology[25]. They offer non-hysteretic IVC's, making the use of shunt resistors unnecessary, and furthermore, high critical current densities J_0, enabling small junction areas. An adequate choice of the interlayer material, with large coherence length (like Al), makes pinholes and inhomogeneities less important than in the single barrier jj. The double-barrier junctions have already successfully been used in Rapid Single Flux Quantum (RSFQ) logic circuits[26], microcircuits for voltage standards[27] and microrefrigerators[28].

In conventional LTS single-barrier jj based SQUIDs (SBSQ), the external shunt resistors needed to avoid hysteresis are the main source of white noise. In a double-barrier jj based dc SQUID (DBSQ), the nature of the intrinsic shunt and its contribution to the noise is not well understood yet. Therefore it is of great interest to investigate the noise properties of the DBSQ.

We realized for the first time[29] SQUIDs based on double-barrier Nb/Al/AlO_x/Al/AlO_x/Al/Nb junctions. These DBSQs are potential good candidates for the readout of a CCC, because while they can be directly coupled to the CCC, a possible enhancement of the noise through the use of the intrinsically shunted jj might be expected.

3.4.1. Design and fabrication

The geometry of the DBSQs is identical to that of the "CCC matched SQUIDs" described in section 3.2, and therefore the direct coupling of the DBSQs to a CCC would be possible. The Nb/Al/AlO_x/Al/AlO_x/Al/Nb junctions were based on the experience of a series of double-barrier junctions made in the past[25]. Those 8x8 μm^2 junctions had a critical current density of 11 A/cm^2 and a normal resistance R_N=5 Ω.

The DBSQs were fabricated following a similar process to that of the SBSQs, slightly modified to adapt for the special requirements of double-barrier junctions. In the SBSQ fabrication process, the shunt and damping resistors are deposited simultaneously, using the same mask. Since this resistor mask was not used for the DBSQs, these SQUIDs were not be damped. First, the base electrode forming the SQUID washer body is deposited. The wetting effect of Al is worse on an oxidized aluminum surface than on a niobium one. Due to this fact, in order to have a smooth second barrier, the base electrode has to be especially smoothed. This is realized as in Ref. 30, by depositing the base electrode as a base plate of 100 nm thick Nb, a 4 nm Al layer and a 40 nm Nb top plate (as thin as possible for smoothness).

To make the first barrier, a 5 nm Al layer is initially deposited. The Al is exposed to a 1 ml/min flow of pure oxygen for 1 min 30 s until an O_2 pressure of 0.020 mbar is built up. Then the gas flow is stopped and the oxidation proceeds for 10 min. These oxidation

conditions were tested before fabrication and proved to be stable and reproducible. The interlayer consists of 9 nm of Al. The second barrier is made under the same conditions as the first one to achieve a symmetrical device, and covered by a 5 nm Al layer. The Nb top electrode (75 nm) subsequently deposited is protected by a 5 nm Al layer, which has to be chemically etched before structuring the junctions. Chlorobenzene soaking is applied *before and after* the developing of the photoresist junction structures to harden the photoresist walls and prevent the degradation of the junction area during the following etching steps. The junctions are structured by reactive ion etching (RIE) with SF_6 at pressure 5.2 Pa, power 20 W, during 7 min. The next chemical etching step was long enough to be able to remove the thick Al multilayer from all the areas different than the junction and contacts areas. The insulation and wiring deposition followed the standard process.

3.4.2. Characterization at 4.2 K

The DBSQs were first electrically characterized at 4.2 K. Some devices showed large leaking currents through the junction area borders. The percentage of leaking devices was larger than for the double-barrier jj made previously, because the junction area A was smaller, thus more difficult to structure. The typical flux dependent IVC and V-Φ curves at 4.2 K of a100 pH, 20-turn input coil DBSQ, not affected by leakage current, are shown in Figure 3.12. The measured critical current was I_c=7.7 μA, and the screening parameter β was 0.6. We measured dips in the $\Phi_0/2$ IVC at m=1, 2, 3, 4, 5, 6, 7, 8 multiples of V~8.5 μV, due to input coil resonances in the 18.9 mm long input coil. The IVC at 4.2 K over expanded I-V ranges is shown in Figure 3.13. The I-V characteristic is non-linear below the niobium gap-voltage (V_{Nb}=2.8 mV), whereas above V_{Nb}, it presents a linear relationship (measured up to 7 mV), with a negative cut-off of the I-axis. This behavior was observed

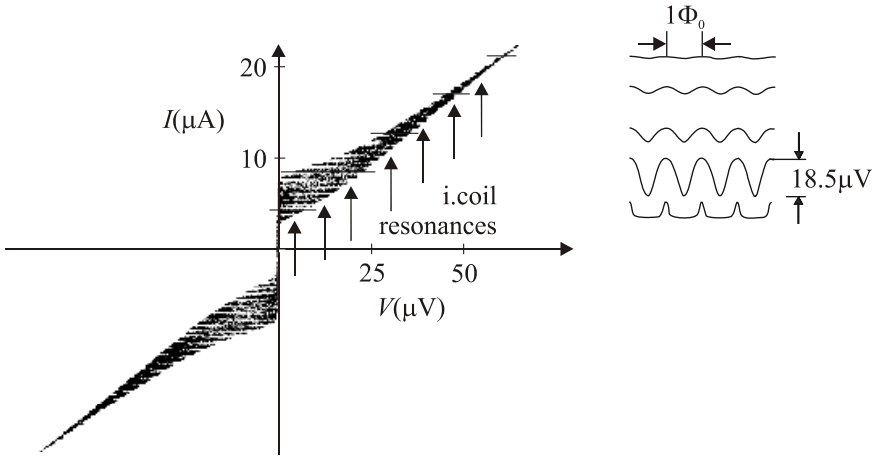

Figure 3.12- *Typical IVC and V-Φ curves at different curves at different bias points of a DBSQ at 4.2 K. The arrows indicate the position of dips caused by input coil resonances.*

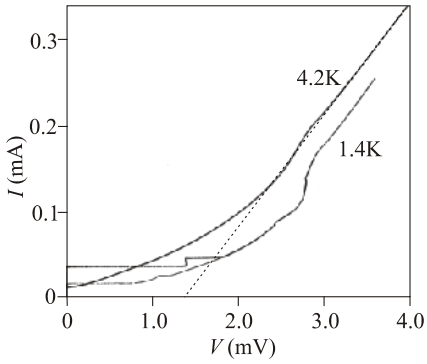

Figure 3.13- *Typical current-voltage characteristics of a DBSQ at 4.2 K and 1.4 K.*

before, e.g. in Refs. 31, 32. The sub-gap resistance R_{subg} (defined here as the ratio V/I measured at 0.5 mV) is around 75 Ω, and the normal state resistance, R_N, is 17.0 Ω, close to the design value.

3.4.3. Temperature dependence

The *I-V* dependence on the temperature was studied by cooling a 200 pH, 28-turn DBSQ from 4.2 K down to 1.4 K. The IVC changes from a typical non-hysteretic SQUID behavior to an extremely hysteretic one at the lowest temperature. The intrinsic resistance is constant R_N~17 Ω with T (e.g., compare the slope above V_{Nb} of the two IVC's characteristic in Figure 3.13, a result expected from the microscopic theory[25]. The sub-gap evolution as function of the temperature is shown in Figure 3.15. The IVC at 1.4 K is given in a scale different from the rest because the critical current is much larger. If all the IVC's are plotted superposed on a common scale, it appears that the return path of the highly hysteretic IVC at 1.4 K bends in a way similar to the non-hysteretic sub-gap IVC's at higher temperatures. The difference is that at 1.4 K, due to the hysteresis, the SQUID jumps to the V=0 state at higher minimum return current than at higher temperatures, (a fact which can also be seen in Figure 3.16). Some of the steps appearing in the IVC at 1.4 K were described also by Nevirkovets *et al.*[32]. The sub-gap resistance decreases with temperature, as seen in Figure 3.14.

We might raise the question: which resistance plays a role in the dynamics of the DBSQ? To investigate this, we calculated the resistance R appearing in the McCumber parameter. β_c could be experimentally determined from the hysteretic IVC at 1.4 K using Eq. 3.5: β_c~94, where I_0~25 μA, and the minimum return current was I_m~3.5 μA. The capacitance C_j of the double-barrier jj was calculated from the washer resonant voltage $V_r = (\Phi_0/2\pi).(L_{SQ}\ C_j/2)^{-0.5}$ measured at 4.2 K, giving 0.23 pF. This value is close to the C_j estimated assuming the capacitance of two single-barrier jj in series: C_j =(0.03 pF/μm^{2}x16 μm^2)/2=0.25 pF. Consequently, the effective resistance $R_{eff} \equiv R$ determining the SQUID dynamics at 1.4 K is 73 Ω. From Figure 3.15 (at 1.4 K), we can see that, indeed, the part of

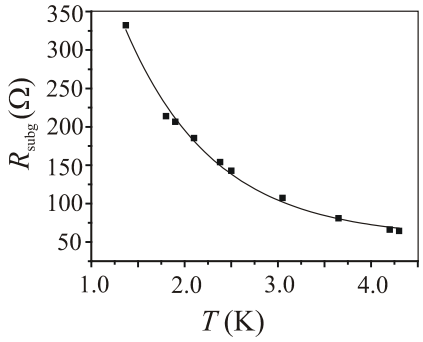

Figure 3.14- *Sub-gap resistance dependence with the temperature. (200 pH, 28 turns).*

the curve which is hysteretic has an inverse slope value between the normal state resistance of 17 Ω and the sub-gap resistance of 332 Ω.
Figure 3.16 shows the critical current measured as a function of the temperature. The data were fitted using the microscopic theory developed for double-barrier jj[25]. In this theory the critical current is controlled by the parameter $\gamma_{eff} = \pi T_{c,Nb}.\tau_{tun}$, where τ_{tun} is the time spend by electrons in the Al interlayer before tunneling to another Nb electrode. The larger γ_{eff} is, the stronger the depairing effect and thus the smaller I_c at $T > T_{c,Al}$. The theoretical fit describes the sudden increase of I_c at the temperature at which the Al intermediate layer, due to the proximity effect, becomes superconducting (Figure 3.16, inset). The theoretical fit gives a critical temperature of $T_{c,Al} \sim 1.4$ K for the aluminium and suppression parameter[25] of $\gamma_{eff} \sim 10^4$.

The measured temperature dependence above 2 K shows a deviation from the theoretical curve. Here, we give a qualitative explanation of this effect. Electron energy relaxation in the Al interlayer was not taken into account in the model[25]. This is justified in many practical situations, when the tunneling time τ_{tun} is much shorter than a characteristic

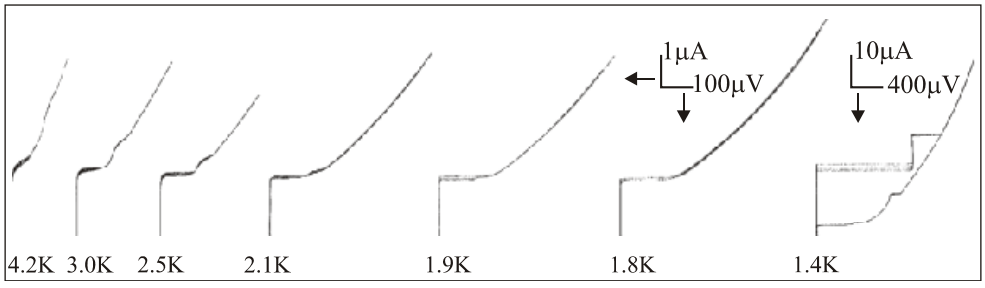

Figure 3.15- *Sub-gap IVC dependence on temperature (DBSQ: 200 pH, 28 turns).*

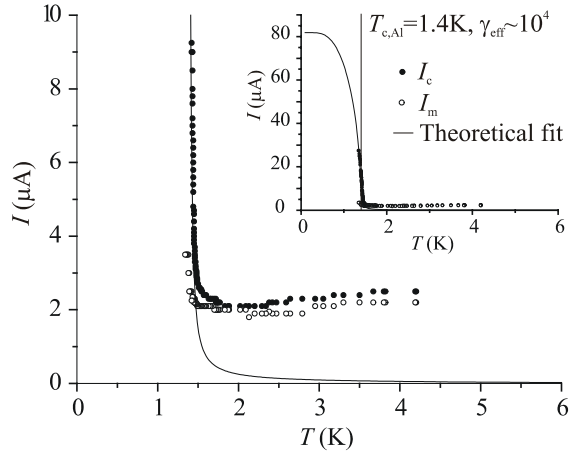

Figure 3.16- *Measured critical current (•) and return minimum current (∘) as a function of the temperature, and theoretical fit (solid line); (DBSQ: 200 pH, 28 turns).*

trapping time τ_{trap} on the defects or dislocations in Al, so that the drift time of electrons through the Al layer is so short that they cannot be captured. However, the stronger the tunnel barriers are, the larger γ_{eff} is. Then, the tunnel time $\tau_{tun}=\gamma_{eff}/\pi T_{c,Nb}$ may become sufficiently long, so that $\tau_{tun}<<\tau_{trap}$ does not hold any more and electrons can get trapped in the Al layer, thus blocking further tunneling. For γ_{eff}~10^4 we estimate τ_{tun}~20 ns. The information on the concentration and the estimate trapping time is not available from our experiments. However, it is reasonable to assume that the electronic trapping in Al is limited by slow energy relaxation of electrons from their equilibrium energy levels corresponding to the Andreev bound states, which carry supercurrent in a junction, down to the energy levels of the localized states. According to Kaplan *et al.*[33], the characteristic time constant for the energy relaxation in Al with emission of photons is ~400 ns. Taking this number as an estimate for τ_{trap}~400 ns, we conclude that trapping is not negligible in our junctions. Trapping is less important at higher temperatures since some captured electrons can escape thanks to thermal activation (de-trapping), but as the temperature decreases, the probability of escaping becomes smaller and in consequence the critical current diminishes. This effect is observable until the large increase in critical current due to the Al proximation overwhelms it.

From the fact that there is a spread in the value of the critical current of the present DBSQs, whereas the normal state resistance is constant, we may conclude that the supercurrent is composed of the true double-barrier junction supercurrent and a leakage current. Therefore, the true critical current density J_0 of the present devices is lower than the 11 A/cm^2 that was obtained for the double-barrier junctions previously characterized. However, the R_NA product for the DBSQs, 2.7 μΩ.cm^2, is close to the 3.2 μΩ.cm^2 obtained for the junctions. According to the theory[25], the critical current density is inversely proportional to γ_{eff}^2: J_0~ γ_{eff}^{-2}. This parameter is proportional to the product of normal state resistance and the ratio of the thickness d and the coherence length ξ of the interlayer:

$\gamma_{eff} \sim R_N A.(d/\xi)$. For constant normal state resistance and thickness of the interlayer, the coherence length of the interlayer of the present devices is consequently smaller than in the separately characterized junctions. This is consistent with the reduced critical temperature of the aluminum, and the observation of the large trapping effect.

3.5. Noise measurements

The noise properties of the three described SQUIDs were measured in a Two-Stage readout system with a DROS with reference junction as second stage. A detailed description of this Two-Stage system and its performance compared to conventional flux modulation electronics will be given in Chapter 4. It is here enough to say that the noise floor of this system is low enough to allow measuring the actual noise of the SQUIDs, without being limited by the electronics. Therefore, a fair comparison between the noise properties of different SQUIDs is possible. On the other hand, the Two-Stage system allows studying the influence of resonances in the IVC's on the noise. We shall present and compare the noise measurements on the three different kinds of SQUIDs developed: (i) a single-barrier, "CCC matched SQUID", which was efficiently damped against resonances; (ii) a single-barrier, insufficiently damped "80$\hbar$" SQUID and (iii) a DBSQ, intrinsically shunted and without damping resistor.

SQUID	I_b (μA)	f_c (Hz)	$S_\Phi^{1/2}$ ($\mu\Phi_0/Hz^{1/2}$)	α	$(\partial V/\partial\Phi_{sig})_{TS}$ (mV/Φ_0)	% preamp	$G_{\Phi,exp}$	
#1	30	12	2	1	3.3	27	27	✓
	40	11	2	1	3.6	25	22	✓
	100	26	2.4	1	2.9	23	6	×
	130	170	3.7	0.75	2.9	17	4	×
	170	35	2.4	1	2.3	25	7	×
	210	190	3.8	0.85	2.3	21	3	×
#6	32	100	1.0	1	4.4	41	50	✓
	172	60	2.3	2.2	1.6	49	8	✓
	208	45	1.6	1	2.1	54	10	×
	232	30	2.5	1	1.9	38	8	×
	250	30	2.3	1	1.5	53	6	×
# 8*	44	120	1.5	1	3.3	37	42	✓
	166	75	2.7	1.3	4.8	22	14	✓
	222	72	2.3	1.2	3.2	25	12	✓
	266	320	4.8	1.25	2.2	17	2	×
	278	90	3.2	1.4	3.0	19	6	×
	286	75	2.5	1.35	3.2	23	8	×

Table 3.4- *Resume of noise measurement results on SQUIDs #1, 6 and 8 from series "80 ħ" (measurements on SQ #7 are given in Figure 3.18). The noise spectrum is fitted with: (white noise).$\sqrt{1+(f_c/f)^\alpha}$. The last column indicates whether the flux gain G_Φ was large enough (✓) or not (x) to guarantee that the DROS second stage did not dominate the noise. The percentage contribution of the preamplifier is given.*

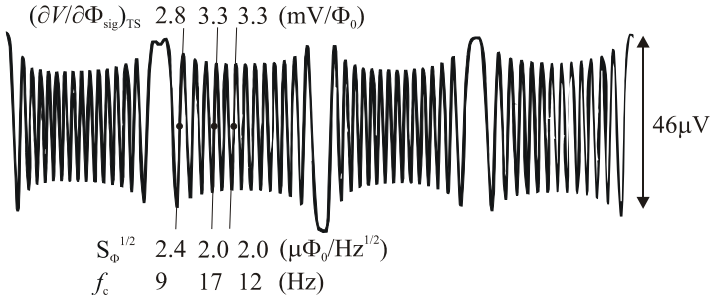

Figure 3.17- *Noise measurements (SQ#1) at three different locking points of the Two-Stage V-Φ curve, for the bias current I_b=30 μA. Above: voltage-to-flux values; below: white noise and corner frequency values (α=1).*

The SQUID *V*-Φ curves (Figure 3.18, center column) are recorded at different constant current bias points. The Two-Stage *V*-Φ curves (Figure 3.18, right column) are measured in open loop at different points in the IVC's (Figure 3.18, left columm) varying the bias current of the first stage $I_{b,1}$. For a given $I_{b,1}$, the second stage is biased at the point $I_{b,DROS}$ where the modulation depth ΔV is the largest, so that the amplifier contribution to the noise is minimized. The system is usually locked at $\Phi_{sig}=(1/4+n/2)\Phi_0$, but in case the modulation disappears at that point, an offset flux can be added in order to shift the *V*-Φ and lock the system at a different point, with enough modulation and the maximum possible gain. Once locked, the voltage noise (from which the flux noise is found back through the transfer function $\partial V/\partial\Phi$) is measured with a spectrum analyzer. Varying the locking point, the noise at the upper, center and lower part of the IVC at a certain $I_{b,1}$ can be determined.

• Consider first the shunted and damped SBSQ (100 pH, 20 turns) from the "CCC matched SQUIDs" series (Figure 3.18a). The white noise value measured[34] at 4.2 K was approximately constant (~1.3 $\mu\Phi_0/Hz^{1/2}$), very close to the value 1.2 $\mu\Phi_0/Hz^{1/2}$ predicted by theory, for bias points between $I_{b,1}$~66 and 150 μA. Since the SQUID resonances were sufficiently damped, the SQUID *V*-Φ curves looked regular (Figure 3.18a, center), and the Two-Stage *V*-Φ curves showed the typical aspect of Figure 3.18a (right), independently of the bias point. The system flux gain was G_Φ≈56 and the flux-to-voltage transfer $(\partial V/\partial\Phi_{sig})_{TS}$=12 mV/$\Phi_0$. Thus, the equivalent flux noise contribution of the preamplifier, calculated as $S_{\Phi,amp}^{1/2}=(1\ nV/Hz^{1/2})/(\partial V/\partial\Phi_{sig})_{TS}$, was as small as 0.2 $\mu\Phi_0/\ Hz^{1/2}$ and did not dominate the overall noise. The low-frequency noise had an 1/*f* dependence, and the corner frequency was f_c~60 Hz.

• The noise of SQUIDs #1, 6, 8 and 7 from the "80 ħ" series was measured at different bias points; the results are summarized in Table 3.4/Figure 3.18 c. For SQ#1, at $I_{b,1}$=30 μA, we studied the dependence of the noise on the locking point chosen (Figure 3.17). As the slope $(\partial V/\partial\Phi_{sig})_{TS}$ at the locking point decreases, the contribution of the preamplifier is larger, and the total noise increases.

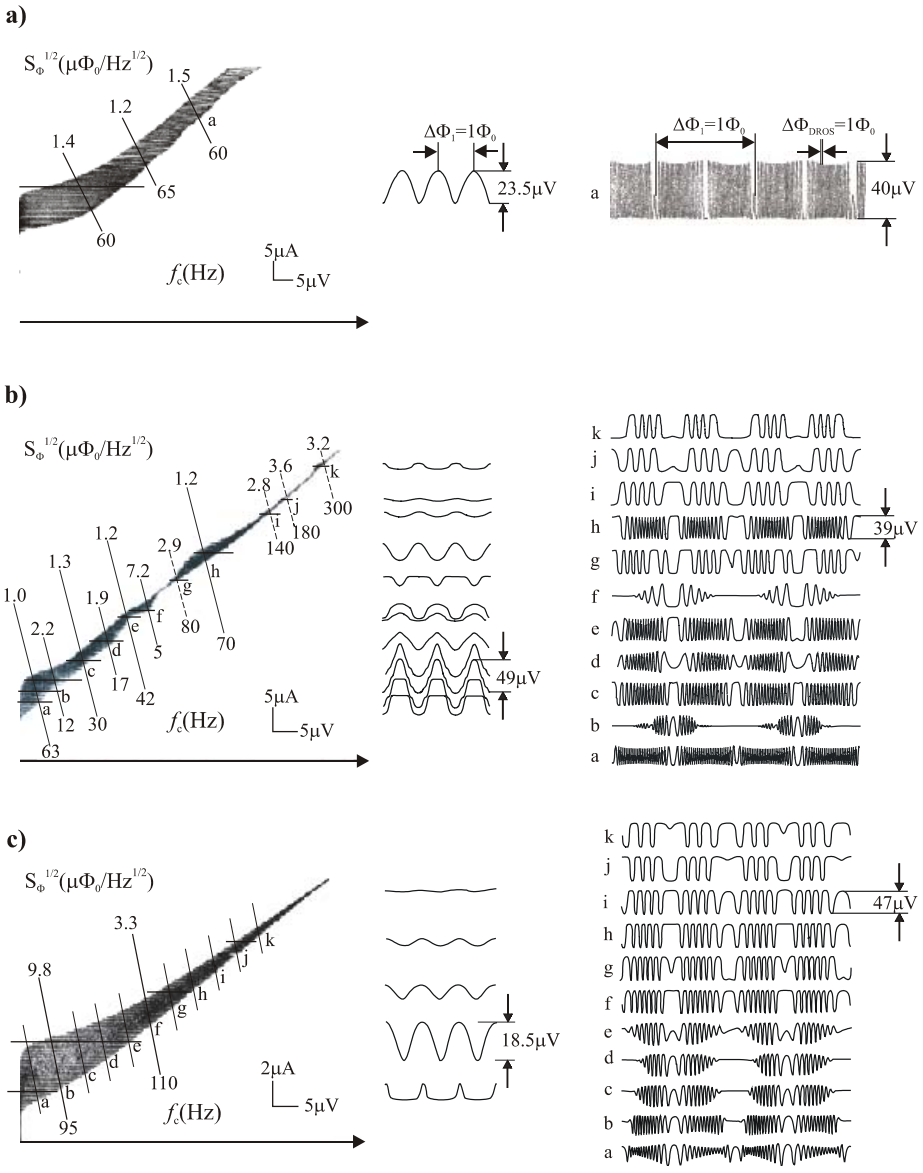

Figure 3.18- *Left column: SQUID IVC. White noise (above IVC) and corner frequency (below IVC) at different bias points; center: SQUID V-Φ curves; right column: Two-Stage V-Φ curves. a) Damped SBSQ, "CCC matched SQUID" (100 pH, 20 turns); b) underdamped SBSQ, "80 ℏ" (200 pH, 50 turns) and c) DBSQ (without R_d) (100 pH, 20 turns).*

The rest of measurements were done at the locking point with the maximum transfer: $\Phi_{sig}=(1/4+n/2)\Phi_0$, or the closest point with enough modulation.

We shall analyze the results for one of the SQUIDs (#7, 200 pH), with the largest number of turns (n=50) with the help of Figure 3.18b. Since this SQUID was insufficiently damped, the IVC was affected by resonances. The noise at the bias points labeled g, i, j, k was dominated by the DROS, since the flux gain was insufficient ($G_\Phi \approx 5$). At the points a, c, e, h, white noise levels around 1.0-1.3 $\mu\Phi_0/Hz^{1/2}$ were measured. These values were a little larger than expected (0.9 $\mu\Phi_0/Hz^{1/2}$), because the flux-to-voltage transfer was only around 2..3 mV/Φ_0, and therefore the preamplifier noise was not negligible (>30%). For certain points (b, d, f), the noise levels are much higher than expected, even when the preamplifier contribution was smaller than 20%. Observe that at those points, as the SQUID *V*-Φ curves show more structure (Figure 3.18b, center), and the Two-Stage *V*-Φ characteristics look more and more deformed with respect to the typical curves (Figure 3.18b, right), the noise is also higher. Thus, the deformation of the Two-Stage *V*-Φ curve is an indication of a large amount of noise in the first stage, owing to the presence of a resonance, which is coupled into the second stage. Note that the appearance of a resonant bump does not necessarily imply that the noise at that bias point is high (point h).

The situation with respect to the low-frequency noise is schematically shown in Figure 3.19. When the flux gain is sufficiently large, the 1/*f* noise is given by the 1st stage SQUID and not by the 2nd stage DROS. At different bias points (see for instance a, b, c),

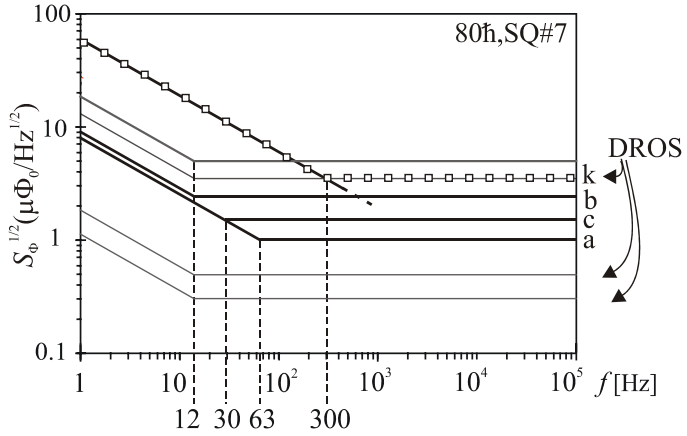

Figure 3.19- *Flux noise levels measured at some bias points in the IVC of SQ80ħ#7. The noise level of the 2nd stage (DROS), 5 $\mu\Phi_0/Hz^{1/2}$ and f_c~12 Hz, is calculated back to a noise level in the 1st stage dividing by the Two-Stage flux gain, G_Φ. At points a, b and c, the gain was sufficient to guarantee the noise is given by the SQUID and not by the DROS. The 1/f noise is practically the same; the corner frequency shifts to lower frequencies when the white noise increases. At point k the gain is insufficient and the white noise is given by the DROS. The corner frequency is given by the intersection of the (calculated back) DROS spectrum with the large low-frequency SQUID spectrum.*

the low-frequency spectra are practically the same; the different corner frequencies result from the intersection of the different white noise levels with the 1/*f* line. At points at which the gain was not large enough (e.g. point k), the DROS dominates the white noise region; the corner frequency at that point results from the intersection of the DROS white level with the SQUID larger low-frequency noise.

• Finally, noise measurements were performed on a DBSQ (Figure 3.18c, left), not affected by leakage current (100 pH, 20 turns). Input coil resonances were observed in the IVC. Apparently, the SQUID *V*-Φ curves are not distorted by the resonances (Figure 3.18c, center). However, the deformed Two-Stage *V*-Φ curves (Figure 3.18c, right) reveal that at some bias points the DBSQ couples noise to the DROS. The white noise at point b was 9.8 $\mu\Phi_0/\mathrm{Hz}^{1/2}$, whereas at point f (where the Two-Stage *V*-Φ was not deformed), a better value was measured: 3.3 $\mu\Phi_0/\mathrm{Hz}^{1/2}$. The corner frequency was at about f_c~100 Hz. The noise spectra of the damped "CCC matched SBSQ" and the DBSQ (both 100 pH, 20 turns) are compared in Figure 3.20. Since the DBSQ is not damped by any kind of resistor, noise levels vary depending on the presence or absence of resonances at a certain bias point. At point a, Figure 3.18c, the Two-Stage curve is regular, and thus, this point is free of resonances, and the noise floor measured (3.3 $\mu\Phi_0/\mathrm{Hz}^{1/2}$) is the noise due to the effective shunt of the DBSQ. The noise floor of the DBSQ is comparatively higher than that of the SBSQ (1.3 $\mu\Phi_0/\mathrm{Hz}^{1/2}$).

The Two-Stage proves to be useful to "scan" an IVC and detect at glance, the bias points where the presence of resonances introduces additional noise. At the bias points such that the Two-Stage curves are regular, the noise levels measured coincide with the noise floor of the SQUID, given by the (external or intrinsic) shunt resistors.

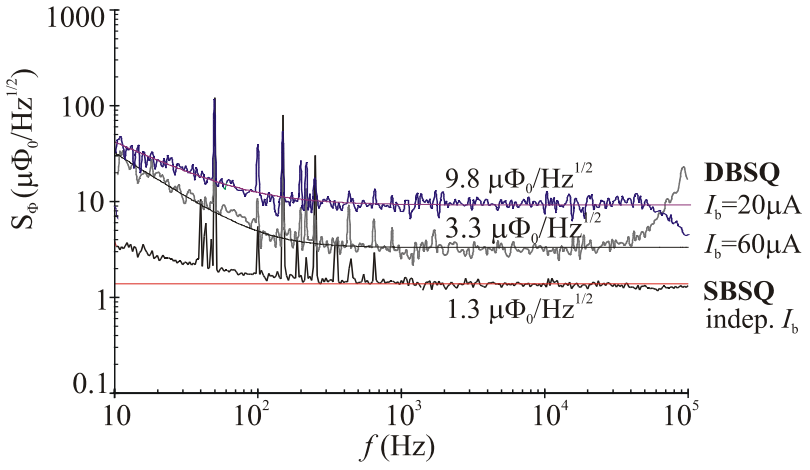

Figure 3.20- *Noise spectra of a DBSQ (at I_b=20 and 60 μA) and an equivalent SBSQ (100 pH, 20 turns).*

3.6. Conclusions

With the aim of improving the current resolution of the CCC-SQUID current amplifier, three different kinds of Nb/Al dc SQUIDs, designed to reach good energy resolution levels, and be able to couple directly to the CCC overlap, have been developed. The noise properties of the three types of SQUIDs have been measured with a Two-Stage readout system. Because the noise measured with this system is really given by the SQUID and not by the readout electronics, a fair comparison between the noise of the different SQUIDs was possible. Besides, the system proved useful to determine at glance the bias points of an IVC at which the noise is high due to resonances.

The *"CCC matched SQUIDs"* were designed so as to have input coil inductances close to the CCC self-inductance. Because the SQUID IVC's were practically free of resonances, the noise levels measured agreed well with the design values (~1.3 $\mu\Phi_0/Hz^{1/2}$) at every bias point. As a result of the very "safe" McCumber parameter chosen, β_c~0.02, the SQUID transfer function was quite small ~25 $\mu V/\Phi_0$.

The series of *"80ħ SQUIDs"* was aimed to explore SQUIDs with "extremer" parameters, that would push down the energy resolution. Thanks to approaching the McCumber parameter to the hysteretic limit, β_c~1, the SQUID transfer was increased (up to ~400 $\mu V/\Phi_0$). We anticipate (see Chapter 4), that the large transfer of the "80ħ SQUIDs" compared to the "matched SQUIDs" will facilitate the readout with conventional electronics. The IVC's were strongly affected by resonances. At the points free of resonances, the measured noise coincided approximately with the designed values (1.0-1.3 $\mu\Phi_0/Hz^{1/2}$), while it was much higher at resonant points.

We have demonstrated the operation of *"double-barrier jj based dc SQUIDs"*. The geometry of the SQUIDs was in essence identical to the "CCC matched SQUIDs", but the single-barrier shunted junctions were replaced by self-shunted double-barrier junctions. The SQUID critical current dependence with temperature can be quantitatively explained in terms of the microscopic theory developed for double-barrier junctions, qualitatively extended to take into account the trapping events at the interlayer. The effective resistance R_{eff}, which determines the SQUID dynamics at 1.4 K has a value between the intrinsic resistance R_N, and the sub-gap resistance R_{subg} at that temperature. The DBSQ was moderately affected by resonances. The best noise level for a DBSQ (3.3 $\mu\Phi_0/Hz^{1/2}$), measured at a point free of resonances, was higher than the noise of the equivalent SBSQ.

The corner frequency of 1/*f* noise in the three kinds of SQUIDs (at points free of resonances) was quite high (~60-100 Hz). In Chapter 5 different methods to reduce or circumvent the problem of 1/*f* noise will be treated.

References

[1] D.J. Harlingen *et al.,Physica.* **108**(B), 1082 (1981).
[2] M.B. Ketchen and R.F. Voss, *J. Appl. Phys.* **35**(10), 812, (1979).
[3] D.J. Adelerhof *et al,. Physica C.* **209**, 477, (1993).

[4] Clewin 2.50, created by Delta Mask and WieWeb software (The Netherlands, 1996-1999) and licenced to MESA$^+$.
[5] Modified system from Nordiko NM2000-T4-SE1 rf/dc magnetron sputtering system.
[6] Perkin Elmer, model 2400 rf sputtering system.
[7] C. Steinbruchel, *Reactive Ion Etching*, in *Handbook of thin film process technology*, Ed. D.A. Glocker and S. Ismat Shah, Institute of Physiscs publishing, Bristol and Philadelphia, C1.1:2 (1995).
[8] CGR-1-1000 Carbon-glass resistance temperature sensor, from Lake Shore Instruments.
[9] L. Vargas, Postgraduate report, University of Twente, (1998).
[10] M. Hiddink, MSc Report, University of Twente, (1999).
[11] http://henry.ee.rochester.edu:8080/users/sde/cad/IND.html
[12] J. Flokstra *et al*., *J. Phys. IV France.* **8**, Pr3-229 (1998).
[13] V. Ambegaokar and A. Baratoff, *Phys. Rev. Lett*. **10**, 486, (1963).
[14] J. Hinken*, Supraleiter-Elektronik: Grundlagen, Anwendungen in der ikrowellentechnik, Springer*, Berlin (1988).
[15] E.P. Howman, PhD Thesis, University of Twente (1990).
[16] J.M. Murdock *et al.*, *IEEE Trans. Magn*. **21**, 1139 (1985).
[17] M. Gurvitch and J. Kwo, *Advances in Cryogenic Engineering Materials*, **30**, 489, Plenum Press, New York (1986).
[18] H.H. Zappe, *J. Appl. Phys*. **44**, 1371, (1973).
[19] E. Bartolomé *et al*., *Proc. of the European Conference on Applied Superconductivity*, Sitges, Spain (1999).
[20] I. Ono *et al.,IEEE Trans. Appl. Supercond*. **7**(2), 2538, (1996).
[21] JSIM 2.1, developed by E.S. Fang, University of California, Berkeley, CA 94720, U.S.A.
[22] V. Polushkin *et al.*, *Rev. Sci. Instr.* **70**(3), 2, (1999).
[23] K. Tsukada *et al*., *Rev. Sci. Instrum*. **66**(10), 5085, (1995).
[24] M.Yu. Kupriyanov and J.S. Tsai, *IEEE Trans. Appl. Supercond.* **5**, 2531, (1995).
[25] M.Yu. Kupriyanov *et al.*, *Physica C.* **16***,* 326 (1999)
[26] D. Balashov *et al.*, *Supercond. Sci. Technol.* **11**, 1401, (1998).
[27] N. Schulze *et al.*, *Appl. Phys. Lett.* **73**, 996, (1998).
[28] A.J. Manninen *et al.*, *Appl. Phys. Lett.* **70**, 1885, (1997).
[29] E. Bartolomé *et al.*, *Physica C*. **340**, 93, (2000).
[30] N.N. Iosad *et al., IEEE Trans. Appl. Sup.* **7**, 2805, (1997).
[31] M.M.Th.M. Dierichs *et al.*, *Appl. Phys. Lett.* **64**, 921, (1994).
[32] I.P. Nevirkovets et al., *Appl. Phys. Lett.* **74**, 1624, (1999).
[33] S.B. Kaplan *et al.*, *Phys. Rev. B.* **14**, 4854, (1976).
[34] M. Podt *et al.*,. *Appl. Phys. Lett*. **75**, 2316 (1999).

Chapter 4

SQUID READOUT

The development of very sensitive SQUIDs would make no sense without the availability of suitable electronics, able to read the SQUID signal without dominating the noise. The direct readout of a conventional dc SQUID with a room temperature amplifier is not possible, because since the SQUID transfer function is quite small (typically 100 $\mu V/\Phi_0$), the SQUID output voltage noise in FLL is at least one order of magnitude smaller than the input voltage noise of the amplifier (~1 $nV/Hz^{1/2}$). To overcome this situation, two solutions are possible: i) to make use of a "standard" flux-modulation scheme with a (resonant) matching circuit, or ii) to pre-amplify the SQUID signal in the cold with a large-transfer second stage SQUID. In this Chapter, we will present and compare the performance of flux-modulation electronics and Two-Stage electronics for the readout of the (single-barrier) SQUIDs developed in Chapter 3. Roughly speaking, the SQUIDs considered can be grouped in two sorts: the "CCC matched SQUIDs", which have low transfer functions (~30 $\mu V/\Phi_0$), and do not present resonances; and the "80$\hbar$ SQUIDs", with a much higher transfer function (~230 $\mu V/\Phi_0$) and affected by resonances.

4.1. SQUID and electronics contribution to the noise

Let us consider the conditions that should be fulfilled by the readout system so that the total noise would be determined by the SQUID, and not by the electronics. For a noise analysis, the flux-modulation and Two-Stage electronic schemes can be represented by the block diagrams shown in Figure 4.1. In the "standard" scheme, the SQUID (with input flux power noise $S_{\Phi,sq}$ and transfer $\partial V/\partial\Phi_{sig}$) converts the flux input signal into a voltage output, which is next amplified (by a factor of G_{step}) at the resonant transformer and then by a preamplifier (with gain G_{preamp} and input voltage noise $S_{v,preamp}$) before entering the flux-modulation block (with input voltage noise $S_{v,elec}$). For the noise to be determined by the SQUID and not by the electronics, the amplified SQUID output voltage noise has to be larger than the total voltage noise at the entrance of the preamplifier, i.e.:

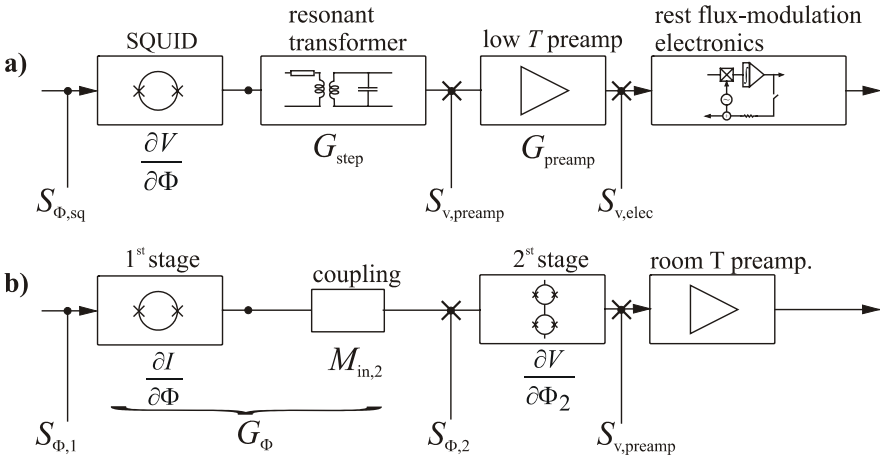

Figure 4.1- *Noise block-diagram for a) "standard" flux-modulation with resonant transformer and b) Two-Stage system.*

$$S_{\Phi,sq} \cdot \left(\frac{\partial V}{\partial \Phi}\right)^2 G_{step}^2 > S_{v,preamp} + \frac{S_{v,elec}}{G_{preamp}^2}. \tag{4.1}$$

Usually the preamplifier is designed to have a gain G_{preamp} large enough to make the flux noise contribution of the rest of the electronics after the preamplifier (last term in Eq. 4.1) negligible small. Thus, the gain of the resonant transformer and SQUID flux-to-voltage transfer should be large sufficiently large to avoid preamplifier limitation of the system noise.

In a Two-Stage system, the input flux signal is first converted to a current signal ($\partial I/\partial \Phi$) at the 1st stage SQUID (with input flux noise $S_{\Phi,1}$), and then transformed (via the mutual inductance $M_{in,2}$) into a flux Φ_2, which feeds the 2nd stage (with input flux noise $S_{\Phi,2}$). The flux gain $G_{\Phi}=(\partial \Phi_2/\partial \Phi)$ is equal to the product $(\partial I/\partial \Phi)M_{in,2}$. Then the flux Φ_2 is amplified by the large transfer-function $\partial V/\partial \Phi_2$ of the 2nd stage, before entering the room T preamplifier, with input voltage noise $S_{v,preamp}$. For the SQUID to determine the overall noise, the flux gain has to be large enough, so that the amplified flux noise of the sensor SQUID is larger than the flux noise added by the second stage and the readout electronics:

$$S_{\Phi,1} \cdot G_{\Phi}^2 > S_{\Phi,2} + \frac{S_{v,preamp}}{(\partial V / \partial \Phi_2)^2}. \tag{4.2}$$

The 2nd stage transfer $\partial V/\partial \Phi_2$ has to be sufficiently large to guarantee that the preamplifier contribution to the flux noise (last term in Eq. 4.2) is negligible small. We shall define p as the ratio between the 2nd stage plus readout electronics noise over the total noise:

$$p \equiv \frac{S_{\Phi,2} + \dfrac{S_{v,preamp}}{(\partial V / \partial \Phi_2)^2}}{S_{\Phi,1} G_\Phi^2 + S_{\Phi,2} + \dfrac{S_{v,preamp}}{(\partial V / \partial \Phi_2)^2}}. \tag{4.3}$$

If the preamplifier flux noise is negligible ($S_{v,preamp}/(\partial V/\partial\Phi_2)^2 << S_{\Phi,2}$), and the 2nd stage should only contribute a fraction p to the total noise, the flux gain should be at least:

$$G_\Phi \geq \sqrt{\frac{1}{p} - 1} \cdot \sqrt{\frac{S_{\Phi,2}}{S_{\Phi,1}}}. \tag{4.4}$$

Thus, in the design of a Two-Stage system, two requirements are important: the transfer of the 2nd stage should be large enough, to have a negligible contribution of the preamplifier noise, and the total gain available (given by Eq. 1.34) should be larger than the limit given by Eq. 4.4, so as to have a negligible contribution of the 2nd stage to the total noise.

4.2. Readout with flux-modulation electronics

For the readout of the final large-ratio CCC-SQUID amplifier, we intended to use a commercial flux-modulation electronics purchased by the NMi from "Oxford Instruments". The standard SQUID provided by "Oxford" was to be replaced by one of our home-made SQUIDs for CCC described in Chapter 3. Section 4.2.1 describes the "Oxford" electronics, and the modifications necessary to be able to read the SQUIDs for CCC. The performance of the SQUIDs using "Oxford" electronics was compared with that obtained using two other flux-modulation electronics: a commercial electronics from "Conductus", and a UT-made "19 Channel" electronics. Typically, each system consists of a module (where the SQUID is located), a header (containing the low noise elements of the electronics, in particular the preamplifier), and a SQUID control unit. The main difference between the three electronics is the type of resonant matching circuit and preamplifier utilized, which will determine the final noise performance of the system.

4.2.1. "Oxford Instruments" electronics

The schematics of the "Oxford Instruments" electronics[1] is shown in Figure 4.2. The "Oxford" SQUID mounted on the as-purchased module has an input coil inductance L_i=0.92 μH (too high for direct connection to the CCC) and a flux noise of ~3.3 $\mu\Phi_0/\mathrm{Hz}^{1/2}$ (~8 $\mu\Phi_0/\mathrm{Hz}^{1/2}$ at 1 Hz). The "Oxford" SQUID was not encapsulated and could be easily replaced by one of our SQUIDs, whose size and layout were designed to fit in (Figure 4.3a). The SQUID (*block G_1*) has a dynamical resistance R_{dyn}. The *LC* resonant transformer (*block G_2*) consists of a 6:80 cold transformer and a 20:60 warm transformer. The cold transformer is placed on the module and has an inductance L_c=1 μH. L_c is interrupted by a C=22 nF capacitor such that the circuit is open for the dc bias current and closed for the ac modulated signal (Figure 4.3b). The secondary cold transformer forms a parallel resonant

a) "Oxford" electronics

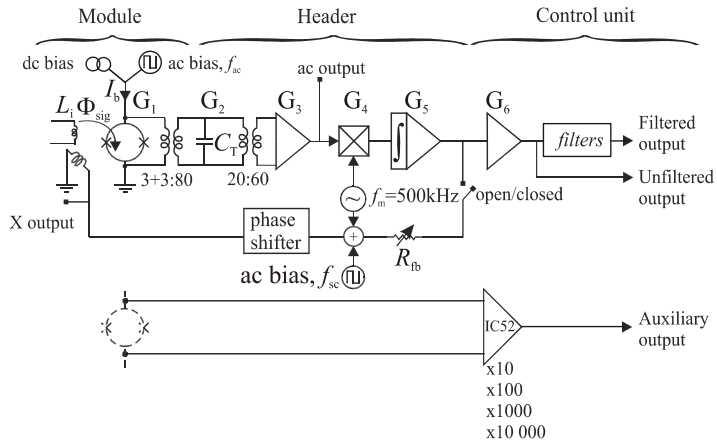

b) "19 Channel" electronics

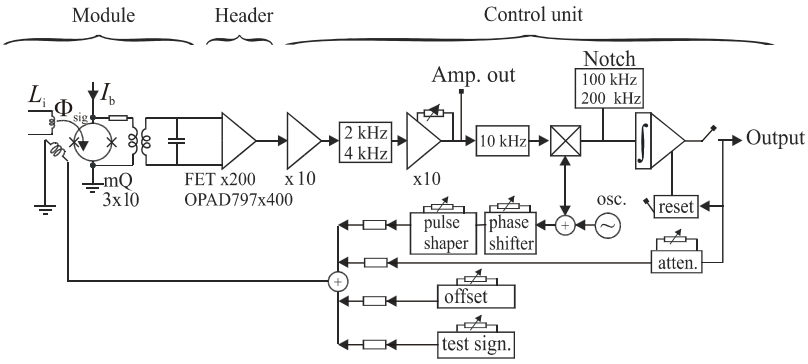

c) "Conductus" electronics

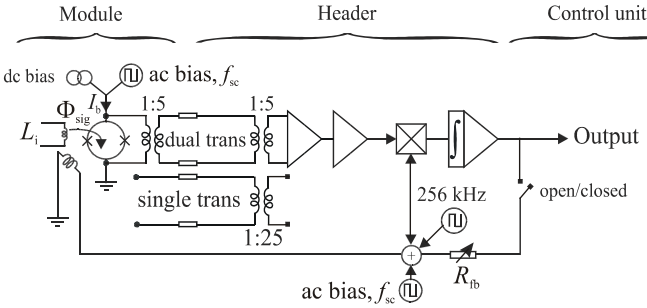

Figure 4.2- *Schematics of the a) "Oxford Instruments" electronics, b) "19 Channel" system;) c) "Conductus" electronics.*

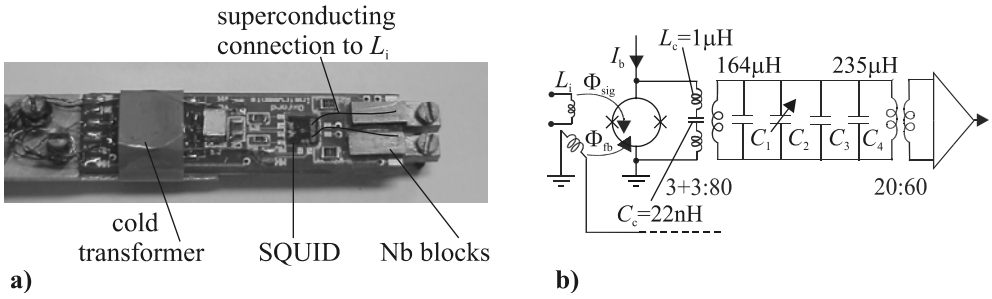

Figure 4.3- *a) Home-made SQUID on the "Oxford" module. The superconducting connection between the SQUID input coil and the Nb blocks is shown (see section 6.1.2); b) Schematics of the SQUID and resonant transformer.*

circuit with four capacitors (C_1-C_4). C_1 is the capacitance of the flexible cable connecting the module and the header, ~150 pF. C_2 is an interchangeable capacitor, which is used to tune the resonant frequency of the circuit to the modulation frequency. C_3 is an internal capacitor of 330 pF and C_4=14 pF is the parasitic capacitance of the warms primary. Thus, the resonance frequency of the circuit is $f_r=(2\pi)^{-1}(L_{eff}C_{eff})^{-1/2}$, where L_{eff} is the sum in parallel of L_{cold} and L_{warm}, and C_{eff} is the sum of C_1 to C_4.

The pre-amplifier *block G_3* contains three stages, the first of which is a low SONY 2SK300 low noise amplifier (nominally <1.5 nV/Hz$^{1/2}$ at 500 kHz), and gain of A_1=17.4. The nominal maximum gain of block G_3 is x1895. Given the voltage input noise of the preamplifier and resonant transformer gain, the voltage noise referred to the input of the transformer would be 25 pV/Hz$^{1/2}$.

The SQUID output signal is flux modulated by a f_m=500 kHz, $\Phi_0/2$ peak-to-peak sinusoidal signal, applied via the same line used for the feedback. The gain of the lock-in detector (PSD), *block G_4* is x2.

The modulated signal can be visualized at the *ac output* port. The *V*-Φ demodulated signal is available at either the *filtered* or *unfiltered* ports. In FLL, four different sensitivity ranges are available: High=10, 1 V/Φ_0, or Low=0.1, 0.01 V/Φ_0. The gain of the integrator+filter block (*block $G_5(f)$*) has a frequency dependent behavior, different for the High and Low sensitivity ranges. The gain of *block G_6* is x1 for the 1 and 0.01 V/Φ_0 sensitivity ranges and x10 for the 10 and 0.1 V/Φ_0 ones.

An ac bias reversal scheme (at frequency f_a=2 kHz) can optionally be applied to reduce the 1/*f* noise due to fluctuations in the SQUID jj critical current.

The SQUID direct IVC and *V*-Φ curves can also be visualized using the parallel scheme contained in the electronics (Figure 4.2a, below). The SQUID output voltage is amplified by a IC52 amplifier, with a nominal noise of 14 nV/Hz$^{1/2}$, and adjustable gain x10, x100, x1000 or x10 000.

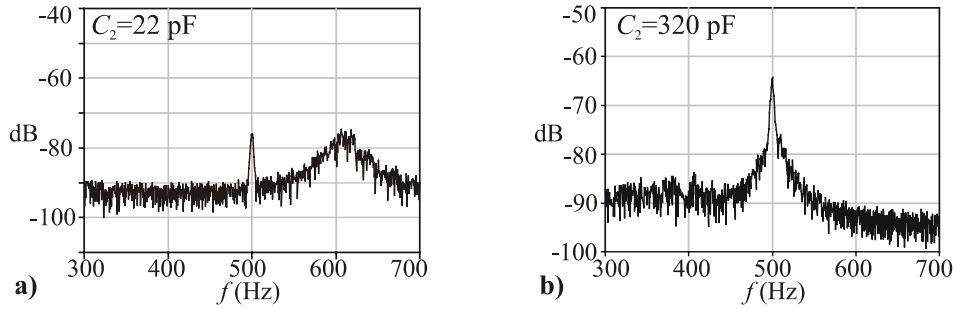

Figure 4.4- *Tuning of the LC resonant transformer. a) A test C_2 is plugged in the header and the ac output is connected to a HP3562A spectrum analyzer. When the oscillator is on, two peaks can be observed: a sharp peak at the modulation frequency 500 kHz, and a broader one (FWHM ~10 kHz) at the resonant frequency f_r; b) For C_2 such that the transformer is tuned, the two peaks coincide. The quality factor is Q~17. The resonant frequency depends on C_2 as: f(Hz)=-0.31C_2+615.2. (The tuning changes from module to module, since the inductance of the cold transformer (hand-wound) can vary, and depends on the length of the flexible cable connecting the header and module).*

When the "Oxford" SQUID was replaced by the home-made one, some adjustments of the electronics were necessary to achieve the best noise performance.

- To operate with the flux-modulation scheme, the *LC* resonant transformer has to be tuned to the modulation frequency, to obtain the maximum gain (see Figure 4.4 for details). We observed that a misstuning of only ±10 Hz affected dramatically the noise (section 4.4 a1).
- The demodulated *V*-Φ signal has to be optimized. In *open loop*, the BIAS and modulation (MOD) current amplitudes should be such to obtain a large voltage amplitude Δ*V*,

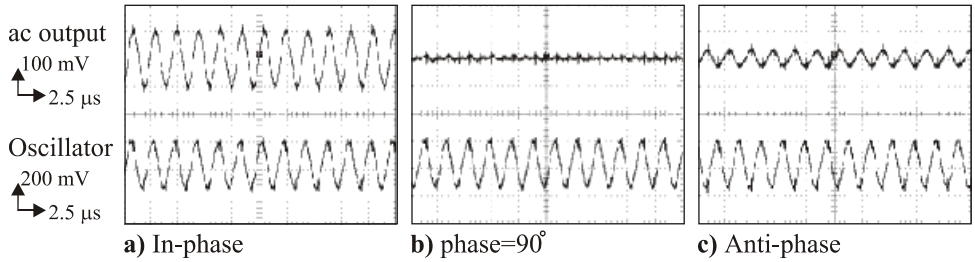

Figure 4.5- *The matching resonant circuit introduces a phase shift, which has to be corrected by a "phase shifter", situated between the oscillator and the feedback coil for the correct operation of the modulation scheme The figure shows the relative phase shift between the modulated signal $V_{sq}(f)$ (measured at the ac output) and the oscillator signal, after the phase shift correction, for an applied flux a) (n+1/4) Φ_0: signals in phase, b) 0 Φ_0: signals at 90°, c) (n+3/4) Φ_0: signals in anti-phase. ("CCC matched SQ#1", at BIAS: 11.8 µA, MOD: 6 µA).*

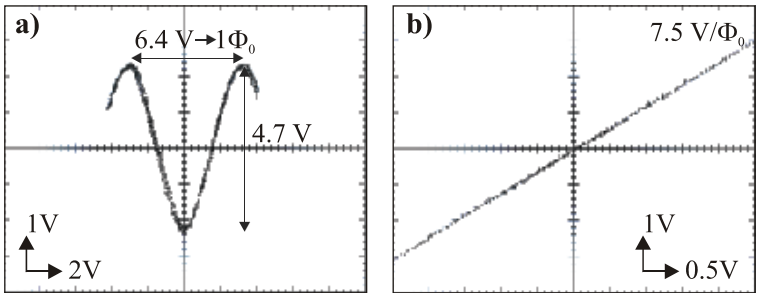

Figure 4.6- *Demodulated V-Φ curves a) in open loop, b) in closed loop, for "matched CCC SQ#7".*

approximately sinusoidal curve. The voltage amplitude ΔV can be maximized with an open loop gain controller. The PSD zero control has to be adjusted to place the curve at V=0. The PSD balance must be varied to obtain a nice symmetrical, sinusoidal curve. A shift between the phases of the modulated and oscillator signals entering the lock-in detector would lead to a reduction of the voltage amplitude, and should be thus corrected (Figure 4.5). In *closed loop*, the sensitivity (measured as the slope (dy/dx) of the FLL linear output, in [V/Φ_0] units) should coincide with the sensitivity setting at the front of the control unit. A possible discrepancy can be also corrected. Figure 4.6 shows the typical demodulated V-Φ curves measured for a "CCC matched SQUID", after the optimization process.

- For correct operation in FLL, the total transfer of the system should be frequency independent. The unfiltered output of the system depends on the gain of the different blocks and on the feedback factor β_{feed}:

$$\frac{V_{out,unfiltered}}{\Phi_{EXT/FB}} = G_6 \cdot \left[\frac{G_1 G_2 G_3 G_4 G_5}{1 + G_1 G_2 G_3 G_4 G_5 \beta_{feed}} \right] \tag{4.5}$$

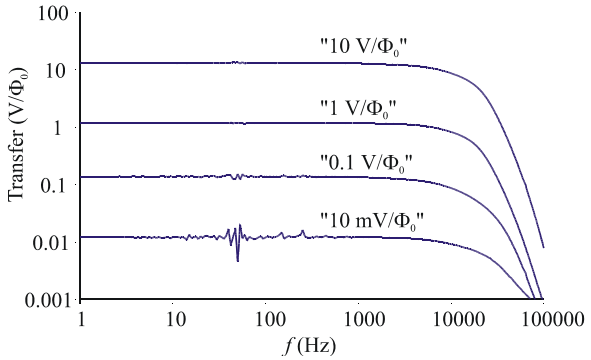

Figure 4.7- *Transfer function for the 4 (nominal) sensitivities available. "CCC matched SQ#1", BIAS=12 μA, MOD=4 μA.*

This expression reduces to G_6/β_{feed} when the factor $G_1G_2G_3G_4G_5\beta_{feed} >> 1$. In that case, the frequency response of the total transfer function should be flat (up to the cut-off frequency), since G_6 and β are frequency independent. We measured the transfer function by applying a test signal (provided by the spectrum analyzer source) via the external feedback EXT F/B input, while reading the response at the filtered output with the channel 2 of the same spectrum analyzer. We checked (Figure 4.7) that the transfer was flat for the 4 sensitivity ranges available.

4.2.2. "19 Channel" home-made electronics

A home-made electronics was developed in the past[2] for the readout of a 19 channel SQUID system for the detection of biomagnetic (neuronal) signals. A slightly modified version of this electronics (Figure 4.2b) was used to measure the SQUIDS for CCC. The matching resonant transformer, placed on the SQUID module, has a step gain of G_{step}=35. Two different preamplifiers can be mounted in the header: a x200 gain FET(2SK146) with a nominal input voltage noise of $S_{v,preamp}^{1/2}$=0.7 nV/Hz$^{1/2}$, or a x400 gain OPAD797 with $S_{v,preamp}^{1/2}$=1.0 nV/Hz$^{1/2}$. Although the FET has a lower noise than the FET preamplifier, oscillation problems have been reported[3]. According to these specifications, a voltage noise level at the input of the transformer of ~20 pV/Hz$^{1/2}$ (using the FET) or 29 pV/Hz$^{1/2}$ (using the OPA) would be expected. A $\Phi_0/2$ peak-to-peak, square 100 kHz signal is used for the modulation. In this electronics no ac bias reversal is possible.

4.2.3. "Conductus" electronics

The schematic of "Conductus" electronics[4] is shown in Figure 4.2c. Two different matching circuits area available: a "single" (1:25) transformer at room temperature or a "dual" (cold 1:5 and warm 1:5) transformer. The specified preamplifier noise is 1 nV/Hz$^{1/2}$, which implies that, using the dual transformer, a voltage noise referred to the input of the transformer of 40 pV/ Hz$^{1/2}$ could be attained. When using the single transformer, however,

	G_{step}		$S_{v,preamp}^{1/2}$ (nV/Hz$^{1/2}$)	$S_{v,input}^{1/2}$ (pV/Hz$^{1/2}$)	$S_{\Phi,preamp}^{1/2}$ ($\mu\Phi_0$/Hz$^{1/2}$) 30 μV/Φ_0	$S_{\Phi,preamp}^{1/2}$ ($\mu\Phi_0$/Hz$^{1/2}$) 230 μV/Φ_0
"Oxford"	x 40		1.0	25	0.8	0.2
"19 Channel"	x 35	FET	0.7	20	0.7	0.08
		OPAMP	1.0	29	1.0	0.1
"Conductus"	x 25	(single)	1.0	200	6.7	0.9
		(dual)	1.0	40	1.3	0.2

Table 4.1- *Expected noise ground levels for the 4 electronics, and the two groups of SQUIDs (with transfer functions ~30 $\mu V/\Phi_0$ or 230 $\mu V/\Phi_0$) considered.*

due to the thermal noise of the resistors in the transformer, only an effective noise of 0.2 $nV/Hz^{1/2}$ can be expected. The modulation signal is a square $\Phi_0/2$ peak-to-peak wave of frequency f_m=256 kHz. The feedback resistance R_{fb} and time constant of the integrator τ can be changed at will to obtain the desired sensitivity. An ac bias mode for reduction of $1/f$ noise is available; the reversal frequency can be chosen between 2.6 or 128 kHz.

The expected noise ground levels of the three electronics described, assuming that the preamplifier dominates the electronic noise, are summarized in Table 4.1. As can be seen, in principle, all electronics (except Conductus with the "single" transformer) should be able to read out the low noise (~1 $\mu\Phi_0/Hz^{1/2}$) CCC SQUIDs.

4.3. Two-Stage: SQUID for CCC + reference junction DROS

The theoretical principle of a Two-Stage system was already explained in section 1.3.5.2. The practical (non-integrated) system consisted of two separate chips (Figure 4.8): The first, sensing stage was one of the low-noise dc SQUIDs for CCC described in Chapter 3; the second, amplifying stage was a gradiometric DROS with reference junction (RJ DROS), developed in Twente by Van Duuren *et al*.[5,6]

The layout and the main parameters of the RJ DROS utilized are summarized in Figure 4.8. The signal SQUID of the DROS consists of two oppositely wound, 50 μm hole square washers connected in series, with a total inductance of L_{sq}≈550 pH. The gradiometric layout helps reducing the influence of homogeneous magnetic fields. A damping resistor of R_w=6 Ω is placed across the SQUID inductance to damp LC resonances. The 2x4 μm^2 junctions have a critical current ~2.5 μA (thus the screening parameter is β_{sig}≈1.2), and an estimated jj capacitance of 0.25 pF. The input coil consists of 2x25-turn coils connected in series, with a total input coil inductance of L_i=150 nH and a mutual inductance with the gradiometric SQUID of M_i=6.7 nH. Optionally, a R_{in}-C_{in} shunt can be placed across the input coil to reduce the influence of input coil resonances. A 1-turn feedback coil with a mutual inductance M_{fb}=220 pH is placed on top of one of the SQUID washers. The 2x6 μm^2 reference junction has a critical current 3.5 μA approximately in the middle of the critical current modulation of the signal SQUID. The DROS relaxation circuit consists of a square shunt inductor L_{sh}=1.8 nH and a series resistance R_{sh}=2 Ω, resulting in a relaxation frequency of about $f_{RO}=R_{sh}/L_{sh}$~1 GHz. Every junction of the DROS is shunted by a 40 Ω resistor to damp L_{sh}-R_{sh} resonances.

The advantage of using a RJ DROS instead of a reference SQUID DROS (RS DROS) is the reduction of the number of wires to the room T electronics and simplified DROS operation. In exchange, a disadvantage of the RJ DROS is that the reference critical current $I_{c,ref}$ cannot be tuned. If due to the fabrication process the shape of the reference junction is very much rounded, the critical current $I_{c,ref}$ will not be exactly in the middle of the modulation range of the signal SQUID, $I_{c,sig}(\Phi_{sig})$, leading to a decrease in the flux-to-voltage transfer and noise performance. This was not the case in the RJ DROS described here. For the optimal bias point $I_{b,2}$~45 μA, the DROS V-Φ had a voltage modulation amplitude of ~60 μV, the transfer function was as large as $\partial V/\partial\Phi_2$≈1.9 mV/Φ_0, and the flux noise was $S_{\Phi,2}^{1/2}$≈7.7 $\mu\Phi_0/Hz^{1/2}$ (f_c≈12 Hz). Thanks to the large transfer function $\partial V/\partial\Phi_2$, the noise of the readout electronics was not dominant.

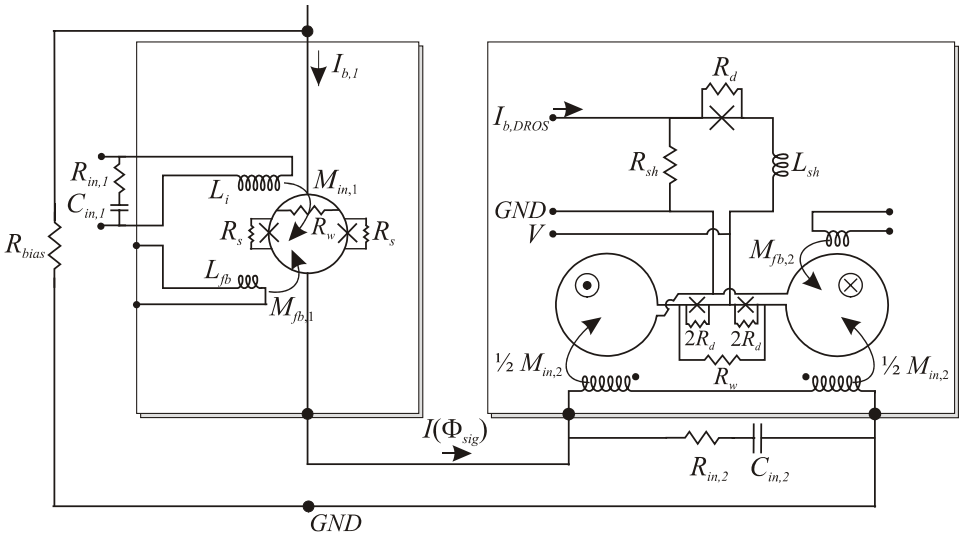

1st stage: sensor dc SQUID	**2nd stage: DROS with ref. junction**		
	- reference junction		**- relaxation circuit**
a) "CCC matched SQUID"	A=2x6 μm^2		L_{sh}=2.1nH
	I_0=3..3.5 μA		R_{sh}=2 Ω
or	**- signal SQUID**		
b) "DBSQ"	A=2x4 μm^2	D=2x50 μm	*i.coil: 2x25 turns*
	$2I_0$=4..5 μA	L_{sq}~550 pH	L_i=150 nH
or	C_{sq}=0.5 pF	$\beta_{,Lsig}$=1.2	M_i=6.78 nH
	R_w=6 Ω		k_i=0.74
c) "80ħ SQUID"			*i.feed.*:M_{fb}=220 pH
	dV/dΦ_2~1.9 mV/Φ_0		
	$S_{\Phi,2}^{1/2}$~7 μΦ_0/Hz$^{1/2}$		
R_{bias}=0.5 Ω			

Figure 4.8- *Schematics and main parameters of the Two-Stage system formed by a SQUID for CCC as 1st stage, and a DROS with reference junction as 2nd stage.*

A completely integrated (on one chip) version of the Two-Stage for CCC readout was also designed, and is further described in Appendix C.

The Two-Stage system is readout by a home-made FLL electronics[6,7] with direct voltage readout (Figure 4.9). The sensor SQUID is biased by a R_{bias}=0.5 Ω resistor. The output voltage of the RJ DROS, readout across the signal SQUID, is measured by a room temperature preamplifier based on LT1028 OPAs[8]. The input voltage noise is $S_{v,preamp}^{1/2}$=1.8 nV/Hz$^{1/2}$ (5 nV/Hz$^{1/2}$ at 1 Hz), and the gain can be adjusted between G=2.10^2-2.10^5.

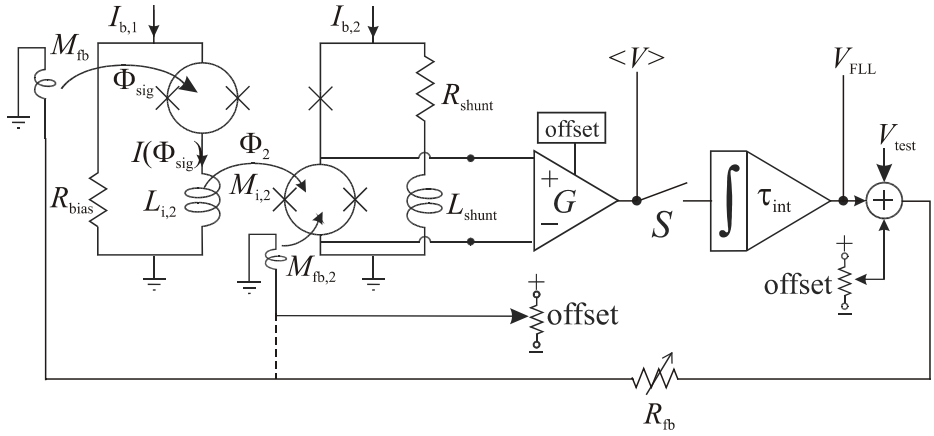

Figure 4.9- *Schematics of the Two-Stage readout system. The radio frequency interference filters (at the input, output voltage, DROS offset and feedback lines) are not represented for the sake of simplicity.*

In FLL operation (switch S closed), the preamplifier output is connected to an integrator, with a time constant $\tau=10^{-2}$, 10^{-3} or 10^{-4}. Test and offset signals can be added to the integrator output signal. The feedback line contains an adjustable resistor, which allows varying the FLL transfer function, $\partial V_{FLL}/\partial \Phi_{sig}=R_{fb}/M_{fb}$. The feedback signal is applied to the sensor SQUID. An offset flux can be applied via $M_{fb,2}$ to the signal SQUID DROS. In open loop (switch S open), the wiggling Two-Stage voltage output $<V>$ as function of the test flux (applied via the feedback line) can be directly observed after the preamplifier. The operation of the DROS alone can be measured by disconnecting the sensor SQUID, and applying the feedback signal to the signal SQUID. *L-C-R* low pass filters in the bias, voltage readout, DROS offset and feedback lines are placed to prevent radio frequency interferences.

As explained in section 4.1, the flux gain $G_\Phi=(\partial \Phi_2/\partial \Phi)$ should be sufficiently large, so that the SQUID determines the overall noise. In order to read out SQUIDs with a flux noise $S_{\Phi,1}^{1/2}$~1 $\mu\Phi_0/Hz^{1/2}$ with the RJ DROS described above, and if the 2nd stage should only contribute a 10 % to the total noise power, the flux gain should be at least G_Φ~21 (Eq. 4.4). The SQUIDs for CCC have junctions with I_0~20-10 μA, shunt resistances R_{sh}~2-5 Ω and β~1, so the maximum current modulation is $\partial I/\partial \Phi$~44-22 $\mu A/\Phi_0$; since the RJ DROS has an input coil inductance $M_{in,2}$~6.7 nH, the maximum flux available for this Two-Stage is G_Φ~60-90, larger than the minimum required. As seen in section 3.6, the flux gain depends on the bias of the sensor SQUID, $I_{b,1}$. For high values of $I_{b,1}$, the current modulation might be too small, and the flux gain be insufficient.

4.4. Comparison of the electronics

In this section we will discuss the suitability of the flux-modulation and Two-Stage systems described before for the readout of the "CCC matched SQUIDs" (which have a small transfer function and present no resonances) and "80$\hbar$ SQUIDs" (with a much larger transfer, and affected by resonances). Most noise measurements were performed at the Low Temperature Division laboratory, in the TN building; some measurements were repeated at the magnetically shielded room of the Biomagnetic Centre Twente (BCT), to check the influence of environmental noise.

a1) "CCC matched SQUIDs" measured with "Oxford" electronics

In order to check the electronics, the commercial "Oxford SQUID" was first measured. For optimum BIAS=23.5 μA and MOD=5.4 μA settings, the voltage amplitude of the V-Φ demodulated curve was ΔV=10 V, and the measured noise level was ~3.3 $\mu\Phi_0/Hz^{1/2}$, as specified in the manual. When we varied the BIAS current while maintaining the MOD current constant (or vice-versa) to reduce deliberately ΔV, we found that for settings such that ΔV>8 V_{pp}, the noise was constant (3.3 $\mu\Phi_0/Hz^{1/2}$), whereas if ΔV<8 V_{pp}, the noise scaled up with the decrease of ΔV (Figure 4.10), indicating that the noise was limited by the preamplifier. Since the open loop gain was measured to be V_{demod}/V_{sq}~240x10^4, this threshold would correspond to a SQUID transfer of ~60 $\mu V/\Phi_0$. Thus for SQUIDs with a transfer <60 $\mu V/\Phi_0$, the system noise would be limited by the preamplifier.

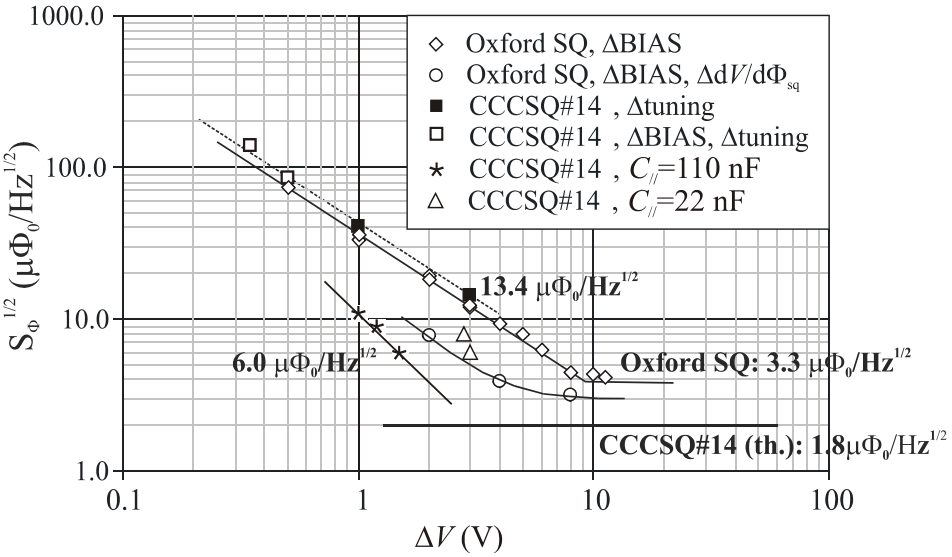

Figure 4.10- *SQUID flux noise as a function of the voltage amplitude ΔV of the demodulated V-Φ (see text).*

A "CCC matched SQUID" (#14), with a transfer 22 μV/ Φ_0, and an expected noise level of 1.8 $\mu\Phi_0/Hz^{1/2}$ was then measured. For the optimal BIAS and MOD settings, the voltage amplitude was ΔV=3 V_{pp}, and the noise level 13.4 $\mu\Phi_0/Hz^{1/2}$. When the BIAS or the MOD were changed to decrease on purpose the voltage amplitude, the noise increased linearly with the decrease of ΔV (Figure 4.10). We also checked the influence of a misstuning of the header. When an additional capacitor C was placed parallel to the tuning capacitor C_2, such as to shift the resonant peak from 500 kHz to 488 kHz, the ΔV_{pp} was reduced by a factor of 3, and the noise increased by the same factor (Figure 4.10). These results confirmed that for SQUIDs with a low transfer function, smaller than the "threshold" 60 $\mu V/\Phi_0$, the noise was determined by the electronics and not by the SQUID noise.

This result was surprising, since according to the "Oxford" specifications for the transformer and preamplifier, a much lower noise floor (~1.3 $\mu\Phi_0/Hz^{1/2}$) could be expected. We found that a possible explanation for this behavior might come from the particular scheme of the SQUID bias and resonant transformer (Figure 4.3b). The circuit formed by the series connection of the SQUID dynamical resistance R_{dyn}=1.4 Ω and L_c=1.μH, in parallel with the C_c=22 nH capacitor might be acting as a voltage divider, reducing the voltage amplitude by a factor:

$$\left|\frac{V_0}{V_i}\right| = \frac{L_c\omega}{\sqrt{R_{dyn}^2 + \left[L_c\omega - (1/C_c\omega)\right]^2}} = 0.3. \tag{4.6}$$

To improve this situation, we placed a capacitor $C_{//}$ in parallel with C_c. Although we achieved a reduction of the noise (down to 6.0 $\mu\Phi_0/Hz^{1/2}$, see Figure 4.10), the increase in voltage amplitude did not correspond to what should be expected according to our hypothesis.

Up to present, the reason for the unexpected high electronics noise floor has not been clarified. The gain of the preamplifier might be smaller or its voltage noise higher than specified, or the electronics stages after the preamplifier add a non-negligible noise.

a2) "CCC matched SQUIDs": comparison between the "Oxford", "19 Channel" and "Conductus" electronics.

For comparison, the noise of the "CCC matched SQUID#7" (with a transfer of 31 μV/ Φ_0 and expected noise 1.8 $\mu\Phi_0/Hz^{1/2}$), was measured with both the "Oxford" and the "19 Channel" electronics. With "Oxford" electronics, the best noise level (measured for BIAS: 11.8 μA, MOD: 6 μA, ΔV=4.7 V), was 7.2 $\mu\Phi_0/Hz^{1/2}$. The noise was still limited by the electronics (because the SQUID transfer was <60 μV/ Φ_0), but was lower than for the SQ#14, which had an even smaller transfer. When measured at the BCT, the noise improved to 6.1 $\mu\Phi_0/Hz^{1/2}$, most probably because the SQUID could be cooled down with less probability of flux trapping than at the TN. With the "19 Channel" electronics, the noise levels measured were 5.0 $\mu\Phi_0/Hz^{1/2}$ (using the OPA preamplifier) and 3.4 $\mu\Phi_0/Hz^{1/2}$ (using the FET). The ratio between the noise levels measured with both preamplifiers $S_\Phi{}^{1/2}{}_{FET}/S_\Phi{}^{1/2}{}_{OPA}$ was equal to the ratio between the preamplifiers voltage noise

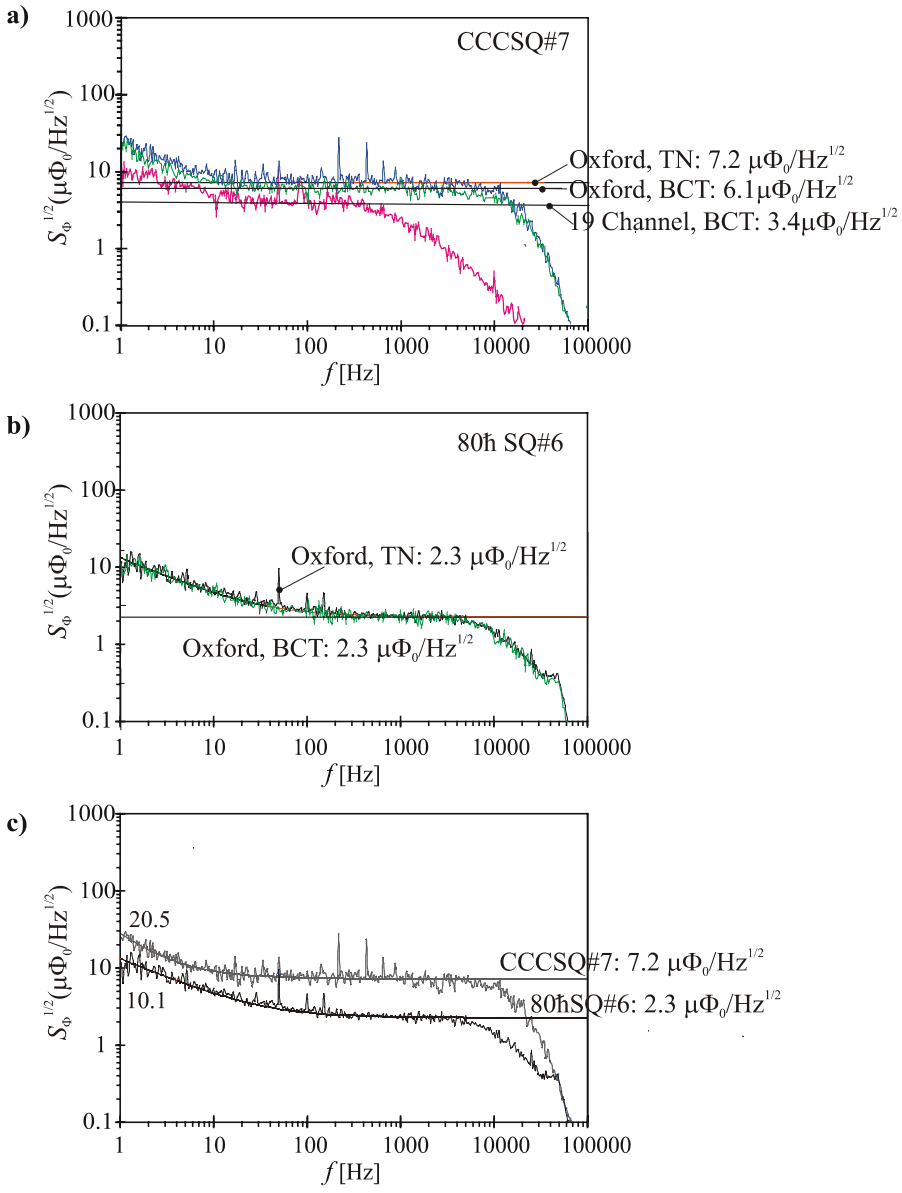

Figure 4.11- *Flux noise spectra of a) "CCC matched SQ#7" measured with Oxford and the "19 Channel" electronics, at the TN and the BCT; b) "80ħ SQ#6.6" with Oxford electronics, at the TN and BCT; c) comparison of the spectra of the same two SQUIDs measured with "Oxford" electronics.*

$S_{V,preamp}{}^{1/2}{}_{FET}/S_{V,preamp}{}^{1/2}{}_{OPA}$, indicating that the preamplifier noise was still the dominant source of noise. The fact that the noise with the "19 Channel" electronics was smaller than with "Oxford" confirmed that the measured noise was attributable to the electronics and not to the SQUID. The noise improvement $S_\Phi{}^{1/2}{}_{19\ Channel,FET}/S_\Phi{}^{1/2}{}_{Oxford}$~0.5 was better than what one could expect (~0.8) considering only the specified values for the preamplifiers noise and the step-up transformers gain of both systems (Table 4.1). This fact would support the argument that the contribution to the noise of the electronic stages after the preamplifier was non-negligible.

The noise of a different "CCC matched SQUID" (#5, 200 pH, 20 turns), with transfer 32.4 $\mu V/\Phi_0$, was measured with "Conductus" electronics, using the "single" transformer. The level measured (~6.0 $\mu\Phi_0/Hz^{1/2}$) corresponds approximately to the ground floor expected for this electronics (Table 4.1).

a3) "CCC matched SQUIDs": comparison between "Conductus" and Two-Stage readout

A "CCC matched SQUID" (L_{sq}~100 pH, 20 turns) with a flux transfer ~70 $\mu V/\Phi_0$ and a theoretical flux noise of 1.2 $\mu\Phi_0/Hz^{1/2}$ was measured with the help of "Conductus" and the Two-Stage system (Figure 4.12a). Using "Conductus" with the "dual" transformer, the preamplifier contribution to the noise would be ~0.6 $\mu\Phi_0/Hz^{1/2}$; thus in principle, it should be possible to measure the intrinsic noise of the SQUID. Experimentally, the noise measured[9] was ~4.3 $\mu\Phi_0/Hz^{1/2}$. When measured with the Two-Stage, the SQUID noise was ~1.3 $\mu\Phi_0/Hz^{1/2}$, very close to the expected value[10]. Therefore, with "Conductus" the system noise was limited by the electronics, whereas with the Two-Stage the noise was actually determined by the SQUID, and not by the 2nd stage or the room *T* amplifier[11].

b1) "80ħ SQUIDs": comparison between "Oxford" electronics and Two-Stage readout

The "80ħ SQUID#6" was measured both with "Oxford" and the Two-Stage system. Because the transfer function of this SQUID was large (230 $\mu V/\Phi_0$), thanks to the high SQUID McCumber parameter β_c~0.5, the noise measured with "Oxford" electronics was not limited by the preamplifier like was the case for the "CCC matched SQUIDs". The level measured (2.3 $\mu\Phi_0/Hz^{1/2}$) was really given the SQUID. The noise spectra measured at the BCT and at the TN were identical, except for the 50 and 100 Hz peaks. Figure 4.11c compares the spectra of "CCC matched SQUID#7" and "80ħ#6", both with a similar input coil inductance L_i close to the CCC self-inductance. Note that although the "80ħ SQUID" has a larger corner frequency (~40 Hz) than the "CCC matched SQUID" (~10 Hz), the noise at 1 Hz for the first SQUID is still a factor of 2 better than for the second.

Yet, the noise measured for "80ħ#6" with "Oxford" was larger than expected (1 $\mu\Phi_0/Hz^{1/2}$), because of the effect of non-efficiently damped resonances. When measured in a Two-Stage system, the SQUID could be biased "diagonally", and one could find points in the IVC free of resonances at which the noise was indeed ~1 $\mu\Phi_0/Hz^{1/2}$ (this topic was already extensively treated in section 3.6). In contrast, with a flux-modulation electronics

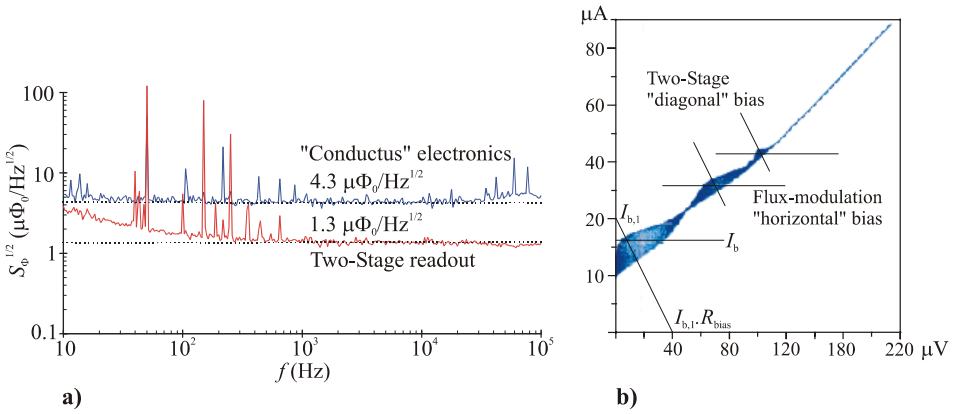

Figure 4.12- *a) "CCC matched SQUID" (100 pH, 20 turns) flux noise spectra measured with "Conductus" ("single" transformer) and Two-Stage system. b) SQUID biasing: with a flux-modulation electronics, the SQUID is biased at a constant current ("horizontally"); in the Two-Stage system, the SQUID is voltage biased at $I_{b,1}.R_{bias}$ ("diagonally").*

like "Oxford", the SQUID is biased at constant current ("horizontally"), so that resonances are inevitably crossed, and the noise increases (Figure 4.12b). The ability to avoid resonances is an additional advantage of the Two-Stage system with respect to conventional electronics[12].

4.5. Conclusions

We have studied the suitability of flux-modulation electronics and a Two-Stage system for the readout of low-noise SQUIDs. The applicability of a "standard" flux-modulation electronics for the readout of a specific SQUID depends on the magnitude of the SQUID voltage-to-flux transfer function. We found that "Oxford" electronics cannot be applied for the readout of SQUIDs with a small transfer function, like the "CCC matched SQUIDs". The noise levels measured with the "19 channel" and "Conductus" systems are somewhat better, but the overall noise is still limited by the electronics and not by the SQUID. On the contrary, thanks to their larger transfer function, the real noise of the "80$\hbar$ SQUIDs" can be measured with "Oxford" electronics.

In a Two-Stage system, thanks to the large flux-to-voltage transfer $\partial V/\partial\Phi_{,TS}$ attained, the room temperature preamplifier noise does not dominate the overall flux noise, and the real SQUID noise can be determined. The Two-Stage system with a RJ DROS as 2nd stage described here is well suited for the readout of the "CCC matched SQUIDs". In addition, the Two-Stage is more advantageous than a conventional electronics for the readout of SQUIDs affected of resonances (like the "80$\hbar$ SQUIDs"), because the sensor SQUID can be "diagonally" (instead of "horizontally") biased at points in the IVC free of resonances.

References

[1] "Φ_0 DC-SQUID" (mark 5G), Oxford Instruments, operator's handbook, (1998).
[2] A. Martínez, PhD Thesis, University of Zaragoza, (1989).
[3] E. Krooshoop, Twente Biomagnetic Centre, *private communicatio*n.
[4] "pc SQUID" (model PFL-100), Conductus, user's manual (1992-1997).
[5] M. van Duuren, PhD Thesis, University of Twente, The Netherlands (1998).
[6] M.J. van Duuren *et al*., *J. Appl. Phys*. **82**, 3598 (1997).
[7] A.W. Hamster et al., *IEEE Trans. Appl. Supercond*. **9**, 2915 (1999).
[8] LT1028 CN8 OPA, Linear Technology Corporation, Milpitas, California, USA.
[9] L. Vargas, Postgraduate report, University of Twente, (1998).
[10] M. Podt, MSc report, University of Twente, (1998).
[11] M. Podt *et al*., *Appl. Phys. Lett*. **75**(15), 2316 (1999).
[12] E. Bartolomé *et al*., *Proc. of the European Conference on Applied Superconductivity*, Sitges, Spain (1999).

Chapter 5

LOW FREQUENCY NOISE REDUCTION

In a large ratio CCC, the frequency of the primary current I_1 must be as low as ~0.01-0.1 Hz, so as to avoid a large ratio error owing to leakage current between the windings (section 1.2.2). Unfortunately, the SQUID sensor is affected by excess 1/*f* noise at frequencies lower than the corner frequency f_c, typically at 1-10 Hz. This confrontation led us to research the manners of reducing the 1/*f* noise in the system. In section 5.1 we present a review of the sources of 1/*f* noise and different noise reduction techniques that can be found in literature. Many of the methods described were originally developed for other applications where low-noise SQUIDs working at low-frequencies were needed, e.g. in biomagnetism[1], magnetic monopole searches[1] or the Relativity Gyroscope experiment[2]. Roughly speaking, two approaches have been followed to try to reduce the 1/*f* noise: attacking the sources of noise, or circumventing the problem by shifting the SQUID operation point to higher frequencies. We investigated the two routes. On one hand we developed washer-structured SQUIDs, to try to get rid of one type of 1/*f* noise, arising from trapped flux lines in the SQUID body (section 5.2). In addition, we studied a signal-modulation technique, which is able to eliminate the 1/*f* noise independently of its origin (section 5.3).

5.1. Sources of 1/*f* noise and corresponding reduction techniques

At least two sources of excess noise have been identified in dc SQUIDs:

a) Firstly, ***fluctuations of the critical current I_0,*** due to random trapping and subsequent releasing of electrons in the junction barrier, produce telegraphic noise[3,4]. A single trap in the barrier causes the random fluctuations of the current between two values. The spectral density of this process is a Lorentzian:

$$S(f) \propto \frac{\tau}{1+(2\pi f\tau)^2}, \tag{5.1}$$

τ being the mean time between pulses. Since the trapping process is thermally activated, τ takes the form: $\tau=\tau_0.\exp(E/k_BT)$, where τ_0 is a constant and E is the trap barrier height. In general there may be several traps in the junction, each with its own characteristic time τ_i. It can be shown that the superposition of several trapping processes (statistically independent) at a certain temperature, results in a $1/f$ spectral density:

$$S(f,T) \propto \frac{k_BT}{f} D(\widetilde{E}), \tag{5.2}$$

where $D(\widetilde{E})$ is the distribution of activation energies evaluated at $\widetilde{E}=k_BT.\ln(1/2\pi f\tau_0)$. In order to have a corner frequency as low as f_c~1 Hz, the stability period of an electron should be in the order of τ_0~10 s.[5]

Fluctuations ΔI_0 in the critical current of the junctions produce a change in voltage across the SQUID given by[6]:

$$\Delta V = \left[\left(\frac{\partial V}{\partial I_0}\right)_I + \frac{1}{2I_0}\left(\frac{\partial V}{\partial \alpha}\right)\right]\Delta I_0 = \left[-R_{dyn} + L_{sq}\left(\frac{\partial V}{\partial \Phi}\right)\right]\Delta I_0, \tag{5.3}$$

where $\alpha=(I_{01}-I_{02})/2$ I_0 is the (temporal) asymmetry in the critical currents of the two junctions. These fluctuations contribute to the output voltage noise according to two distinct modes (Figure 5.1). In the ***in-phase-mode***, the two junctions suffer a fluctuation of the same polarity, producing a voltage change across the SQUID proportional to the dynamical resistance R_{dyn} (first summand of Eq. 5.3). Ideally, this component is eliminated by the conventional FLL readout scheme. In the ***out-of phase mode***, the fluctuations in the two

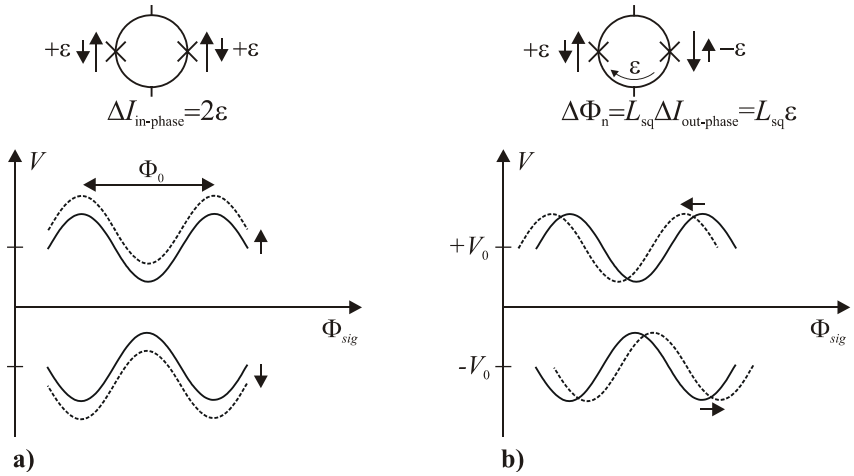

Figure 5.1- *SQUID V-Φ characteristics for positive $+I_b$ and negative $-I_b$ bias currents. a) Effect of in-phase fluctuations; b) effect of out-of-phase fluctuations (from Ref. 1).*

junctions have opposite polarity, and produce an "extra" screening current around the SQUID loop. This appears as a flux noise and consequently the voltage change is proportional to the transfer function $\partial V/\partial\Phi$ (second summand of Eq. 5.3). This term is not reduced by the conventional FLL. However, several modulation schemes can eliminate both the first and second component:

a1) The ***bias reversal scheme*** proposed by Kock *et al*.[6] is the most used technique. The SQUID is modulated by a flux square wave of peak to peak amplitude $\Phi_m=\Phi_0/2$ at a typical frequency f_m~100 kHz, whereas the bias current is reversed at a lower frequency, e.g. f_a~1 kHz. Two variants of this scheme have been proposed. In *method A*, an additional flux change $\Delta\Phi=\Phi_0/2$ is applied synchronously with the bias current. Both in-phase and out-of-phase variations of I_0 are eliminated. In *method B*, no flux change is made. This method eliminates all small flux variations (both signal and noise) sensed by the SQUID. These flux demodulation schemes involve only one synchronous detection at frequency f_Φ.
Other variants of these schemes were later developed. For instance, Dossel *et al*.[7], proposed to modulate both the flux and the bias current at the same frequency, the two modulating signals being in quadrature, thus simplifying the lock-in demodulator circuit. Drung[8] reported a simple reversal scheme for dc SQUIDs with APF, which does not deteriorate the white noise level.

a2) Foglietti *et al*.[9] proposed a different method, using both the flux and bias current modulation and a ***Second Harmonic Detection (SHAD)*** readout. This scheme is particularly helpful in cases where the V-Φ is strongly asymmetric respect to $\Phi_0/2$, and the slopes at the two sides are very different.

In anyone of the schemes describe above, the reduction of 1/*f* noise is at the expense of a small increase of the white noise level. An interesting mathematical presentation and comparative study of the different techniques mentioned can be found in Ref. 10.

b) The second source of 1/*f* noise arises from the ***hopping of flux lines in the SQUID body***. During the cooling down of the SQUID in a (local) background magnetic field, some vortices can be trapped in the SQUID washer. These vortices are usually pinned at impurities or thickness variations of the superconducting ring. Thermal fluctuations can however change the pinning energy and allow the vortices to escape and move across the ring, thus producing "real" flux noise. The 1/*f* noise originating from flux hopping cannot be eliminated by any of the modulation schemes described above. The following approaches have been suggested in the past to reduce this kind of 1/*f* noise:

b1) The ***improvement of the SQUID fabrication process*** has led progressively to lower 1/*f* noise levels, although the direct correlation between the changes introduced and noise improvement is not fully understood and the reproducibility is quite poor. The device with the "record" lowest 1/*f* noise is the niobium-lead alloy edge junction SQUID fabricated by Tesche *et al*.[11] (350$\hbar$ at the white noise region and 770$\hbar$ at 0.1 Hz). However, the result was not reproducible. In general, the quality and conditions of deposition of the electrode (non-

stressed Nb films) play a significant role[4]. Also, the careful deposition of the interlayer dielectric SiO_2 layer (by sputtering or plasma enhanced chemical vapor deposition: PECVD) leads to lower $1/f$ noise, due to the reduction of traps where the flux lines can weakly pin. The Nb/Al based SQUIDs reported in Ref. 12,13, incorporating several of these improvements attained a white noise level of $5x10^{-31}$ Js and a $1/f$ knee below 0.1 Hz.

b2) ***Avoiding flux entry in the SQUID body*****:** In controlled laboratory conditions, the devices are surrounded by high permeability magnetic shields that attenuate ambient magnetic noise. Note that this is not possible in geophysical or biomagnetic applications, where the SQUIDs must be operated in the earth's magnetic field. Several methods have been suggested to prevent the entrance of residual flux lines in the SQUID washer:

- ***Slots and/or holes*** have been patterned in the washer body of HTS SQUIDs, with the idea of reducing the inter-slot superconducting zones where the flux lines can be trapped[14,15]. The superconducting film of width w cooled in a perpendicular field $\boldsymbol{B}$ will exclude superconducting flux for fields below the threshold value $B_T=\pi\Phi_0/4w^2$.[16] Thus no increase in the low-frequency noise occurs if $B<B_T$. Above B_T, as flux enters the superconductor and vortices can move in the YBCO, the S_Φ(1 Hz) noise scales approximately linearly with B_0.[17] The effectiveness of this method is still very controversial[18]. We have investigated the application of slots and holes in LTS SQUIDs (see section 5.2).

- Implementation of a ***flux-dam***[19]: The flux-dam consists of a Josephson junction in the SQUID pick up loop, such that, for small changes in the field ($I_{scr}<I_{0,dam}$) the dam remains closed (hence the magnetometer works as usual), while for large changes ($I_{scr}>I_{0,dam}$), the dam allows the flux to enter and leave the pick up loop. This prevents the circulating current from being large enough to trap flux in the pick-up loop, thus reducing the extra low-frequency noise. Magnetometers using flux dams can operate in moderate magnetic fields at performance levels competitive to similar-sized devices without flux dams operated in zero field.

- On-chip shielding of the SQUID using "moats" at the periphery of the washer, to trap residual vortices that may be present as the device goes through the superconducting transition (see e.g. the schemes proposed in Ref. 20, 12). The idea, already applied in superconducting electronic circuits[21], is to attract and trap flux lines in sections of the chip where they will do the least harm. This method will be tested on one of the SQUIDs described in section 5.2.2.

b3) ***Creating strong pinning sites in the superconductor,*** so vortices are more tightly bound and possibly move less. Several possibilities are under test:

- The ***roughness of the washer edges*** can act like strong pinning sites. Additional pinning centers could be introduced by elongating on purpose the slot edges, e.g. by patterning the slots in the form of a "***zipper***"[12]. This design will be also explored in section 5.2.2.

- ***Artificially-patterned non-superconducting sub-micrometer holes***[22] and ***artificial defects*** have been introduced in HTS SQUIDs, to study the effect on the $1/f$ noise. Selders *et al.*[23] patterned an array of antidots on top of the grain boundary of an rf (HTS) SQUID. Two matching conditions played a role: the matching between the vortex lattice and the

grain boundary in the washer, and the matching between the vortex and the antidot lattice. They observed a reduction of the 1/*f* noise when the two matching conditions were fulfilled. Also, they observed more 1/*f* noise for positions in which the grain boundary and the antidot lattice compete to attract vortices to their positions.

- Shaw *et al.*[24] tried to reduce the flicker noise in HTS films by producing an ***irradiation damage*** of the sample. However, it seems that the noise remains higher than in high quality thin films, thus this is unlikely to be a tool for reducing 1/*f* noise in thin-film HTS SQUIDs.

b4) ***Removing vortices from the SQUID body****:* An rf demagnetization scheme, applying a radio-frequency magnetic field with a certain power, can remove weakly pinned vortices from the SQUID, or move them to pinning centers with a higher pinning energy, thus reducing the low frequency excess noise[25,26,27].

5.2. LTS slotted SQUIDs

The problem of vortex hopping in LTS SQUIDs is less severe than for HTS SQUIDs, because of the lower operation temperature and the possibility of shielding the device to a great extent from environmental noise. In spite of that, flux generated within the LTS device itself can be trapped, move around and produce non-negligible excess noise[28,29]. A possible way of reducing the 1/*f* noise arising from flux hopping is preventing the penetration of vortices in the SQUID, by reducing the width of the strips forming the washer. Based on this idea, slotted and/or holed SQUID washers have used in HTS SQUIDs for use in ambient magnetic fields (~50 μT). The application of slot and hole structures to LTS SQUIDs has not been studied yet. Alternatively, flux trapping can be prevented by patterning a "moat" around the superconducting device[21]. A different strategy to reduce flux hopping is to use the washer slit edge roughness to create strong pinning centers in the SQUID, where vortices can be tightly trapped and possibly move less[29]. We have developed Nb/Al dc SQUIDs with all these different structures to investigate the reduction of 1/*f* noise[30].

5.2.1. Slotted SQUIDs theory

In this section we will justify that, in theory, slotted/holed structures can be applied both to LTS and to HTS devices. Consider a type II superconducting strip (Figure 5.2a) of width w and thickness t, such that $t<<w$, and $t > 2\lambda$, to ensure a complete Meissner effect in the vertical direction. Suppose first that the strip is cooled down through T_c *in the absence of an applied magnetic field* B_a. In the superconducting state, the penetration depth $\lambda(T)$, diverging at T_c, is given by:

$$\lambda(T) \approx \frac{\lambda(0)}{\sqrt{1-\left(\frac{T}{T_c}\right)^{\alpha}}}, \tag{5.4}$$

with $\alpha \approx 2$ for YBCO and $\alpha \approx 4$ for Nb.[31] Just below T_c, the production of vortex-antivortex pairs is energetically very favorable. Indeed, the energy to produce such a pair in the superconductor is[32]:

$$E_{pair} \approx \frac{4\pi}{\mu_0} \frac{\Phi_0^2}{16\pi^2 \Lambda}, \tag{5.5}$$

where $\Lambda(T)=2\lambda^2(T)/d$ is the two-dimensional screening length. Since $\lambda(T_c)\rightarrow\infty$, E_{pair} is very small compared to the kinetic energy of the vortex, $k_B T$. Thus, the strip will be filled with a gas of vortex-antivortex pairs. As the temperature decreases, the energy E_{pair} raises. Below the so-called Kosterlitz-Thouless transition temperature T_{KT}, such that per definition $E_{pair} \equiv k_B T_{KT}$, vortices and antivortices start annihilating each other. If the sample does not contain pinning sites where the vortices and antivortices can be pinned during the freeze-out process, the annihilation will be total at sufficiently low temperatures. It is important to note that at temperatures near T_c, at which the freeze-out process occurs, Λ is much larger than the typical strip width w. This fact, which holds as much for HTS as for LTS strips (Figure 5.2b), enables us to describe the vortex energy during the freeze-out process with expressions that, strictly, are only valid when $\Lambda >> w$.

In the presence of an applied field B_a perpendicular to the strip, there will be an excess of vortices over antivortices. At low temperatures, once the annihilation process has finished, there will remain a density of vortices B_a/Φ_0, separated from each other a distance $(\Phi_0/B_a)^{1/2}$. If w is much larger than the inter-vortex distance, $w >> (\Phi_0/B_a)^{1/2}$, many vortices will remain in the strip after cooling. Let us analyze now the situation in which $w \leq (\Phi_0/B_a)^{1/2}$. As we have seen, just below T_c, it holds that $\Lambda >> w$; thus, the freeze-out process is dominated by the kinetic energy of the vortex, whereas screening effects, which occur on the length scale of $\Lambda(T)$, can be neglected. The Gibbs energy of a vortex, at a position x ($0<x<w$) inside the strip can be described by:

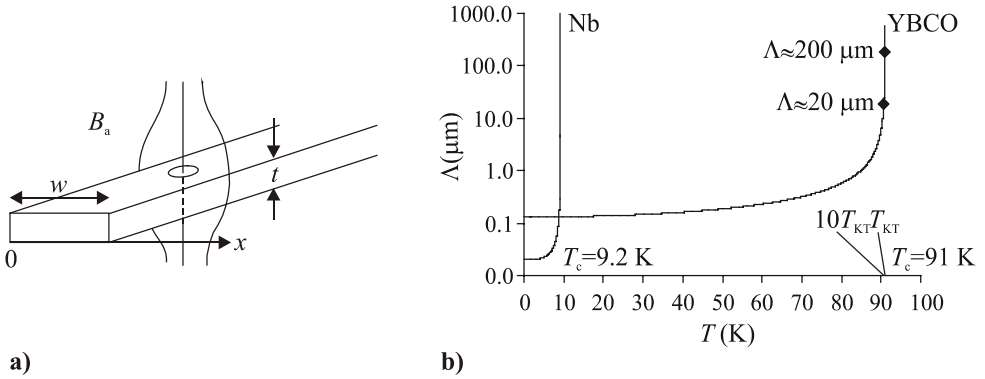

Figure 5.2- *a) Dimensions of the superconducting strip in an applied field B_a; b) Dependence of the two-dimensional screening parameter with the temperature $\Lambda(T)$, for Nb and YBCO.*

$$G(x) = \frac{4\pi}{\mu_0}\frac{\Phi_0^2}{8\pi^2\Lambda}\ln\left(\frac{2w}{\pi\xi}\sin\left(\frac{\pi x}{w}\right)\right) - \frac{4\pi}{\mu_0}\frac{\Phi_0 B_a}{4\pi\Lambda}x(w-x). \tag{5.6}$$

The first term corresponds to the kinetic self-energy of the vortex. The second term represents the energy involved when the field B_a succeeds in penetrating locally in the superconducting strip. The minima-maxima analysis of this function, represented in Figure 5.3, provides information about how favorable it is for a vortex to remain in the strip.

- For fields $B_a > B_{c1} \equiv (2\Phi_0/\pi w^2)\ \ln(2w/\pi\xi)$, $G(x)$ has an absolute minimum at the center of the strip, $x_{amin}=w/2$. Therefore vortices will remain, aligned in a row, at the center of the strip.
- If $B_T < B < B_{c1}$, where B_T is the *threshold field*:

$$B_T \equiv \frac{\pi\Phi_0}{4w^2}, \tag{5.7}$$

$G(x)$ has a local minimum at $x_{lmin}=w/2$, and two local maxima at $x_{max}=w/2\pm\Delta x$, where $\tan(\pi\Delta x/w)/(\pi\Delta x/w)=B_a/B_T$. At $T\sim T_c$, thanks to thermal fluctuations some vortices can be found in the local potential well between the two maxima. If T decreases, the height of the well barrier $\Delta G=G(x_{max})-G(w/2)$ will increase, and soon become much larger than the kinetic energy $k_B T$. Therefore, the probability of escape of the vortex out of the well, $P\alpha\exp(-\Delta G/k_B T)$, will decrease.

- If $B_a < B_T$, $G(x)$ has a single local maximum at the center of the strip, $x_{MAX}=w/2$. Thus, all vortices that might be present in the strip near T_c will be expelled from the strip as the potential maximum at $x_{MAX}=w/2$ grows with decreasing temperature. For a given field B_a, and provided there are not strong pinning sites, no vortices will be trapped in the strip, if the strip width is small enough: $w<(\pi\Phi_0/4B_a)^{1/2}$. Note that this result is material independent, so it is physically correct to apply it to LTS structures.

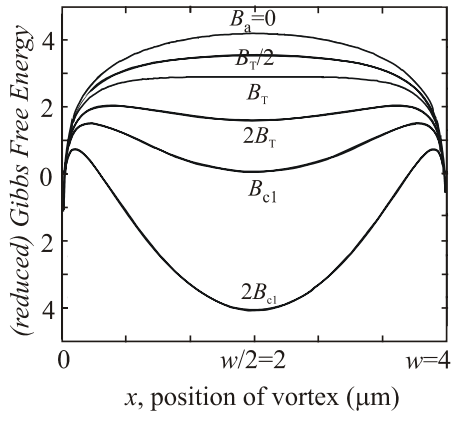

Figure 5.3- *Gibbs free energy (reduced with respect to $\Phi_0 2/8\pi\Lambda$) of a vortex trapped in a superconducting stripe as a function of the position x of the vortex within the strip (of width e.g. w=4 μm).*

5.2.2. Washer-structured SQUID design

We designed 9 differently structured washers (Figure 5.6), including slots and/or holes, a moat surrounding the washer and a zipper-slit to study the reduction of 1/*f* noise. The washer outer size (445 μm) and central hole (77 μm) were in all cases the same. A ***Bold***, non-structured SQUID was used as reference; its main characteristics are summarized in Figure 5.7a. The design of this SQUID was based on the "CCC matched SQUIDs" already described in Chapter 3.

The design of the LTS slotted and/or holed SQUIDs ran in parallel to that of the HTS ones. However, a significant difference should be noted. The HTS slotted SQUIDs developed e.g. for biomagnetism applications, are directly connected to a pickup loop, and placed in the environment where the signal field B has to be detected. To reach the larger signal-to-noise ratio: $S_B^{1/2}= S_\Phi^{1/2}/A_{eff}$, the effective area A_{eff} (defined as the total magnetic flux detected per unit of applied magnetic field) has to be maximized, while keeping the flux noise $S_\Phi^{1/2}$ small. In the case of LTS slotted SQUIDs, the field B is sensed by a pickup coil connected to the input coil of the (shielded) SQUID, forming a flux transformer. The best signal-to-noise ratio: $S_I^{1/2}= S_\Phi^{1/2}/M_i$, will be obtained by maximizing the input coil mutual inductance M_i (while respecting the matching condition to the sensing coil or CCC).

The optimization of the washer geometry with respect to A_{eff} was studied for the case of slotted HTS SQUIDs[33,34]. First, the optimum number of slots maximizing A_{eff} was determined, in a washer configuration in which only slots were present. A model was developed in which, assumed a certain parameterization of the washer in paths of constant current, the current distribution in a slotted washer, and thus also the inductance L_{sq} and effective area could be predicted. It was found both theoretically and experimentally (Figure 5.4) that A_{eff} was maximum when the innermost half part of the washer was slotted. A gain of more than the 20% in A_{eff} was observed with respect to the solid washer SQUID. For the optimal half-slotted SQUID, the remaining outermost part of the washer was filled in with different slot or hole structures, to try to obtain an even larger A_{eff}. The different SQUIDs fabricated are shown in Figure 5.5. Families A, B and C were formed by three samples with the same geometry, but different size of the outermost slots or holes. The simulation model turned inadequate to treat these "exotic" SQUIDs, due to requirement of choosing *a priori* a parameterization, which is not so obvious as in the case of only slotted SQUIDs. The results of the effective area measurements are summarized in Figure 5.4b, where the different geometries have been ordered form the one with the largest A_{eff} to the one with the smallest one. Within a family, A_{eff} was larger the smaller the structures patterned were. The A_{eff} of half-slotted SQUIDs with fine structure at the outermost side of the washer was found to be smaller than that of a simple half-slotted SQUID, indicating that the current distribution in the innermost strips was affected by the complicated distribution at the outermost strips.

In the case of the LTS slotted SQUIDs, the washer geometry should maximize the mutual inductance M_i, instead of the effective area A_{eff}. SQUIDs with ***¼-slotted***, ***½ slotted*** and ***all-slotted*** washers were designed. Two more "exotic" washers, an ***all-holed*** and a ***½ slotted/holed*** washers were included. The width of the inter-slot strips was the smallest possible with our photolithographic process, w=4 μm. The slots and holes width was 8 μm.

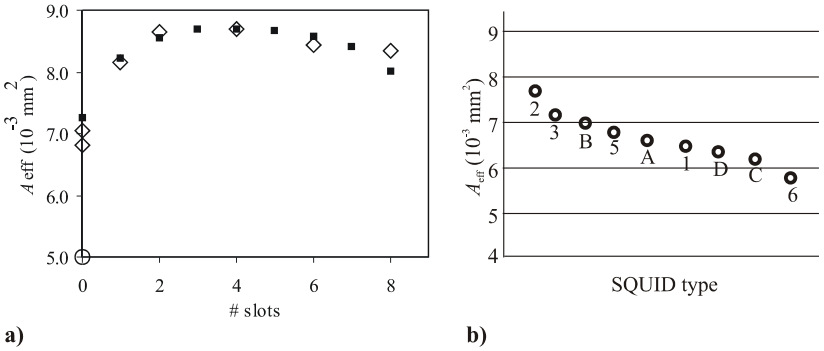

Figure 5.4- *a) Effective area for HTS slotted SQUIDs at 77.4 K. (■) experimental results, (◇) results from the model; b) Measured A_{eff} for the different "exotic" geometries proposed in Ref. 33.*

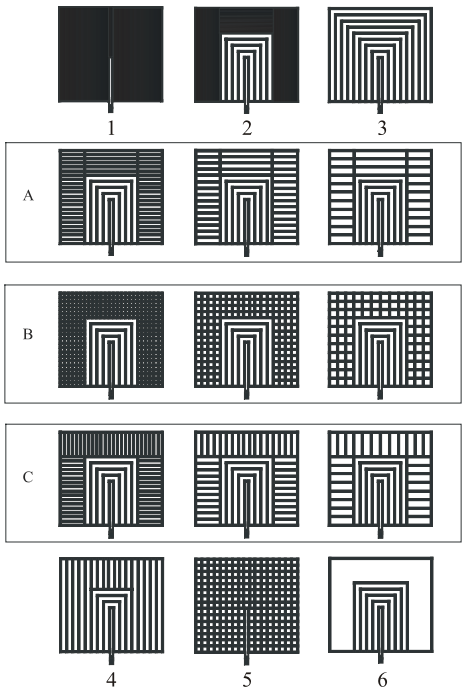

Figure 5.5- *Washer geometries studied for the "HTS slotted SQUIDs" (from Ref. 33). The SQUIDs were grain-boundary junction based YBCO SQUIDs. The width of the slots was 8 μm and the strip lines were w=4 μm for which the predicted threshold field was 100 μT.*

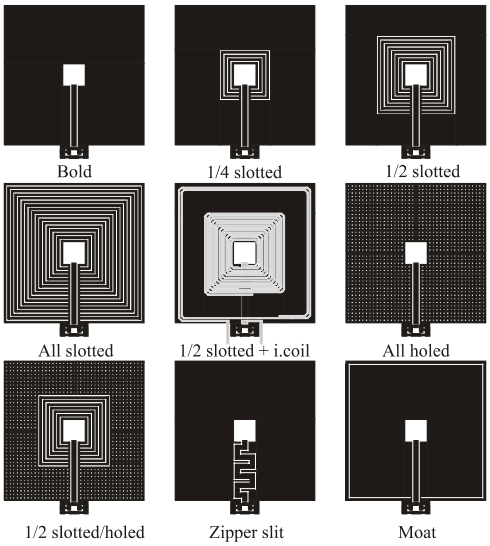

Figure 5.6- *Schematics of the 9 SQUID washer designs investigated.*

The threshold field is larger for the SQUIDs with smaller size of the widest superconducting strip contained in the washer. The expected B_T values for the slotted SQUIDs are given in Figure 5.7b.

We designed also a SQUID with a washer ***moat***, which should prevent the entrance of vortices. It has been shown that the threshold field for complete vortex shielding strongly depends on the configuration, size and gap of the moat. Long, continuous moats seem more effective than broken moats[35]. We patterned a continuous 4 μm width moat at 8 μm from

Washer-structured SQUIDs

	Bold	*Slotted*
D=77 μm	β=1.2	w=4 μm
A=4x4 μm^2	β_c=0.04	slots, holes=8 μm
$2I_0$=12.8 μA	Γ=0.005	
C_j=0.48 pF	L_{sq}=188.8 pH	
R_{sh}=2 Ω	L_i=78.6 nH	
R_d=2 Ω	M_i=3.56 nH	
	$dV/d\Phi$=24 μV/Φ_0	
	$S_\Phi^{1/2}$=1.5 μΦ_0/ Hz$^{1/2}$	

a)

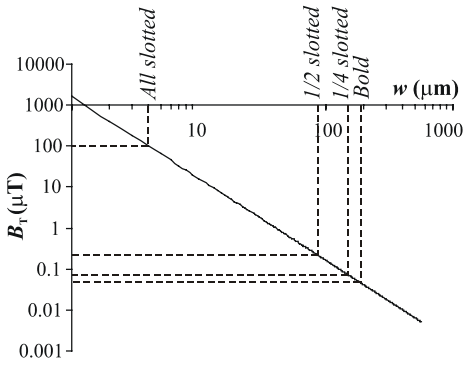

b)

Figure 5.7- *a) Main parameters for the reference (bold) and washer structured SQUIDs; b) Threshold field as a function of the superconducting strip width w; the expected B_T values for the slotted SQUIDs are indicated.*

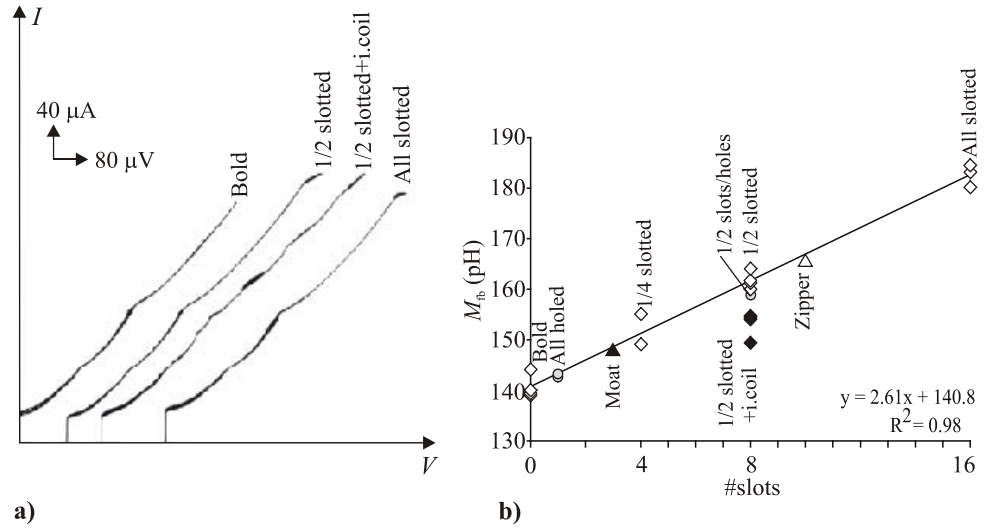

Figure 5.8- *a) IVC's of the slotted SQUIDs (shifted in the V-axis for clarity); b) Feedback mutual inductance M_{fb} for the different geometries tested. The linear fit is based on the slotted washers; the other SQUIDs are positioned in the x-axis according to the "number of slots" to which the area of the structures is equivalent.*

the edge of the washer. Finally, we included a SQUID with a ***zipper***-like slit to favorise the strong pinning of vortices at the rough edge of the slit. This series was mainly aimed to study the reduction of 1/*f* noise using structured washers, reason why most of the SQUIDs were uncoupled. The flux was applied via a 1-turn feedback coil surrounding the washer. A 23-turn ***input coil***, covering the whole washer, was only implemented for the ½ slotted SQUID.

5.2.3. Measurements

5.2.3.1. Fabrication and characterization; coupling

The "LTS slotted SQUIDs" were fabricated in our standard Nb/Al process. Particularly difficult was the lift-off photoresist after the deposition of the trilayer for the washers containing small holes, while the lift-off of the slots was much easier. Owing to a sudden change in the oxidation conditions in the load-lock chamber, the critical current density was much higher (125 A/cm^2) than expected (40 A/cm^2). The measured *I*-*V* and *V*-Φ characteristics of the nine SQUIDs were very similar. The critical current was I_0~20 μA and the shunt resistor R_{sh}~2 Ω. The IVC's showed some resonances, which were independent of the washer structures (Figure 5.8a); additional resonances are naturally observed for the ½ slotted SQUID with an input coil. The SQUIDs have growing M_{fb} according to the total area of the structures, taking into account that the slots and holes closest to the central hole

contribute more than those far away (Figure 5.8b). The smallest M_{fb} corresponded thus to the Bold SQUID (143 pH) and the largest to the All slotted SQUID (180 pH). The ½ slotted SQUID with input coil had a M_{fb} smaller than that of the SQUID without it, due to the shielding effect of the coil on the SQUID washer inductance. Although the deposition of the input coil on top of the slotted area can potentially increase the risk of shorts between the input coil and the washer, the 80% of the devices tested functioned properly. The input coil mutual inductance was M_i=3.6 nH, approximately the same that could be expected for a bold SQUID with input coil. Therefore, the presence of the slots is not detrimental for the coupling of flux to the SQUID.

5.2.3.2. Noise measurements

Noise measurements down to 0.2 Hz were performed with the SQUIDs shielded by a Nb can and a room temperature μ-metal can, and read out with "Oxford Instruments" electronics. A conventional bias reversal scheme at f_a=2 kHz was used to get rid of the 1/*f* noise owing to ΔI_0 fluctuations (Figure 5.9a). Each SQUID was cooled down at least 5 times. In each thermal-cycling, the local field might be different, and thus the probability of flux entry vary a little. Noise results are summarized in Figure 5.10.

The white noise level ~7.5 $\mu\Phi_0/Hz^{1/2}$ is dominated by the electronics, since the transfer function of the SQUIDs was only ~39 $\mu V/\Phi_0$ (<60 $\mu V/\Phi_0$), and the corner frequency is at ~4 Hz. Despite the shielding, the flux-hopping 1/*f* noise is large, as can be concluded from the large variations of the noise at 0.2 Hz for different cool-downs. The strip-width is such (184 μm), that vortices will penetrate even if the local field is as small as 0.05 μT.

A reduction of the low-frequency noise is measured as the number of slots increases. The improvement when the solid inner half of the washer was replaced by slots is larger than when also the outermost half of the washer was slotted, because moving vortices couple more noise the closer they are with respect to the central hole. The typical, average

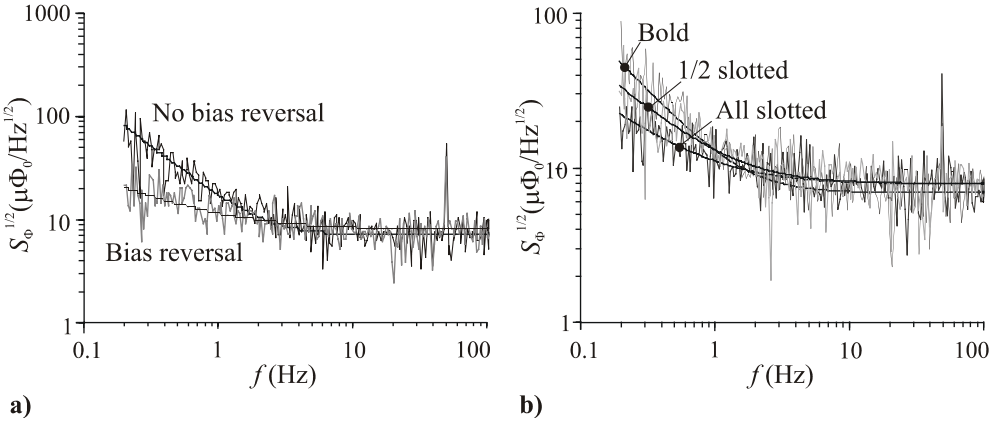

Figure 5.9- *Noise spectra a) All slotted SQUID with and without bias reversal scheme applied; b) typical flux spectra for the Bold, ½ slotted and All slotted SQUIDs.*

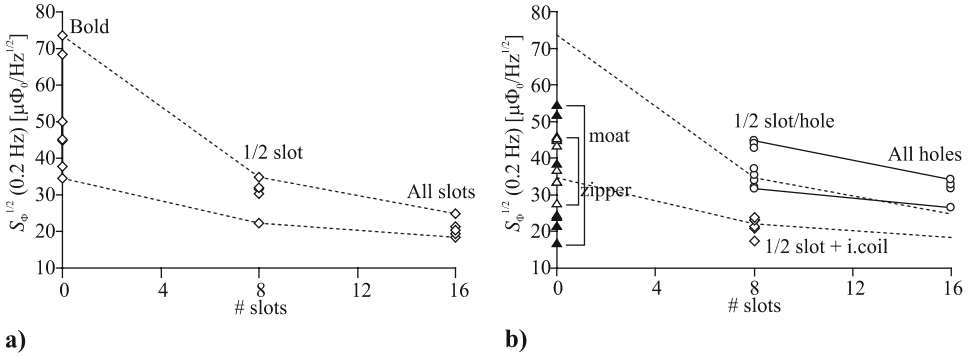

Figure 5.10- *Flux noise measured at 0.2 Hz for several cool-downs, a) for the Bold and Slotted SQUIDs (the dashed lines are only guides for the eye); b) for the other structured SQUIDs (the results for the Slotted geometries (dashed lines) are also shown for comparison).*

noise spectra for the Bold, ½ slotted and al slotted SQUIDs are compared in Figure 5.9b. The noise of the ½ slotted SQUID with input coil is even smaller than that of the SQUID without it. Since the width of the Nb input coil wiring is w=4 μm, vortices are not trapped in the coil. But even more, the input coil partially shields the washer thus reducing the area where vortices might enter. The holed SQUIDs seem less effective than the slotted ones in expelling vortices, a result also found in Ref. 15. The completely holed SQUID is less noisy than the ½ slotted/holed one. The SQUID with a moat had an average noise ~36 $\mu\Phi_0/\mathrm{Hz}^{1/2}$ (at 0.2 Hz) smaller than the Bold SQUID, but the spread was comparable. The "zipper-slit" SQUID showed a smaller average noise (~37 $\mu\Phi_0/\mathrm{Hz}^{1/2}$ at 0.2 Hz) and spread than the Bold one, probably thanks to the combined effect of having a smaller trapping area and the pinning of vortices at the slit. However the method is less effective than the slots in reducing the average flicker noise.

In conclusion, we have shown that structured patterned in LTS washer SQUIDs can help to reduce the 1/*f* noise due to flux hopping. The slotted structures were the most efficient method from the different techniques studied. The low-frequency noise measured down to 0.2 Hz could be reduced by a factor of 2 in average.

5.3. 1/*f* noise reduction by modulation at flux transformer

The techniques described in section 5.1 attempted to reduce the 1/*f* noise by directly attacking the different sources of flicker noise in the SQUID. An alternative approach is to shift the SQUID operation point from the low-frequency region to the white, low-noise region, by modulating the input signal applied to the SQUID at the flux transformer. This technique can thus *eliminate* completely the 1/*f* noise, regardless of its source, by *avoiding* the problematic region at all. In this section, the application of this modulation technique to the reduction of low-frequency noise in a CCC-SQUID system is examined.

5.3.1. Modulation at the flux transformer technique

The technique, proposed by Anderson *et al.*[36], consists in modulating the input signal entering the SQUID at a high frequency, larger than the SQUID 1/*f* knee, so that the SQUID can operate at the white-noise region. The modulated signal is then demodulated and low pass filtered to recover the original signal.

Two different methods have been proposed to modulate the input signal.
- The first utilizes *direct switching of the SQUID input circuit*[36]. A superconducting, double-pole, double-throw switching network is placed between the pick-up coil and the SQUID input coil (Figure 5.11a). The chopping is done by heating locally sections of the superconducting lines with the help of laser-driven switches (Figure 5.11c). This method has the advantage of producing full signal amplitude modulation, and thus the best possible signal-to-noise ratio. An important drawback is that, since the flux transformer is interrupted, a random integer of flux quanta can enter the circuit during each switching event.

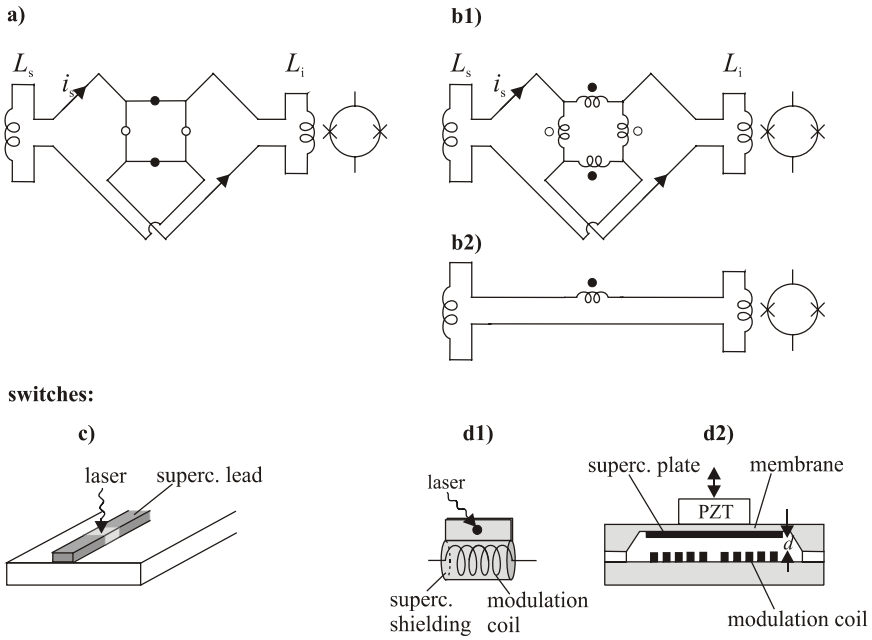

Figure 5.11- *Modulation of the signal at the flux transformer. Left: direct input circuit switching (a), using a laser-driven switch (c); Right: modulated inductance switching, through a switching network (b1) or with a single modulation-switch placed at one of the SQUID input leads (b2) network. The modulation-switch can be laser-driven (d1) or mechanically driven (d2). In the later case, the inductance L_m is a function of the distance d between the modulation coil and the superconducting plate. Similar devices processed with "micromechanics" are currently used in integrated optics*[1].

- The second method consists in *varying indirectly the inductance* of a part of the flux transformer[37]. The modulation can be done with a single inductive-switch placed in one of the SQUID input leads (Figure 5.11, b2), in which case an asymmetrical signal is obtained, or with a switching network (Figure 5.11, b1), to get a symmetrical modulated signal. The main advantage of this method is that the flux transformer is not interrupted, and the probability of flux entering is much smaller than in the first method. A disadvantage is the unavoidable loss of signal-to-noise resulting from the non-full modulation.

The switches used to implement the inductance modulation technique should fulfill a number of requirements: The physical geometry of the switch should be designed to minimize the pick-up of stray magnetic signals. A large modulation depth should be attained. The speed of the switching mechanism should be large enough to guarantee that the modulation frequency exceeds the SQUID corner frequency. The modulation frequency should be given by a sharp, unique frequency to facilitate demodulation. And finally, since the new noise possibly introduced by the switch will not be removed, the low-frequency noise of the switch should be smaller than the SQUID low-frequency noise that has to be avoided.

Laser-driven switches, consisting of a solenoidal coil surrounded by a tightly coupled superconducting cylinder, have been reported[37]. By driving the cylinder normal, its shielding properties and thus the inductance of the solenoid are varied (Figure 5.11, d1). These switches have very low thermal noise. Besides, the modulation frequency is only limited by the speed of the normal/superconducting switch, which can be better than 6 ns for Nb based switches. In practice, these switches are cumbersome to realize on a cryostat. A more convenient on-chip implementation was proposed in Ref. 38,39, but never realized. The switch would consist of a Nb planar coil covered by three concentric PbInAu washers, that could be illuminated by optical fiber.

Alternatively, a mechanical-driven switch[40] could be implemented by oscillating a superconducting plate face-to-face to a pancake-like coil modulation coil. (A similar principle has been applied to detect tiny vibrations in gravitational wave antennae[41]). The superconducting plate could be fixed to a silicon membrane or diaphragm, mechanically driven by a piezoelectric (PZT) element (Figure 5.11, d2). The change in the modulation coil inductance ΔL_m would be linearly dependent on the distance variation Δd between the N-turn coil and the superconducting plate as: $\Delta L_m = \pi \mu_0 N^2 \Delta d$, provided that the diameter of the coil is $R_c >> d$.[42] Commercial PZT translators can produce length displacements of the order of 5-200 μm at room temperature (a 20-30 % reduction can be expected at 4.2 K)[43]. The main difficulty of this design would be to drive the superconducting plate close enough to the coil to reach a large attenuation of L_m, while avoiding the sticking of the two surfaces.

5.3.2. CCC-SQUID with modulation at the flux transformer.

We shall analyze here the possibility of applying the signal-modulation technique to a CCC-SQUID current bridge. Consider a configuration in which the CCC is directly coupled to the SQUID input coil (Figure 5.12). The primary, quantized current $I_1 \equiv I_{SET}$ feeds the large N_1 primary winding, while the secondary current I_2 feeds the single-turn winding N_2.

I_2 is automatically adjusted, so that in the balanced situation, $I_2= N_1 I_1/N_2$. In the schematic, I_e has been modeled by a current source controlled by N_1 and N_2. I_e is split into a current I_{CCC} running on the CCC surface, and a current I_i injected into the flux transformer: $I_e= I_{CCC}+I_i$. The modulation should be applied on the input current I_i at this level. It is important to note that from the two modulation-methods described in section 5.3.1, only the inductance-modulation technique could be applied, since the interruption of the flux transformer would introduce an unacceptable error in the balance current signal to be measured.

Assume, for simplicity, that the modulation is applied by varying the inductance L_{mod} of a coil placed at one of the SQUID input leads. The signal flux coupled to the SQUID is given by: $\Phi_{sig}=I_i M_i$, where $M_i=k_{sq}(L_i L_{sq})^{1/2}$ is the mutual inductance between the SQUID inductance and the input coil. In FLL operation, Φ_{sig} is exactly compensated by a feedback flux $\Phi_{fb}=-I_{fb}M_{fb}$, where $M_{fb}=k_{fb}(L_{sq}L_{fb})^{1/2}$ is the feedback mutual inductance. The feedback coil couples back also some flux into the flux transformer, $\Phi_{fT}=I_{fb}M_{fT}$, with $M_{fT}=k_{fT}(L_{fb}L_i)^{1/2}$ the cross-talk inductance between the SQUID input and feedback coils.
The flux conservation condition in the flux transformer requires:

$$I_i (L_m + L_i) - I_{CCC} L_{CCC,eff} - M_{fT} I_{fb} = 0. \tag{5.8}$$

From the above expression it follows that the modulated input current can be expressed as:

$$I_{i,\mathrm{mod}} = \frac{AI_e}{B + M_{fb} L_{\mathrm{mod}}}, \tag{5.9}$$

where $A=M_{fb}L_{CCC,eff}$, and $B=M_{fb}(L_i+L_{CCC,eff})-M_i M_{fT}$. If the modulation coil was not implemented ($L_m=0$), the input current would take the form:

$$I_{i,no-\mathrm{mod}} = \frac{AI_e}{B} \equiv \Delta_{no-\mathrm{mod}} I_e, \tag{5.10}$$

Assume that the modulation coil inductance L_m is varied with a modulation frequency $f_m=\omega_m/2\pi$, larger than the SQUID corner frequency f_c according to:

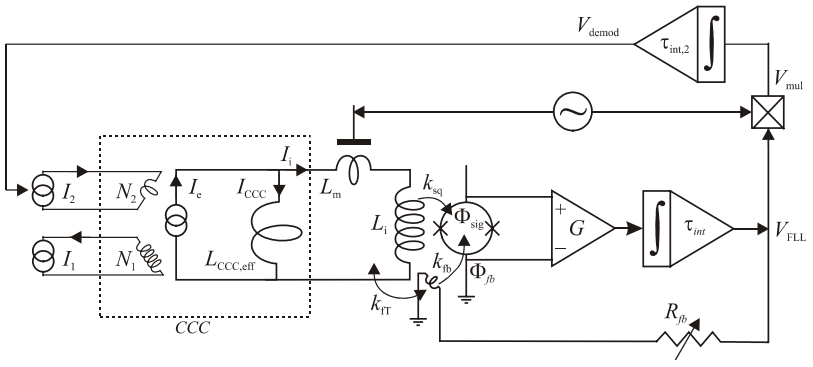

Figure 5.12- *Schematics of the CCC-SQUID I-bridge using the signal-modulation technique.*

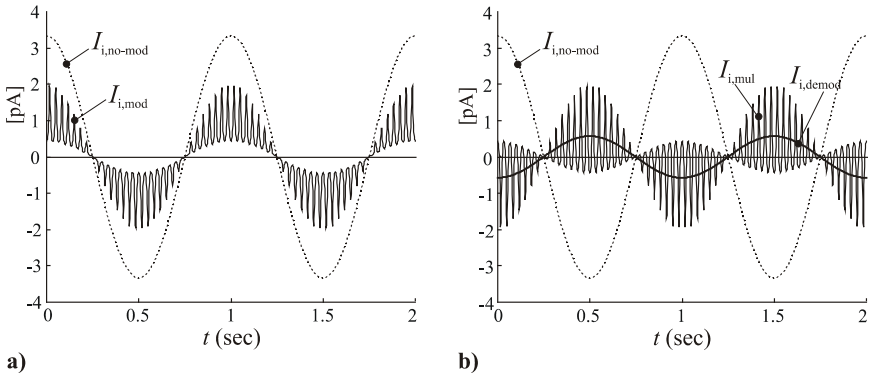

Figure 5.13- *a) Non-modulated $I_{i,no\text{-}mod}$, and modulated $I_{i,mod}$, input current as a function of time; b) Multiplied $I_{i,mul}$, and demodulated input current (RMS value) $I_{i,demod}$, as a function of time ($I_{i,no\text{-}mod}$ is also given for comparison).*

$$L_m = L_{m,mean} + \Delta L_m \cdot \cos(\omega_m t), \tag{5.11}$$

with:

$$L_{m,mean} = \frac{(1+\gamma)L_{m,H}}{2}, \qquad \Delta L_m = \frac{(1-\gamma)L_{m,H}}{2}. \tag{5.12}$$

γ is the modulation depth, defined as the ration between the higher and the lower value attained by the modulation coil: $\gamma = L_{m,H}/L_{m,L}$. The modulated input current can then be written as:

$$I_{i,\mathrm{mod}} = \frac{AI_e}{B'}\left[\frac{1}{1+M\cos(\omega_m t)}\right], \tag{5.13}$$

where $B' = B + M_{fb}L_{m,mean}$ and $M = M_{fb}\Delta L_m/B'$.
The V_{FLL} signal coming out from the SQUID readout, which is proportional to $I_{i,mod}$, will be demodulated with the help of a lock-in amplifier, referenced to the modulation frequency f_m. Thus the lock-in will only detect the Fourier component of Eq. 5.13 containing this frequency:

$$I_{i,\mathrm{mod}} = \frac{AI_e}{B'} D\cos(\omega_m t), \qquad \mathrm{D} \equiv \left[\frac{2\left(-1+\sqrt{1-M^2}\right)}{M\sqrt{1-M^2}}\right]. \tag{5.14}$$

At the lock-in detector, $I_{i,mod}$ is multiplied by the reference signal $\sim\cos(\omega_m t)$, and divided by $\sqrt{2}$ to obtain the Root Mean Square (RMS) value of the signal:

$$I_{i,mul} = \frac{AI_e}{\sqrt{2}B'} D\cos^2(\omega_m t) = \frac{AI_e}{\sqrt{2}B'} D\left(\frac{1}{2} + \frac{\cos(2\omega_m t)}{2}\right). \tag{5.15}$$

The dc component of $I_{i,mul}$ is obtained by using a first order low pass filter (6 dB/oct) with a time constant τ, which should fulfill $1/2\pi\omega_d >> \tau > 1/2\ \pi\omega_m$, where ω_d is reversal frequency of the balance current I_e. The final demodulated signal will be:

$$I_{i,de\,\mathrm{mod}} = \frac{AI_e}{\sqrt{2}B'} D \equiv \Delta_{de\,\mathrm{mod}} I_e . \tag{5.16}$$

To have an idea about the shapes and amplitudes of the different signals, a practical example was simulated. We assumed that the balance current was a signal $I_e=I_{e0}.\cos(2\pi f_s t)$, with a small $2I_{e0}$=10 pA amplitude, and low frequency f_s=1 Hz. The modulation frequency was taken f_m=30 Hz. (Though in a real case f_m should be larger to guarantee that $f_m > f_c$, 30 Hz was a convenient value to visualize the modulated curves). Realistic values for the inductances and coupling constants were taken: L_{sq}=200 pH, L_{fb}=200 pH, $L_{CCC,eff}$=80 nH and L_i=80 nH; k_i=0.8, k_{fb}=0.8, k_{fI}=0.5. We took for the high value of the modulation coil $L_{m,H}=5(L_i+L_{CCC,eff})$, and for the modulation depth γ=0.1.

The input current in the not-modulated case $I_{i,no\text{-}mod}$, calculated with Eq. 5.10, is shown in Figure 5.13a. Only a fraction A/B=0.7 of I_e will run through the SQUID input coil. The input current in the modulated case $I_{i,mod}$, calculated with Eq. 5.14 is shown on the same figure for comparison. The atypical shape of this curve, compared to the standard Amplitude Modulation picture, owes to the fact that the modulation term appears as a summand in the denominator of Eq. 5.9. The multiplied signal $I_{i,mul}$, as given by Eq.5. 15 and the demodulated signal $I_{i,demod}$, (Eq.5.16) are shown in Figure 5.13b. The demodulation introduces a phase shift of π.

The largest drawback of applying modulation is the reduction in signal amplitude, which can be seen from the comparison of $I_{i,no\text{-}mod}$ and $I_{i,demod}$. The loss in signal is given by:

$$\eta = \left| \frac{\Delta_{de\,\mathrm{mod}} \cdot \sqrt{2}}{\Delta_{not-\mathrm{mod}}} \right|. \tag{5.17}$$

The figure of merit η has been represented as a function of the high modulation inductance

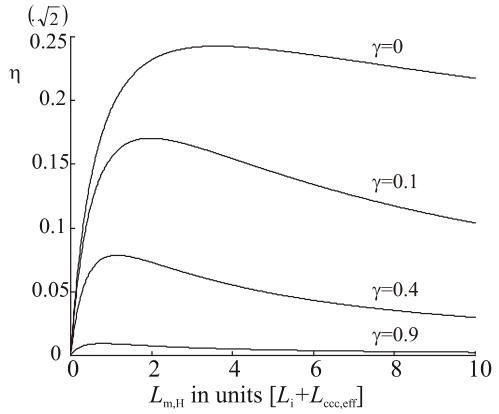

Figure 5.14- *Figure of merit η as function of $L_{m,H}$ and the modulation depth γ.*

$L_{m,H}$, and the modulation depth γ (Figure 5.14). It can be observed that the reduction of signal is larger for modulation depth ratios $\gamma=L_{m,H}/L_{m,L}\rightarrow 0$. η reaches a maximum for a certain value of $L_{m,H}$, which is different for every modulation depth γ. The decrease of η for large values of $L_{m,H}$ is due to the fact that in the Fourier development of $I_{i,mod}$, the higher harmonic components become more important, while the 1st harmonic component, which is the only one seen by the lock-in, decreases.
In general, the modulation-at-flux-transformer method will be advantageous if the reduction of noise is larger than the loss of signal, or in other words, if:

$$\frac{\int_{BW} \text{noise at the modulation frequency, } f_m}{\int_{BW} \text{noise at the frequency } f_s \text{ of } I_e} < \eta. \tag{5.18}$$

5.3.3. Experimental verification of the signal-modulation technique

In this section, an experiment aimed to test the efficiency of the signal-modulation technique to reduce the 1/*f* noise will be described. The modulated input current signal $I_{i,mod}$ was artificially generated with the help of a function generator. With this approach, the implementation of the device needed to modulate L_m, whose design will depend on the noise reduction achieved in this experiment, can be left for a second stage. The generated modulated signal was applied (via a resistance network) to a low white-noise SQUID, forming part of a Two-Stage system, and the output signal was detected with a lock-in amplifier. The out-coming signals and noise spectra when modulation was applied or not were compared.

5.3.3.1. Experimental set-up

The schematics of the experimental set-up used to test the signal-modulation principle is shown in Figure 5.15. A function generator (Philips/Kluke PM 5139) was used to produce either a *non-modulated*, oscillating voltage signal: $V_{i,no\text{-}mod}=V_0.\cos(\omega_{sig}t)$, or a *modulated* signal: $V_{i,mod}=(V_0/2).\cos(\omega_{sig}t)[1\text{-}m.\cos(\omega_m t)]$, where V_0 is the selected amplitude, $f_s=\omega_s/2\pi$ the carrier frequency, $f_m=\omega_m/2\pi$ is the modulating frequency and m is the % of modulation. A resistance network was built up to convert the generated mV voltage signal to an input current $I_{i,mod}$ (respectively $I_{i,no\text{-}mod}$) of some pA, and filter it from interferences with frequencies higher than f_m. The voltage-to-current transfer of the network, when the insert was placed in the cold was $515\text{x}10^{-12}$ A/V (for frequencies f<200 Hz). The input current created a flux $\Phi_{sig,mod}=I_{i,mod}L_i$ (respectively $\Phi_{sig,no\text{-}mod}=I_{i,no\text{-}mod}L_i$), which was applied to an integrated Two-Stage SQUID[44]. This readout was chosen to ensure that the noise measured was given by the SQUID, and not limited by the preamplifier (see Chapter 4). The 1st stage SQUID had an inductance L_{sq}=200 pH and a measured input coil inductance of M_i=1.9 nH. The 2nd stage was a gradiometric 550 pH DROS with a reference junction. The DROS was biased at a current $I_{b,DROS}$=52 μA such that the DROS V-Φ curve had maximum transfer, and a large voltage amplitude (40 μV_{pp}). The SQUID was biased at a current $I_{b,1}$=120 μA for which a nice Two-Stage V-Φ curve was observable. The output of the Two-Stage was directly measured with a room temperature amplifier, with a voltage noise $S_{V,preamp}^{1/2}$=1.8

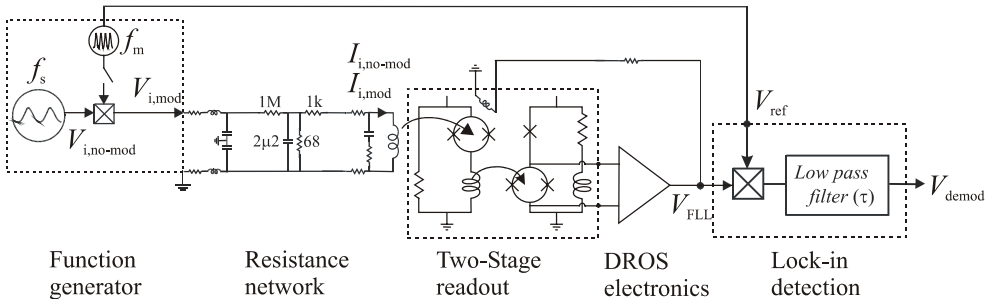

Figure 5.15- *Schematics of the experiment to test the signal-modulation technique to reduce 1/f noise.*

nV/Hz$^{1/2}$ (5 nV/Hz$^{1/2}$ at 1 Hz), and gain set to G=2000. The Two-Stage voltage-to-flux transfer in FLL was measured to be 7.5 V/Φ_0. The flux noise of the SQUID in Two-Stage (when no modulation was applied) was measured to be $S_{\Phi,TS}^{1/2}$=1.5 $\mu\Phi_0$/Hz$^{1/2}$, with a corner frequency f_c~10 Hz. We checked that the current noise of the function generator and the resistance network were negligible small compared to the input noise of the Two-Stage system: $S_{I,TS}^{1/2}$= $S_{\Phi,TS}^{1/2}/M_i$=1.6 pA/Hz$^{1/2}$.

The demodulation was performed with a Stanford SR830DSP lock-in amplifier. The output signal V_{FLL} was multiplied by the reference signal V_{ref}=cos($\omega_m t$), taken from the function generator. The result was low-pass filtered to extract the dc component of the demodulated signal. The filter time constant could be varied between τ=1 µs to 300 ks, and the roll off between 6-24 dB/oct. The demodulated output, $V_{i,demod}$ was displayed in RMS values (i.e., the amplitude of the first harmonic Fourier component was divided by √2):

$$V_{i,demod} = -m\frac{V_0}{\sqrt{2}}\cos(\omega_s t). \tag{5.19}$$

5.3.3.2. Measurements

Initially, the overall transfer between a non-modulated voltage generated by the function generator and the output voltage of the DROS in FLL was measured to check the system. We obtained a transfer: V_{FLL}/V_i=3.2.10^{-3} for frequencies between 16 to 200 Hz, decreasing to 3.0.10^{-3} for f=400 Hz. These values agreed very well with the calculated ones:

$$\frac{V_{FLL}}{V_i} = \frac{\partial V_{FLL}}{\partial \Phi_i}\frac{\partial \Phi_i}{\partial I_i}\frac{\partial I_i}{\partial V_i} \approx 3.5\cdot 10^{-3} \text{ (0 - 200 Hz); } 3.2\cdot 10^{-3} \text{ at 400 Hz.} \tag{5.20}$$

To test the principle of the signal-modulation technique, we applied a known input current signal $I_i(t)$=515 pA/V.$V_i(t)$, and compared the $V_{demod}(t)$ and $V_{FLL}(t)$ output signals when modulation was respectively applied or not to it. First, a non-modulated, triangular signal $V_s(t)$ with amplitude $2V_0$=2.0 V_{pp} (corresponding to a current $I_{i,no-mod}$=1.03 nA_{pp}) and frequency f_s=0.1 Hz was applied. The measured V_{FLL} signal had an amplitude of 6 mV_{pp}, as expected from Eq. 5.20, was noisy and affected by a drift (Figure 5.16, a1).

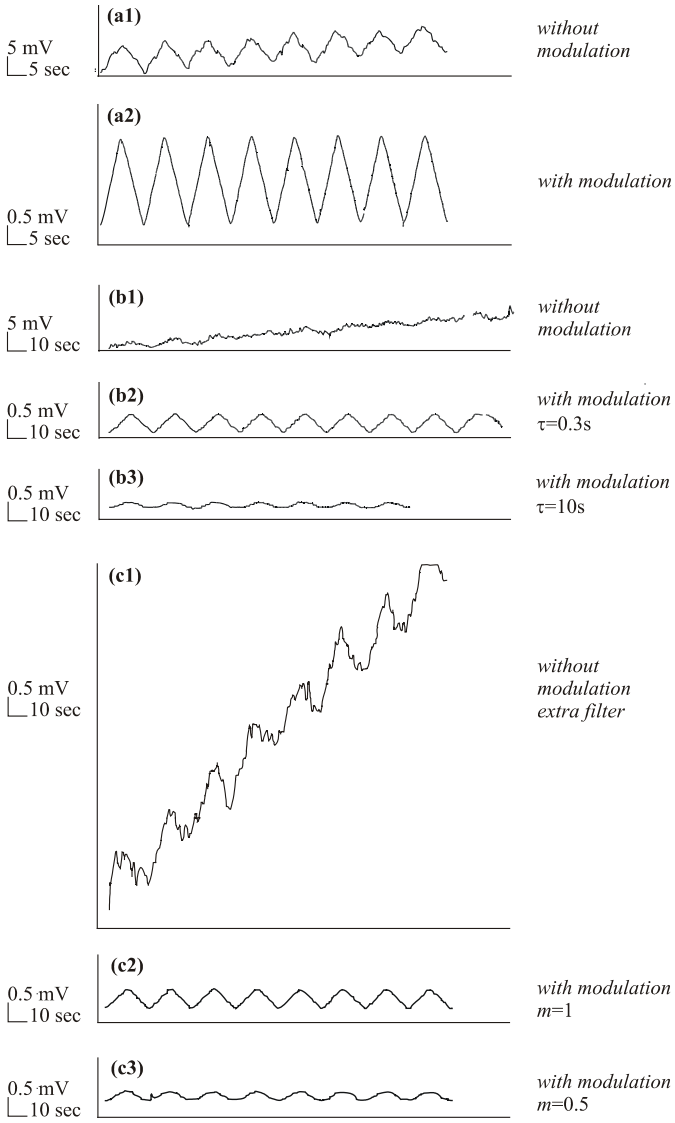

Figure 5.16- *a) Comparison between $V_{FLL}(t)$ and $V_{demod}(t)$ output signals, without and with using the modulation scheme. (a1) No-mod: V_s=2.0 V_{pp}, f_s=0.1 Hz, (a2) Mod: f_m =180 Hz, m=100%, τ=0.3 s; (b1) No-mod: smaller, lower frequency unmodulated signal (V_s=0.4 V_{pp}, f_s=0.05 Hz), (b2) Mod: f_m =180 Hz, m=100%, τ=0.3 s, (b3) same f_m and m(%), but τ=10 s; (c1) No-mod: V_s=0.4 V_{pp}, f_s=0.05 Hz and extra RC-filter (τ_{RC}=0.5s) added, (c2) Mod: f_m =180 Hz, τ=0.3 s, m=100%, (c3) same f_m and τ, but m=50%.*

Then, V_{sig} was modulated at frequency of f_m=180 Hz, with a modulation factor m=100%. The lock-in filter time constant was τ=300 ms (cut-off frequency 0.5 Hz) and the slope 6 dB/oct. As expected, a clean, 2.0 mV_{pp} triangular demodulated signal was recovered (Figure 5.16, a2). The reduction in amplitude when modulation was applied was V_{demod}/V_{FLL}=0.33, around the value that could be expected (m/2√2=0.35).

We checked then the efficiency of the technique when a much smaller signal of amplitude V_s=0.40 V_{pp} (I_i=0.2 nA_{pp}) and lower frequency f_s=0.05 Hz was applied. The V_{FLL} signal measured without modulation was almost indistinguishable from the noise (Figure 5.16, b1). On the contrary, when modulation at a frequency f_m=180 Hz was applied, the V_{demod} was perfectly measurable (Figure 5.16, b2). For time constant values between τ~300 ms-1s, the measured amplitude was V_{demod}=0.4 mV_{pp}, in good agreement with the expected value (0.5 mV_{pp}). For τ~10 s, the V_{demod} signal flattened and faded away (Figure 5.16, b3). This effect results when the filter time constant becomes larger than the time constant of the signal ($\tau_s=1/2\pi f_s$=3 s), so that the signal itself is filtered.

In order to make sure that the observed reduction owed to the modulation scheme and not just to the beneficiary effect of the lock-in filter, we placed also an extra RC filter (τ_{RC}=0.5 sec) at the output of V_{FLL}. When the same, 0.4 V_{pp}, f_c=0.05 Hz unmodulated signal was applied, the V_{FLL} signal could be better recovered than in the non-filtered case (compare, Figure 5.16, c1 with b1), however an important drift due to the filter was introduced. In contrast, when the signal was modulated with a frequency f_m=180 Hz and a modulation factor m=100%, a noise-free, non-drifting V_{demod} curve was obtained (Figure 5.16, c2). The lock-in constant was adjusted to be τ=0.3 s, approximately the same as the constant of the added extra filter τ_{RC}. The dependence of the recovered signal V_{demod} on the modulation factor m was also verified. An amplitude reduction by a factor of 2 was measured when the modulation factor was decreased to m=50 % (Figure 5.16, c3)

To show the effect of signal-modulation over a larger frequency range, the voltage noise spectra *with* and *without modulation* were recorded at respectively the V_{demod} output and the V_{FLL} output, when the Two-Stage was operated in FLL and no generated $V_s(t)$ signal was applied. In both cases, the voltage noise was calculated back to a flux noise at the

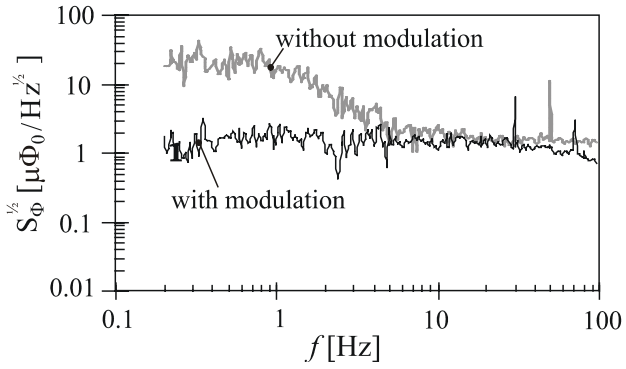

Figure 5.17- *Comparison of the noise spectra measured with and without applying modulation.*

SQUID level. In the non-modulated case, the white noise was ~1.5 $\mu\Phi_0/Hz^{1/2}$, and increased to ~12 $\mu\Phi_0/Hz^{1/2}$ at 0.2 Hz. In the modulated case, a modulation frequency of f_m=180 Hz was chosen, far above the corner frequency (f_c~10 Hz), and the lock-in filter set to τ=3 ms. From Figure 5.17, it can be seen that the low-frequency noise was reduced by more than an order of magnitude, and no 1/*f* noise is present down to the lowest frequency measured (0.2 Hz). From the previous experiments it can be concluded that the noise-reduction mechanism worked to frequencies as low as 0.05 Hz.

5.4. Conclusions

The operation of the CCC system at frequencies as low as $1\text{-}10^{-3}$ Hz shocks with the large amount of flicker noise of the SQUID at those low frequencies. The sources of 1/*f* noise and the different techniques available to reduce it, scattered through literature, have been reviewed. We investigated two different approaches to reduce the low-frequency noise in our system.

On one hand, we developed Nb/Al dc SQUIDs with different structured washers (including slots and/or holes, a moat and a zipper-slit) to study the reduction of 1/*f* noise owing to hopping of flux vortices trapped in the SQUID process during the cool-down process. We showed that slotted and holed washers could be applied to LTS devices as much as to HTS ones, since the underlying theoretical condition holds in both cases. A gradual reduction of the 1/*f* noise (on average from ~55 to 22 $\mu\Phi_0/Hz^{1/2}$ at 0.2 Hz) was measured for SQUIDs with increasing number of slots. Holes proved to be less effective than slots in reducing the flicker noise. The 1/*f* noise of the SQUIDs with a moat and zipper-slit was smaller than that of a bold SQUID, but the reduction of noise (a factor of 1.5) was on the average less significant than for the slotted SQUIDs.

On the other hand, we studied the application to the CCC-SQUID system of a signal modulation technique, which is able to get rid of all low-frequency noise, independent of its origin, by shifting the SQUID operation frequency to the white-noise, higher frequency region. In an experiment designed to test the reduction of noise that could be attained with this method we observed no 1/*f* noise down to frequencies ~0.05 Hz. The development of an inductance switch, preferably integrated on-chip, capable of producing the necessary modulation depth remains a challenging task for the future. Some optically-driven as well as mechanically-driven switches have already been proposed.

References

[1] A.H. Miklich *et al*., *Appl. Phys. Lett*. **60**, 1899 (1992).
[2] J.M. Lockhart, *Proc. of SPIE*, **619**, 148 (1986).
[3] C.T. Rogers and R.A. Buhrman, *Phys. Rev. Lett.* **53**, 1272 (1984).
[4] J. Clarke, SQUID fundamentals, in *SQUID Sensors: Fundamentals, Fabrication and Applications*, Eds. H. Weinstock, NATO ASI series, **329**, 13 (1995).
[5] B. Savo *et al*., *Appl. Phys. Lett*. **50**, 1757 (1987).
[6] R. H. Koch *et al.*, *J. Low Temp. Phys.* **51**(207), 207 (1983).

[7] O. Dossel *et al., IEEE Trans. Magn.* **27**(2), 2797 (1991).
[8] D. Drung, *Appl. Phys. Lett.* **67**(10), 1474 (1995).
[9] V. Foglietti *et al.*, *Appl. Phys. Lett.* **49**(20), 1393 (1986).
[10] M. Lam Chok Sing *et al*., *Rev. Sci. Instrum.* **67**, 796 (1996).
[11] C. D. Tesche *et al.* LT-17, BH2, 263 (1984).
[12] M. E. Huber and M. W. Cromar, *Physica B.* **165&166,** 77 (1997).
[13] J. E. Sauvageau *et al*., *IEEE Trans. Appl. Supercond.* **5**, 2303 (1995).
[14] E. Dantsker *et al.*, *Appl. Phys. Lett.* **69**(26), 4099 (1996).
[15] E. Dantsker *et al.*, *Appl. Phys. Lett.* **70**(15), 2037 (1997).
[16] J.R. Clem, *Effects of trapped vortices in SQUIDs*, presented at the University of Twente, June 1997 and *private communication*.
[17] A.H. Miklich *et al*., *App. Phys. Lett*. **64**(25), 3494 (1994).
[18] A. B. M. Jansman *et al*., *Physica C.* **322**, 137 (1999).
[19] R. H. Koch *et al*., *Appl. Phys. Lett.* **67**(5), 709 (1995).
[20] S. Bermon and T. Gheewala, *IEEE Trans. Magn.* **MAG-19**, 1160 (1983).
[21] M. Jeffrey et al., *Appl. Phys. Lett.* **67**(12), 1769 (1995).
[22] P. Selders *et al.*, *Appl. Supercond.* **5**, 269 (1998).
[23] P. Selders *et al., IEEE Trans. Appl. Superc.* **9**(2), 2967 (1999).
[24] T. J. Shaw *et al.*, *Phys. Rev. B.* **54**(21), 15411 (1996).
[25] S. Schöne *et al.*, *Appl. Phys. Lett.* **68**(6), 859 (1995).
[26] S. Schöne *et al.*, *Rev. Sci. Instrum*. **68** (1), 85 (1997).
[27] M. Mück *et al.*, *IEEE Trans. Appl. Superc*. **7**(2), 3263 (1997).
[28] J. Gail *et al.*, *Appl. Phys. Lett.* **73**(18), 2663 (1998).
[29] M. Huber *et al*., *IEEE Trans. Appl. Supercond*. **7**, 2882 (1997).
[30] E. Bartolomé *et al*., *in press in Physica C* (2001).
[31] M. Tinkham, *Introduction to superconductivity*, McGraw-Hill International Editions, New York, 2nd edition (1996).
[32] J.R. Clem, *Phys. Rev. B.* **43**(10), 7837 (1991).
[33] A. B. M. Jansman, PhD Thesis, Univeristy of Twente (1999).
[34] A. B. M. Jansman *et al*., *Appl. Phys. Lett*. **72**, 3515 (1998).
[35] K. Suzuki *et al*., *IEEE Trans. Appl. Superc.* **11**, 238 (2001).
[36] J.T. Anderson *et al*., *Rev. Sci. Instrum.* **60**(2), 202 (1989).
[37] J.T. Anderson *et al*., *Rev. Sci. Instrum*. **60**(2), 209 (1989).
[38] C.E. Cunningham *et al*., *Appl. Phys. Lett.* **63**(8), 1152 (1993).
[39] G.S. Park *et al*., *IEEE Trans. Appl. Superc*. **5**(2), 3214 (1995).
[40] E. Hoenig, *SQUID magnetometer including a flux-gate chopper using a mechanically vibrating mirror*, US patent number: 4804915, (1988).
[41] D.G. Blair, in *Detection of gravitational wave antennas*, Ed. D.G. Blair, Cambridge Univ. Press (1991).
[42] A.T.A.M. de Waele, *Detector-coil aspects of transducers*, University of Eindhoven, Dept. of Physics (1998).
[43] http://www.physikinstrumente.com
[44] M. Podt *et al*., *Appl. Phys. Lett.* **75**, 15 (1999).

Chapter 6

CCC-SQUID SYSTEM INTEGRATION

The integration of a complete CCC-SQUID system, towards the realization of a SET based current standard is the subject of this chapter. The operation of such a system can be hindered by several practical trouble sources acting simultaneously, among others: the non-perfect coupling between the CCC and the SQUID; vibrations and instability problems arising from the large CCC radius; resonances caused by the many primary turns etc…For test purposes, a large ratio, 1:1 CCC with a home-made, directly-coupled SQUID readout was initially built up (section 6.1). This system allowed studying the CCC-SQUID direct coupling configuration, and problems arising from the CCC size, without having to deal with the additional problems arising from having many primary turns. The knowledge acquired was applied in the realization of an ultra-sensitive, moderate-sized, large gain (1:30000) CCC with directly-coupled SQUID readout. The system and the experiments realized are described in section 6.2.

6.1. Test 1:1, large CCC

Before undertaking the integration of the final large-ratio CCC, a test 1:1, large diameter CCC with direct coupling to one of the matched SQUIDs described in Chapter 3 was fabricated. The system helped studying several aspects needed for the experimental implementation of the direct-coupling configuration (e.g., the determination of the CCC effective inductance to which the SQUID should be matched, the realization of superconducting bonds between the SQUID and its module, and the very low inductance wires required to connect the CCC to the SQUID). The sensitivity reached could be thus experimentally compared to the theory. The system allowed also investigating the CCC shielding, and the sources of noise appearing in a large diameter CCC.

6.1.1. Description of the system

The schematics and dimensions of the 1:1 CCC[1,2] are shown in Figure 6.1. The overlapped tube, with an outer diameter of 168 mm, was made of 0.5 mm thick, 99.95 % magnetically pure lead. The length of the overlap was half a turn, for which the ratio error would theoretically be (Eq. 1.4) ~10^{-19}. The CCC tube locates two single turn windings, made of 80 μm diameter copper cladded superconductor surrounded by a thin insulation of 140 μm thickness. The CCC was fixed to a perpex plate covered by a Pb foil. This plate could move up and down (like an embolus) inside a cylindrical perpex piece, covered with Pb foil to shield the CCC. In this way, the value of the effective CCC self-inductance $L_{CCC,eff}$ could be varied by changing the distance h from the CCC to the to the bottom of the shield. The dependence of $L_{CCC,eff}(h)$ was both numerically calculated and measured[3], as explained in Figure 6.2.
To prevent mechanical vibrations, the CCC was clamped with additional perpex pieces. The lateral and bottom parts of the shielding were soldered with Sn-Pb, a fact that will have important consequences (section 6.1.3). The shielded CCC was fixed at the cold side of a simple insert, consisting of a brass tube terminated by the SQUID "Oxford" module. The SQUID was shielded with a lead open cylinder instead of the standard "Oxford" can, to facilitate the connection between the lead foil and the module Nb blocks. The CCC should be connected to the SQUID by negligible low inductance wires, to achieve maximal transfer in the flux transformer. We used 10 cm of a low self-inductance (1 nH/m) folded thin lead foil construction[2] for the connection. The lead foil was soldered at the CCC end, and screwed to the Nb blocks on the SQUID module. The superconducting connection between the SQUID chip and the Nb blocks is detailed in section 6.1.2. Galvanic connections were made to the flux transformer, close to the CCC side and at the SQUID

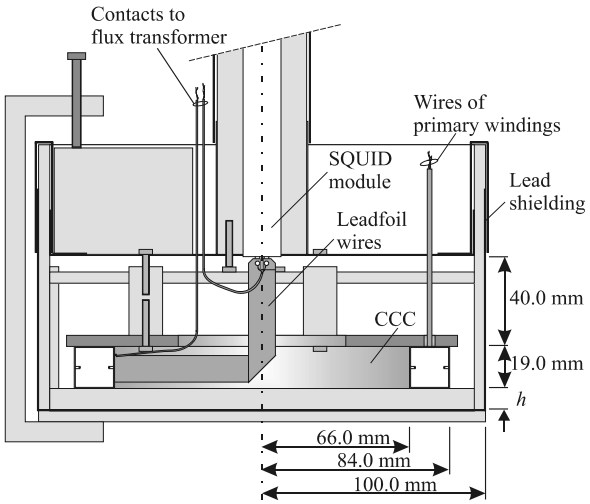

Figure 6.1- *Cross section schematics of the 1:1, large CCC.*

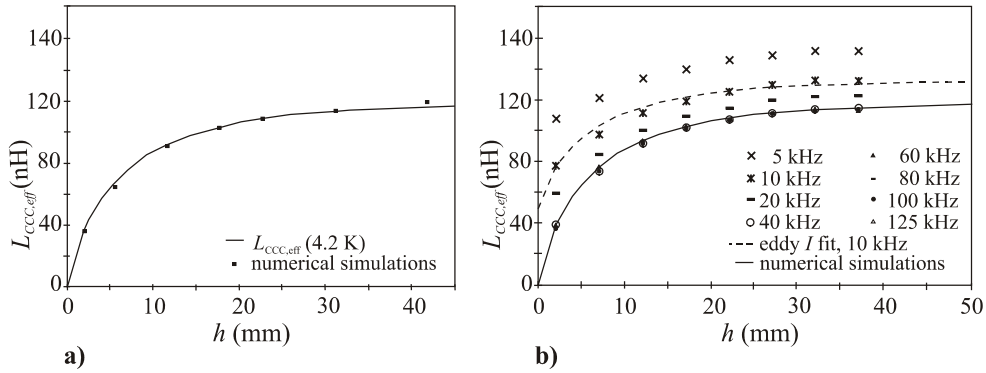

Figure 6.2- *Effective CCC inductance $L_{CCC,eff}$ as function of the distance from the CCC to the bottom of the shielding h. a) $L_{CCC,eff}(h)$ was measured at 4.2 K; when the CCC is sufficiently far away from the shielding, $L_{CCC,eff}$ tends to the limit value ~115 nH. $L_{CCC,eff}(h)$ was also numerically calculated using a finite element software; the simulation coincides with the experimental values[3]. b) $L_{CCC,eff}(h)$ was also measured at room temperature at different frequencies. Resistive screening eddy current appear in the lead surrounding the CCC. At large enough frequencies (>40 kHz), the screening due to eddy currents is almost perfect, and behaves as the screening superconducting current. Thus the $L_{CCC,eff}$ of the CCC coincides with that of the shielded CCC at 4.2 K. This method is very useful to determine the effect of the shields on the CCC inductance at room temperature.*

side, for the direct coupling verification experiment. The base of the CCC shield laid (on a cork disc) at the bottom of the cryostat, to avoid oscillations of the insert. At the warm side of the insert, 4 sets of BNC connectors (shunted by 2x22 kΩ resistors inside a well shielded Al box) allowed injecting currents to one of the 2 primary windings, or to the 2 lines connected to the "CCC side" or the "SQUID side" of the flux transformer (Figure 6.5).

6.1.2. Superconducting bonding

The superconducting connections between the SQUID input coil paths and the Nb blocks at the SQUID module were realized in two different ways.

a) Using a commercial, 47 μm superconducting "Tanaka" wire[4], ultrasonically (US) wedge bonded to the chip, and fixed under screws to the Nb blocks. To make the US superconducting bonding, the SQUID surface should be very clean, and preferably the chip should not be yet glued onto the module (otherwise most US energy is dissipated at the gluing GE varnish). The bonding conditions are very critical. For the wedge bonder used[5], the bonds succeeded using a 50 μm wedge, a weight of 30 gr, and settings of power ~8.8 and time ~8. Each wire is cut at around 1.5 cm from the bond. The SQUID is then glued on the module, and the normal Al bonds made. The Nb blocks have to be polished to remove the superficial oxide layer that could prevent a good superconducting connection. The wires

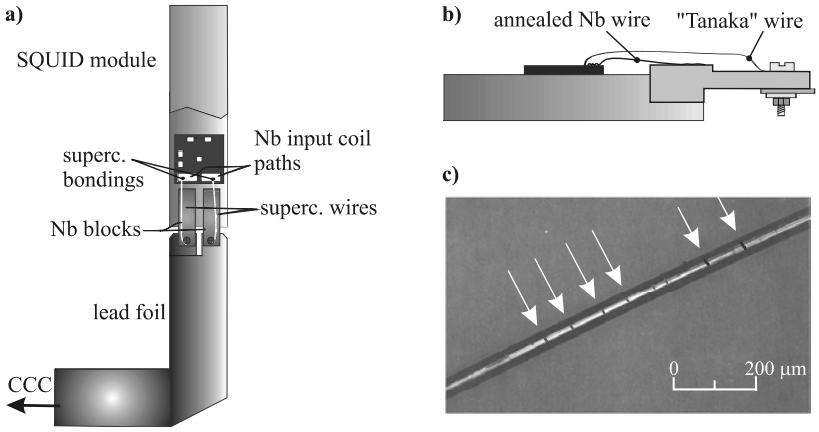

Figure 6.3- *a) Direct connection between the SQUID and the CCC; b) superconducting connections with the "Tanaka" and annealed Nb wires; c) microscope photograph of the crystalline aspect of the Nb wire after annealing (0.3 A, 5 min).*

are fixed under long screws to the Nb blocks. The lead foil, which has also to be also polished to remove the oxide layer, is fixed with a ring and a nut at the other side of the screw (Figure 6.3b). This method is not very convenient because the wires can easily break when dismounting the module.

b) Using annealed Nb, US wedge bonded to the chip and soldered by spot welding to the Nb blocks[6] (Figure 6.3b). The Nb wire has to be annealed to make it ductile enough for making the US bonds. The process[7] consists in heating the wire (~25 cm long) in a vacuum chamber just below its melting temperature, by passing a current of ~0.5 A for about 5 min.

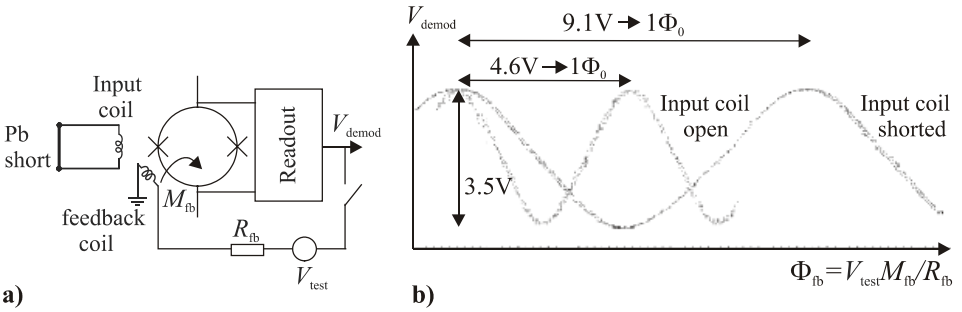

Figure 6.4- *Check of the superconducting bonds. a) The input coil is shorted fixing a lead strip between the two Nb blocks at the module. b) The demodulated voltage in open loop is measured as function of a test applied signal applied, $V=\Phi_{fb}R_{fb}/M_{fb}$. When the input coil is shorted and if all the connections were superconducting, a reduction in M_{fb} due to the shielding effect occurs, observed as a broadening of the V_{demod}-Φ_{fb} curve. (E.g., for the "CCC matched SQ#1", a factor of 2 reduction in the M_{fb} was measured).*

After annealing, the wire is brighter, softer and appears crystallized under the microscope (Figure 6.3c). Two different types of Nb wires purchased from "Goodfellow"[8] were used with good results: i) The 50 μm Nb wire was protected by a polymide insulation, which had to be removed with sand paper before the annealing; ii) The 25 μm non-insulated wire was annealed at a lower current (~175 mA) to avoid the wire melting. The superconducting Nb wires were first spot-welded to the Nb blocks. The welding conditions were not very critical, provided good electrical contact existed between the two parts to be soldered. Several spots on a row were made, to ensure a good connection. Then the wires were US bonded to the SQUID input coil paths. The Nb wire oxidizes quickly after annealing. By applying the maximum available weight (~90 gr) of the US welder, bonding was only successful within ½ hour after annealing. When we applied an external, extra force (estimated to be ~200 gr), the oxide layer could be broken through, and good, successive bonds could be made for large ranges of time-power bonding settings, during months. We tested that the quality of the bonds was not degraded after 10 thermal cycles between 77 K and room temperature.

In order to check if the connections were superconducting, we measured the reduction of the feedback mutual inductance, due to the shielding effect, when the SQUID input coil was shorted at the Nb blocks (Figure 6.4).

6.1.3. Experiments

The schematics of the experimental set up electronics is shown in Figure 6.5. A "CCC matched SQUID" (#14), with a measured input coil inductance L_i=55.7 nH and mutual inductance M_i =2.6 nH, was mounted on an "Oxford" module and directly connected to the CCC. The distance from the CCC tube to the shielding bottom was h=7 mm, for which the effective inductance was $L_{CCC,eff}$=76 nH. The SQUID was readout with "Oxford" electronics. The system operated in internal feedback mode, i.e., with the FLL output feeding back the SQUID, and not the primary turns (external mode).

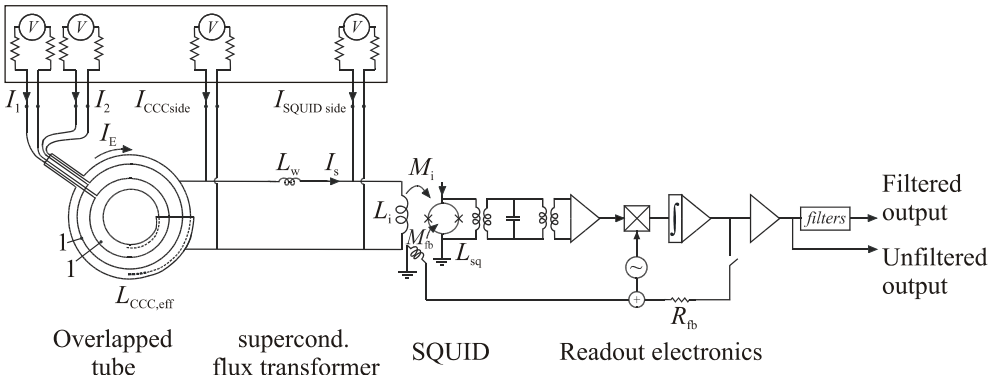

Figure 6.5- *Schematics of the set-up for the experiments with the test 1:1, large CCC.*

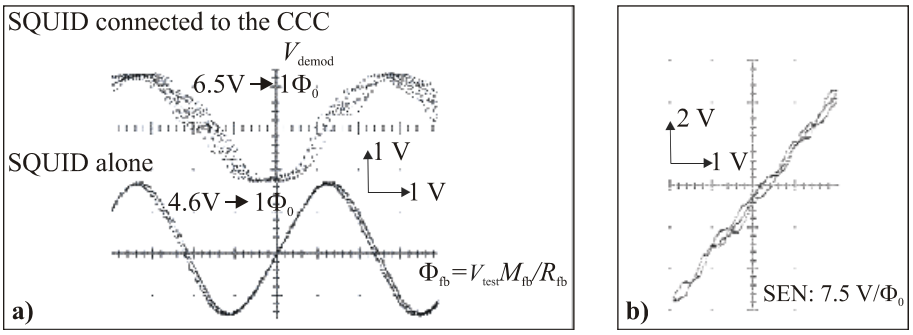

Figure 6.6- *Demodulated V-Φ characteristics. a) Open loop, characteristic of the SQUID alone, and connected to the CCC; b)Closed loop (CCC connected).*

The characteristics of the SQUID with the CCC connected were measured. The CCC connected to the SQUID input coil forms a superconducting circuit that shields the mutual inductance M_{fb} between the feedback coil and the SQUID. This results in a broadening of the demodulated V-Φ curve respect to the curve of the SQUID alone (Figure 6.6a). The $1\Phi_0$ period when the CCC is connected corresponds to 6.5 V, an intermediate value between the open input coil situation (4.6 V for $1\Phi_0$) and the shorted input coil one (9 V for $1\Phi_0$).

In order to study the sensitivity of the system in the direct coupling configuration, we measured the SQUID demodulated V-Φ curve in open loop when a current $I=V/22$ kΩ was applied: a) to one of the single-turn primary turns (I_1 or I_2); or b) to the flux transformer, either at the "CCC side" ($I_{CCC\ side}$) or at the "SQUID side" ($I_{SQUID\ side}$). The V-Φ degraded (sometimes to the point of disappearing) when the BNC's for applying the current where connected. Experimentally, the 4 transfers were equal, within a 2% (Figure 6.7). From the analysis of the circuit of Figure 6.5, one can easily show that the necessary voltage (respectively applied to the "CCC side" or the "SQUID side") to produce 1 Φ_0 in the SQUID is:

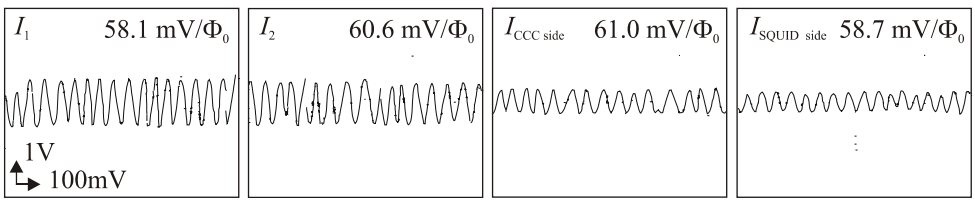

Figure 6.7- *Transfer function measured when a current I=V/22 kΩ was applied (from left to right) to each of the two primary turns, and to the flux transformer, at the "CCC side" and at the "SQUID side" (see Figure 6.5).*

$$\left.\frac{V}{\Phi_0}\right|_{\substack{SQUID\\side}} = \frac{1}{M_i}\frac{x+L_i}{x}R(44\,\mathrm{k\Omega}), \tag{6.1}$$

$$\left.\frac{V}{\Phi_0}\right|_{\substack{CCC\\side}} = \frac{1}{M_i}\frac{x+L_i}{x-L_w}R(44\,\mathrm{k\Omega}), \tag{6.2}$$

where x=$L_{CCC,eff}$ +L_w is the sum of the CCC and the wire inductances. From these two equations, an experimental value for $L_{CCC,eff}$≈73.4 nH, close to the expected value (76 nH) was found. The small difference can be explained by a is slightly (~0.5 mm) larger distance h from the CCC to the shielding than presumed. The inductance of the wires was found to be L_w≈3.2 nH, negligible small (~4%) compared to $L_{CCC,eff}$, as desired. Thus, the matching parameter between the CCC and the SQUID in this case was $(L_i/L_{CCC,eff})^{1/2}$=0.87±0.07, and the dimensionless sensitivity S_{CCC}=0.49±0.07, close to the maximum. S_{CCC} falls onto the ideal sensitivity curve (Figure 6.8), as a result of the direct coupling. By varying the distance h from the CCC to the bottom of the shielding the dimensionless sensitivity could be measured for various values of the matching parameter, although given the slow dependence of $L_{CCC,eff}(h)$, only a small range could be swept.

The CCC-SQUID flux noise spectrum was measured down to 1 Hz (Figure 6.9). A large amount of noise compared to the SQUID alone was present below ~500 Hz. To investigate the sources of low frequency noise, the SQUID FLL output (filtered at 1 Hz) was recorded as a function of time. Large drifts were observed (Figure 6.10a). The main origin of the drifts was the insufficient shielding of the CCC. E.g., the polarity change of a

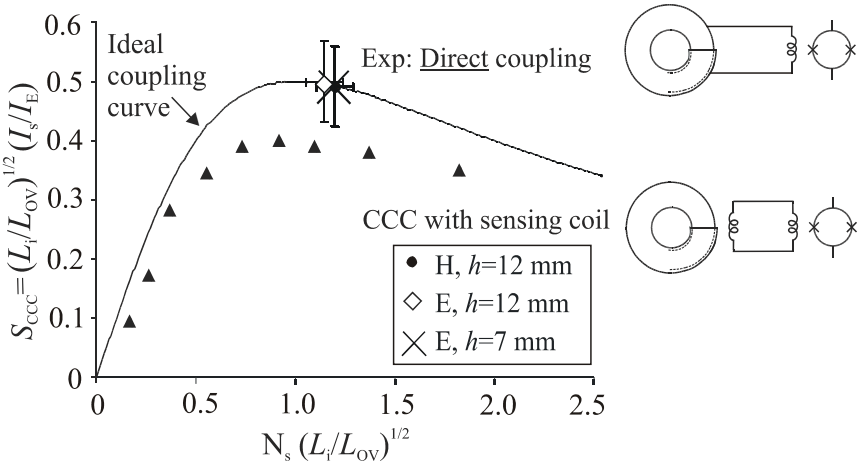

Figure 6.8- *Dimensionless sensitivity vs. matching factor; ideal coupling curve (line) and reduced sensitivity (triangles) for a CCC-SQUID using a sensing coil. The measured sensitivity points obtained with the directly coupled CCC-SQUID fall onto the ideal sensitivity curve, as expected from theory.*

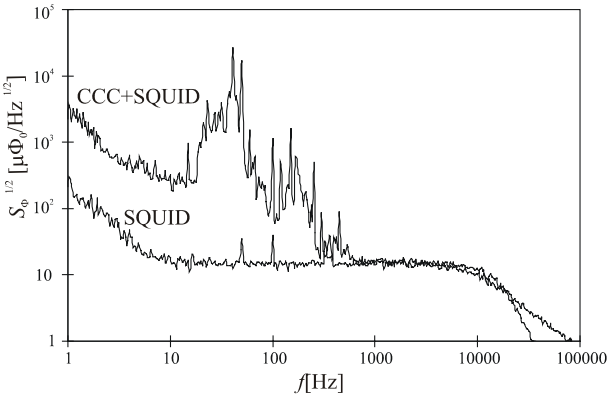

Figure 6.9- *Flux noise spectra of the SQUID ("matched SQ#14") alone, and directly connected to the large, 1:1 CCC (without any current applied).*

small magnet (Figure 6.10b) or even the movement of current carrying cables in the neighborhood of the cryostat was perfectly followed by the SQUID. A large dependence of $V_{FLL}(t)$ with the He bath pressure was measured (Figure 6.10c); in addition the system was extremely sensitive to vibrations. These problems have the following origin. Since the system is cooled down in the absence of any ferromagnetic shielding, the background field at which the superconducting shields become superconducting is quite high. Flux lines can be trapped, especially at the soldering points. Indeed, we measured (Figure 6.11) that the soldering tin used expelled only a 10% of the flux. The relative movement of the large area CCC with respect to the trapped flux lines, caused by vibrations or induced by pressure variations has thus a great influence. Therefore, in the final CCC design, a ferromagnetic shielding as well as the minimum soldering tin necessary should be used. The experimental ratio error could not be determined because of the large noise.

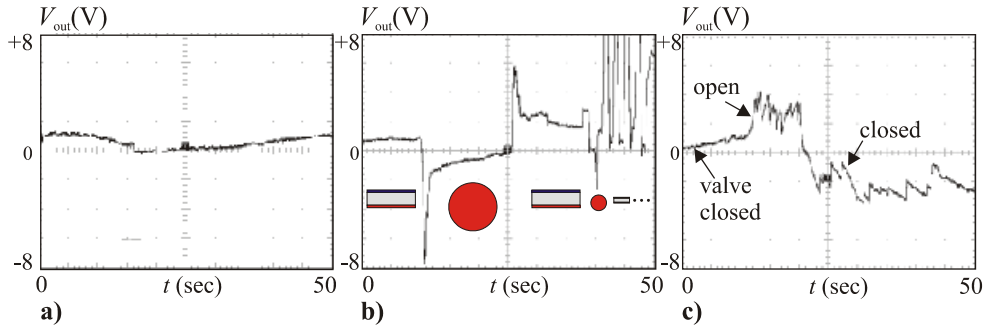

Figure 6.10- *SQUID FLL output as a function of time, $V_{FLL}(t)$; a) System drift; b) Influence of a magnet outside the cryostat; c) Influence of pressure variations, caused by opening and closing the cryostat He recycling valve.*

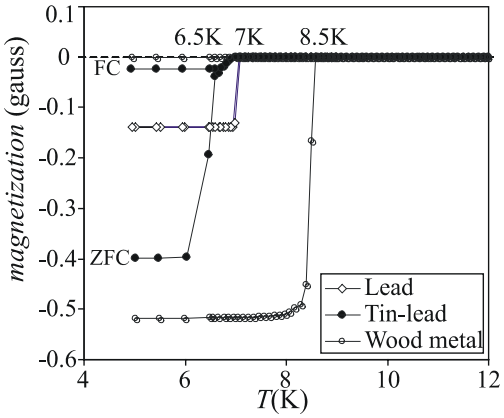

Figure 6.11- *Measurement of the magnetization in a Zero Field Cooling (ZFC) and Field Cooling (FC) experiment for Pb, Pb-Sn (used for our CCC) and Wood's metal[1] (Sn=12.5%, Pb=25%, Bi=50%, Cd=12.5) used by other authors[17]. In the ZFC experiment, a 50 gauss field is applied when the sample is at T=5 K, and then T is increased above 12 K. The FC curve is recorded as the T is decreased from 12 K to 5 K, with the field constantly applied. The critical temperatures obtained were 6.5 K (Sn-Pb), 7 K (Pb) and 8.5 K (Wood's metal). The transition of Sn-Pb is broader than that of the other two metals. Pure Pb behaves as expected as a type I superconductor: the magnetic field is completely expelled and the ZFC and FC curves coincide. Sn-Pb and the Wood's metal behave like type II superconductors. The tin-lead alloy expels only a 10 % of the field, while Wood's metal expels less than a 1%. The measurements were done at the University of Zaragoza SQUID facility.*

6.2. 1: 30 000 CCC

In this section we will describe the development and test of a complete large ratio (>1:30000) CCC with direct coupling to one of the SQUIDs, for the amplification of very small currents.

6.2.1. Description of the system

A general view of the integrated setup is shown in Figure 6.12. The core of the system is a CCC, with 1 turn overlap, containing the following sets of windings, that form a self-checking system:

A: 1, 1, 2, 4, 4, 10, 10, 20, 20, 40, 40 turns
B: 100, 100, 200, 400, 400, 1000, 1000, 2000, 4000, 4000 turns
C_1: 10000 and C_2: 10000 turns.

The maximum amplification ratio available is thus 1:33351. The windings are made of isolated 70 μm thick insulated Cu wire. Ideally the primary windings should be made of superconducting thin wire. However, given the high price of the long piece of wire required[9], and the risks of fracture during winding, it was decided to make initially the

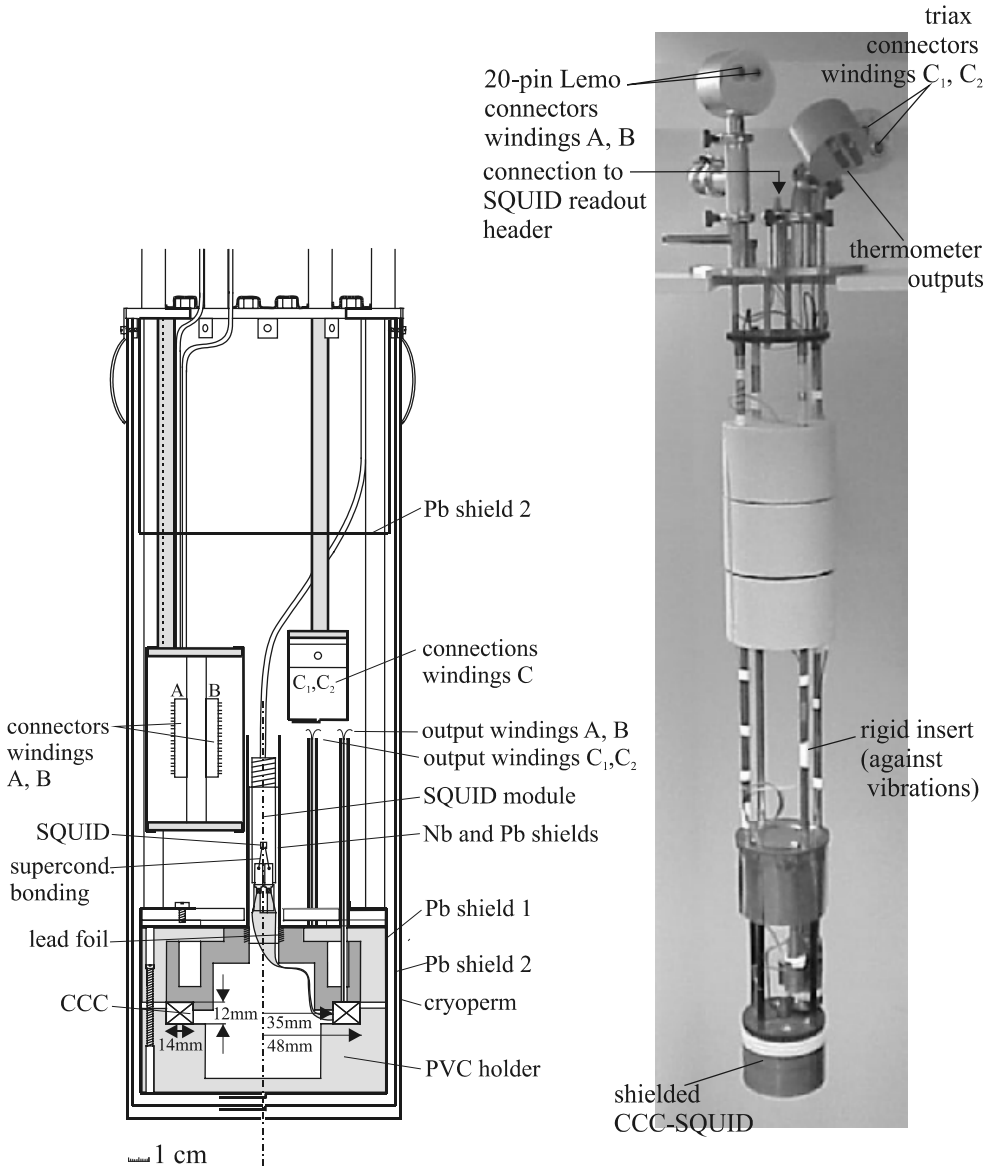

Figure 6.12- *Right: General view of the 1:30000 CCC-SQUID insert; Left: Schematic cross-section of the cryogenic part.*

windings with Cu wire, and check if the ratio error was sufficiently low. Windings A, B and C_1, C_2 came out from two different lead tubes from the CCC toroid. The winding ends of A and B were soldered to two PCB multiple-pin connectors, and shielded by a small Pb can. All winding ends should be connected and conveniently fixed, or as we observed experimentally, the noise would increase to the point of making the internal feedback loop impossible. The windings C_1 and C_2 were soldered to a different connecting plate, and shielded with Pb. Two 10 MΩ resistors in the cold were soldered to one of the 10000 windings, to facilitate applying a small current.

The CCC tube was tightly fixed between two hard PVC pieces. So as to reduce the input current noise, the effective CCC inductance in the shielding $L_{CCC,eff}$ should be as large as possible. Since the neck of the cryostat available had a diameter of 160 mm, and some space had to be left for the shields and liquid He filling, the outer diameter of the CCC was finally 96 mm. The inductance of the (unshielded) CCC, L_{CCC}, was obtained by measuring the impedance as a function of frequency at room temperature. A resonant peak at ~1.6 kHz appeared excited in the many-turn CCC *LC* resonant circuit (Figure 6.13a). The CCC was completely surrounded by a cylindrical Pb shield of high purity (99.95%). The effect of the superconducting shields on the CCC inductance was also studied (Figure 6.13b). The effective inductance found for the large 1:30000 CCC, $L_{CCC,eff}$=55 nH, agreed with the value calculated with a finite element program[10].

A "CCC matched SQUID" (#10, L_{sq} =150 pH, 23 turns), with a measured input coil inductance of L_i=45 nH close to $L_{CCC,eff}$, and a design (white) noise of $S_\Phi^{1/2}$~1.6 $\mu\Phi_0/Hz^{1/2}$ was chosen. The SQUID was readout with "Oxford Instruments" electronics. As seen in Chapter 4, because of the small transfer of the SQUID (~30 $\mu V/\Phi_0$), the noise (in the white region) was dominated by the electronics, and was measured to be ~7 $\mu\Phi_0/Hz^{1/2}$. At low frequencies however the noise was given by the SQUID, and amounted only ~11 $\mu\Phi_0/Hz^{1/2}$ at 1 Hz (Figure 6.17).

Annealed Nb wires, wedge bonded to the SQUID input coil paths and soldered by spot welding to the SQUID module Nb blocks were used (section 6.1.2). A low inductance lead foil construction (identical to the one used in the test 1:1 CCC) was used to connect the SQUID module to the CCC tube. Special care was taken to fix the foil to the CCC support pieces, to avoid its vibration. The SQUID module was shielded by two concentric, Nb and Pb shields.

The whole shielded CCC-SQUID was fixed at the end of the insert, and surrounded by a lead shield and a 1.5 mm thick cryoperm[11] shield. We took care to use the minimum amount of soldering Sn-Pb in the fabrication of the several CCC lead shields, to avoid as much as possible the problem of flux trapping observed in the test 1:1 CCC (section 6.1.3). The efficiency of the magnetic shielding is very important to ensure that the total system noise is not dominated by environmental noise. The intrinsic SQUID noise is equivalent to a field noise in the (directly) coupled CCC:

$$S_{B,CCC}^{1/2} = \frac{S_{\Phi,CCC}^{1/2}}{AreaCCC}; \quad \text{with } S_{\Phi,CCC}^{1/2} = \frac{L_i + L_{CCC}}{M_i} S_{\Phi,sq}^{1/2}. \tag{6.3}$$

For the CCC and SQUID described above, this means that for the SQUID to be the dominant source of noise in the system, magnetic fields inside the shielding should be

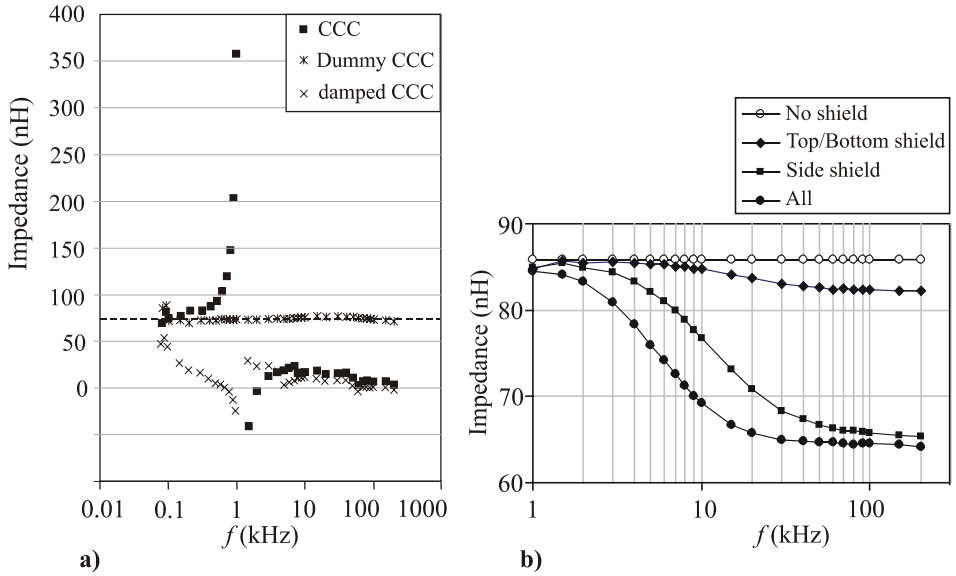

Figure 6.13- *Measurements of the CCC self-inductance as function of the frequency performed at room temperature with a Quad Tech 7600 LCR bridge. a) $L_{CCC}(f)$ of the 1:30000 CCC without shielding. A resonance at ~1.6 kHz appears, which is excited in the LC circuit formed by the inductance of the windings, inductively coupled to the CCC tube inductance (L_N~N^2L_{CCC}), and the capacitance between the winding turns. The capacitance of the overlapped piece of CCC does not play a role, since the resonant peak did not appear in the measurement of the L_{CCC} of a "dummy CCC", consisting just of the overlapped tube without windings inside. By short-circuiting one of the largest windings (10000 turns), the resonance could be damped. b) Effect of a lateral, top and bottom shields on the self-inductance of the "dummy" CCC. For high frequencies the screening due to eddy currents is perfect and has the same effect on the L_{CCC} as the superconducting screening currents. The inductance is constant (~85 nH) for the unshielded CCC. When the effect of the shields is present, the inductance decreases to an effective $L_{CCC,eff}$~63 nH. Note that the effect of the top and bottom shields (placed at the same distance from the CCC) is identical; the effect of the lateral shielding is larger than that of the top/bottom shields, and the effects of the different shields on L_{CCC} sum each other.*

reduced below 0.2-0.6 fT/Hz$^{1/2}$ (at 1 Hz). The shielding factor of the ferromagnetic shield used, calculated as[12]:

$$Att_{ferr} \approx 0.22\mu_b\left[1-\left(1-\frac{e}{v^{1/3}}\right)^3\right], \tag{6.4}$$

(with v the volume, e and thickness and μ_b (>10000 at 4.2 K) the relative permeability of the cryoperm can), and expressed in dB was ~32 dB. The shielding factor of the

superconducting shield is dependent on the ratio between the length and radius z/r of the shield[13]:

$$Att_{\text{sup}} \approx 1.33 \cdot \exp\left(3.83\frac{z}{r}\right). \tag{6.5}$$

With the dimensions of the two Pb shields used, the shielding factors would be respectively ~100 dB and 50 dB. Therefore, the total shielding factor would be ~180 dB; assuming that the field noise in a laboratory environment is typically[14] ~10^6 fT/Hz$^{1/2}$ (at 1 Hz), the residual field noise inside the shields would be in theory smaller than the necessary level (Eq. 6.3). In practice however, the experimental shielding factor at low frequencies is always smaller than calculated, because the movement of trapped flux lines within the shields themselves introduces additional flicker noise. Two (Pt and a Si resistance) thermometers, placed on the insert just above the cryoperm shielding allowed verifying that the complete shielded system was at 4.2 K.

The rigid part of the insert[15] consisted of 4 long rods with transversal bars between them, such designed to damp possible vibrations. The wires A and B were shielded in stainless steel tubes, and brought to room temperature, where the different windings were available at two 20-pin Lemo[16] connectors. The wires of the two 10000-windings were carried inside one of the supporting rods, to provide extra electromagnetic shielding, and ended up in two triaxial connectors. The wires carrying small (C_1, C_2) and high (A, B) currents were separated to avoid possible crosstalk. For applying a small current to the windings, an Al shielded battery powered current source was made. The current could be manually varied between either 0-26.4 μA, or 0-11.8 pA. It was essential to provide a continuous electrostatic shielding to all the cables going from the winding connectors to the current source, and to ground the current source to the unique ground of the system, the cryostat. Cables were also tightly fixed to prevent magnetic flux fluctuations in the neighborhood of the cryostat.

6.2.2. Experiments

Before cooling down the system, the resistance of the different primary windings was measured to check for continuity. Only one of the windings (with 4000 turns) was broken. No shorts between windings were present. Because of the large mass of the cryogenic system, the insert was first pre-cooled with liquid nitrogen and then cooled down in liquid helium, the procedure taking 2 days. Since the system can be extremely sensitive to vibrations and pressure variations, a reasonable time should be allowed after the He transfer to allow the stabilization of the He bath.

The ***characteristics of the SQUID connected to the CCC*** were measured. The direct V-Φ had an amplitude of 14 μV_{pp} (for a bias current $I_b \sim 2I_0 = 16$ μA), and no high frequency components were visible (Figure 6.14a). When we produced on purpose a small vibration by ticking the cryostat, the curve was almost not distorted. We observed that if the oscillator producing the modulation frequency was switched on, high frequency components would appear in the V-Φ direct curve (Figure 6.14c), and the curve was much more sensitive to vibrations. The demodulated V-Φ curve, for the optimal settings

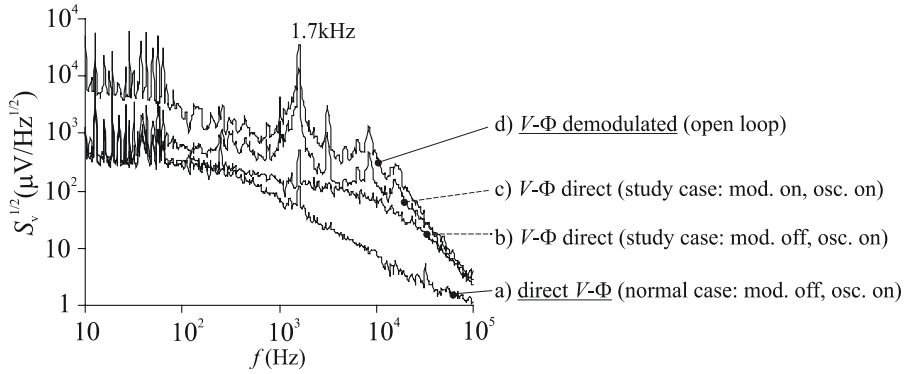

Figure 6.14- *High frequency components of the direct and demodulated V-Φ curves. a) In the normal V-Φ direct mode the oscillator is switched off. Only the white noise is amplified by the resonances, thus only a small peak at the main dominant frequency 1.7 kHz appears. c) If in the V-Φ direct mode the oscillator is turned on, the 500 kHz modulation frequency, excites all the resonant frequencies. (Note (b) that the electronics is such that even when the modulation switch is off, a small current containing the 500 kHz couples into the SQUID and excites some resonant peaks). d) In the demodulated V-Φ the resonant peaks corresponding to the different N-turn windings are present.*

BIAS=16.4 μA and MOD=12.3 μA, had a voltage amplitude of 5.9 V_{pp}. The voltage period corresponding to $1\Phi_0$ was 5.5 V, an intermediate situation between the SQUID with open input coil leads (4.5 V for $1\Phi_0$) and the input coil shorted (9 V for $1\Phi_0$). In contrast to the normal direct *V*-Φ curve, the demodulated *V*-Φ curve was affected by superimposed large frequency signals (Figure 6.14d). The curve was very much distorted as consequence of vibrations (caused by the on-purpose ticking of the cryostat or accidental vibrations of the floor), and acoustic noise. This behavior can be explained by the appearance of ***LC resonances*** in the multi-turn CCC, excited by the modulation frequency. The 500 kHz modulation frequency of the SQUID readout electronics can couple back to the flux transformer via the mutual inductance between the feedback and the input coil. This signal will also run on the overlap tube, and will excite resonances in the low quality factor resonant circuit formed by the overlap and the primary windings (Figure 6.15a). The demodulated *V*-Φ contains thus all the excited resonant peaks corresponding to the different windings, with dominance of a ~1.7 kHz peak corresponding to the largest 10000 turn coil. The amplitude of the peaks is proportional to the amplitude of the 500 kHz modulation current applied.

The resonant peaks can be assigned to the N-turn coils, as explained in Figure 6.15b. Gay *et al.*[17] reported also the presence of a resonant peak at 4 kHz in a large ratio (1:10000) CCC. According to these authors, for larger number of primary turns, the resonance peak might prevent the operation of the CCC-SQUID in internal feedback mode[18]. For the present CCC, however, the internal loop could be closed without problem. The sensitivity in FLL of the SQUID was 9.1 V/Φ_0. Since in practice the system will be operated at very low frequencies, the resonant behavior at very high frequencies should not be a problem.

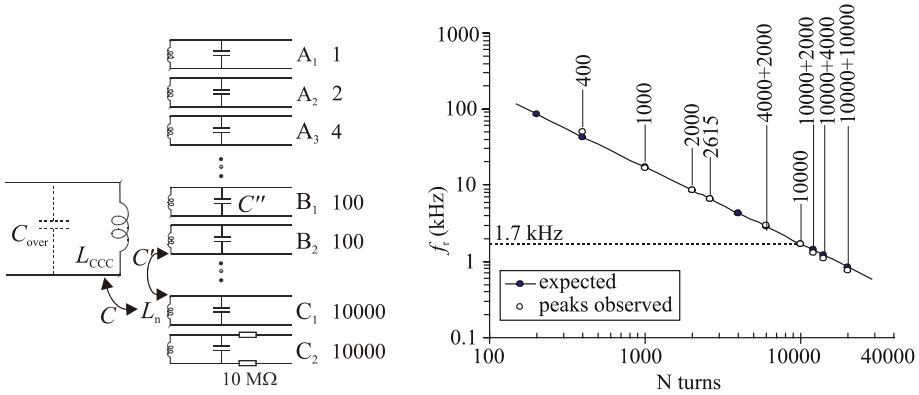

Figure 6.15- *a) Schematics of the equivalent LC resonant circuit formed by the CCC overlapped tube and the primary windings; b) The real system is a complicated resonant circuit; a simple model can be used to assign the observed resonant peaks to the N-turns windings. Assume that the major peak (1.7 kHz) corresponds to the largest N=10000 winding, the coupling between the CCC and the winding inductances is inductive ($L_N=N^2L_{CCC}$), and the effective capacitance of the total resonant system is dominated by the capacitance of this winding, C≈1.6 nF. The resonant peaks corresponding to the rest of the windings would be expected at $f_{r,N}$=1.7 kHz*10000/N. The peaks predicted under these assumptions correspond well with the peaks observed. The winding with 4000 turns was broken at the level of the CCC, so no peak at N=4000, but at a smaller N~2615 appears.*

The ***current sensitivity*** (i.e, the current necessary to inject in a 1 turn coil to detect 1 Φ_0 in the SQUID), in the case that the coupling between the CCC and the SQUID was perfect, was expected to be 2.2 μA.turn/Φ_0. The sensitivity was measured with two different methods. In open loop, the sensitivity was determined from the flux shift of the demodulated *V*-Φ curve when an increasing current from 0 to 26.4 μA was applied to a 1-turn winding. In closed loop, we measured the SQUID FLL output when a current of 4.3 μA was applied. The result in both cases was the same, and equal to S=2.3 μA.turn/Φ_0. The result is in fair agreement with the theoretical value, indicating that optimal coupling is reached within a 4%.

In order to measure the ***ratio error***, we applied a current, reversed every ~5 s between 0 and 26.4 μA, to two N-turn windings, connected in series opposition. The measurement was performed for several winding pairs (Figure 6.16). No error signal could be detected within the SQUID noise, $\sim 10^{-4}$ Φ_0. Since the error signal is given by the SQUID-CCC noise, the minimum limit for the ratio error is obtained for the measurement with the pair of windings (2x1000) were the signal applied can be larger. In that case the ratio error was found to be $F<8.7.10^{-9}$. Since the real value will be smaller than this limit, we can conclude that the ratio error is sufficiently low, even if the primary windings were made of Cu instead of superconducting wire.

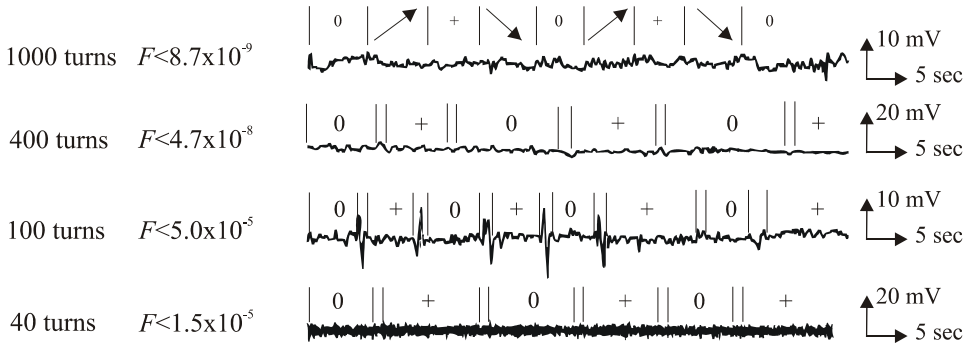

Figure 6.16- *Ratio error measurements for the pairs of windings with 40, 100, 400 and 1000 turns. The current was progressively increased (↑) from 0 to +26.4 μA, and after some seconds decreased again (↓) to zero; the sequence is repeated several times.*

The ***noise*** in FLL of the SQUID connected to the CCC was measured without any current applied to the primary windings. Figure 6.17 shows the flux noise of the CCC-SQUID compared to the noise of the SQUID alone. At high frequencies, the system noise spectrum shows the resonance behavior already commented. However, at lower frequencies, a flat noise level of $S_{CCC\text{-}sq}^{1/2}$~45 $\mu\Phi_0/Hz^{1/2}$ was measured. No trace of 1/*f* noise was observed down to a frequency of 0.1 Hz. The noise of the SQUID (plus the readout electronics) was ~7.0 $\mu\Phi_0/Hz^{1/2}$, and the corner frequency appeared at ~4 Hz. Therefore, from Figure 6.17 one can see that connecting the CCC only adds white noise, and not significant 1/*f* noise. The corner frequency of the CCC-SQUID system (<0.1 Hz) is directly determined by the 1/*f* noise behavior of the SQUID.

Despite the shields used, the system noise was still dependent on the environmental magnetic noise conditions (e.g., the white noise increased to ~80 $\mu\Phi_0/Hz^{1/2}$ when a very

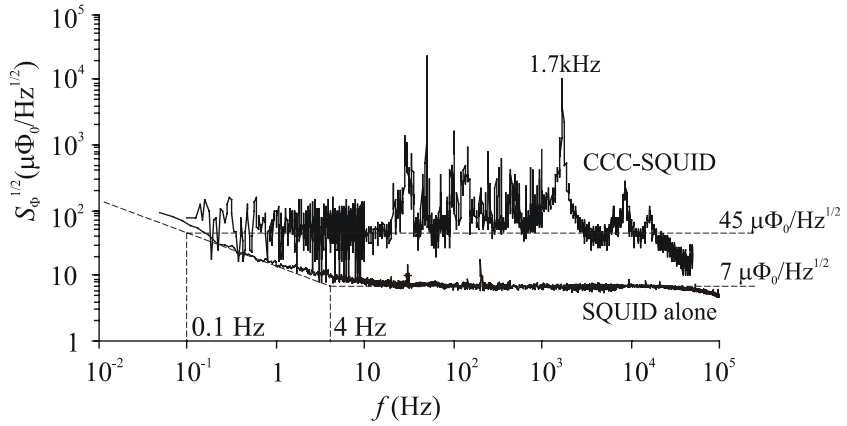

Figure 6.17- *Flux noise of the SQUID with the CCC connected and alone.*

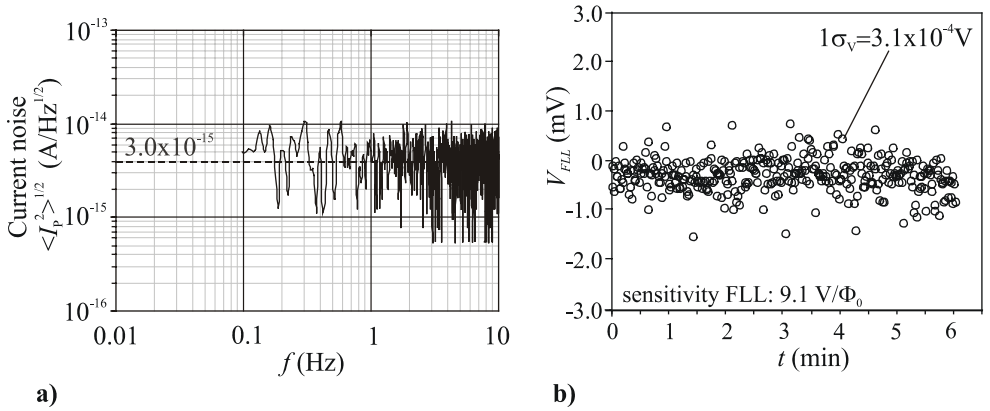

Figure 6.18- *a) Equivalent current noise at low frequencies calculated for 33351 turns; b) FLL SQUID output as a function of time after a 1 Hz filter.*

small motor was working one floor above our laboratory). The noise level could also vary from one cooling-down to another, because in each procedure, the amount of flux trapped in the lead shields could be different.

Since the CCC will be utilized as a current amplifier at low frequencies, it is useful to translate the flux noise measured into the input current noise per turn winding of the CCC. Since the sensitivity is S_{CCC}=2.3 μA.turn/Φ_0 and the maximum number of turns N_{CCC}=33351, the current noise is:

$$< I_P^2 >^{1/2} = \frac{S_{CCC-sq}^{1/2} \cdot S_{CCC}}{N_{CCC}} = 3.0 \text{ fA/Hz}^{1/2}, \tag{6.6}$$

down to 0.1 Hz (Figure 6.18a).

To measure the noise at very low frequencies, the FLL output, filtered at 1 Hz, was recorded during ~6 min. The standard deviation measured was σ_V=3.1x10^{-4} V (Figure 6.18b), corresponding to a current standard deviation per turn of:

$$\sigma_I = \sigma_V \cdot \left(\frac{\partial V}{\partial \Phi} \right)_{FLL}^{-1} \cdot S_{CCC} \cdot \frac{1}{N_{CCC}} = 2.3 \text{ fA}. \tag{6.7}$$

The final test of the system was the injection of a very small current (simulating the SET current) into one of the 10000-turn windings. Figure 6.19 shows for instance the CCC-SQUID output when a current applied to the C_2-10000 turn winding was several times successively turned from 0, +I=11.8 pA, 0, +I… every ~30 s. The current standard deviation within a plateau was 1σ_I=38 fA, larger than what should be expected if the noise was only due to the CCC-SQUID (~10 fA), indicating that the (non-optimized) current source and connecting cables added noise to the system.

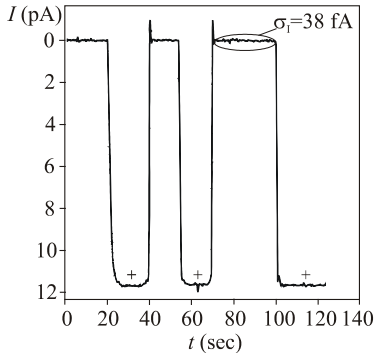

Figure 6.19- *CCC-SQUID current output signal obtained applying a current of 11.8 pA (switched every ~30 s) to a 10000 turn winding.*

6.2.3. Current uncertainty; frequency considerations

So as to evaluate the current uncertainty that could be finally reached in the amplification of a SET current with the present CCC-SQUID system, some previous frequency considerations are necessary. In a SET current measurement experiment (Figure 6.20), the current is reversed at a frequency f_{S1}, and the CCC-SQUID output signal is recorded up to a frequency f_{S2} during a certain time t_T. We will define "one measurement" as the record of one single cycle "+*I*, 0, -*I*, 0, +*I*", from which the current can be determined as [(+I)-(-I)]/2. The (power) standard current deviation within a plateau is given in general by the current noise per turn CCC integrated over the measurement BW:

$$\sigma_I^2 = \int_{BW} < I_P^2 > df = \int_{BW,white} < I_P^2 > df + \int_{BW,1/f} < I_P^2 > \frac{f_c}{f} df, \tag{6.8}$$

where f_c is the corner frequency of the CCC-SQUID current noise $<I_P^2>^{1/2}$ spectrum (Figure 6.20). The lower limit of the BW, f_{S1}, should be low enough to guarantee that the ratio error due to leakage current is negligible. Besides, in order to reduce more efficiently σ_I, f_{S1} should be (if possible) in the white noise region. The higher BW limit, f_{S2}, should be the minimum allowed by the experiment, to have the narrowest BW and hence decrease σ_I. Only in the case that the whole BW is in the white noise region, the standard deviation reduces to: $\sigma_I=<I_P^2>^{1/2}.(f_{S2}-f_{S1})^{1/2}$. After a time t_T, a total number of measurement cycles $N_{rep}=t_T f_{S1}$ will have been recorded. Assuming that the N_{rep} measurements are independent and distribute statistically, the current standard deviation of the mean would be:

$$\sigma_{I,av} = \frac{\sigma_I}{\sqrt{N_{rep}}}. \tag{6.9}$$

The final current uncertainty in the measurement of the current will be given by the ratio:

$$u_I = \frac{\sigma_{I,av}}{I_{SET}}. \tag{6.10}$$

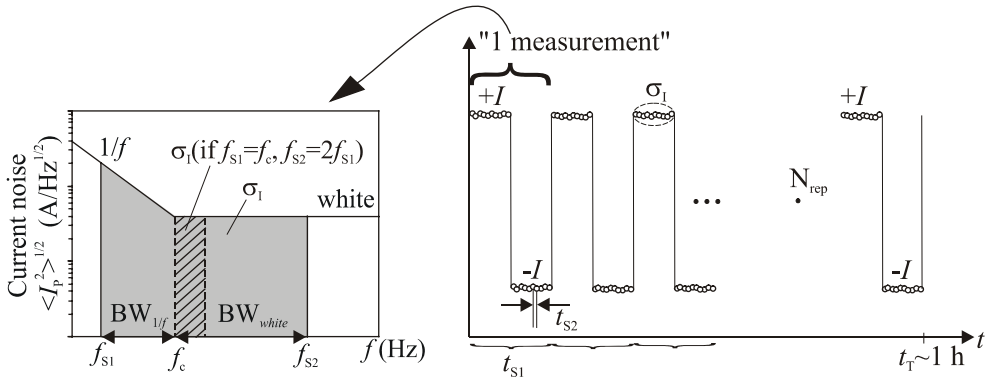

Figure 6.20- *Right: Typical experiment of measurement of a current I with the CCC-SQUID. Left: Current noise spectrum and current standard deviation σ_I of "one measurement" (see text).*

In our large-ratio CCC-SQUID system, the current noise is white and equal to $\langle I_P^2\rangle$=3.0 fA/Hz$^{1/2}$ down to 0.1 Hz. A SET current measurement experiment could be done, choosing the reversal frequency to be f_{S1}~f_c=0.1 Hz; the BW should be of the order of f_{S1}. The current standard deviation of the mean would then be as small as:

$$\sigma_{I,av} = \frac{3.0\,\text{fA/Hz}^{1/2}\cdot\sqrt{0.1}}{\sqrt{720}} \approx 35x10^{-18}\ \text{A} = 35\,\text{aA}, \tag{6.11}$$

for a 2 h experiment. Hence the total uncertainty that could be reached in the amplification of a SET current would be:

$$u_I \approx 3.10^{-5}\ (\text{if } I_{SET} = 1\,\text{pA}),\ \text{or} \qquad u_I \approx 3.10^{-6}\ (\text{if } I_{SET} = 10\,\text{pA}). \tag{6.12}$$

6.3. Conclusions

A large size, 1:1 CCC with direct coupling to a SQUID with matched inductance $L_i \approx L_{CCC,eff}$ has been designed and tested. We verified experimentally that, thanks to the perfect coupling between the CCC and the SQUID, ideal sensitivity was reached. We learned also that the CCC superconducting shields should be soldered with the minimum quantity of Sn-Pb possible, and protected by a cryoperm shield to prevent the trapping of flux lines during cool-down, whose relative movement with respect to the large-size CCC due to small vibrations increase enormously the noise.

A large ratio (>1:30000) CCC system for the measurement of very small currents has been completely integrated and characterized. A low-noise, directly coupled self-made dc SQUID was used for the readout. The direct-coupling allowed reaching a sensitivity close to ideal (~2.3 μA.turn/Φ_0). The ratio error was better than F<8.7x10^{-9}. The flux noise of the CCC-SQUID was ~45 $\mu\Phi_0$/Hz$^{1/2}$, corresponding to a current input noise (for a

33351-turn winding) of 3.0 fA/Hz$^{1/2}$, measured down to 0.1 Hz. We were able to measure a ~10 pA current, turned from 0 to +*I* every ~30 sec, and being applied to a 10000-turn winding with a current standard deviation of $1\sigma_I$~38 fA. In a SET current measurement, a current standard deviation of the mean around ~35 aA might be expected when using a 33351 turn winding, and measuring the reversed current during 2 h. Consequently, a quantized SET current of 1-10 pA could be measured with a relative uncertainty of ~$3x10^{-5}$-10^{-6}. If SAW devices were available that could give accurate quantized currents of 1 nA, an uncertainty of 10^{-7} might be reached.

The integration of the system was successful, and noise results are very promising, considering that the system was tested in a noisy laboratory environment. Even better current noise levels could be reached when the system is finally measured at the final destination Dutch National Metrology Institute. On place, the CCC-SQUID shielding can be improved (e.g., by substituting the external Pb shield by a Nb shield, and shielding the whole cryostat with an available Fe ferromagnetic shield). Besides, the system will be located in a Faraday cage, in a chamber less affected from floor vibrations than in the current location.

References

[1] M. Hiddink, MSc report, University of Twente (1999).
[2] J. Sesé, PhD Thesis, University of Zaragoza, (1999).
[3] G. Rietveld *et al*., *Sens. Act. A.* **A85**(1-3), 54 (2000).
[4] T. Ogashiwa *et al*., *Jap. J. Appl. Phys*. **28**(12), 2479 (1989).
[5] Model TU-907 Ultrasonic Wedge bonder, Mech-el industries inc., Semtec (1983).
[6] J. Sesé, internal report, University of Twente (2001).
[7] W. Jaszczuk *et al*., *Meas. Sci. Technol.* **2**, 1121 (1991).
[8] www.goodfellow.com, ref. NB005100.
[9] e.g.: Insulated 0.55 mm diameter Cu/NbTi wire from Gec Alsthom Power Generation superconductors, 6 km lenght (in 4 pieces) costs ~2400 €; Insulated 0.554 mm diameter Cu/sc from Outokumpu copper superconductors, 5 km length (in one piece) costs 1581 € (prices 1996).
[10] Quickfield 4.0 for Windows 95/NT 93-97, student edition, http://tera-analysis.com
[11] Cryoperm©, ferromagnetic material registerd by Vacuumschmelze GnbH.
[12] A.L. Mager, *IEEE Trans. Mag*. **6**, 67 (1970).
[13] T.I. Smith, *J. Appl. Phys*., **44**(2), 852 (1973).
[14] J.P. Wikswo, in *Applications of superconductivity*, NATO series, Kluwer Academic Publishers (Dordrecht/Boston/London), **365**, 139 (1997).
[15] L. Vargas, Postgraduate report, University of Twente (1998).
[16] www.lemo.nl
[17] F. Gay *et al*., *Rev. Sci. Instrum*. **71**(12), 4592, (2000).
[18] F. Gay, PhD Thesis, Conservatoire National des Arts et Métiers (2000).

Chapter 7

AN OUTLOOK OF THE QUANTUM METROLOGICAL TRIANGLE OF ELECTRICAL UNITS

The quantum metrological triangle (QMT) of electrical units is a planned experiment, which would consist in realizing Ohm's law using the voltage, resistance and current quantum standards. The main objective of this experiment (section 7.1) is to check the consistency of the quantum electrical effects involved with a high level of accuracy ($<10^{-8}$). The present state-of-art of the different elements taking part in the experiment is exposed in section 7.2. The analysis of the noise sources in the triangle (section 7.3) will evidence that a major bottleneck is the current resolution of the CCC-SQUID system, necessary to amplify the quantized current. The third part of this thesis was devoted to improve the performance of the CCC-SQUID current amplifier. The expected levels of uncertainty that could be reached nowadays are commented in section 7.4.

7.1. The QMT experiment and implications

Following the recommendations of the Comité International des Poids et Mesures (CIPM), quantum standards have been adopted in the last decade for the establishment of the electrical primary standards. The reproducibility of the quantum physical effects (10^{-9}) is two orders of magnitude better than the uncertainty attained from the direct realization of the units, according to the SI definition. The state-of-the-art regarding electrical quantum standards at the moment is the following.

The voltage quantum standard is based on the ac Josephson effect, predicted in 1962 by B. D. Josephson[1]. This effect states that the voltage across a Josephson junction (jj) exposed to microwave radiation of frequency f_1 is quantized:

$$V_J = n_1 \frac{1}{K_J} f_1, \tag{7.1}$$

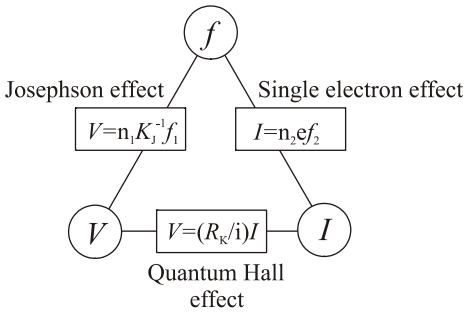

Figure 7.1- *The QMT relates the three quantum electrical effects via Ohm's law (V=IR).*

where n_1 is an integer and K_J is the Josephson constant, expected to correspond to the ratio 2e/h.

The resistance quantum standard is based on the quantum Hall effect (QHE)[2]. The transversal resistance of a Hall sample, at low temperature (T~1 K) and under a high magnetic fields (B~10 T) is quantized:

$$R_H(i) = \frac{R_K}{i}, \tag{7.2}$$

i being an integer and R_K the von Klitzing constant, presumed to be h/e^2.
To improve the worldwide consistency of electrical measurements, the Comité Consultatif d'Électricité (CCE) recommended the use by convention of the following values for the constants: $R_{K\text{-}90}$=25812.807 Ω and $K_{J\text{-}90}$=483597.9 GHz/V, known with relative uncertainties with respect to the SI of 2×10^{-7} and 4×10^{-7} respectively.

At present, the quantum standard for the current is still under development. Some special devices have been developed which can deliver quantized currents:

$$I = n_2 e f_2, \tag{7.3}$$

where n_2 is equal to 1 or 2 if the charge is respectively an electron or a Cooper pair. The driving frequency f_2 can be adjusted very precisely, with parts in 10^{10}. As we have seen, the problem at the moment is the amplification of the very small current provided by these devices to a useful level, with sufficient accuracy.

The three quantum effects can be related by the so-called quantum metrological triangle (Figure 7.1). The QMT experiment[3,4] would consist in feeding a Hall sample with the current delivered by a SET device I_{SET}, amplified by a Cryogenic Current Comparator of large gain N_{CCC}, read out with a dc SQUID. The voltage across the Hall sample should then be compared to the Josephson voltage generated by the Josephson standard with the help of a null detector (Figure 7.2):

$$V_H = I_{SET} N_{CCC} \cdot R_H \leftrightarrow V_J. \tag{7.4}$$

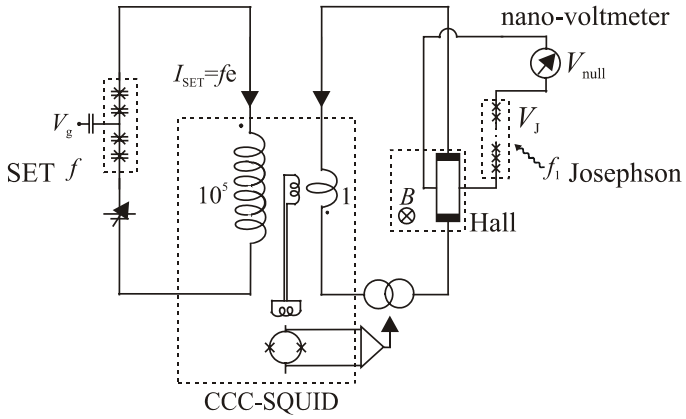

Figure 7.2- *Set-up for the QMT experiment.*

Showing that the two voltages are equal (with high precision, $<10^{-8}$) would prove the consistency of the constants involved in the three quantum phenomena to that level of uncertainty. This can be better seen as follows. Eq. 7.4 can be put as function of the constants R_K, K_J and a "new" constant Q_x that we define as the estimate for the electron charge e. Re-arranging terms we obtain:

$$R_K K_J Q_x = \frac{n_1}{n_2}\frac{i}{N_{CCC}}\frac{f_1}{f_2}. \tag{7.5}$$

The frequencies do not have to be known in absolute units, since only the ratio has to be measured. In case that R_H, R_J and Q_x would have deviations with respect to their assumed values: $R_H=(h/e^2)\,(1+\delta_R)$, $K_J=(2e/h)(1+\delta_V)$, $Q_x=e(1+\delta_I)$, Eq. 7.5 would read:

$$\delta = \frac{n_1}{2n_2}\frac{i}{N_{CCC}}\frac{f_1}{f_2} - 1, \tag{7.6}$$

where $\delta \approx \delta_R+\delta_V+\delta_I$ to the first order. Therefore, a measurement of the residual term δ provides information about the consistency level of the three quantum phenomena. Note though that the experiment would not be able to distinguish which one of the presumed constant assumptions was not correct.

A different approach to close the metrological triangle has been put forward[5]. In this case the electron pump is used to charge a cryogenic capacitor with a number n_2' of electrons with charge e. The voltage difference across the capacitor can be then measured with a Josephson voltage standard: $V_J=n_1' K_J^{-1} f_1'$. The measurement would give a quantum determination of the capacitance:

$$C_S = \frac{n_2' e}{V_J} \equiv \frac{n_2' Q_x K_J}{n_1' f_1'}. \tag{7.7}$$

The cryogenic capacitor should then be compared to a Thomson-Lampard calculable capacitor[6] at room temperature. Up to now, the accuracy in the comparison is limited to a few parts in 10^6. Hopefully the improvement in the performance of high-accurate ac bridges could reduce this uncertainty.

The combination of the two experiments would yield a new, direct determination of R_K in SI units, which could be expressed (Eq. 7.5 and 7.7) as:

$$R_K = \frac{n_1 n_2'}{n_2 n_1'} \frac{i}{N_{CCC}} \frac{f_1}{f_2 f_1'} \frac{1}{C_s}. \tag{7.8}$$

7.2. Elements in the QMT realization

In this section we will briefly describe the elements included in the first of the QMT approaches, which was sketched in Figure 7.2.

• ***The Quantized current generator:*** There are at present two sorts of devices, based on different physical effects, which are able to control electrons one-by-one.

Single Electron Tunneling (SET) devices are based on the Coulomb blockade[7]. The basic elements to observe this phenomenon are metallic islands with very small capacitance (C=10^{-16} F), at a temperature of some mK. At this T, the thermal energy of an electron is smaller than its electrostatic energy (e^2/C), and the electron can only leave the island if a voltage larger than a certain threshold is applied. If the voltage applied is a signal of frequency f_2, a quantized current I_{SET}=$n_2 e f_2$ appears through a series of these islands. Within SET devices, two variants have been developed: the so-called electron turnstiles[7] and electron pumps[8,9,10,11,12]. At this moment, the state of art of SET devices does not allow to achieve currents larger than 10 pA (f~40 MHz), with uncertainty 10^{-6}. Errors arise mainly from missing tunneling effects due to a too high frequency, photon assisted co-tunneling effects and thermally activated processes[13].

Ref.	Device	Frequency	Current	T_{bath} (mK)	Pump accuracy
(7)	electron turnstile[a]	< 10 MHz	~ 1 pA	10-40	10^{-3}
(8)	3-jj electron pump[a]	2-20 MHz	~ 1 pA	20	10^{-3}
(9)	3-jj electron R-pump[a]	10 MHz	~ 1 pA	10	10^{-4}
(10)	5-jj electron pump[a]	2 MHz	0.3 pA	200	5.10^{-7}
(11)	5-jj electron pump[a]	40 MHz	6.4 pA	20	10^{-6}
(12)	7-jj electron pump[a]	5 MHz	~ 1 pA	35	15.10^{-9}
(14)	SAW[b]	2.7 GHz	0.4 nA	300	10^{-3}
(15)	SAW[b]	4.7 GHz	0.8 nA	1400	10^{-3}

[a] based on the Coulomb blockade (SET devices)
[b] based on Surface Acoustic Waves (SAW devices)

Table 7.1- *Review of one-by-one current source devices.*

Another kind of devices are based on Surface Acoustic Waves (SAW), transmitted through a quasi-one dimensional channel defined in a GaAs-AlGaAs heterostructure by a split gate technique[14,15.] Local potential minima are created which move with the sound velocity. At high SAW power, the charge is transported along the channel in the form of electron packets residing in the SAW minima. At small wavelength, these minima can be considered as moving quantum dots, each carrying an integer number of electrons, thus delivering a current $I_{SAW}= n_2 e f_2$, where n_2 is the number of electrons per dot. SAW devices can deliver larger currents (~1 nA) at 4.2 K, since electrons can be transported at higher frequencies (a few GHz) than SET devices. However, the uncertainty (10^{-3}) is still too large for metrological applications. A review of the different SET/SAW devices, the maximum currents they are able to generate and the achieved uncertainties is shown in Table 7.1.

• ***The current amplifier:*** The quantized current has to be amplified to the level of μA with the best accuracy possible with the help of a large-ratio CCC-SQUID, before entering the Hall sample. For a CCC-SQUID with a current noise $<I_P^2>^{1/2}$ (equal to the current

a)

Ref.	N_{CCC} (turns)	Ext.Ø (mm)	SQUID type	$S_{sq,\Phi}^{1/2}$ ($\mu\Phi_0/Hz^{1/2}$)	N_s (turns)	S_{CCC} ($\mu A.turn/\Phi_0$)	$<I_P^2>^{1/2}$ ($fA/Hz^{1/2}$)
NPL,I	109999	160	QD	3.2	3	(2.88)	0.08
						2.33	
NPL,II	40960	64	QD	3.2	9	7.6	0.6
						10.7	
LCIE	10000	44	QD	3.2	11	4.4	3.0
						5.0	
Thesis	33351	100	Twente	1.0	direct coupling	2.2	0.07
							0.5
				7.0*		2.3	

b)

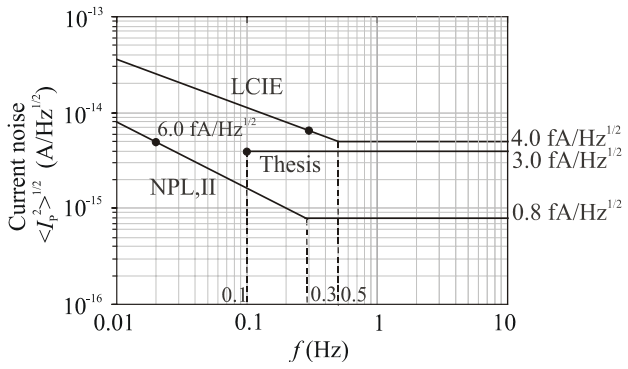

Figure 7.3- *a) Review of the CCC-SQUID current amplifiers currently available. Grey: theoretical values; White: measured values (Refs. Table: NPL,I[16], NPL,II[17,18], LCIE[19,20,21]); (*Noise from the SQUID+electronics); b) Input current noise $<I_P^2>^{1/2}$ of the three CCC-SQUID systems (no data were available from the NPL,I system). The points indicate the current reversal frequency f_{SI} used.*

resolution $<i_P^2>^{1/2}$ divided by the amplification factor N_{CCC}), the uncertainty in the scaling of the SET current I_{SET} would be:

$$u_I = \frac{\sigma_{I,av}}{I_{SET}} = \frac{1}{I_{SET}} \cdot \frac{1}{\sqrt{N_{rep}}} \left[\int_{BW} < I_P^2 > df \right]^{1/2}, \tag{7.9}$$

with N_{rep} the number of cycle repetitions in the total experiment time t_T (section 6.2.3). The current noise spectrum $<I_P^2>^{1/2}(f)$ is an adequate figure of merit to compare different CCC-SQUID systems. However, the final uncertainty in the SET amplification will depend on the conditions (the current reversal frequency, f_{S1}, the frequency BW of the bridge, and the total measuring time) at which the experiment can be realized. Figure 7.3 reviews the large-ratio CCC-SQUID current amplifiers currently available and their current noise spectra. The 1:40960 CCC system built at NPL[17,18] shows the lowest white current noise (~0.8 fA/Hz$^{1/2}$), but has a large low-frequency noise (with slope larger than 1/*f*) for frequencies f<0.4 Hz. Since the reversal frequency was limited to f_{S1}~0.02 Hz, the system was obliged to operate in the 1/*f* region, at which $<I_P^2>^{1/2}$(0.02Hz)~6 fA/Hz$^{1/2}$. The 1:10000 CCC at LCIE[19,20,21] has a white noise level ~4.0 fA/Hz$^{1/2}$, and a corner frequency f_c~0.6 Hz. The 1:33351 system presented in this thesis has a slightly better white noise (~3.0 fA/Hz$^{1/2}$), with the advantage that no 1/*f* noise has been observed down to a frequency of 0.1 Hz.

• ***The Hall resistance:*** The SET current, amplified by the CCC-SQUID, will then feed a quantum Hall sample, stabilized at the second plateau: R(i=2), typically at 10 T. It has been shown[22] that the thermal noise of a Hall device can be described by the Nyquist formula:

$$< V_{RH}^2 >^{1/2} = \sqrt{4 k_B T R_H (2)}. \tag{7.10}$$

Since the sample has to be cooled down at 0.3 K, the thermal contribution will be very small. The signal to noise ratio could be improved a factor of √10 by using a device consisting of ten QHE samples in series[23].

• ***The voltage Josephson standard:*** Modern voltage standards are based on Josephson Array Voltage Standards (JAVS). Conventional 1-V or 10-V JAVS use a series of 3000 or 20 000 hysteretic SIS junctions (S a superconductor, I an insulator) driven at a frequency of 70-90 GHz to generate about 200 000 voltage steps that span the desired voltage range, and can be separately selected[25]. However, the selection process is relatively slow, and the steps have a stability of around 15 minutes. In the QMT experiment, perfect stability and fast programmability are desired.

An alternative is the use of a programmable JAVS[26]. It consists of an array of non-hysteretic jj, segmented in a binary sequence (1, 2, 4, 8,...) of m smaller and independently biased arrays. This setup allows the rapid selection of any step number, and thanks to the non-hysteretic IVC's, the steps are not longer metastable. Although the working principle of the programmable voltage standard was demonstrated using externally shunted SIS jj, these junctions can be replaced by intrinsically shunted SNS or SINIS jj (where N is a normal metal). Thanks to the large critical current of these jj (I_c>1 mA), higher current output and stability against thermal and electrical noise are attained[27]. SINIS jj are preferable with respect to SNS jj because the spread on the normal resistance R_N can be

Ref.	Type	Junction	Number	Max. V
(24)	1 jj voltage standard	SIS	1jj	~ mV
(25)	Conventional JAVS	SIS	3000 jj	1V
			20000 jj	10V
(26)	Programmable JAVS	SIS	8192 jj	77mV
(27)	Programmable JAVS	SNS	32768 jj	1V
(28)	Programmable JAVS	SINIS	7024 jj	1V

Table 7.2- *Brief review Josephson voltage standards.*

better controlled, and because SINIS jj based JAVS can be operated at the same frequency range as the conventional SIS JAVS, thus the same microwave equipment can be used[28]. A brief review of different alternatives available is summarized in Table 7.2.

• ***The voltage detector:*** The voltage across the Hall sample V_H and the Josephson voltage V_J have to be compared with the help of an accurate null detector. The Hall voltage will be of the order of:

$$V_H = I_{SET} N_{CCC} R_H(2) = 6.4\,\text{pA}.10^5.12.9\,\text{k}\Omega \sim 10\,\text{mV}. \tag{7.11}$$

The V_J produced by the JAVS can be adjusted finely to that value. The null detector should be able to measure the difference $V_{null}= V_H-V_J$ with accuracy ~10^{-5}-10^{-6}.

7.3. Equivalent noise circuit of the QMT

We will consider here the different sources of noise introduced by each one of the elements, to obtain an equivalent noise circuit of the QMT (Figure 7.4). The quantum Hall element can be substituted by an ideal voltage source, of value (Eq. 7.11) V_H~10 mV, and two voltage noise sources in series. The first one, $\langle V_{RH}^2\rangle^{1/2}$~0.5 nV/Hz$^{1/2}$ (Eq. 7.10), is the thermal noise arising from the Hall resistance. The second one, $\langle V_{CCC}^2\rangle^{1/2}=\langle i_P^2\rangle^{1/2}.R_H$, originates from the current noise of the CCC-SQUID, translated into voltage noise via de Hall resistance. If,

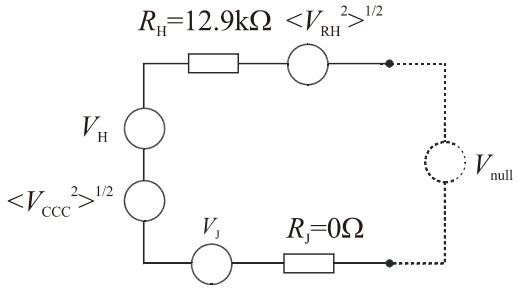

Figure 7.4- *Equivalent noise circuit of the metrological triangle.*

e.g., $<i_P^2>^{1/2}$=1 pA.turn/Hz$^{1/2}$, then $<V_{CCC}^2>^{1/2}$=13 nV/Hz$^{1/2}$. The Josephson element has a "zero" resistor associated, since the voltage steps are perfectly vertical. Resuming, the noise over signal ratio of this system is:

$$\frac{<V_\Delta^2>}{V_H} = \frac{\sqrt{(<i_P^2>^{1/2} R_H) + (4k_B T R_H)}}{I_{SET} N_{CCC} R_H} \approx \frac{<i_P^2>^{1/2} / N_{CCC}}{I_{SET}} = \frac{<I_P^2>^{1/2}}{I_{SET}} . \quad (7.12)$$

The expression has been simplified, considering that the Hall resistance thermal noise is negligible with respect to the noise introduced by the CCC-SQUID system. Thus, in order to enhance the signal over noise one must either, i) obtain a larger quantized current, I_{SET}, or ii) reduce the current noise of the CCC-SQUID, $<I_P^2>^{1/2}=<i_P^2>^{1/2}/N_{CCC}$.

The final uncertainty in the closure of the triangle u_Δ would be thus determined by the uncertainty in the amplification of the current in the CCC-SQUID, which was calculated in section 6.2.3:

$$u_\Delta = u_I = \frac{\sigma_{I,av}}{I_{SET}} = \frac{1}{I_{SET}} \cdot \frac{1}{\sqrt{N_{rep}}} \left[\int_{BW} <I_P^2> df \right]^{1/2} . \quad (7.13)$$

7.4. QMT uncertainty expectations

The final uncertainty that could be reached in the triangle experiment will depend mainly (Eq. 7.13) on the magnitude of the quantized current available and the current noise in the CCC-SQUID system. A comparative study of the levels of current uncertainty reached by the different CCC-SQUIDs currently available is difficult because $\sigma_{I,av}$ depends on the particular conditions (the current reversal frequency f_{S1}, sampling frequency f_{S2} and total measurement time t_T) utilized in the experiment. Table 7.3 summarizes the $\sigma_{I,av}$ levels

							u_Δ		
Ref.	f_{S1}	f_{S2}	$<I_P^2>^{1/2}$	t_T	N_{rep}	$\sigma_{I,av}$	I_{SET}=1pA	I_{SET}=10pA	I_{SET}=1nA
NPL,II	0.02Hz	?	6 fA/Hz$^{1/2}$	1 h	10	3 fA	3.10^{-3}	5.10^{-4}	5.10^{-6}
LCIE	0.3Hz	0.4Hz	4 fA/Hz$^{1/2}$	1 h	1000	(50 aA)	5.10^{-5}	5.10^{-6}	5.10^{-8}
Thesis	0.1Hz	0.1Hz	3 fA/Hz$^{1/2}$	2 h	720	35 aA	3.10^{-5}	3.10^{-6}	3.10^{-8}

Table 7.3- *Current standard deviation $\sigma_{I,av}$ using the CCC-SQUID amplifiers from Refs. 17,19 and the 1:30000 system of this thesis. The $\sigma_{I,av}$ levels depend on the specific conditions of the experiment: the reversal frequency of the current f_{S1}, the recording frequency f_{S2}, the current noise at the frequency f_{S1} (calculated for the maximum ratio N_{CCC} available) $<I_P^2>^{1/2}$ and the number of measurement N_{rep} in the total recording time t_T. The uncertainty levels that could be reached in the final closure of the triangle, u_Δ, depending on the magnitude of the quantized current available, are given.*

reported[17,19] in measurements with two different CCC-SQUID systems. Using the 1:30 000 CCC-SQUID system of this thesis, a $\sigma_{I,av}$ standard deviation of ~35 fA for a 2 h experiment could be reached (6.2.3). Using today's best SET device, capable of giving a current of 6.4 pA (Table 7.1), and our CCC-SQUID system, the triangle might be closed with an uncertainty of ~10^{-6}. If SET technology improves enough to provide quantized currents ~1 nA (with metrological accuracy), the triangle could be finally closed with parts in ~10^{-8}. This will allow checking the consistency of the three electrical quantum standards, and the fundamental constants involved to that level of uncertainty.

References

[1] B.D. Josephson, *Phys. Rev. Lett*. **1**, 251 (1962).
[2] K. v Klitzing *et al*., *Phys. Rev. Lett*. **45**(6), 494 (1980).
[3] F. Piquemal and G. Geneves, *Metrologia.* **37**(2), 207(2000).
[4] E. Bartolomé *et al*., *Proc. of the 4th Workshop on Low Temperature Electronics*, ESA, Nordwijk (1999).
[5] M.W. Keller *et al*., *Science.* **285**, 1706 (1999).
[6] A.M. Thompson and D.G. Lampard, *Nature (London).* **177**, 888 (1956).
[7] L.J. Geerlings, *Phys. Rev. Lett*. **64**(22), 2691 (1990).
[8] H. Pothier *et al*., *Europhys. Lett*. **17**(3), 249 (1992).
[9] S.V. Lotkhov *et al*., *Appl. Phys. Lett.* **78**, 946, (2001).
[10] J.M. Martinis *et al*., *Phys Rev. Lett*. **72**(6), 904 (1994).
[11] H. Pothier, PhD Thesis, University of Paris 6 (1991).
[12] M.W. Keller *et al*., *Appl. Phys. Lett.* **69**(12), 1804 (1996).
[13] H.D. Jensen *et al*., *Phys. Rev. B.* **46**(20), 13407 (1992).
[14] J.M. Shilton *et al*., *J. Phys. Condens. Matt*. **8**, L531 (1996).
[15] J. Ebbecke *et al*., *Appl. Phys. Lett*. **77**(16), 2601 (2000).
[16] A. Hartland, *Proc. of the International Conference on Electromagnetic Measurements*, **18**, 1 (1993).
[17] T.J.B.B. Janssen and A. Hartland, *IEE Proc. Sci. Meas. Technol*. **147**(4), 174 (2000).
[18] J. T. Janssen *et al*., SETamp/EUROMET meeting, Paris 14-16 september (1999).
[19] F. Gay *et al*., *Rev. Sci. Instru*m. **71**(12), 4592 (2000).
[20] F. Gay, PhD Thesis, Conservatoire National des Arts et Métiers, (2000).
[21] Y. De Wilde *et al*., *IEEE Trans. Instrum. Meas*. **50**(2), 231 (2001).
[22] F. Delahaye and D. Bournaud, *IEEE Trans. Instrum. Meas*. **40**(2), 237 (1991).
[23] F. Piquemal *et al*., *IEEE Trans. Instrum.* Meas. **48**(2), 296 (1999).
[24] B.W. Petleyn, *Quantum Metrology and fundamental constants* (Edited by P H Cutler & A A Luces), New York, Plenum (1983).
[25] Kohlmann *et al*., *IEEE Trans. Appl. Supercond*. **7**(2), 3411 (1997).
[26] C.A. Hamilton *et al*., *IEEE Trans. Instrum. Meas*. **44**(2), 223 (1995).
[27] S.P. Benz *et al*., *Appl. Phys. Lett*. **71**(13), 1866 (1997).
[28] H. Schulze et al., *IEEE Trans. Appl. Supercond*. **9**(2), 4241 (1999).

Appendix A

SIMPLIFIED CALCULUS FOR THE DESIGN OF A CCC

The ultimate current noise a CCC, which is reached in the direct-coupling configuration was shown to be (Eq. 1.46): $\langle i_P^2 \rangle = 8\varepsilon/(k_{sq}^2 N_{CCC}^2 L_{CCC,eff})$. Thus, for a fixed number of primary turns N_{CCC}, the optimum CCC will be the one with maximum effective self-inductance $L_{CCC,eff}$. The optimization of $L_{CCC,eff}$ with respect to the distance to the CCC superconducting shields, based on different numerical methods has been the subject of several papers[1,2,3]. Numerical methods have proven to give accurate results but are time-consuming and not straightforward to use. Besides the underlying physics of the problem is hardly seen. In this Appendix we will derive a very simple condition for the optimization of $L_{CCC,eff}$. We will use a numerical simulation to validate our intuitive approach. The "rule of thumb" obtained simplifies considerably the design of the CCC and its surrounding shielding[4].

- ***Design of an optimum CCC***

The inset of Figure A.1 shows the CCC surrounded by the superconducting shield, and the relevant dimensions for the optimization problem. The cross section of the CCC tube, hxw, will be fixed by the number of primary turns and the diameter of the wire used. We are interested in the dependence of $L_{CCC,eff}$ with the internal radius R. $L_{CCC,eff}$ increases with R; however, when the side of the CCC tube comes close to the superconducting shield, a rapid decrease in $L_{CCC,eff}$ is observed. Thus, the design of the optimal CCC and shielding implies to solve one of the two following equivalent problems:

i) For a fixed R_{shield} (which may be limited by the internal diameter of the cryostat), what is the value of R that makes $L_{CCC,eff}$ maximum ?

ii) If the windings and overlapped tube have already been constructed, one would like to reduce the R_{shield} as much as possible to be less sensitive to external magnetic fields. Thus one would like to know what is a reasonable value for R_{shield} such that the effective inductance $L_{CCC,eff}$ is not too much decreased.

• ***Calculations***

Figure A.1 shows the calculated value of $L_{CCC,eff}$ vs. R for h=w=10 mm, H_{shield}=80 mm and R_{shield}=60 mm following the method described in Ref. 3. An initial increase of $L_{CCC,eff}$ as function of R is observed until a maximum is reached, and then it rapidly decreases towards zero when the overlapped tube approaches the shield. The maximum value that R may take is (L_{shield}-w). Our objective is to understand why the maximum appears, and to find the geometrical condition that fulfills this point.

The insets of Figure A.1 shows the distribution of magnetic flux lines[3] for different values of R: before the maximum (R=20 mm), at the maximum (R=40 mm) and after the maximum (R=48 mm). Flux lines are all contained inside the superconducting shield. Flux that crosses the internal area of the overlapped tube (A_{int}=πR^2) returns via the space existing between the overlapped tube and the shield, A_{ext}=[π R_{shield}^2]-[π(R+w)^2].

Shielding currents in the superconducting shield are responsible for the decrease in $L_{CCC,eff}$ when R approaches (R_{shield}-w). The shielding current density in a point of the shield is proportional to the value of the magnetic flux density at that point. When the overlapped tube approaches the shield, the shielding current increases considerably because the flux lines have less space, and hence a high flux density is created. Intuitively, one should expect the maximum value of $L_{CCC,eff}$ to happen for the value of R such that flux lines can follow paths with no constrictions in the transversal area. Thus, provided that we do not

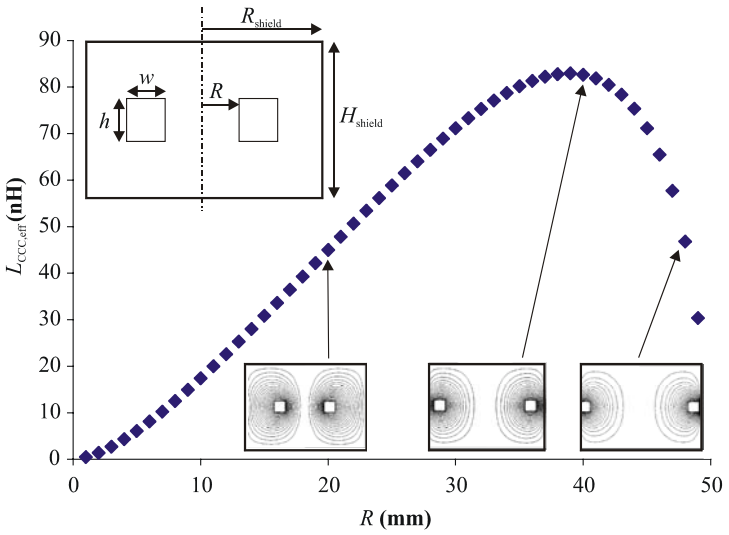

Figure A.1- *Inset above: CCC and shielding dimensions. Calculated values of $L_{ccc,eff}$ vs. the internal radius R, for h=w=10 mm, H_{shield}=80 mm and R_{shield}=60 mm. The maximum value for R is (R_{shield}-w)=50 mm. The inset figures show the flux lines distribution for R =20 mm, 40 mm and 48 mm. The compression of flux lines towards the shield is clearly seen when R approaches its maximum value, Due to this effect, high shielding currents are created that make $L_{ccc,eff}$ to go down.*

compress flux lines with the top and bottom part of the shielding, the maximum value of $L_{CCC,eff}$ will occur when $A_{int}=A_{ext}$:

$$\pi R^2 = \pi R_{shield}^2 - \pi(R+w)^2. \tag{A.1}$$

For a given R_{shield} and w, Eq. A.1 allows to calculate the value of R that makes $L_{CCC,eff}$ maximum:

$$R(L_{CCC,eff,Max}) \equiv R_{opt} = \frac{1}{2}\left[\sqrt{2R_{shield}^2 - w^2} - w\right]. \tag{A.2}$$

On the other hand, for a given R and w, Eq. A.1 allows the calculation of the minimum value of R_{shield} for which the shielding effect still is not very high:

$$R_{shield},\min \equiv \sqrt{2R^2 + w^2 + 2Rw}. \tag{A.3}$$

Note that this approach is only exactly valid when the flux density inside the areas A_{int} and A_{ext} is homogeneous. This will not be the case for arbitrary dimensions. For example, when h, w are much smaller than R, R_{shield}, the magnetic flux density will be higher near the overlapped tube, decreasing inversely with the distance. Nevertheless, the dimensions of typical CCC's are such that h, w, R, R_{shield} are of the same order, hence we believe that our approach will be a good approximation.

In order to validate this intuitive approach, we have numerically calculated (as described in Ref. 3) the dependence of $L_{CCC,eff}$ as a function of $A_{int}/(A_{int}+A_{ext})$ for several cases with dimensions that are typical in the construction of a CCC. The studied cases are summarized in Table A.1.

Figure A.2 shows the results of the calculations. For each case (h, w, H_{shield}, R_{shield}) the values of $L_{CCC,eff}$ have been normalized with the value of $L_{CCC,eff}$ at the maximum. It follows from the figure that the value of $L_{CCC,eff}/L_{CCC,eff,Max}=1$ appears in all cases in the proximity of $A_{int}/(A_{int}+A_{ext})=0.5$ (i.e. when $A_{int}=A_{ext}$). A zoom of the region around the maximum is shown in the inset of the figure. It can be observed that when the condition $A_{int}=A_{ext}$ holds, then $L_{CCC,eff}$ equals $L_{CCC,eff,Max}$ within less than 2% for all the studied cases. In the practical

h x w (mm^2)	R_{shield} (mm)	H_{shield} (mm)	R_{opt} (mm)	$L_{ccc,effmax}$ (nH)
10 x 10	30	80	15	22.7
10 x 10	40	80	23	40.6
10 x 10	50	80	31	60.9
10 x 10	60	80	39	82.9
15 x 15	30	80	12	12.3
15 x 15	40	80	19	21.8
15 x 15	50	80	27	41.8
15 x 15	60	80	35	59.3
20 x 20	30	80	8	5.8
20 x 20	40	80	16	16.2
20 x 20	50	80	23	29.1
20 x 20	60	80	31	43.6

Table A.1- *Summary of the relevant dimensions in the different cases studied.*

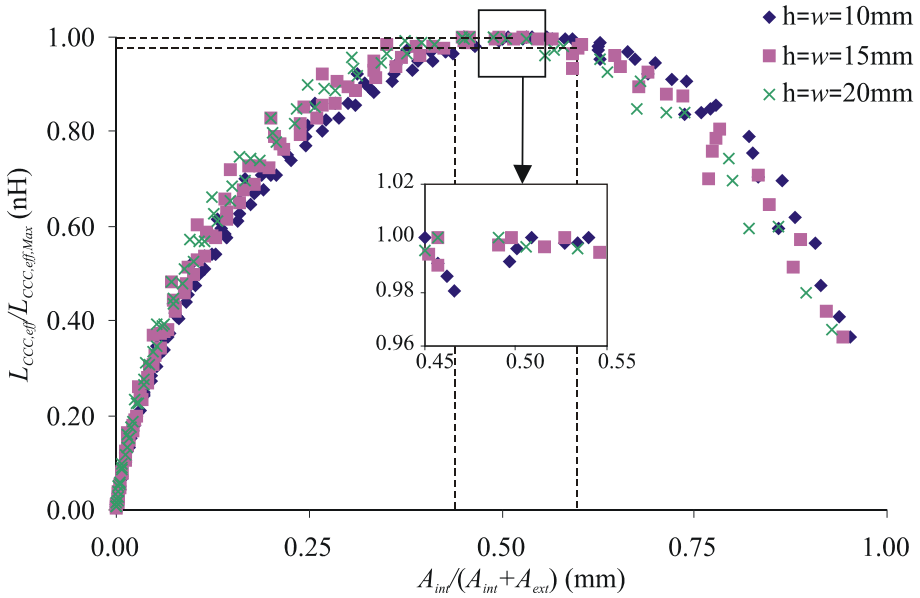

Figure A.2- *Values of $L_{CCC,eff}$ calculated for the geometries shown in Table A.1. $L_{CCC,eff}$ has been normalized to the maximum $L_{CCC,eff,max}$. The inset shows an amplification of the region around $A_{int}/(A_{int}+A_{ext})$.*

fabrication of a CCC, it might haven that one cannot exactly achieve: $A_{int}=A_{ext}$. Observe though that if the two areas are only ~30% from being equal, the self-inductance is still ~3% from the maximum.

- ***Conclusions***

Following physical arguments, we have deduced a simple geometrical condition that should be fulfilled to maximize the inductance of the overlapped tube inside the superconducting shield. Using numerical calculations, we have shown that when this condition holds, the effective self-inductance approaches its maximum within less than 2% for typical CCC dimensions. Our approach simplifies considerably the calculations for the design of an optimum CCC.

References

[1] G.T. Symm, in *Proc. Boundary Elements XIV: Field Problems and Applications*, **1**, Eds. C.A. Brebbia, J. Dominguez and F. Paris, 519 (1992).
[2] M.D. Early and K. Jones, *IEEE Trans. Instrum. Meas*. **46**, 459 (1997).
[3] J. Sesé *et al*., *IEEE Trans. Instrum. Meas*. **48**(6), 1306 (1999).
[4] paper in preparation for *IEEE Trans. Instr. Meas*.

Appendix B

COMMENTS ON FORWARD ESTIMATE OF THE SENSITIVITY OF A CCC

The sensitivity of the CCC, $S_{CCC}=\Phi_{sq}/I_e$, is determined by the mutual inductance between the input coil and the SQUID, $M_i=\Phi_{sq}/I_s$, multiplied by the magnitude $T\equiv I_s/I_e$. For a given CCC geometry and SQUID, the goal is to maximize S_{CCC} as a function of N_s. From flux conservation in the flux transformer, T can be expressed as:

$$T = \frac{M_{ov,s}}{L_{s,eff} + L_i}, \tag{B.1}$$

where $M_{ov,s}$ is the mutual inductance between the superconducting overlapped tube and the sensing coil, and $L_{s,eff}$ is the effective inductance of the sensing coil in the presence of the superconducting tube. Both are related with $L_{CCC,eff}$, which is the inductance of the superconducting overlapped tube placed inside a superconducting magnetic shield (see Appendix A).

There is a fundamental limit for T given by the fact that the maximum flux (energy) that can be transferred with a flux transformer is 1/2 of the detected flux (1/4 of the detected energy). In the equivalent circuit of Figure 1.18, this can be expressed by $T/\sqrt{L_{CCC,eff}/L_i} \leq 0.5$. This limit is only reached when, ideally, all the flux generated by I_e is picked-up by L_s. This implies also that $N_s\sqrt{L_{CCC,eff}/L_i} = 1$. More generally, if we call $T'=T/\sqrt{L_{CCC,eff}/L_i}$, and $x=N_s\sqrt{L_{CCC,eff}/L_i}$, in the ideal case T' takes the universal form:

$$T' = \frac{x}{x^2+1}. \tag{B.2}$$

Therefore, for given L_i and $L_{CCC,eff}$ values, one can easily determine the optimum N_s ($x_{max}=1$) and the problem of maximizing T' is solved.

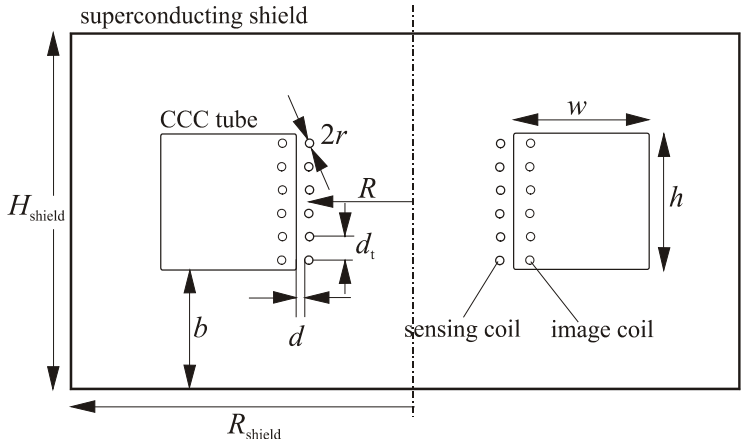

Figure B.1- *The CCC (inside the superconducting shield), coupled to the SQUID with a sensing coil of N_s turns. An image of the real sensing coil with respect to wall of the CCC has to be considered, which represents the reaction of the superconducting material to cancel the perpendicular component of the magnetic field in the surface of the CCC open structure.*

However, in practice, the coupling between L_s and $L_{CCC,eff}$ is not ideal and $T'(x)$ does not follow the ideal expression Eq. B.2. On the other hand, $L_{CCC,eff}$ cannot be analytically calculated. There have been several approaches in literature to estimate practical T' values using numerical methods.[1,2,3,4]

Frantsuz[1], gives tables with calculated values of T' for different CCC dimensions and L_i values, so that a CCC designer may always find a similar case already solved. It is very surprising that his calculations for wire sensing coils (which were not experimentally verified), give maximum T'_{max} values of ≈0.25 at x_{max}≈0.5, too far away from the ideal case. Even more surprising is that for wide tape roll coils, the calculations give T_{max} values ≈0.67, well above the theoretical limit (in this case x_{max}≈1).

Sesé *et al.*[2] made experimental measurements of the sensitivity for different x values and found perfect agreement with calculations using finite element methods. They obtained T_{max}≈0.4 at x_{max}=1. They also verified that using wide tape roll T' was improved by a factor of 10%.

Using numerical methods, Early *et al*[3,4] found good agreement between experimental and calculated values, but also too far from ideal, since T_{max} was ≈0.16.

The origin of the above discrepancies cannot be understood in the absence of analytical approaches for the calculation of $T'(x)$. Here we will show the analytical conditions under which analytical expressions for T'(x) could describe the experimental and numerical results[5].

- ***Analytical expression for the sensitivity of a CCC***

It was already demonstrated[6] that $M_{ov,s}$ and $L_{s,eff}$ can be written as:

$$M_{ov,s} = kN_s L_{CCC,eff}\,, \tag{B.3}$$

$$L_{s,eff} = L_s(1-k') + kN_s^2 L_{CCC,eff}\,, \tag{B.4}$$

where L_s is the nominal self-inductance of the coil; k' is the coupling constant between the real coil and its image in the CCC open structure; $L_{CCC,eff}$, is the effective self-inductance of the CCC, as if it were closed, in the presence of the closed shield; and k is a geometrical parameter that relates the flux picked-up by the sensing coil when a current is circulating in the open cylinder.

The first term in Eq. B.4 is the reduction of the nominal self-inductance due to the coupling between the real and the image coils. The image coil represents the reaction of the superconducting material to cancel the perpendicular component of the magnetic field in the surface of the open cylinder. For $d/R<<1$ the image coil can be approximated by a concentric coil (Figure B.1) inside the superconductor at a distance d from the surface, which carries a current equal in magnitude, but opposed to that of the real coil. In our approximation the magnetic field created by the real and image coils at the surface of the closed cylinder is negligible, so this cylinder is not relevant for the calculation of k'. k' can then be estimated from the magnetic vector potential created by a circular loop. For $N_s>1$ the various terms which appear due to the coupling between each turn of the real coil with all the turns of the real and image coils have to be added.

The second term in Eq. B.4 takes into account that the cylinder is not closed and its origin is justified in the following. Since no net current can flow in the open cylinder, the surface reaction current, represented by the current in the image coil, has to be compensated by an opposite current distributed over the whole surface, thus having the same direction as the current in the real coil. This compensating surface current will circulate through the effective inductance $L_{CCC,eff}$ and will produce a flux that will be picked-up by the sensing coil. A typical situation in which only a term like this second one is used is the calculation of the input coil inductance of a planar integrated SQUID, that is approximated by n^2L_{SQ} where n is the number of turns of the input coil and L_{SQ} is the SQUID ring self-inductance. We stress that if the open cylinder were closed, only the first term in Eq. B.4 would exist, because it accounts for the well known reduction of the self-inductance of a coil inside a superconducting closed cylinder. The calculations of $L_{S,eff}$ and k have been explained and their meanings clarified in Sesé *et al*.[6]

For $d/R<<1$, one can consider k~1, and using Eq. B.1 and B.3-4, T' takes the form:

$$T' = \frac{x}{x^2 + 1 + \dfrac{L_S(1-k')}{L_i}}. \tag{B.5}$$

T' depends on N_s through x and the $L_s(N_s)$ and k'(N_s) dependences.

• ***Particular cases and discussion***

In the following, we will try to obtain analytical expressions for $T'(x)$ in particular cases in which the term $L_s(1\text{-k'})$ can be written as function of x. Obviously the ideal case given by Eq. B.2 is reproduced when k'=1, i.e., perfect coupling.

When the different turns of the sensing coil are far away from each other ($d_t >> d$) and very close to the CCC side, each coil is only coupled to its own image, and not to the rest of real and image turns. Thus,

$$L_S(1-k') = N_S A_S (1-k_S'), \tag{B.6}$$

where A_s and k_s' are the single turn inductance and coupling constant of the real coil with its own image. Then Eq. B.5 takes the form:

$$T' = \frac{x}{x^2 + \mathrm{a}x + 1}, \qquad \text{with a} \equiv \frac{A_S(1-k_S')}{\sqrt{L_{CCC,eff} L_i}}. \tag{B.7}$$

This expression has a maximum $T'_{max}=1/(2+a)$ at $x_{max}=1$. Using (Eq. B.7) we can justify the experimental results and numerical calculations of Sesé *et al*. This is nicely demonstrated in Figure B.2, where the experimental data have been fitted with Eq. B.7, with a=0.56.

In the (theoretical) case that all the turns are wound coincidentally ($d_t=0$), then each single turn is coupled to all the others and all the image turns. Hence,

$$L_S(1-k') = N_S^2 A_S (1-k_S'), \tag{B.8}$$

and Eq. B.5 takes the form:

$$T' = \frac{x}{(1+\tilde{\mathrm{a}})x^2 + 1}, \qquad \text{with } \tilde{\mathrm{a}} \equiv \frac{\mathrm{a}}{\sqrt{L_{CCC,eff} / L_i}}. \tag{B.9}$$

This expression has maximum $T'_{max}=1/2(\sqrt{1+\tilde{a}})$ at $x_{max}=1/\sqrt{1+\tilde{a}}$. Taking Eq. B.9 with ã=4.5 we can explain the results of Frantsuz (Figure B.2); he found T'_{max} at $x_{max}\approx 0.52$.

Frantsuz suggested that T' could be improved using wide tape roll, since he calculated values $T'>0.5$. The improvement due to the use of tape instead of wire has been experimentally demonstrated by Sesé *et al*.[2] In fact, a 10% increase is easily obtained (see Figure B.2). But the prediction of $T'>0.5$ by Frantsuz must be due to an error on his numerical calculation, since T' can not be larger than 0.5. The low T' values (≈0.25) obtained by this author when using wire coils were due to the fact that he used the approximation that all coil turns were placed at one point. By simply distributing the turns over the inner (or outer) CCC surface T' can be improved up to ~0.4, as numerically and experimentally demonstrated by Sesé *et al*.[2], and by the analytical expression (Eq. B.9) in this work. Sesé *et al.*[7] also demonstrated that soldering the flux transformer directly to the CCC, the values of T' are those given by the ideal sensitivity expression (Eq. B.2).

Based on all these arguments, tables given by Frantsuz should not be used to optimise T'. Instead we propose the following design guidelines for optimisation of the sensing coil, once a low noise SQUID has been selected:

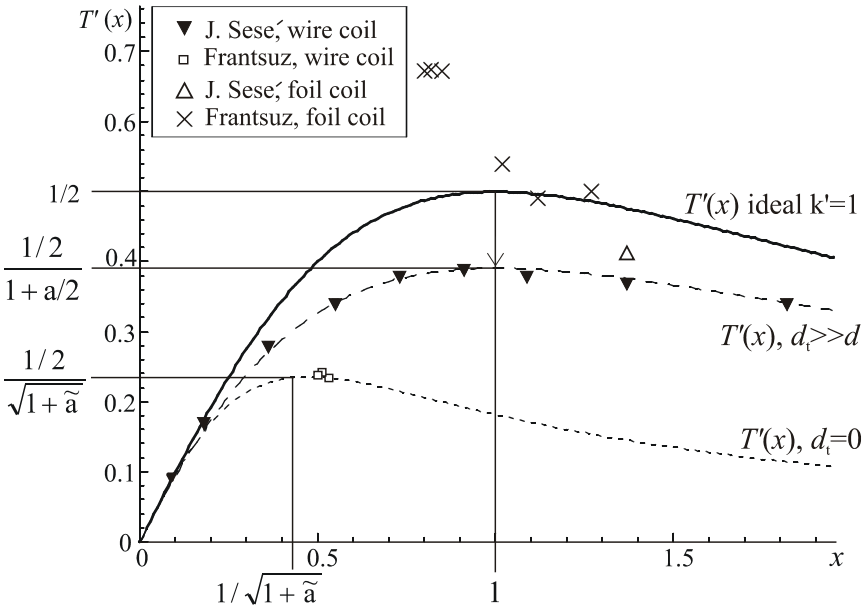

Figure B.2- *Dimensionless sensitivity T' as function of the reduced parameter x. Experimental data from Sesé et al., using a sensing coil made of wire coil(▼), fitted with Eq. B.7 , and using lead foil (Δ). Numerical calculations from Frantsuz using wire coil (□), fitted with Eq. B.9, and lead foil (x).*

1. Determine the maximum CCC size, following guidelines given in Appendix A.
2. Determine $L_{CCC,eff.}$ This can be done by measuring T' with direct connection of the flux transformer, and obtaining $L_{CCC,eff}$ from Eq. B.2. Alternatively one can use the eddy screening current impedance method at room temperature[8] explained in section 6.1.1.
3. Determine the optimum number of sensing coil turns N_s from the point $x_{max}=1$.
4. Place the N_s turns over the CCC side as widely distributed as possible, so that $d_t>>d$.

References

[1] E.T. Frantsuz, *Metrologia.* **35**(6), 847 (1998).
[2] Sesé *et al*., *IEEE Trans. Instrum. Meas*. **48**(6), 1306 (1999).
[3] M.D. Early and K. Jones, *IEEE Trans. Instrum. Meas*. **46**, 459 (1997).
[4] M.D. Early and M.A. van Dam, *IEEE Trans. Instrum. Meas*. **48**(2), 379 (1999).
[5] paper in preparation for *Metrologia.*
[6] J. Sesé *et al*., *IEEE Trans. Appl. Superc,* **9**(1), 58 (1999).
[7] J. Sesé *et al*., *IEEE Trans. Appl. Superc.* **9**(2), 3487 (1999).
[8] G. Rietveld *et al*., *Sens. Act. A*. **A85**(1-3), 54 (2000).

Appendix C

INTEGRATED TWO-STAGE (WITH RS DROS 2ND STAGE) FOR CCC-SQUID READOUT

The Two-Stage system, presented in section 4.3, was formed by two separate chips: the 1st , sensor chip was one of the SQUIDs for CCC (from Chapter 3), and the 2nd, amplifier chip was a DROS with reference junction. Based on the same operation principle, a completely integrated (on a single chip) Two-Stage system for the readout of a CCC has been designed (Figure C.1). The layout of this chip is similar to the integrated Two-Stage system reported in Ref. 1. The 1st stage is a dc SQUID with an input coil inductance able to match the CCC, L_i~80 nH. Two different versions have been designed, with McCumber parameters β_c=0.3 and 0.6, designed to attain (white) noise levels of $S_{\Phi,1}^{1/2}$~0.8 and 1.2 $\mu\Phi_0/Hz^{1/2}$ respectively. The correct operation of Two-Stage chips using a DROS with reference junction (RJ DROS) can be hindered by a different-than-designed value of the ref. jj critical current, due for instance to rounding of the small junction during the fabrication process. To avoid this problem, we decided to include in our integrated Two-Stage a DROS with reference SQUID as 2nd stage (RS DROS). In this way the critical current of the reference SQUID can be tuned to fall in the middle of the current modulation of the signal SQUID, and the optimal DROS transfer can be obtained. For that purpose, some properties of the RS DROS were further investigated.

• *RS DROS optimum operation points*

For our study we considered a gradiometric RS DROS developed in the past[2], with similar characteristic as the DROS presented above. Assume that the RS DROS forms part of a Two-Stage system with total flux gain G_Φ, and 1st stage (biased at point $I_{b,1}$) with noise $S_{\Phi,1}^{1/2}$. The optimal operation bias point $I_{b,2}$ of the 2nd stage DROS should be such that (see section 4.1): i) the DROS voltage-to-flux transfer $\partial V/\partial\Phi_2$ is large enough to guarantee that the preamplifier contribution to the noise $S_{\Phi,preamp}^{1/2}$ is negligible, and ii) the 2nd stage flux noise $S_{\Phi,2}^{1/2}$ adds a small contribution to the total noise.

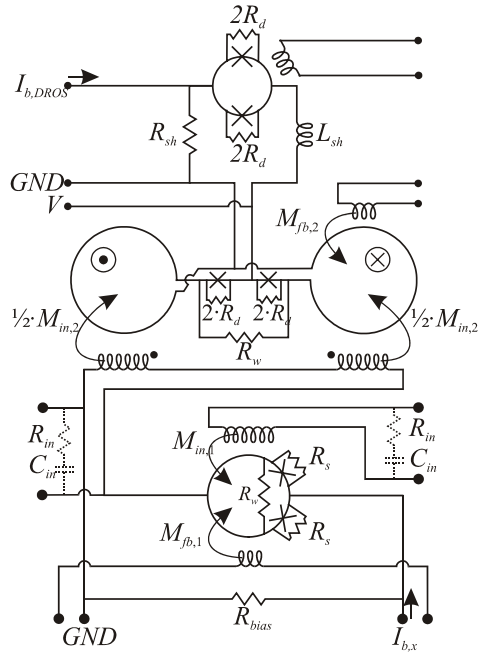

a)

	1st stage SQUID for CCC	2nd stage Ref. SQ DROS
		Reference SQUID
	A=4x4 μm^2	A=2x4 μm^2
	$2I_0$=12.9 μA	I_0=4.5 μA
	C_{sq}=1.0 pF	β_{ref}=1
	D=60 μm	
	L_{sq}=160 pH	Signal SQUID
	β=1	A=2x4 μm^2
		$2I_0$=6 μA
	i. fb: 3/4 turn	C_{sq}=0.5 pF
	i. coil: 26 turns	R_w=6 Ω
	L_i=80 nH	D=2x50 μm
	M_i=2.3 nH	L_{sq}=550 pH
		β_{ref}=1.6
	β_c = 0.6;0.3	*i. coil:* 2x25 turns
	R_{sh}= 9; 6 Ω	L_i=150 nH
	R_d= 11; 11 Ω	M_i=6.7 nH
		i. fb: M_{fb}=220 pH
	$dV/d\Phi_{sq}$=78; 56 μV/Φ_0	$dV/d\Phi_2$=0.7-1 mV/Φ_0
	$S_\Phi^{1/2}\approx$ 0.8;1.2 μΦ_0/Hz$^{1/2}$	$S_\Phi^{1/2}$~5.0 μΦ_0/Hz$^{1/2}$

b)

Figure C.1- *a) Schematics of the integrated Two-Stage formed by a SQUID for CCC as 1st stage and a DROS with reference SQUID as 2nd stage; b) Main characteristics of the SQUID and RS DROS.*

We studied first the ***RS DROS transfer function.*** $\partial V/\partial \Phi_2$ was measured as a function of the DROS bias current $I_{b,2}$, while the flux applied to the reference SQUID was constant (Figure C.2). According to theory[2,3] the maximum bias current $I_{b,2}$, at which a DROS works correctly is given by:

$$I_{b,\max} = \frac{2I_0}{\sqrt{\beta_c^*}} \cdot \sqrt{\frac{I_0 \Phi_0}{\pi C_{sq}}}, \qquad \beta_c^* = \frac{2\pi \cdot 2I_0 \cdot R_{sh}^2 \cdot C_{sq}}{\Phi_0}. \tag{C.1}$$

We observed typical DROS behavior up to a $I_{b,max}$~30.4 μA. Above $I_{b,max}$, the relaxation oscillation mechanism should stop because the hysteretic SQUID is unable to switch to the superconducting state. JSIM simulations of a RS DROS predict this effect too. In practice, thermal excitations allow the signal SQUID to jump to the superconducting state. Therefore, the DROS still operates above $I_{b,max}$, although the transfer function is much smaller. This cannot be observed in the simulations, which do not include thermal effects.

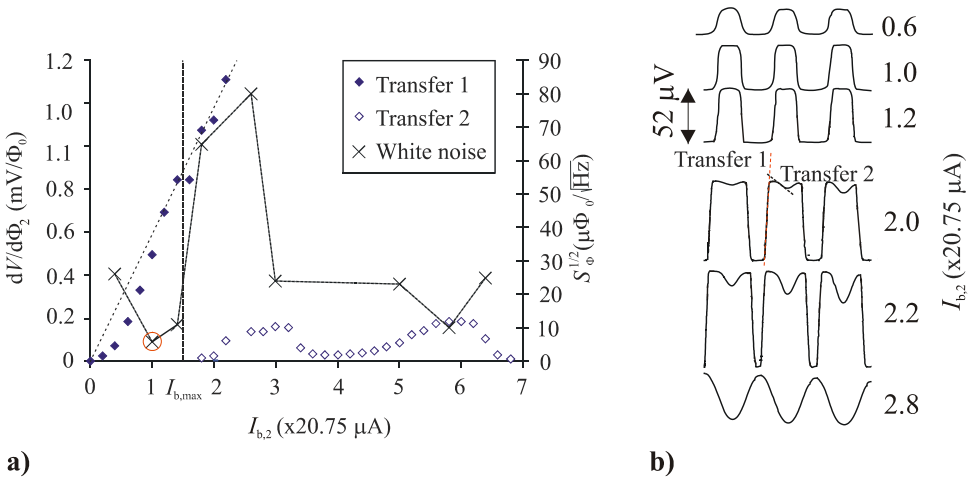

Figure C.2- *a) Transfer function of a RS DROS for different $I_{b,2}$ bias points. The white noise levels at some of the points are shown. (The line connecting them is just a guide for the eye); b) RS DROS V-Φ curves for different $I_{b,2}$ and constant flux Φ_{ref} applied to the reference SQUID.*

The maximum output voltage swing of a DROS is given by: $V_{c,max}$=KI_b.R_{sh}, where the proportionality factor K is typically ~(0.5..0.75). We measured a maximum $V_{c,max}$~53μV, that results in a factor K~0.87. Up to $I_{b,max}$, the transfer $\partial V/\partial\Phi_2$ is expected to increase as:

$$\frac{\partial V}{\partial \Phi_2} = g \cdot \frac{I_0^{2/3}}{(1+\beta_{sig})} \cdot \frac{V_c}{\Phi_0}, \qquad g \approx \frac{1.72}{\alpha} = 7 \cdot 10^4 \ \mathrm{A}^{-2/3} \ @4.2\,\mathrm{K}, \tag{C.2}$$

where α is a fit parameter obtained from numerical simulations, that describes the thermal spread of the critical current ΔI_0:

$$\Delta I_0 = \alpha \cdot I_0^{1/3}, \qquad \alpha \approx 2.5 \cdot 10^{-5} \ \mathrm{A}^{-2/3} \ @4.2\,\mathrm{K}. \tag{C.3}$$

Substituting our particular DROS parameters and V_c ($I_{b,DROS}$) dependence into Eq. C.2, we obtain:

$$\frac{\partial V}{\partial \Phi_2} = \mathrm{C}' \cdot I_{b,2} \approx 10.2 \cdot I_{b,2}[\mu\mathrm{A}] \ [\mathrm{V}/\Phi_0]. \tag{C.4}$$

Experimentally, the proportionality factor is larger (C'~28), probably because Eq. C.2 does not exactly hold anymore for DROSes with extreme parameters. When the junctions have a small C and I_0 (like it is our case), α becomes smaller[3], and C' increases. We found a spread factor α =8.8x10^{-6} A$^{2/3}$ at 4.2 K.

For applications in which the DROS has to work at temperatures lower than 4.2 K (e.g., in order to use the Two-Stage for the readout of a Gravitational Wave antenna at mK temperatures), it is important to know the transfer dependence with temperature. According

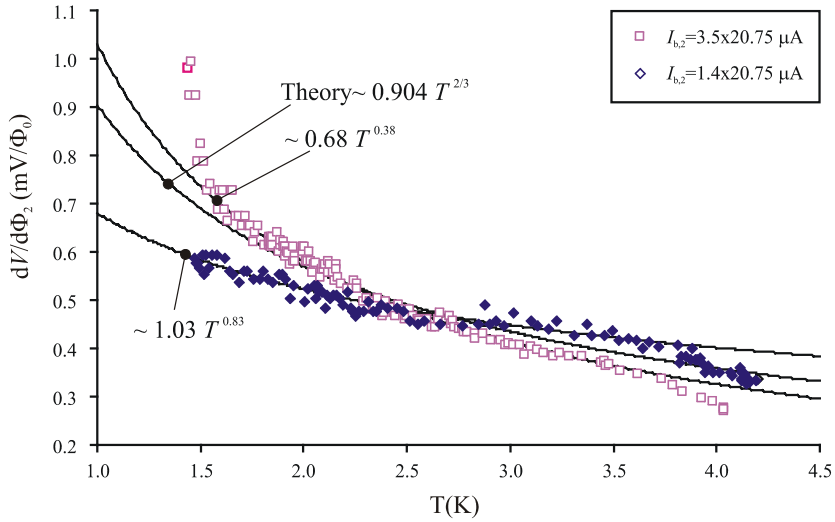

Figure C.3- *Temperature dependence of the RS DROS transfer function at two different bias points $I_{b,2}$ respectively smaller and larger than $I_{b,2}$, and theoretical expectations.*

to theory, the DROS transfer should increase with decreasing temperature, as a consequence of a smaller spread in the critical current. From Eq. C.3-C.4 the following theoretical dependence would be expected:

$$\frac{\partial V}{\partial \Phi_2}(T) = 0.904 \cdot T^{2/3} \ [\mathrm{mV}/\Phi_0]. \qquad \text{(C.5)}$$

We measured the DROS transfer dependence from 4.2 K to 1.6 K at two different bias points, respectively below and above $I_{b,max}$ (Figure C.3). Experimentally, we observed that at $I_{b,2}$=1.4x20.75 μA<$I_{b,max}$ the $\partial V/\partial\Phi_2(T)$ dependence was smaller than expected, whereas at $I_{b,2}$=3.5x20.75 μA>$I_{b,max}$ it was larger. The explanation for this effect has not been completely clarified yet. However, an important conclusion is that thanks to the increasing $\partial V/\partial\Phi_2(T)$ dependence, a DROS with insufficiently high transfer to work in Two-Stage at 4.2 K, could still be usable at a lower temperatures.

The ***noise*** in FLL of the RS DROS was measured at different values of $I_{b,2}$ (Figure C.2a). The white noise level increases as $I_{b,2}$ approaches $I_{b,max}$. For bias points such that the transfer is smaller than ~0.2 mV/Φ_0, the noise is dominated by the amplifier. The most suitable point to operate in Two-Stage would be $I_{b,2}$~1x20.75 μA, at which the transfer is moderately large ~0.5 mV/Φ_0. and the DROS noise is low $S_{\Phi,2}^{1/2}$~5.7 $\mu\Phi_0/\mathrm{Hz}^{1/2}$. At this point, the DROS V-Φ curves and noise spectra were measured for different values of flux Φ_{ref} applied to the reference SQUID (Figure C.4). The transfer decreases slightly (from 0.6 to 0.4 mV/ Φ_0) and the noise degrades (from 5.6 to 7.0 $\mu\Phi_0/\mathrm{Hz}^{1/2}$) when the reference SQUID is not optimally tuned.

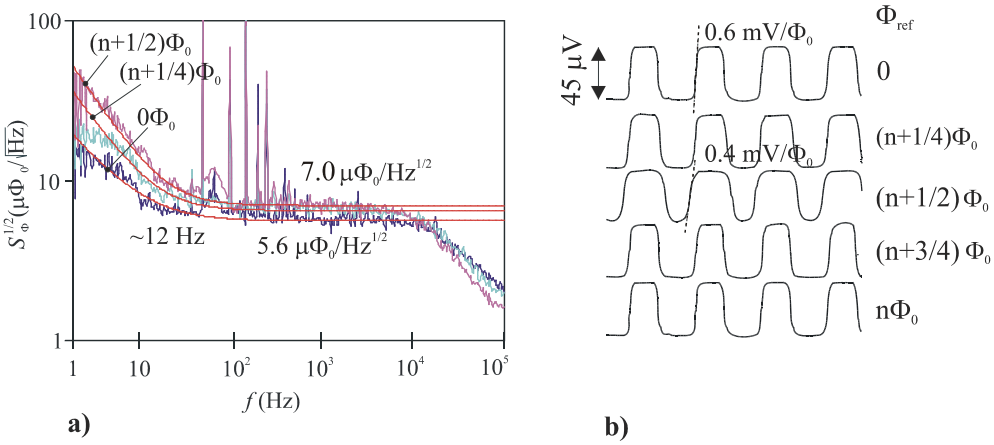

Figure C.4- *a) Noise measurements and b) V-Φ curves for different values of applied flux to the reference SQUID, at $I_{b,2}$=1x20.75 μA.*

References

[1] M. Podt *et al*., *Appl. Phys. Lett*. **75**, 2316 (1999).
[2] M. van Duuren, PhD Thesis, University of Twente, The Netherlands (1998).
[3] D.J. Adelerhof *et al*., *J. Appl. Phys*. **76**, 3875 (1994).

Summary

This thesis describes the development of several systems based on the Cryogenic Current Comparator with optimum SQUID readout, for current and resistance metrology applications. the *CCC-SQUID* is at present the most accurate current comparator available. A (type I) *CCC* consists basically of a superconducting tube containing two sets of windings N_1 and N_2, carrying the two currents I_1 and I_2 to be compared. As a result of the Meissner effect, a screening current equal to (I_2N_2-I_1N_1) circulates in the tube (overlapped "like a snake swallowing its own tail" to shield the windings from the sensing circuit). The flux associated to the unbalance current is coupled to a *SQUID*, the most sensitive flux sensor available nowadays. The SQUID is basically a superconducting ring interrupted by one (rf SQUID) or two (dc SQUID) weak links called Josephson junctions. The device works basically as a flux-to-voltage converter.

The performance of a CCC-SQUID is described by two figures of merit: i) the *ratio error* is the deviation of the currents ratio I_2/I_1 from the ratio winding N_1/N_2, and is due to three sources: flux leakage through the overlap tube gap; resistive current leakage between the primary turns; and capacitive current leakage between the wires. The later limits the operation frequency of the CCC-SQUID to 10^{-3}-1 Hz. Typically, ratio errors better than 10^{-10} can be achieved. ii) The *current noise* depends on the total *system flux noise*, and the *coupling* between the CCC and the SQUID, described by the CCC-SQUID *sensitivity* (or current necessary to be applied to 1 CCC turn to detect $1\Phi_0$ at the SQUID). If a very effective shielding (consisting of several superconducting and ferromagnetic shields) is used, the influence of environmental noise is negligible, and the system noise is determined by the SQUID flux noise, which should be made as low as possible. The CCC-SQUID coupling depends on the relative magnitude of the CCC and the SQUID input coil inductance, which should be thus well known. Due to the image effect, the inductance of the CCC in the presence of its surrounding superconducting shield is reduced to an effective value, $L_{CCC,eff}$, which can be numerically calculated with the help of finite element programs, or measured at room temperature with an impedance meter at sufficiently high frequencies, with an "eddy current" method. We showed that for a given shield size, the CCC geometry that maximizes $L_{CCC,eff}$ is such that the area enclosed by the CCC toroid equals the area between the CCC and the shield.

Two situations can be encountered when coupling a SQUID to a CCC: If L_i<$L_{CCC,eff}$, a "fractional number of turns" sensing coil is needed; the "chariot-wheel" sensing coil

required is only feasible for large fractions (1/2-1/3). Commercial SQUIDs usually have $L_i > L_{CCC,eff}$; thus, a sensing coil with $N_s=(L_i/L_{CCC,eff})^{1/2}$ turns is required. Due to the non-perfect coupling between the CCC and the SQUID, the system (dimensionless) sensitivity decreases. To have the minimum reduction possible, the sensing coil turns should be widely distributed along the CCC side. Also, a ~10% improvement can be obtained using tape roll instead of wire sensing coil. Optimal coupling between the CCC and the SQUID can be reached winding the sensing coil on a set of ferromagnetic cores placed inside the CCC; however additional flicker noise is introduced by the cores. Alternatively, the SQUID input coil can be directly connected to the CCC toroid, in which case optimal coupling is reached per definition. If the CCC and input coil inductances match: $L_i=L_{CCC,eff}$, the maximum, ideal dimensionless sensitivity $S=0.5$ is obtained. The theoretical knowledge learned on the optimization of the CCC-SQUID performance has applied in the development of two different sorts of bridges:

- CCC-SQUID based bridges are used to calibrate secondary resistors to the Quantum Hall Effect primary resistance standard, or to compare secondary resistors between them. The uncertainty reached ($<10^{-8}$) is at least one order of magnitude better than that of room temperature bridges. However, the need for helium recycling facilities to operate the CCC-SQUID bridge has limited their use to a few specialized laboratories. We developed a relatively economic, user-friendly CCC-SQUID system which can be cooled down in a commercial transportable Dewar (periodically refilled outside the user's institute or industry). The CCC-SQUID was mounted on a telescopic insert, allowing the cooling down with a small consumption of liquid helium (~0.5 l). An available commercial rf SQUID was used. The sensing coil needed to couple the SQUID to the CCC was placed on the inner side of the CCC, and shielded with lead foil to avoid the influence of moving trapped flux within the flux transformer. An optimized current controller was build up. Using the "difference compensator" method, a (type A) uncertainty in the comparison of two 100:100 Ω resistors of 7.10^{-9} was achieved. For larger ratio calibrations, a cryoperm shielding (which was not included to keep the budget low) would be indispensable. The simplicity, low cost and better uncertainty level makes the instrument competitive with respect to room temperature comparators. We studied also the feasibility and performance of a CCC-SQUID completely made in YBCO HTS planar technology, that could be cooled down in a small liquid nitrogen dewar. The estimated current resolution (630 pA.turn/$Hz^{1/2}$) might be better than that of room temperature CC's; the main problem is the realization of a good enough shielded structure for the primary turns, that guarantees a ratio error $<10^{-7}$.

- The development of a CCC-SQUID amplifier is essential for the future establishment of a Single Electron Tunneling (SET) quantum current standard. At present, SETs can only deliver very small quantized currents (1-10 pA). For metrology uses, this tiny current has to be amplified to the μA level (without losing the relative uncertainty) with the help of an ultra-sensitive, large-ratio CCC-SQUID. We undertook the development of a complete large ratio (1:30000) CCC with optimum SQUID readout.

Towards improving the CCC-SQUID current resolution, we developed three different types of Nb/Al dc SQUIDs, designed to reach good energy resolution levels, and be able to couple directly to the CCC overlap. The *"CCC matched SQUIDs"* were designed

so as to have input coil inductances close to the CCC self-inductance. Because the SQUID IVC's were practically free of resonances, the noise levels measured agreed well with the design values (~1.3 $\mu\Phi_0/Hz^{1/2}$) at every bias point. As a result of the very "safe" McCumber parameter chosen, β_c~0.02, the SQUID transfer function was quite small ~25 $\mu V/\Phi_0$. The series of *"80ħ SQUIDs"* was aimed to explore SQUIDs with "extremer" parameters, that would push down the energy resolution. Thanks to approaching the McCumber parameter to the hysteretic limit, β_c~1, the SQUID transfer was increased (up to ~400 $\mu V/\Phi_0$). The IVC's were strongly affected by resonances. At the points free of resonances, the measured noise coincided approximately with the designed values (1.0-1.3 $\mu\Phi_0/Hz^{1/2}$), while it was much higher at resonant points. We have demonstrated the operation of *"double-barrier jj based dc SQUIDs"*. The SQUID critical current dependence with temperature could be quantitatively explained in terms of the microscopic theory developed for double-barrier junctions, qualitatively extended to take into account the trapping events at the interlayer. The effective resistance R_{eff}, which determines the SQUID dynamics at 1.4 K has a value between the intrinsic resistance R_N, and the sub-gap resistance R_{subg} at that temperature. The DBSQ was moderately affected by resonances. The best noise level for a DBSQ (3.3 $\mu\Phi_0/Hz^{1/2}$), measured at a point free of resonances, was higher than the noise of the equivalent SBSQ.

Because the SQUID transfer is usually quite small, direct readout of the SQUID with a room temperature amplifier is not possible, and a suitable readout system is required. The above noise levels were measured in a Two-Stage readout system, consisting of a 1st, sensing SQUID, and a 2nd, amplifier Double Relaxation Oscillation SQUID (DROS). Thanks to the large flux-to-voltage transfer attained in a Two-Stage configuration, the room temperature preamplifier does not dominate the overall flux noise, and the noise measured is really given by the SQUID. A fair comparison between different SQUID noise levels is hence possible. The Two-Stage system also proved to be useful to detect at glance the bias points of a IVC at which the noise is high due to resonances. Because for the complete CCC-SQUID amplifier we intended to read out the SQUID with a commercial electronics, we studied the suitability of (three different) flux-modulation electronics for the readout of the developed SQUIDs. The applicability of a "standard" flux-modulation electronics for the readout of a specific SQUID depends on the magnitude of the SQUID voltage-to-flux transfer function. Because of the small transfer function of the "CCC matched SQUIDs", the noise measured with "Oxford" commercial electronics (~7 $\mu\Phi_0/Hz^{1/2}$) is limited by the electronics. The noise levels measured with a home-made "19 Channel" and "Conductus" electronics were somewhat better, but the overall noise was still limited by the electronics and not by the SQUID. On the contrary, thanks to their larger transfer function, the real noise of the "80ħ SQUIDs" could be measured with any of the studied electronics. Yet, the Two-Stage system proved more advantageous than a conventional electronics for the readout of SQUIDs affected of resonances (like the "80ħ SQUIDs"), because the sensor SQUID can be "diagonally" (instead of "horizontally") biased at points in the IVC free of resonances.

The operation of the CCC system at frequencies as low as 1-10^{-3} Hz shocks with the large amount of flicker noise of the SQUID at those low frequencies. We investigated two different approaches to reduce the low-frequency noise in our system. On one hand, we

developed Nb/Al dc SQUIDs with different structured washers (including slots and/or holes, a moat and a zipper-slit) to study the reduction of 1/*f* noise owing to hopping of flux vortices trapped in the SQUID process during the cool-down process. We showed that slotted and holed washers could be applied to LTS devices as much as to HTS ones, since the underlying theoretical condition holds in both cases. A gradual reduction of the 1/*f* noise (on average from ~55 to 22 $\mu\Phi_0/Hz^{1/2}$ at 0.2 Hz) was measured for SQUIDs with increasing number of slots. Holes proved to be less effective than slots in reducing the flicker noise. The 1/*f* noise of the SQUIDs with a moat and zipper-slit was smaller than that of a bold SQUID, but the reduction of noise (a factor of 1.5) was on the average less significant than for the slotted SQUIDs. On the other hand, we studied the application to the CCC-SQUID system of a signal modulation technique, which is able to get rid of all low-frequency noise, independent of its origin, by shifting the SQUID operation frequency to the white-noise, higher frequency region. In an experiment designed to test the reduction of noise that could be attained with this method we observed no 1/*f* noise down to frequencies ~0.05 Hz.

A test, 1:1 CCC with direct coupling to a SQUID with matched inductance was build up to learn the practical realization of this configuration, and problems arising from the CCC size. Annealed Nb wire, US wedge bonded to the SQUID chip and soldered by spot welding to the Nb module blocks were used. A very low inductance (<1 nH/m) lead foil construction was used to connect the CCC to the SQUID module. Ideal sensitivity was reached, as predicted by theory. The minimum amount of soldering tin in the fabrication of the CCC and a cryoperm shield should be used to prevent the trapping of flux lines during cool-down, whose relative movement with respect to the large-size CCC due to small vibrations increase enormously the noise.

The knowledge acquired was applied in the fabrication of the large ratio (>1:30 000) CCC system with direct-coupled home-made SQUID. The direct-coupling allowed reaching a sensitivity close to ideal. The ratio error was better than $F<8.7\text{x}10^{-9}$. The flux noise of the CCC-SQUID was ~45 $\mu\Phi_0/Hz^{1/2}$, corresponding to a current input noise (for a 33351-turn winding) of 3.0 $fA/Hz^{1/2}$, measured down to 0.1 Hz. We were able to measure a ~10 pA current, turned from 0 to +*I* every ~30 sec, and being applied to a 10000-turn winding with a current standard deviation of $1\sigma_I$~38 fA. In a SET current measurement, a current standard deviation of the mean around ~35 aA might be expected when using a 33351 turn winding, and measuring the reversing current during 2 h. Consequently, a quantized SET current of 1-10 pA could be measured with a relative uncertainty of $2\text{x}10^{-5}$-10^{-6}. Even better current noise levels could be reached when the system is finally measured at the final destination Dutch National Metrology Institute, where the system can be better shielded and be less affected by floor vibrations.

The establishment of the quantum current standard would allow closing the Quantum Metrological Triangle of electrical units. The experiment, consisting in realizing Ohm's law with the voltage, resistance and current quantum standards, is mainly aimed to verify the degree of coherence of the fundamental constants. Using the 1:30 000 CCC-SQUID system developed and today's best SET device, capable of giving a current of 6.4 pA the triangle might be closed with an uncertainty of $\sim10^{-6}$. If SET/SAW technology improves to yield quantized currents ~1 nA (with metrological accuracy), the triangle could be finally closed with uncertainty $\sim10^{-8}$.

Samenvatting (Summary in Dutch)

Dit proefschrift beschrijft de ontwikkeling van verschillende systemen gebaseerd op de Cryogene Stroom Vergelijker met optimale SQUID uitlezing (afgekort met CCC-SQUID) voor elektrische stroom en weerstand quantum metrologische toepassingen. De CCC-SQUID is de meest nauwkeurige stroomvergelijker dat op dit moment beschikbaar is. De (type I) CCC bestaat uit een supergelidende buis met 2 spoelen met resp. N_1 en N_2 windingen die de twee stromen I_1 en I_2 voeren die vergeleken moeten worden. Ten gevolge van het Meissner effect loopt er een afschermstroom (I_2N_2-I_1N_1) in de buis, waarvan de uiteinden elkaar overlappen als een slang die zijn staart opeet om de spoelen van het leescircuit af te schermen. De magnetische flux ten gevolge van deze afschermstroom is gekoppelt aan de SQUID, de gevoeligste sensor voor magnetisch veld. Een SQUID is een supergeleidende ring die door een (voor een rf SQUID) of twee (voor een dc SQUID) zwakke contacten, zogenaamde Josephson juncties, onderbroken wordt en magnetische flux in spanning omzet.

De werking van een CCC-SQUID wordt bepaald door twee kengetallen: i) De “ratio error” (foutratio) is de afwijking van de stoomverhouding I_2/I_1 ten opzichte van de verhouding van de windingen N_1/N_2, hetgeen drie oorzaken heeft: Lekken van magnetische flux daar waar de buis zichzelf overlapt; resistieve stroomverlies tussen de spoelen; en capacitieve koppeling tussen de draden. Dit laatste beperkt de frequentie van de CCC-SQUID tot 10^{-3}-1 Hz. Foutratios in de orde van 10^{-10} of beter zijn typische waarden. ii) Stroomruis hangt af van de totale systeem fluxruis en de koppeling tussen de CCC en het SQUID, de CCC-SQUID gevoeligheid (de benodigde hoeveelheid stroom in 1 CCC winding om 1 Φ_0 in het SQUID te detecteren. Als het systeem goed afgeschermd is door verschillende supergeleidende en ferromagnetische schilden, dan is de invloed van omgevingsruis te verwaarlozen en wordt de systeemruis gedomineerde door de SQUID ruis welke zo laag mogelijk gehouden moet worden. De CCC-SQUID koppeling hangt af van de grootte van de inductie van de CCC en de SQUID .ingangsspoel; deze moeten dus nauwkeuring bepaald worden. Door het spiegeleffect, de inductie van de CC vlak bij een supergeleidend scherm reduceert tot een effectieve waarde $L_{CCC,eff}$ welke numeriek berekend wordt door middel van eindige elementen methode danwel gemeten wordt bij kamertemperatuur met een impedantie meter bij een voldoende hoge frequentie door een eddy stoom methode. Hier wordt laten zien dat voor een gegeven schermgrootte, de effectieve waarde maximaal is als het oppervlak omsloten door de CCC gelijk is aan het oppervlak tussen de CCC en het scherm.

Er bestaan twee verschillende situaties wanneer het SQUID met een CCC gekoppeld wordt: Als L_i<$L_{CCC,eff}$ dan moet de meetspoel een fractioneel aantal winding hebben; de

benodigde “chariot-wheel” meetspoel is alleen haalbaar voor grote verhoudingen 1/2-1/3. Met commerciele SQUIDs wordt gewoonlijk de andere situatie bereikt namelijk $L_i > L_{CCC,eff}$; derhalve is een meetspeol met $N_s=(L_i/L_{CCC,eff})^{1/2}$ winding noodzakelijk. De (dimensieloze) systeemgevoeligheid vermindert door onvolledige koppeling tussen de CCC en het SQUID. Om dit effect te minimaliseren moeten de windingen van de meetspoel breed over het CCC-vlak verdeeld worden. Bovendien kan een ~10% verbetering behaald worden door tape roll te gebruiken in plaats van een draad meetspoel. Optimale koppeling tussen de CCC en de SQUID kan bereikt worden door de meet spoel op ferromagnetische kernen te rollen die zich in de CCC bevinden; echter door deze kernen wordt extra flickerruis gegenereerd. Een alternatief is de ingangsspoel van het SQUID direct met de CCC buis te verbinden, waardoor automatisch de koppeling optimaal is. In geval de inductanties van CCC en ingangsspoel gelijk zijn dan is de dimensiloze gevoeligheid ideaal en gelijk aan 0.5. De theorie voor de optimalisatie van de CCC-SQUID werking werdt in de ontwikkeling van twee verschillende bruggen toegepast:

- Bruggen gebaseerd op de CCC-SQUID worden gebruikt om de afgeleide weerstand te calibreren met de weerstandsstandaard gebaseerd op het Quantum Hall Effect of om afgeleide weerstanden onderling te vergelijken. De bereikte nauwkeurigheid van $<10^{-8}$ is tenminste één orde groter dan die van bruggen bij kamertemperatuur. Door het gebruik van helium koelmethoden om de CCC-SQUID te gebruiken is zijn toepassing beperkt gebleven tot enkele gespecialiseerde laboratoria. In dit werk is een relatief economisch en gebruiksvriendelijk CCC-SQUID systeem ontwikkeld dat gekoeld kan worden met een commercieel verkrijgbaar en transportabel koelvat (periodiek te vullen buiten de plaats van gebruik). De CCC-SQUID wordt gemonteerd op een telescopische insert waardoor het afkoelen slechts een beperkte hoeveelheid vloeibaar helium kost, ~0.5 l. In dit geval wordt een commercieel rf SQUID gebruikt. De meetspoel die de SQUID aan het CCC koppelt, is aan de binnenkant van de CCC gemonteerd en wordt afgeschermd met loden folie om het effect van bewegende ingevroren flux van de flux transformator te vermijden. Hierna is een geoptimaliseerde stoomvergelijker opgebouwd. Met behulp van de verschil methode is een type A onzekerheid van 7.10^{-9} in de vergelijking van twee 100 Ω weerstanden bereikt. Voor calibratie van grotere verschilratios is een cryoperm afschermschilm noodzakelijk, hetgeen hier achterwege gelaten is vanwege budgetredenen. De betere nauwkeurigheid, eenvoud en lage kosten maken het instrument competitief ten opzichte van kamertemperatuur vergelijkers. De mogelijkheid tot en prestatie van een CCC-SQUID gefabriceerd in YBCO HTS planaire technologie wordt ook beschreven, waardoor afkoeling in een kleine vloeibaar stikstof koelvat mogelijk zou zijn. De geschatte stoom resolutie van 630 pA.turn/$Hz^{1/2}$ zou beter kunnen zijn dan kamertemperatuur CC’s ware het niet dat het grootste probleem de realisatie van een afdoende magnetische afscherming is van de wikkelingen welke een foutratio van $<10^{-7}$ moet garanderen.

- De ontwikkeling van een CCC-SQUID versterker is essentieel voor de ontwikkeling van de toekomstige Single Electron Tunneling (SET) quantum stroom standaard. Op dit moment kunnen SET’s slechts kleine gequantiseerde stromen leveren, van 1-10 pA. Voor metrologische toepassing moet deze kleine stroom versterkt worden tot het niveau van μA zonder verlies van relatieve nauwkeurigheid met behulp van een ultragevoelig, grote ratio CCC-SQUID. Hier wordt de ontwikkling beschreven van een complete grote ratio 1:30.000 CCC, met een optimale uitlezing door een SQUID.

Ter verbetering van de CCC-SQUID stroom resolutie zijn drie verschillende typen Nb/Al dc SQUIDs ontwikkeld om een goede energie resolutie niveau te halen en om direct

met de CCC overlap te koppelen. Deze *"CCC matched SQUIDs"* zijn ontwikkeld om ingangs inducties te hebben die dicht bij de zelfinductie van de CCC liggen. Omdat de SQUID stroom spannings karakteristieken vrijwel geen resonanties hebben komen de ruisniveaus gemeten op elk instelpunt goed overeen met de ontwerpwaarde, ~1.3 $\mu\Phi_0/Hz^{1/2}$. Door een "veilige" McCumber parameter te kiezen van β_c~0.02 was de SQUID transfer functie erg klein ~25 $\mu V/\Phi_0$. De serie *"80ħ SQUIDs"* heeft tot doel om SQUIDs met extreme parameters te onderzoeken om de energieresolutie te maximaliseren. Doordat de McCumber parameter de hysteretische limiet dicht benaderde, werd de SQUID transfer groter tot ongeveer 400 $\mu V/\Phi_0$. De stroom spannings karakteristieken werden sterk beinvloed door resonanties. Op instelpunten vrij van resonanties kwam de ruis dicht in de buurt bij de ontwerpwaarden 1.0-1.3 $\mu\Phi_0/Hz^{1/2}$ terwijl die veel hoger was op de resonantiepieken. De werking van *dubbele bariere Josephson junctie dc SQUIDs* (DBSQs) is ook gedemonstreerd. De relatie tussen de SQUID kritische stroom en de temperatuur wordt quantitatief verklaard in termen van de microscopische theorie ontwikkeld voor dubbele barriere juncties en qualitatief uitgebreid om trapping events in de tussenlaag in rekening te brengen.De effectieve weerstand welke het dynamische gedrag van het SQUID bij 1.4 K bepaalt, heeft een waarde tussen de intrinsieke weerstand en de sub-gap weerstand bij die temperatuur. Het DBSQ werd enigszins aangetast door resonanties. Het beste ruisniveau voor een DBSQ was 3.3 $\mu\Phi_0/Hz^{1/2}$, gemeten op een instelpunt zonder resonanties en was hoger dan de ruis van een vergelijkbaar SBSQ.

Omdat de SQUID transfer over het algemeen vrij klein is, is directe uitlezing van het SQUID met een kampertemperatuur versterker niet mogelijk en moet een speciaal uitlees systeem toegepast worden. De bovenstaande ruisniveaus zijn gemeten met een "Two-Stage" uitleessysteem bestaande uit een eerste trap met een meet SQUID en een tweede trap met een versterkende Double Relaxation Oscillation SQUID (DROS). Dankzij de grote flux naar spanning omzetting bereikt met de twee trapsconfiguratie, wordt de gemeten fluxruis niet door de kampertemperatuur elektronica gedomineerd maar geeft de gemeten ruis die van het SQUID weer. Hierdoor kunnen de verschillende SQUID ruisniveaus op een eerlijke manier met elkaar vergeleken worden. Het twee trapssysteem was ook zeer bruikbaar om in vogelvlucht de instelpunten van de stoom spanningskarakteristiek te vinden waar de ruis groot is door de resonanties. Omdat we de complete CCC-SQUID versterker probeerden uit te lezen met behulp van commerciele elektronica, wordt de bruikbaarheid van drie verschillende flux modulatie elektronica voor het uitlezen van de ontwikkelde SQUIDs beschreven. De toepasbaarheid van standaard flux modulatie technieken voor het uitlezen van een speciaal SQUID hangt af van de grootte van de spanning naar flux transferfunctie. Vanwege de kleine transferfunctie van de "CCC matched SQUIDs" wordt het ruisniveau gemeten met "Oxford" commerciele elektronica, ~7 $\mu\Phi_0/Hz^{1/2}$, gelimiteerd door de elektronica. De ruisniveaux gemeten met de home-made "19 kanaals" en een "Conductus" elektronica waren iets beter maar het algehele ruisniveau werd ook gelimiteerd door de elektronica en niet door het SQUID. Echter dankzij de hoge transferfunctie kon de echte ruis van de "80ħ SQUIDs" met elk type elektronica gemeten worden. Desalniettemin, was het twee trapssysteem beter geschikt voor het meten van SQUID waar resonanties in optraden dan de conventionele elektronica omdat het meetSQUID diagonaal in plaats van horizontaal gevoed kan worden op de instelpunten die vrij zijn van resonanties.

De werkfrequentie van het CCC systeem welke ligt tussen 1 en 10^{-3} Hz bijt met de grootte van flicker ruis in het SQUID bij zulke lage frequenties. Twee verschillende benaderingen zijn gevolgd om deze laagfrequente ruis in het systeem te verminderen. Aan de ene kant zijn Nb/Al dc SQUIDs met verschillend gestructureerde washers ontwikkeld

(zoals washers met "slots"en/of "holes", "moats" of en "zipper-slit" structuren) om het effect van 1/*f* ruis veroorzaakt door het springen van flux vortexen ingevroren in de washer tijdens het afkoelproces te verminderen. Het blijkt dat zulke washers zowel in LTS als in HTS devices toegepast kunnen worden aangezien de onderliggende theoretische principes in beide gevallen geldig zijn. Een geleidelijke afname van de 1/*f* ruis is gemeten bij een toename van het aantal grachten in de washer, gemiddeld genomen van ~55 tot 22 $\mu\Phi_0/Hz^{1/2}$ gemeten bij 0.2 Hz. Gaten blijken minder effectief te zijn dan grachten. De 1/*f* ruis van SQUIDs met structuren als een "moat" en een "zipper-slit" was kleiner dan die van een ongestructureerd SQUID maar de reductiefactor van 1.5 was gemiddeld minder significant dan die van SQUIDs met grachten. Aan de andere kant is er de toepassing van signaalmodulatie in het CCC-SQUID systeem waardoor alle laagfrequente ruis vermeden kan worden door de werkfrequentie te verschuiven naar een hogere frequentie in het witte ruis gebied. In een experiment om deze ruis reductie methode te testen is geen 1/*f* ruis waargenomen tot frequentie van 0.05 Hz.

Een proof 1:1 CCC met directe koppeling aan het SQUID met een gelijke inductantie is getest om zowel de praktische realisatie hiervan te bestuderen als ook de problemen gerelateerd aand deze CCC grootte. Hierbij is gebruik gemaakt van temperatuur behandelde niobium draden, ultrasoon wedge verbonden aan het SQUID en spot-gesoldeerd aan de niobium blokjes. De CCC is verbonden met de SQUID module door middel van een zeer kleine inductance <1nH/m loden folie constructie. De ideale gevoeligheid is bereikt zoals voorwacht was vanuit de theorie. Een minimale hoeveelheid soldeertin moet gebruikt worden in de constructie van de CCC en de cryoperme afscherming om het invriezen van fluxlijnen te voorkomen tijdens het afkoelproces. Juist de beweging van deze fluxlijnen in de grote CCC veroorzaakt door kleine trillingen geven een enorme bijdrage tot de ruis.

Met behulp van de opgedane kennis is een grote ratio CCC, > 1:30.000, gebouwd met een direct gekoppelde home-made SQUID. Door de directe koppeling werd een gevoeligheid bereikt die bijna ideaal was. De foutratio was beter dan $F<8.7\text{x}10^{-9}$. En de fluxruis van de CCC-SQUID was ~45 $\mu\Phi_0/Hz^{1/2}$ wat overeenkomt met een stroomingangsruis van 3.0 $fA/Hz^{1/2}$ (tot 0.1 Hz) voor een 33351 windingen bereikent.
Een stroom van ~10pA is gemeten welke elke 30 sec. veranderde tussen 0 en +*I* in 10.000 windingen met een stroom standaard deviatie van $1\sigma_I$~38 fA. In een SET stroommeting is een stroom standaard deviate van ~35 aA te verwachten bij 33351 windingen en door de omkerende stroom gedurende 2 uur te meten. Hierdoor kan een gequantiseerde SET stroom van 1-10 pA gemeten worden met een relatieve onzekerheid van $2\text{x}10^{-5}$-10^{-6}. Betere stroomruisniveaux kunnen bereikt worden door de uiteindelijke metingen te door in het Nederlands Meetinstituut waar het systeem beter afgeschermd zal zijn tegen velden en trillingen

De realisatie van de quantum stroom standaard zou het mogelijk maken om de Quantum metrologische driehoek van elektrische eenheden te sluiten. Het experiment, het verifieren van de wet van Ohm met de quantum standaarden voor spanning, weerstand en stroom, is voornamelijk bedoeld om de coherentie tussen de verschillende natuurconstanten te controleren. Met behulp van het ontwikkelde 1:30.000 CCC-SQUID systeem en het huidige beste SET device, welke een stroom geeft van 6.4 pA kan de driehoek gesloten worden met een nauwkeurigheid van $\sim10^{-6}$. Als de SET/SAW technologie verbetert tot gequantiseerde stromen van ~1 nA met metrologische nauwkeurigheid te kunnen leveren, kan de driehoek eindelijk gesloten worden met een nauwkeurigheid van $\sim10^{-8}$.

Resumen (Summary in Spanish)

Esta memoria de tesis describe el desarrollo de sistemas basados en el Comparador Criogénico de Corriente con sistema óptimo de lectura SQUID, para uso en aplicaciones de metrología cuántica de resistencia y corriente. El CCC-SQUID es actualmente el comparador de corriente más preciso que existe. Un CCC (de tipo I) esta formado por un tubo superconductor que contiene dos (o más) bobinados N_1 y N_2, por los que circulan las dos corrientes I_1 y I_2 a comparar. Como resultado del efecto Meissner, circula una corriente igual a (I_2N_2-I_1N_1) por el tubo (el cual se superpone sobre sí mismo como una "pescadilla que muerde la cola", para aislar los bobinados del sistema sensor). El flujo asociado a esta corriente diferencial es acoplado a un SQUID, que es el detector de flujo magnético más preciso existente hoy en día. Un SQUID es básicamente un anillo superconductor interrumpido por un (SQUID rf) o dos (SQUID dc) contactos débiles, llamados uniones Josephson. Este dispositivo funciona como un convertidor de flujo-a-voltaje.

Un CCC-SQUID se caracteriza por dos figuras de mérito importantes: i) El error de cociente de transformación o "*ratio error"* del CCC es la desviación de la relación I_2/I_1 respecto de la relación entre vueltas de los bobinados N_1/N_2, y es debido al flujo magnético que se escapa del tubo solapado del CCC, y a la fuga de corriente resistiva y capacitiva entre bobinados primarios. Esta última limita la frecuencia de trabajo del CCC-SQUID al rango 10^{-3}-1 Hz. Típicamente puede obtenerse un "ratio error" mejor que 10^{-10}. ii) El *ruido en corriente* depende del *ruido total del sistema*, y del *acoplamiento* entre el CCC y el SQUID, descrito por la *sensibilidad* (o corriente que es necesaria aplicar a una vuelta del CCC para detectar 1 Φ_0 en el SQUID). Si se utiliza un apantallamiento magnético efectivo (consistente en varias pantallas superconductoras y ferromagnéticas), la influencia del ruido ambiental será despreciable, y el ruido del sistema estará determinado por el ruido del SQUID, que deberá por tanto minimizarse. El acoplamiento entre el CCC y el SQUID depende de la magnitud relativa de las inductancias del CCC y de la bobina de entrada del SQUID, las cuales deben conocerse con exactitud. La inductancia del CCC en presencia de una pantalla superconductora se reduce a un valor efectivo $L_{CCC,eff}$ debido al efecto imagen. $L_{CCC,eff}$ puede calcularse numéricamente con ayuda de programas de elementos finitos, o medirse a temperatura ambiente con un medidor de impedancias a frecuencias suficientemente altas mediante un método basado en las corrientes de Foucault. Hemos demostrado que dada una pantalla con diámetro dado, la geometría del CCC que maximiza $L_{CCC,eff}$ es aquella en que el área encerrada por el toroide del CCC iguala el área entre el CCC y la pantalla.

A la hora de acoplar un SQUID a un CCC, pueden darse dos situaciones distintas: Si L_i<$L_{CCC,eff}$, se necesita una bobina sensora con un "numero fraccionario de vueltas", lo cual puede implementarse en una geometría de "rueda de carro"; en la práctica sólo es posible

realizar fracciones sencillas (1/2-1/3). Los SQUIDs comerciales suelen tener una $L_i > L_{CCC,eff}$; y por tanto se necesita una bobina sensora con un numero de vueltas $N_s=(L_i/L_{CCC,eff})^{1/2}$. Debido al acoplamiento no ideal entre el CCC y el SQUID, se observa una disminución de la sensibilidad (adimensional). Para minimizar la reducción, la bobina sensora debería distribuirse a lo largo de la pared del CCC. También puede conseguirse una mejora del ~10% usando una bobina sensora hecha con cinta de plomo en vez de hilo superconductor. En principio, se puede lograr un acoplamiento ideal entre el CCC y el SQUID enrollando la bobina sensora en torno a núcleos ferromagnéticos situados en el toroide del CCC; sin embargo, los núcleos introducen ruido $1/f$ adicional. Otra alternativa es conectar la bobina de entrada del SQUID directamente al toroide CCC, en cuyo caso se obtiene acoplamiento ideal por definición. Si los valores de la bobina de entrada y del CCC coinciden: $L_i=L_{CCC,eff}$, se puede alcanzar la sensibilidad ideal: $S=0.5$. Estos conocimientos teóricos se han aplicado para obtener las mejores prestaciones en los dos tipos de puentes CCC-SQUID:

- Los puentes basados en el CCC-SQUID se vienen utilizando en la calibración de resistencias secundarias respecto de la resistencia primaria Hall cuántica, o en la comparación de resistencias secundarias entre sí. La incertidumbre que se alcanza ($<10^{-8}$) es al menos un orden de magnitud mejor que la de los puentes a temperatura ambiente. Sin embargo, debido a la necesidad de contar con una instalación de recuperación de Helio, el uso de los puente CCC-SQUID se ha limitado a unos pocos laboratorios especializados. La segunda parte de la tesis describe el desarrollo de un puente CCC-SQUID relativamente económico y sencillo, que puede ser enfriado en un dewar de transporte comercial, que puede enviarse a rellenar periódicamente. El CCC-SQUID se montó en un insert telescópico que permite el enfriamiento con un bajo consumo de helio líquido (~0.5 l). Se utilizó un SQUID rf comercial. La bobina sensora se colocó en el interior del toroide CCC, y se apantalló con cinta de plomo para evitar la influencia del movimiento de flujo atrapado dentro del transformador de flujo. Se construyó un nuevo controlador de corrientes optimizado. La incertidumbre (de tipo A) conseguida en la comparación de dos resistencias 100:100 Ω , usando el método del "compensador de diferencias", fue de 7.10^{-9}. Para la calibración de resistencias en una relación mayor seria indispensable la utilización de una pantalla de cryoperm (la cual no se incluyo inicialmente para reducir costes). La simplicidad, reducido coste y mejor incertidumbre de este instrumento resulta competitiva respecto de los comparadores a temperatura ambiente. Estudiamos también la posible realización y características de un CCC-SQUID completamente fabricado en tecnología planar de alta temperatura critica en YBCO, que pudiera ser enfriado en un pequeño dewar de nitrógeno líquido. Estimamos que la resolución en corriente (630 pA.vuelta/$Hz^{1/2}$) podría ser mejor que la de los CC's a temperatura ambiente. El principal problema sería la realización de una estructura que apantallara suficientemente los bobinados primarios para garantizar un *ratio error* $<10^{-7}$.

- El desarrollo de un amplificador CCC-SQUID es crucial para el establecimiento futuro de un estándar de corriente cuántico basado el dispositivo SET (Single Electron Tunneling). En la actualidad, los SET's pueden producir sólo pequeñas corrientes cuantizadas (1-10 pA). Para su uso en metrología, esta pequeña corriente debería ser amplificada al orden de μA (sin perder la incertidumbre relativa) con ayuda de un CCC-SQUID ultra-sensible de ganancia grande. La tercera parte de la tesis describe el desarrollo de un CCC de ganancia (1:30000), con sistema de lectura SQUID óptimo para amplificación de corrientes SET.

Con el objetivo de mejorar la resolución en corriente, hemos desarrollado tres tipos distintos de SQUIDs dc (fabricados en Nb/Al), diseñados para alcanzar una buena

resolución en energía, y poder ser acoplados directamente al CCC. Los "*CCC matched SQUIDs"* se diseñaron de manera que la inductancia de entrada fuera cercana a la inductancia (efectiva) del CCC. Como las curves de corriente-voltaje (IVC's) no presentaron resonancias, los niveles de ruido medidos concordaron bien con los valores de diseño (~1.3 $\mu\Phi_0/Hz^{1/2}$) en cada uno de los puntos de polarización. Como resultado del valor "prudente" escogido para el parámetro de McCumber (β_c~0.02), la transferencia del SQUID fue bastante pequeña ~25 $\mu V/\Phi_0$. Los dispositivos de la serie "*80ħ SQUIDs"* fueron realizados con parámetros mas "extremos", para poder mejorar la resolución en energía. Aproximando el parámetro de Mc Cumber al limite, β_c~1, la transferencia del SQUID aumentó (hasta ~400 $\mu V/\Phi_0$). Las IVC's estuvieron fuertemente afectadas por resonancias. En aquellos puntos libres de resonancias, el ruido medido coincidió aproximadamente con los valores diseñados (1.0-1.3 $\mu\Phi_0/Hz^{1/2}$), mientras que en los puntos resonantes el ruido fue mucho mayor. Se demostró la operación de *SQUIDs dc basados en uniones Josephson de barrera doble (DBSQs)*. La dependencia de la corriente critica del SQUID con la temperatura pudo explicarse mediante la teoría microscópica desarrollada para las uniones de barrera doble, extendida cualitativamente para tener en cuenta los efectos de atrapamiento en la interfase. La resistencia efectiva R_{eff}, que determina la dinámica del SQUID a 1.4 K tiene un valor comprendido entre el valor de la resistencia intrínseca R_N, y la resistencia sub-gap R_{subg} a esa temperatura. El DBSQ estuvo afectado moderadamente por resonancias. El mayor nivel de ruido de un DBSQ (3.3 $\mu\Phi_0/Hz^{1/2}$), medido en un punto libre de resonancias, fue mayor que el ruido para un SQUID (con uniones de barrera simple) equivalente.

Debido a que normalmente la función de transferencia del SQUID es bastante pequeña, el SQUID no puede leerse directamente con un amplificador a temperatura ambiente, y es necesario acoplarle una electrónica de lectura adecuada. Los niveles de ruido arriba mencionados se midieron con un sistema de lectura en dos etapas (Two-Stage), consistente en un SQUID sensor como primera etapa, y un SQUID basado en Oscilaciones de Relajación (DROS) como segunda etapa amplificadora. Gracias a la gran función de transferencia conseguida por el sistema Two-Stage, el ruido del preamplificador a temperatura ambiente no domina el ruido total, y el ruido está realmente dado por el SQUID. Por tanto es posible comparar adecuadamente los niveles de ruido de distintos SQUIDs. El sistema Two-Stage también ha demostrado ser útil para detectar de un vistazo aquellos puntos de operación en la IVC afectados por resonancias. Para el CCC-SQUID amplificador SET final deseábamos utilizar uno de nuestros SQUIDs con una electrónica de lectura comercial ("Oxford"). Por esa razón, se estudio la utilidad de ésta y otras dos electrónicas con modulación en flujo para la lectura de nuestros SQUIDs. La aplicabilidad de una electrónica "estándar" con modulación en flujo depende de la magnitud de la transferencia del SQUID. Debido a la pequeña función de transferencia de los "CCC matched SQUIDs", el ruido medido con la electrónica comercial de "Oxford" (~7 $\mu\Phi_0/Hz^{1/2}$) estuvo limitado por la electrónica. Los niveles de ruido medidos con la electrónica casera de "19 Canales" y la electrónica de "Conductus" fueron algo mejores, pero el ruido total aun estuvo limitado por las electrónicas y no por el SQUID. En cambio, gracias a su gran función de transferencia, el ruido real de los "80ħ SQUIDs" pudo ser medido con cualquiera de las tres electrónicas. Aun así, el sistema Two-Stage demostró ser mejor que una electrónica convencional para la lectura de SQUIDs afectados por resonancias (como los "80ħ SQUIDs"), ya que el SQUID sensor puede polarizarse "diagonalmente" (en vez de "horizontalmente"), en puntos de la IVC libres de resonancias.

La necesidad de operar el CCC a bajas frecuencias 1-10^{-3} Hz está en conflicto con el ruido 1/*f* que presenta el SQUID en ese rango. Hemos investigado dos caminos diferentes para reducir el ruido de baja frecuencia en nuestro sistema. Por una parte, desarrollamos

SQUIDs dc con arandelas (washers) estructuradas de diversos modos (se hicieron *ranuras* ("slots") y/o *agujeros* ("holes"); *fosos* ("moat") y *cremalleras* ("zipper-slit")) para estudiar la reducción de ruido 1/*f* causado por el salto de vortices de flujo atrapados en el SQUID durante el proceso de enfriamiento. Demostramos que los "slots" y "holes" pueden aplicarse a los dispositivos de baja temperatura crítica tanto como a los de alta porque la condición teórica de fondo se cumple en ambos casos. Se midió una reducción gradual del ruido 1/*f* (en promedio de ~55 a 22 $\mu\Phi_0/Hz^{1/2}$ a 0.2 Hz) para SQUIDs con numero creciente de "slots". Los "holes" demostraron ser menos efectivos que los "slots" en la reducción de ruido 1/*f*. El ruido 1/*f* de los SQUIDs con un "moat" o "zipper" fue menor que el ruido del SQUID sin ninguna estructura (usado como referencia), pero la reducción fue en promedio menos significativa (un factor 1.5) que la observada para los "slotted" SQUIDs. Por otro lado, estudiamos la aplicación al sistema CCC-SQUID de una técnica de modulación de la señal de entrada que permite eliminar todo el ruido de baja frecuencia, ya que el punto de operación del SQUID se traslada a la región de ruido blanco a altas frecuencias. En un experimento diseñado para demostrar la reducción de ruido que podría lograrse utilizando este método, no se observó ruido 1/*f* hasta una frecuencia de ~0.05 Hz.

Hemos construido un CCC 1:1 de prueba, con acoplamiento directo a un SQUID con inductancia adaptada, para estudiar los aspectos prácticos en la realización de esta configuración, y los problemas asociados al gran tamaño del CCC. Utilizamos hilo (recocido) de Nb, soldado por ultrasonidos al chip del SQUID y soldado por soldadura de punto a los bloques de Nb del módulo del SQUID. Se empleó una construcción de cinta de plomo de muy baja inductancia (<1 nH/m) para conectar el CCC al modulo del SQUID. La sensibilidad obtenida fue la ideal prevista por la teoría. Se debe usar la mínima cantidad de estaño en la fabricación del CCC y las pantallas de plomo del CCC para evitar el atrapamiento de flujo durante el enfriamiento, cuyo movimiento relativo respecto al CCC de gran diámetro debido a pequeñas vibraciones aumenta enormemente el ruido.

La experiencia adquirida se aplicó en la fabricación de un CCC de gran ganancia (>1:30 000) con detector SQUID directamente acoplado. El acoplamiento directo permitió alcanzar una sensibilidad próxima a la ideal. El error en la relación fue $F<8.7\text{x}10^{-9}$. El ruido en flujo del CCC-SQUID fue ~45 $\mu\Phi_0/Hz^{1/2}$, correspondiente a un ruido en corriente a la entrada de un bobinado de 33351 vueltas de 3.0 $fA/Hz^{1/2}$, medido hasta una frecuencia de 0.1 Hz. Se pudo medir una corriente de ~10 pA, alternada de 0 a +*I* cada ~30 sec, aplicada a un bobinado de 10000-vueltas con una desviación estándar de $1\sigma_I$~38 fA. En la medida de una corriente SET se podría esperar una desviación estándar respecto de la media ~35 aA usando un bobinado de 33351 vueltas, y midiendo la corriente alterna durante 2 h. En consecuencia, una corriente SET cuantizada de 1-10 pA podría medirse con una incertidumbre relativa de $2\text{x}10^{-5}$-10^{-6}. Podrían alcanzarse niveles incluso mejores cuando el sistema sea finalmente trasladado y puesto en funcionamiento en el Instituto de Metrología Holandés (NMi), donde podrá ser apantallado mejor, y situado en un emplazamiento menos sensible a las vibraciones del suelo.

La existencia del estándar cuántico de corriente permitiría cerrar el Triangulo Metrológico Cuántico de unidades eléctricas. Este experimento, consistente en realizar la ley de Ohm con los estándares cuánticos de voltaje, resistencia y corriente, estáa dirigido principalmente a verificar el grado de coherencia de las constantes fundamentales implicadas. Usando el sistema 1:30000 CCC-SQUID desarrollado y el mejor SET disponible en la actualidad capaz de dar una corriente de 6.4 pA, se podría cerrar el triangulo con una incertidumbre de $\sim10^{-6}$. Si los dispositivos SET/SAW mejoraran lo suficiente para poder dar corrientes del orden de ~1 nA (con precisión metrológica), se podría finalmente cerrar el triangulo con incertidumbre $\sim10^{-8}$.

Acknowledgements

Although this thesis turned out already quite thick, there should always be place for gratitude. I would like to thank all the people who helped me reaching this point.

Allereerst wil ik Horst Rogalla bedanken voor de mogelijkheid om dit onderzoek binnen de Lage Temperaturen groep te doen. Jaap Flokstra ben ik dankbaar voor de disscussies, en het aanleren van zijn nauwgezetheid om diepte in het onderzoek te halen. Me gustaría darle las gracias a Conrado Rillo, por darme la oportunidad de trabajar en la Universidad de Zaragoza, por su dirección, y las discusiones que me han ayudado tanto a afinar conceptos. A Javier Sesé le debo gran parte de esta tesis. Tu imaginación, ingenio, unas hábiles y pacientes manos de artesano "zapatero", y tu manera de hacer los conceptos difíciles fáciles me han sorprendido y enseñado cada día. Gert Rietveld wil ik graag bedanken voor de vruchtbare samenwerking vanuit en met het NMi.

Quiero dar las gracias al Servicio de Instrumentación de la Univ. Zaragoza por la construcción de la electrónica del puente, y en particular a Nico por explicármela en la práctica. También me gustaría agradecer a la gente del Taller de Precisión Y Centro Electrotécnico de Artillería el haberme permitido conocer el centro y participar en medidas metrológicas "reales".

Alle AIO's van de LT wil ik bedanken voor de leuke jaren in de vakgroep. In het bijzonder wil ik sommige mensen bedanken voor hun bijdrage aan dit proefschrift. Van de "veteranen": Michiel (altijd klaar om je concepten op een begrijpelijke manier uit te leggen); André en Manuel voor vele discussies op het gebied van HTS SQUIDs en slots; Gert-Jan K. voor mijn eerste lessen Nederlands; Arnaud en Christian die mij de SQUID fabricage hebben aangeleerd; Martin H. en Laura, voor de CCC-SQUIDs "heritage"; en van de "nieuwe generatie": Martin voor je hulp op het experimentele vlak; Alexander en Sasha voor de samenwerking met de double-barrier SQUIDs; en Bert en Prof. Peters om me de gelegenheid te geven om in de BCT kamer te meten…I would like to thank also the students I worked with, from which I learned so much myself: Cornelis, Patrick, Sergio, Raquel en Ana. Voor de technische hulp wil ik graag aan Dick, Frank en Harry S. (ik vond het altijd indrukwekend hoe kon je zo makkelijk de loodzware CCC in de cryostaat zette) bedanken; en Ans en Inke voor het regelen van alle burocratische zaken en voor de gezelligheid.

Muchas gracias a toda la "colonia española" (Javier, Astrid, Elisa, Belén, Emilio, Sonia, Luises…) y francesa (Benjamin, J-Y, Chemama), siempre dispuestos a coger una guitarra, o los pinceles; echar un café, un mus, unas risas, unas "bitterballen" o lo que hiciese falta... A Gloria, Luz y Johaness, María y Nick, gracias por vuestra amistad y por permitirme a veces "intercambiar experiencias" sobre este singular pais. Dankjewel Gert-Jan voor je vrindschaap en om mij je geliefde (en daarom bekritiseerde) land te leren kennen. Bedankt Marc en Nur; Benno, Patricia en...x ? omdat jullie altijd wel tijd vinden om een keer een wandeling te maken of een koffie te gaan drinken. Ik heb veel plezierige momenten bij het koor Musilon gehad: bedankt om mij muziek te brengen in de regenachtige dagen. A María y Oscar, Celia y Rafa, Ana y Félix, Beatrice et Nicolas…haber venido de tan lejos para aguantar la sonrisa en una boda "polar"…

Ik wil van harte mijn Nederlandse familie bedanken, papa en mama S., schoonbroers en zusjes (en Niek), voor jullie warme welkom, steun en liefde gedurende deze jaren. Sobretodo quiero darles las gracias a mis padres y a Cristi, por todo (¿cómo resumir ?): la educación, el cariño, los "15 minutos" diarios de ánimo desde casa…

Tonny, cariño, mijn "zon" om elke "berg" te klimmen…Lo hemos conseguido, y esto acaba de empezar…

Elena Bartolomé

Curriculum Vitae

Elena Bartolomé was born in Zaragoza (Spain) on 21th August, 1974. She graduated with honors from the high school "Miguel Catalán" in June 1992. Thereafter she studied Physics at the University of Zaragoza and obtained her diploma in June 1997. Besides her studies, she performed some research activities in the field of Archaeometry (physics-chemistry applied to archaeology), and participated in several prehistoric excavations organized by the University of Bellaterra (Barcelona, Spain). In 1996, she followed a 4 month "Erasmus" traineeship at the Groupe de Géophysique Nucléaire of the CNRS-Université Joseph Fourier (Grenoble, France). Under the supervision of Dr. G. Poupeau, she studied obsidian artifacts coming from prehistoric sites in Ecuador and Colombia, by means of PIXE analysis (at the AGLAE accelerator, Louvre Museum, Paris) and Fission Trace dating.

In September 1997 she joined as "Research Fellow" the Low Temperature Division of the Applied Physics Dept. at the University of Twente (The Netherlands). Under guidance of Dr. ir. J. Flokstra and Dr. C. Rillo, she investigated the develpment of nearly Quantum Limited SQUIDs for the GRAIL gravity wave antenna and CCC detectors, and obtained in October 1998 the "Tesina" (MSc.) degree at the University of Zaragoza. From October 1998 to March 2002 she performed her PhD at the Low Temperature Division of the Applied Physics Dept., at the University of Twente, under supervision of Prof. H. Rogalla and Dr. ir. Flokstra. Some parts of this thesis were done at the Dept. of Condensed Matter of the University of Zaragoza-CSIC, under the direction of Dr. C. Rillo; and at the Dutch Metrology Institute (NMi van Swinden Laboratorium, Delft), in collaboration with Dr. G. Rietveld. The research focused on the development and optimization of systems based on the Cryogenic Current Comparator with SQUID readout used in current and resistance metrology systems. The results are described in this PhD thesis.